Doctoral   Science

2019-11

Development and Characterisation of High Surface Energy Microstructured Sol-gel Coatings for Sensing Applications

Emma MacHugh

Development and Characterisation of High Surface Energy Microstructured Sol-gel Coatings for Sensing Applications

By

Emma MacHugh

A thesis presented to

Technological University Dublin for the award of PhD

Prepared under the supervision of

Dr Mohamed Oubaha,

Prof. Declan McCormack

and

Prof. Brendan Duffy

Centre for Research in Engineering Surface Technology, FOCAS Institute,

Technological University Dublin, Kevin St., Dublin 8

School of Chemical and Pharmaceutical Sciences

November 2019

Abstract

This study investigates the development of high surface energy photoreactive organic-inorganic hybrid sol-gel coatings for the microstructuration of high-resolution microfluidic platforms and optofluidic biosensor platforms by standard photolithography processes.

To achieve this, the first step of our work consisted of identifying the fundamental physico-chemical processes governing the structuration and surface properties of hybrid organic-inorganic sol-gel coatings. For this purpose, a reference material based on the combination of an organosilane (3-Methacryloxypropytrimethoxysilane, MAPTMS) and a transition metal (zirconium propoxide, ZPO), was firstly developed and characterised. It was highlighted that chemical, physical and combined physical and chemical processes can be performed to impact the structure, morphology and surface properties of hybrid sol-gel coatings. Therefore, our work progressed towards the investigations of chemical strategies that may impact the general properties of hybrid coatings, with a specific objective on the alteration of their surface properties. For this purpose, 3 strategies have identified including (1) to alter the content of transition metal, (2) to vary the hydrolysis degree and (3) to form core-shell nanoparticle by the surface functionalisation of the reference material during its preparation along with the curing process of the coatings. The materials were characterised employing a set of structural, thermal and surface characterisations techniques namely Contact Angle measurements (CA), DLS, DSC, FTIR, ^{29}Si-NMR. Fundamentally, a triangular relationship between the wettability, the condensation and curing process of the coatings was taking place. More specifically, the wettability was governed by the occurrence of parallel and competitive hydroxylation and condensation processes of the coatings.

Having performed the identified chemical strategies, our work has progressed towards the investigations of physical and physico-chemical treatments of the final coatings. Here, the effects of air-plasma, nitrogen-plasma and plasma treatments combined with post-silane

surface functionalisation were performed and the durability of the treatments investigated. Although hydrophobic recovery was observed for all materials, it was found that air-plasma enabled to achieve the most stable surface properties due to the formation of hydrophilic hydroxyl groups at the surface of the coatings.

The next step of the work focussed on the microstructuration fabrication of a microfluidic platform. The photolithography fabrication conditions were established to enable the successful preparation of well-defined microchannels with resolutions ranging from 50 to 500 microns.

Having developed our microfluidic platform, our work concentrated on developing strategies to integrate an optical transducer onto the platform to enable the fabrication of an optofluidic device that may be applied as biosensor, thus demonstrating the potential of our technology for biosensing applications. The biosensor design we proposed consisted of integrated optical waveguides onto microfluidics that would also be fabricated employing a photolithography process. The fabrications conditions of the optofluidic platform were established by considering the required optical conditions that enable efficient light propagation in the waveguides, which can be used as an optical excitation to fluorophores located within sensor spots in the microchannels. The successful demonstration of concept of the optofluidic-based biosensor concept was successfully performed by recording optical emissions of biomolecules fluorophores under optical excitations with the optical waveguides integrated on the microfluidic platform.

The work reported in this thesis has been multidisciplinary requiring chemistry, physics, biotechnology and engineering competencies which have been synergised for the development of the first "whole hybrid sol-gel optofluidic biosensor platform". It is also showing the potential of the proposed technology for applications where functional microstructured coatings are required.

Declaration

I certify that this thesis which I now submit for examination for the award of PhD, is entirely my own work and has not been taken from the work of others, save and to the extent that such work has been cited and acknowledged within the text of my work.

This thesis was prepared according to the regulations for graduate study by research of the Technological University of Dublin and has not been submitted in whole or in part for another award in any other third level institution. The work reported on in this thesis conforms to the principles and requirements of the TUD's guidelines for ethics in research.

TUD has permission to keep, lend or copy this thesis in whole or in part, on condition that any such use of the material of the thesis be duly acknowledged.

_____

Emma MacHugh

November 2019

Acknowledgements

Firstly, I would like to thank my supervisor, Dr Mohamed Oubaha. Your guidance, patience and understanding have been exemplary and without which I would not have been able to achieve everything I have over the last four years.

To Prof Declan McCormack and Prof Brendan Duffy, thank you for always being there to lend a hand when needed.

To all the staff in CREST, thank you for all your help and eureka moments over the last four years.

I would also like to thank all the technical staff in FOCAS and in Kevin St for always being more than willing to lend a hand and help me when I needed it.

A huge thank you to Dr Jennifer Gaughran and Dr Rob O'Connor in the School of Physical Sciences and Dr Barry O'Connell in the NRF in DCU for your invaluable support and help throughout my work in DCU.

I would also like to extend my thanks to Dr Arun Mallick of the photonics research group in TU Dublin, and to Dr Tatsiana Mikulckyk and Mr Greyson Antony of the IEO group in FOCAS for your help and support with the final optical element of my project.

To all my friends and colleagues in FOCAS, thank you for keeping me sane throughout the last four years.

Finally, I would like to whole heartedly thank my family, my parents- Barry and Bernadette, and my brother Tadhg. Without whose unwavering love, support, encouragement and sometimes brutal honesty over the last 4 years has been invaluable and without which I would not have been able to achieve any of this. To my aunt Joan for all the help with proof-reading my thesis. A special thank you to my late uncle, Dr Niall MacHugh for being one of the people who inspired me to pursue a PhD and for being the first person to tell me to "grab this opportunity with both hands".

Abbreviations

APTES: 3-Aminopropyltriethoxysilane

ATR: Attenuated total reflectance

BL: Buffer Layer

BODs: Biological oxygen demands

BPM: Beam propagation method

CA: Contact Angle

CAD: Computer Aided Design

DCU: Dublin City University

DEPT: Distortionless Enhancement by polarisation transfer

DLS: Dynamic Light Scattering

DSC: Differential Scanning Calorimetry

DMSO: Dimethyl sulfoxide

DTA: Differential scanning calorimetry

EDC: 1-Ethyl-3-(3-dimethylaminopropyl) carbodiimide

EDX: Energy dispersive x-ray spectroscopy

ELISA: Enzyme linked immunoabsorbant assay

ETEOS: Ethyltriethoxysilane

FDTD: Finite Difference Time Domain

FRET: Fluorescence resonance energy transfer

FTIR: Fourier Transform Infrared Spectroscopy

FWHM: Full width at half maximum

IEO: Industrial and Engineering Optics

INEPT: Insensitive nucleus enhancement through polarization transfer

IPA: Isopropanol

hCG: Human chorionic gonadotropin

HD: Hydrolysis Degree

HIV: Human Immunodeficiency Virus

GL: Guiding Layer

GPTMS: 3-Glycidoxytrimethoxysilane

LFIA: Lateral Flow Immuno-chromatographic assay

LVDT: Linear Variable Differential Transformer

MAPTMS: 3-Methacryloxypropytrimethoxysilane

MAAH: Methacrylic Acid

MEMs: Micro-electrochemical mechanical systems

MPTS: 3-Mercaptopropyltriethoxysilane

MTEOS: Methyltriethoxysilane

NRF: Nano-Bioanalytical Research Facility

NMR: Nuclear magnetic resonance spectroscopy

NPs: Nanoparticles

OFM: Optofluidic microscope

PBS: Phosphate buffer solution

PCBs: Polychlorinated biphenyls

PCS: Photon correlation spectroscopy

PDMS: Polydimethoxysilane

PGI: Phase Grating Interferometer

PI: Photo-initiator

PL: Protective Layer

PMMA: Polymethylmethacrylate

POC: Point-of-care device

PR: Photoresist

PTEOS: Propyltriethoxysilane

QELS: Quasi-electric light scattering

RCA: Radio Corporation of America

RI: Refractive Index

RIE: Reactive Ion Etching

SCCM: Standard cubic centimetres per minute

SEM: Scanning electron microscopy

TE: Transverse electric

TEOS: Tetraethyl orthosilicate

Tg: Glass transition temperature

TIR: Total internal reflection

TM: Transverse magnetic

TU Dublin: Technological University Dublin

UV-vis: Ultra-violet spectroscopy

VTES: Vinyltriethoxysilane

XPS: X-ray photoelectron spectroscopy

ZPO: Zirconium (IV) propoxide

Table of Contents

Table of Figures

Table of Tables

Table of Schemes

1 Introduction and Objectives

Over the past decade, the biosensor research community has intensively investigated the development of innovative point-of-care (POC) devices often targeting the improvement of the platforms sensitivities for single analyte detection. However, single analyte detection is not always sufficient, especially in the case of early detection of diseases such as the early detection of certain cancers and cardiovascular diseases. In these cases, the monitoring of several analytes in parallel (glucose, cholesterol, triglycerides etc) is necessary. Therefore, the development of multianalyte platforms is one of the most promising methodologies in the medical diagnostic industry.

Most biosensor platforms also require an integrated microfluidic system for the flow of analyte liquids (blood, saliva and urine) onto the sensor areas of the POC. In order to enable a rapid and efficient delivery of these analytes and improve fluid flow within the platform, the surface properties of the microchannels have to exhibit as high surface energy as possible. Unfortunately, to date, most of the materials employed in the fabrication of microfluidics are based on hydrophobic polymers such as polydimethylsiloxane (PDMS) or polymethylmethacylate (PMMA), the most popular being PDMS, and often require external pumps to activate the circulation of the liquids. Relatively low Young's modulus for polymers such as PDMS can make channels fabricated from these materials prone to collapse and deformation more so than other materials such as glass or silicon. Another drawback with using polymers such as PDMS is the non-specific adsorption of biomaterials which can pose a contamination risk for biosensor systems[1]. Optofluidic devices, which incorporate both a microfluidic and optical component onto a single platform have also found use towards biosensor and POC applications.

Therefore, this project aims to address these issues by developing a novel optofluidic sol-gel based biosensor device. Of the most recent materials proposed in the literature for use in biosensor devices, sol-gel materials are amongst the most promising candidates for the development of functional biosensor systems[2]. Sol-gel materials are ideal for thin film deposition and microfabrication of mechanically stable submicron structures[3]. In addition, the tunability and functionality of the surface characteristics of hybrid sol-gel materials makes them ideal for the use in microfluidic biosensor systems to overcome the use of external pumps, by increasing the overall hydrophilicity of the microchannels and to avoid the non-specific binding of biomolecules. This is a clear advantage over the use of PDMS for microfluidic sensor systems. The use of hybrid sol-gel materials for microfabrication has already been demonstrated using 3-Glycidoxytrimethoxysilane (GPTMS) as an alternative to polymers[4], in the fabrication of waveguide based photonic platforms[5], and in biosensors for medical diagnostics[2].

The work undertaken within this project will not only be multidisciplinary in nature, combining expertise in both inorganic and organic chemistry, fluid physics, micro-engineering, biotechnology and microfluidic disciplines but will also combine several innovative aspects of microfluidic device fabrication and biosensor platforms.

The issues addressed above will be carried out by the following objectives:

1. Development of a photocurable reference hybrid sol-gel material.

2. Fabrication and characterisation of a microfluidic platform

3. Fabrication and characterisation of an optofluidic platform

4. Proof of concept of an optofluidic platform towards sensing applications

To our knowledge, this project is the first study that targets the development of a sol-gel-based optofluidic platform for sensing applications. Fundamentally, this project aims at

demonstrating the proposed concept, proposing a new approach for the development of multifunctional biosensor devices. The successful demonstration of the proposed concept may initiate future multidisciplinary and transdisciplinary projects with high socio-economic interests, which may have a direct impact on day to day people's life. These may be in relation with the development of biosensor platforms for the detection of illicit drugs, bio warfare threats and food pathogens, water pollutants and more generally environmental monitoring. The sol-gel material chosen as the photocurable reference material has already shown promise as the fabrication material for biosensor devices [2,5]. To achieve the objectives proposed above, the thesis will be structured into a total of 11 chapters with 7 experimental working chapters. Chapters 1 to 3 will situate the context of our work against the state-of-the-art, present the required scientific and technological concepts as well as describing the materials and characterisation techniques of interest to our study. Chapter 4-7 will investigate various chemical routes to improve the wettability and increase the surface energy of the materials. Chapter 8 investigates both a physical and chemical route to achieve the same objective. Chapter 9 and 10 will concentrate on the microfabrication of the novel microfluidic and optofluidic devices incorporating some of the results from the previous chapters. A brief overview of each chapter is outlined below.

Chapter 1 will introduce the topic and objectives of the work and the novel concepts that will be undertaken.

Chapter 2 establishes the state of the art and introduces the most important concepts, as well as the history and applications of each area of the project, including microfluidics, optofluidics, biosensors and hybrid sol-gel materials.

Chapter 3 presents the experimental techniques used throughout the work as well as the fabrication methods used. For ease, the chapter has been divided into 4 separate sections, surface characterisation, material characterisation, fabrication and optical techniques.

Chapter 4 investigates and defines the photocurable hybrid sol-gel material that will be used as a reference material throughout this work. The chemical and physical strategies for improving the surface properties of this material are discussed to explain the objectives of the following chapters.

Chapter 5 investigates the effects of the curing process and transition metal content on the wettability of the sol-gel coatings. This is the 1st strategy implemented to improve the wettability of the sol-gel coatings and is the first of 3 chemical routes to do so.

Chapter 6 deals with the hydrolysis degree and its role in the hydrolysis and condensation reactions of the sol-gel material and its effect on the wettability of the hybrid coatings.

Chapter 7 focuses on the fabrication of core-shell nanoparticle materials via the incorporation of 4 functional alkoxysilanes- APTES, TEOS, VTES and GPTMS. This is the final strategy within the chemical route to improve the wettability of the materials.

Chapter 8 investigates both a physical and chemical route to improve the wettability and stability of the coatings over a time period of 4 weeks. The coatings will be subjected to a pre –treatment, either N_2 or Air plasma surface modification or a surface treatment of 3 different dilute alkoxysilane washes. The alkoxysilanes chosen were APTES, GPTMS and a mixture of both.

Chapter 9 focuses on the microfabrication and characterisation of both linear micro-channels and a microfluidic sensor platform via a standard photolithography process using the reference hybrid material as the microfabrication material.

Chapter 10 gives an insight into the fabrication, characterisation and testing of a proof of concept optofluidic device towards sensing and bio-sensing applications employing fluorescence optical detection.

Chapter 11 provides an overview of the work undertaken, summarising the conclusions of each chapter and provides some suggestions for further development within the field.

2 Literature Review

2.1 Microfluidics

Microfluidics can be defined as both a science and technology. Scientifically, microfluidics is the study and manipulation of small amounts of liquid flows at a submillimetre and commonly at a micron scale. Technologically, microfluidics are systems with a width/height scale between 100 nm and 100μm which can be simple or complex, mono or multi phasic, inside micrometre size channels[6,7].

2.2 History of Microfluidics

The birth of microfluidics can be traced back to the 1950's with the development of transistors that gradually replaced the lamps used in the manufacture of radios, computers and similar electronic devices. Photolithography development in the 1960's enabled the miniaturisation and integration of transistors on semiconductor silicon wafers. With the advent of micro electro-mechanical systems (MEMs), came microfluidic devices that were initially fabricated using silicon and glass which both relied upon the infrastructure of microelectronics industry.

Very distinct origins of microfluidics lie in the field of microanalytical methods- Gas-phase chromatography (GC), High Pressure Liquid Chromatography (HPLC) and Capillary Electrophoresis (CE). The 1st miniature GC system was fabricated in 1975[6]. When these methods were miniaturised into capillary versions, they revolutionised chemical analysis and made it possible to achieve both high sensitivity and high resolution simultaneously while using very small amounts of a sample [8]. Miniaturisation of such systems during the 1980's and the use of silicon etching techniques gave rise to MEMs, electrochemical systems that typically range in size between 1 - 300 micrometres. The field of molecular biology was also a motivational force for the creation of

microfluidics. During the 1980's with the advent of genomics and other microanalysis, analytical methods were needed that were capable of achieving a high throughput, higher sensitivity and resolution than had been previously seen. Microfluidics provided some of the answers to these problems. During the 1990's scientists researched the possible applications of MEMS in the chemical, biological and biomedical fields[6]. These applications needed to be able to control the movement of liquids in micro-channels and hence the discipline of microfluidics came about. Inkjet printer heads became popular MEMs and "lab-on-a-chip" devices became widely researched. Silicon and glass were used to fabricate the majority of microfluidic devices which relied heavily on the infrastructure of the microelectronic companies[6].

The area of biodefence also had an impact on the development of the field of microfluidics. After the cold war, it was realized that both chemical and biological weapons posed major military and terrorist threats. To counter this, many programmes during the 1990's aimed at developing microfluidic devices that would serve as detectors for both chemical and biological threats. These research programmes were supported by the Defence Advanced Research Projects Agency (DARPA) and the US Department of Defence[9]. The rapid growth of microfluidic technology in academic settings can be attributed to many of these programmes.

During the early 2000's different technologies for the fabrication of microfluidic devices started to emerge mainly on moulding micro-channels in polymers such as polydimethylsiloxane (PDMS). PDMS was widely used as a microfabrication material due to its elastomeric properties, high optical transparency[10] and easy processability (flexibility and moldability).

2.3 Physics of Microfluidics

As microfluidics is the manipulation of small volumes of fluids, the behaviour of these fluids will therefore differ somewhat from fluids at a macroscale[11]. It is also therefore important to understand certain physical phenomena that dominate the behaviour of fluids at the microscale. The behaviour of systems changes dramatically due to strong increases in surface-to-volume ratios when fluidic devices are decreased from the macroscale to the microscale. Microfluidic devices also offer shorter reaction times, smaller reagent volumes and the possibility of parallel operation[12]. Characteristic aspects that dominate the behaviour of fluids at the microscale include: laminar flow, surface tension, surface area to volume ratio, diffusion and fluidic resistance[12]. Some of these aspects are discussed in more detail below.

2.3.1 Reynolds Number

Reynolds number (Re) is a dimensionless parameter that describes the ratio of inertial forces to viscous forces in a fluid. Inertial force is the force arising from the momentum of the fluid. Gradients in viscous stress give rise to viscous forces[13]. Re is given by the following equation:

$$Re = \frac{\rho v l_c}{\eta}$$

Where ρ, v, l_c, and η are the density of the fluid, average velocity, characteristic length of the flow and the viscosity respectively. Re is proportional to the characteristic velocity of the fluid and the length scale of the system. It is inversely proportional to the viscosity of the fluid. The Reynolds number is typically laminar in microfluidic systems. This allows for flow regimes which are highly predictable, as there is little to no mixing of liquids at the microscale. The critical dimension, often the height of the channel, decreases for microfluidics and consequently corresponds to the increasingly small Re number,

typically below 2300. As microfluidic systems decrease in size so does the role of inertial forces in such systems. Convective mixing does not occur at the microscale and as such molecular transport changes dramatically. This allows for highly predictable diffusion kinetics [14].

2.3.2 Surface and Interfacial Tension

The cohesion between liquid molecules at the liquid/gas interface is known as surface tension. The molecules at the surface of a liquid tend to have a higher surface energy than those in the bulk[15]. The interfacial tension arises from the difference of cohesion forces between two materials and is generally applied to two immiscible liquids such as oil and water or at a liquid/solid interface. Both forces play a more dominant role at the microscale compared to gravity at the macroscale which is more dominant[14]. A schematic of interfacial forces on liquid molecules can be seen in Fig. 2.1, the yellow arrows indicate the overall attractive forces acting on the molecule. A higher surface energy will lend itself to more wettable and hydrophilic surfaces while the opposite is true for low surface energy surfaces.
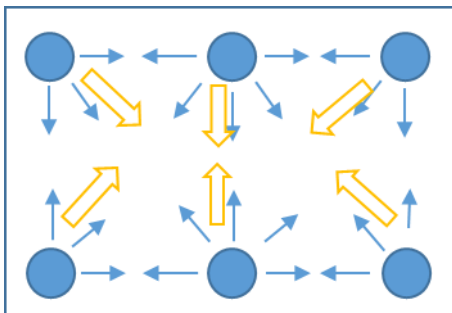
Figure 2. 1: Schematic of interfacial forces in liquid molecules

2.3.4 Capillary Forces

A common means of pumping fluid in microfluidic devices is capillary flow[16]. The movement of a fluid through a narrow constriction such as a porous material or narrow

tube is referred to as a capillary action[14]. The capillary action is due to capillary force, arising from the interfacial tension. Capillary flow results from the pressure differential between a liquid on one side of a meniscus and gas on the other and the interaction of the channel surface with the liquid. Capillary action in a wide and narrow tube is represented in Fig. 2.2. It is a more dominant force at the microscale and allows fluids to advance in opposition to gravity. Glucometers and home pregnancy tests are two examples where capillary forces have been applied to microfluidic applications to manipulate the flow of fluids[14].
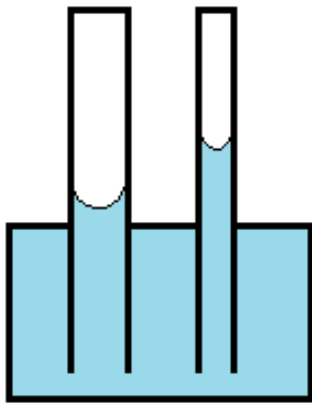
Figure 2. 2: Schematic of capillary action in a wide and narrow tube

2.4 Materials Used in Microfluidics

Materials used for the fabrication of microfluidics include silicon, glass, and various polymers including PMMA and PDMS.

2.4.1 Silicon

Silicon was one of the early materials used in the fabrication of microfluidic devices. The reason being, the strong link between microfluidic devices, MEMS and the microelectronics industry where silicon is one of the most widely used material[17]. Silicon substrates may be etched isotropically, (the Si wafer is etched at the same rate in all

directions), or anisotropically, (the Si wafer is etched unequally due to different crystal planes)[18].

Silicon is a good choice of material for microfluidic devices that have integrated sensors or detectors. There are a large number of well-established techniques using silicon that enable the fabrication of valves[19], pumps[20] and complex structures such as electrospray tips[21], nebulizer chips[22] and micro-reactors[23]. As silicon is opaque to visible and ultraviolet light this makes it incompatible with popular microscopy techniques and also makes optical detection impossible in these spectral domains.

2.4.2 Glass

For many chemical and biological applications glass is the material of choice. Along with silicon, glass was also one of the first materials used in early microfluidic device fabrication[17]. Glass is biocompatible, chemically inert and optically transparent. It is a dielectric material and widely used where electroosmotic flow is applied e.g. for microchip capillary electrophoresis[24]. It also has applications in gas chromatographs and polymerase chain reactions (PCR)[25]. Disadvantages of using glass as a material for the fabrication of microfluidic devices include the high cost of raw materials and its brittleness[17].

2.4.3 Polymers and PDMS

Polymer or elastomeric materials are widely used in the fabrication of microfluidic devices. Different polymer materials with various properties are available: different thermal characteristics, surface chemistry and mechanical stability and deformability. Most polymer materials used do not absorb water and are stable against aqueous acids and bases but swell or dissolve in organic solvents. Cyclo-olefin polymers and thermoplastics- polycarbonate and polymethylmethacyrlate (PMMA) are commonly used

11

materials for the fabrication of microfluidic devices. One of the most used polymer materials for microfluidic applications however is PDMS, which is discussed further below.

PDMS is a mineral organic polymer belonging to the siloxane family of compounds. It is used in cosmetic products, lubricating oils and as a food additive. PDMS was first used by Whitesides in 1998 to fabricate more complex microfluidic devices[26]. Adoption of PDMS as a material for the fabrication of microfluidics can be attributed to several important attributes, including processing, optical and mechanical properties[17]. The fabrication of a small number of microfluidic devices using PDMS is relatively easy, low-cost and suitable for rapid prototyping[17]. PDMS is an optically transparent material for visible light and is suitable for adaptation to optical microscopy. It is a flexible and elastic material. This allows for easy removal from silicon moulds which may be delicate. Its elasticity also allows for the fabrication of actuators and valves. PDMS is also quite thermally stable up to temperature of 200℃. Although PDMS is a hydrophobic material its surface can be modified with plasma treatment or tuned to take on hydrophilic surface properties.

There are several pitfalls to using PDMS as a fabrication material such as the ageing effects of PDMS. Over time the plasma treated hydrophilic surface of the PDMS converts back to its natural hydrophobic state. This limits the performance of the microfluidic device over time. PDMS permeates water vapour and absorbs small hydrophobic molecules such as dye molecules or lipids [27]. PDMS has also shown to be gas and vapour permeable, air bubbles may form during long term use of the microfluidic devices[27].

2.5 Photolithography

Photolithography or optical lithography is a process of transferring a prescribed pattern onto a photosensitive film by using UV radiation to transfer geometric patterns from a photomask to a light sensitive photoresist (PR). It is one of the most commonly used microlithographic techniques in microelectronics and MEM industries and is arguably the most important step in the microfabrication process[18,28].

There are a number of steps involved in a photolithographic process for the fabrication of microfluidic devices. These steps include preparation of the substrate, application of a PR, prebaking or softbaking, UV exposure, and development and removal.

2.5.1.1 Substrate Preparation

Prior to the application of priming agents and to achieve highly reliable devices and improve yield rates, any contaminants on the Si wafer substrate must be removed before microfabrication[28]. Typical contaminants include dust particles, organic residues from any previous processes and metal ions. The films deposited on the wafer and the substrate used will dictate the cleaning procedure used. Radio corporate of America (RCA) is the standard industrial cleaning procedure for silicon wafers. RCA 1 removes organic contaminants whereas RCA 3 removes ionic contaminants. There are 3 major steps to the process-

1. Immersion of the wafers at ~75-80℃ for 10 minutes in a RCA solution of 1:1:5 of NH_4OH: H_2O_2: H_2O. This removes any organic residues or contaminants.

2. The brief immersion of the wafers at room temperature into a solution of 1:50 of HF and H_2O. This step removes the native oxide layer that was formed in the previous step.

3. Immersion of the wafers at 75-80℃ for 10 minutes in a solution of 1:1:6 of HCl: $H_2O_2:H_2O$. This removes any remaining ionic or metallic contaminants present on the wafers.

This RCA procedure is recommended to be carried out immediately before any critical steps in the process are preformed, especially if high temperature processes are being used. After cleaning and to remove any moisture, the wafers are put through a bake out process above 100℃.

In microfluidic and MEM applications or research laboratories a full RCA clean is rarely done. Depending on the nature of contaminants on the wafers steps 1 or 3 may be carried out. An alternative process can be used to remove organic matter using a piranha solution of 3:1 H_2SO_4: H_2O_2.

2.5.1.2 Photoresist Application

The application of a photoresist (PR) occurs after the wafers have been cleaned. A photoresist is a light sensitive polymer that is applied to the wafer as a thin film. The substrate is primed with an adhesion promoter to increase the adhesion of the photoresist to the substrate. Adhesion promotors include; organosilanes such as APTES and GPTMS- a general chemical scheme is shown in Scheme 2.1. PR materials include SU-8 and more recently acrylate and epoxy based sol-gel materials. The PR is generally applied via spin coating deposition. A small amount of PR solution is carefully applied to avoid any air bubbles to a wafer mounted on top of a flat vacuum chuck. The wafer is then spun at high speeds (2000-3000 rpm) to achieve a thin film. The thickness of the film can be controlled by the spinning speed. The thinner the film thickness of the PR the better pattern resolution is. For Si-integrated circuit fabrications the thickness of the film ranges from 0.5-2.0μm. The wafer is then subjected to a soft bake for ~ 1 minute at 75-100℃ to

remove any excess solvents and improve the adhesion of the PR to the wafer substrate. Soft baking densifies and smooths the PR film.
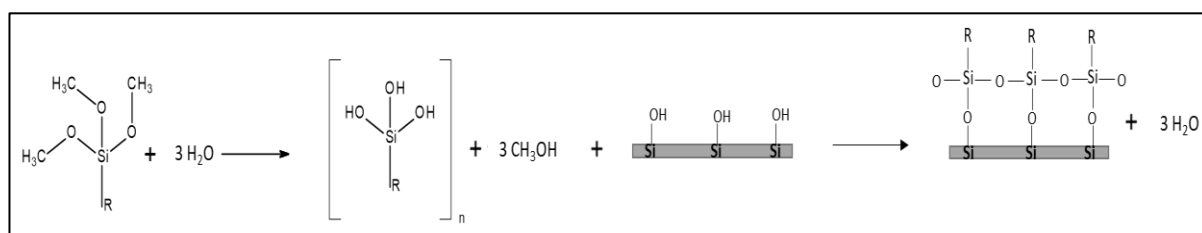
Scheme 2. 1: General reaction scheme of an organosilane adhesion promoter

2.5.1.3 UV Exposure

After the PR application and once it has been soft baked the PR film is exposed to UV light to transfer the geometric pattern from the photomask. Both the photomask and PR are placed into the UV exposure mask aligner instrument. A microscope and micrometre manipulator allow for precise alignment of the fiducial markers on both the photomask and wafer. Correct alignment is critical for the fabrication of a multi-layered structure. The PR is exposed to UV light for a specified time, which is determined by the energy absorption of the PR. The wavelength of light in the exposure machine spans from the deep UV region – 150-300 nm to the near UV region- 300-500 nm. In academic and research laboratories a near UV light source is typically used [28].

2.5.1.4 Development and Removal

Once the PR is exposed to the UV light it is then developed to remove any unwanted regions. For the fabrication of high-resolution patterns control of the development time is critical. Alkaline aqueous solutions and organic solvents are typical developers for positive and negative PRs respectively. Prior to any further step the wafers are subjected to gentle oxygen cleaning to remove any residual layers including adhesion promotors. Any remaining PR layers after the pattern is transferred from the photomask are stripped or etched away.

2.5.2 Photomasks

A photomask is a square plate of either glass or quartz – depending on the type UV radiation being used, that is covered in a patterned layer of opaque light absorbing material and is used to transfer this pattern via UV exposure to a photoresist in order to fabricate microfluidic patterns[29]. This opaque material can either be an emulsion, iron oxide or chromium, and will depend upon what type of photomask is used. Chromium is used as the light absorbing material for binary photomasks. A binary photomask is one in which the geometric design in patterned into the chromium layer itself [30]. Photomasks are generally designed using computer programs such as Computer aided design (CAD). The geometric patterns that can be created from CAD files can vary depending on different parameters such as minimum feature size and tolerance.

2.5.3 Photoresists (PRs)

PRs are used in the microstructuration of patterns from a physical system-generally a photomask. Photoresists can be either positive or negative- depending on their polarity. For positive photoresists, the areas exposed to light will become soluble and dissolve once etched in an aqueous developer and the unexposed regions will remain intact. For negative photoresists the opposite is true, the areas that are exposed to light will polymerise and will stay intact after development in an organic developer whereas the unexposed area will become soluble and be dissolved[28]. A schematic of both a positive and negative photoresist is sketched in Fig 2.3. The pattern obtained from a photomask is therefore determined by the polarity of the photoresist used. Some examples of negative PR's include- SU-8 – an epoxy-based PR and more recently hybrid sol-gel materials have been used as negative PR's. Positive PR's include PMMA.
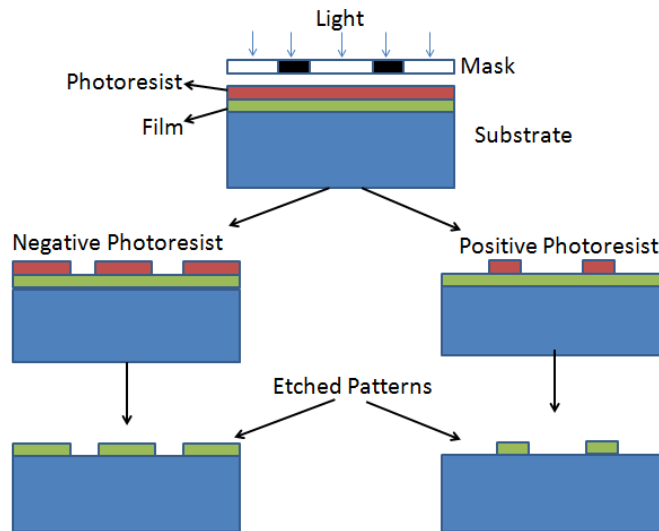
Figure 2. 3: Positive PR vs negative PR [31]

2.5.4 Additive Techniques

Thin-film deposition is an additive technique that deposits or coats a thin film onto a substrate [28]. These thin films can be metallic, semiconducting or insulating and can serve as electrical, mechanical or process assisting components. Therefore, thin films are essential to provide many MEMs and microfluidic devices with a variety of functionalities. There are many different depositions and coating techniques to apply thin films onto substrates- physical vapour deposition e.g. evaporation and sputtering, chemical vapour deposition, oxidation, liquid-phase depositions e.g. spin coating and dip coating, electroplating etc.[28]. The most common liquid phase coating technique for thin film deposition is spin coating. Thin films deposited or grown on a substrate are often characterised using electrical, optical, mechanical or spectroscopic methods to monitor certain properties of the material [28]. These properties include thickness, resistivity, index of refraction, breakdown voltage, transmittance or reflectance, hardness, residual stress etc. Changing process conditions, using different deposition techniques or implanting multilayer structures can be used to adjust the material and film properties to meet the requirements of different applications.

2.5.5 Subtractive Techniques

The transfer or transcription into the substrate of patterns defined in lithography is done using subtractive or etching processes. Reactive ion etching (RIE) can be accomplished by chemical reactions under low pressure, both physical and chemical etching take place simultaneously. This process removes material on the substrate by physical or chemical etching. Etching can be classified as wet etching or dry etching depending on whether the etching medium used is a liquid or a vapour. Etching techniques can be further classified as either isotropic or anisotropic etching depending on the type of etchants used. Isotropic etching etches in all directions at approximately the same speed, whereas anisotropic etching etches in one particular direction. In the case of Si, a common isotropic etchant is HNA, a mixture of HF, HNO_3 and CH_3COOH. Hydroxides of alkalis e.g. KOH, NaOH, CeOH, RbOH, are used as crystal-orientation dependent anisotropic etchants of Si wafers[28]. Removal mechanisms have to do with etching directionality. Physical etching relies on either energy transfer or momentum of ions or photons. Physical etching tends to be anisotropic because of the removal of material in the direction of the highest momentum or energy density. Chemical etching is governed by thermodynamics and reaction kinetics. It tends to be isotropic[28].

2.5.6 Substrate Bonding

Microfluidic platforms must be covered to prevent contamination or interferences towards sensing. In the fabrication of microfluidic devices substrate bonding is very important because of the generation of one-sided cavity structures created by most patterning or pattern transfer techniques. Bonding the substrates seals these cavities and creates enclosed channels for the handling of fluids [28]. Silicon to silicon bonding can be achieved by fusion or direct bonding. Silicon to glass bonding can be achieved by anodic

bonding. Fusion bonding irreversibly binds two mirror polished surfaces to each other either spontaneously or forcibly. Substrates need to be sufficiently flat, smooth and clean for bonding to take place. Fusion bonding is highly susceptible to particle defects. In microfluidic devices and MEMs anodic bonding is used to bond silicon and glass substrates to each other. Silicon devices are typically bonded with a glass top cover because the optical transparency of glass is preferred for characterisation and device testing. The silicon and glass substrates are bonded together using heat- ~400°C, pressure- 100-500 kPa and voltage 1000 V across the device. Glass acts as the cathode and silicon acts as the anode. Anodic bonding is less susceptible to particle defects than fusion bonding, as the glass materials are able to flow around the defect and heal it[18].

2.6. Soft Lithography

Soft lithography is a non-photolithographic technique that is based on self-assembly and replica moulding to carry out both micro and nanofabrication[26]. It uses soft elastomeric polymers for moulding and patterning of substrates. The most common elastomeric element used in soft lithographic techniques is PDMS. The fabrication of a soft polymer block with a patterned relief structure on its surface is a key element in soft lithography[18]. One of the reasons that soft lithography is widely used is due to the fact that it can be performed outside of a clean room[18]. Some of the advantages of soft lithography include; low operating and capital costs, simple fabrication and the capability of relatively rapid prototyping. A number of different soft-lithographic methods exist including micro or replica moulding and micro contact printing. Both these techniques will be discussed in more detail below.

2.6.2 Micro moulding

Micro moulding is a technique that reproduces microstructures onto a polymer substrate via the creation of a master mould. Micro moulding methods include PDMS replication, injection moulding and hot embossing. Bell Labs developed micro moulding techniques using elastomers in the 1970's and these techniques were applied to microfluidics and cell biology in the early 1980's[14]. In recent years PDMS replications has become one of the most common moulding techniques used for the fabrication of microfluidic devices[18]. The moulding template can be fabricated one of two ways, either by patterning a negative PR such as SU-8 onto a Si wafer for precise microstructures or if larger microstructures are needed a PMMA substrate can be directly micro machine[18]. The technique of micro-moulding is both inexpensive and simple and high aspect ratios of the desired microstructures can be obtained in the PDMS substrate. One disadvantage of the PDMS replication is that it is not suitable for mass production of microfluidic devices as the entire process takes several hours. This is due to the various different steps needed to fabricate the moulds, including – degassing the PDMS to remove bubbles, PDMS baking and PDMS bonding. In general and depending on the ratio of PDMS to curing agent the bake out process alone can take between 1-2 hours for a specific mould. Creating the masters for the moulds is also quite time consuming[12]. Microstructures may be fabricated using alternative methods such as hot embossing or injection moulding. These techniques are employed in industry because of their mass production capabilities[18].

2.6.3 Micro contact Printing

Micro contact printing is the transfer of materials both organic and biologically active molecules to a surface in a well-defined pattern [18]. The technique is illustrated in Fig. 2.4. The technique uses a high-resolution elastomeric stamp- usually PDMS, with a

desired convex pattern. The material that is to be transferred from the stamp to the substrate is suspended in solution and this solution is used to wet the PDMS stamp. The stamp is then pressed onto the surface of the substrate and the material is transferred onto the substrate based on the pattern of the PDMS stamp. The material is patterned onto the surface of the substrate once the stamp is removed. This process is used widely in surface chemistry, cell biology and soft electronics[32].
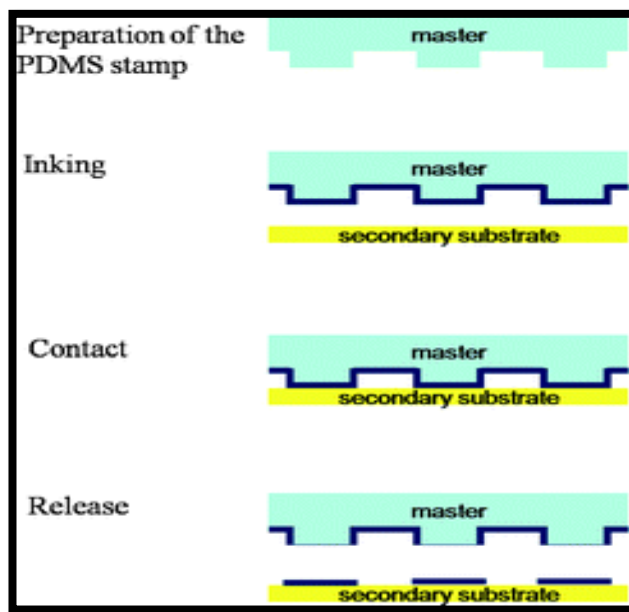
Figure 2. 4: Schematic of micro-contact printing using PDMS stamp[33]

2.7 Applications of Microfluidics

Emerging from a decade of research and development in microfluidic technology a wide variety of applications ranging from inkjet printers, biosensors and point-of–care diagnostic devices to microscale genetic and proteomic analysis kits and high-throughput combinatorial drug screening platforms have been developed. Microfluidics also have applications in a range of scientific fields including physics, chemistry, biology and chemical biology, often in multidisciplinary fields.

Several parameters that are indicative of microfluidic technology can be exploited for many different areas of study. These include the miniaturisation of systems, the smaller samples volumes and the larger surface area to volume ratios. In chemical biology and for biological systems such as cells, and small multicellular organisms this is especially useful. The miniaturisation of systems allows for the manipulation, isolation and examination of cells[34]. Reaction times can also be reduced by introduction of passive or active micro-mixing to combat the absence of turbulence and hence mixing of fluids in microfluidic devices. Passive micro-mixing of fluids in microfluidic devices is generally obtained via the use of mixers and is termed passive as it does not involve any active elements. These include T and Y shaped channels, staggered herringbone mixer and 3D serpentine channels[35,36]. Active micro mixing is obtained by the incorporation of particles which introduces a hyperbolic flow e.g. two dimensional serpentine channels, acoustic waves or magnetic beads[35,36].

For drug delivery, microfluidic technology can enhance the passage of drugs and therapeutic agents into the human body, making drug administration more accessible, portable and efficient. Two areas that microfluidic technology can offer improvements on existing administration is transdermal and pulmonary drug delivery. Microfabricated needles are another way of delivering drugs transdermally. They can offer a pain free alternative to intravenous and intramuscular injection. The needles can be coated or encapsulated with the drug which can then serve as a carrier for transport after insertion[37]. In pulmonary drug delivery, microfluidic technology allows the miniaturisation of the aerosolisation process onto a chip-based device that affords simultaneous production and delivery of drug particles. This also provides more efficient automated, precise and controllable means for generation of monodispersed droplets for optimum respirable size range.

Recently the Whitesides Research Group at Harvard University has developed low cost microfluidic devices that are based on paper and thread. By using a conventional office printer, they have been able to create fluidic circuits in paper that produces a hydrophobic barrier which can selectively block wicking in areas of the paper that are covered in wax ink[38]. Commercial examples of POC microfluidic devices include lateral flow immunochromatographic assays (LFIA). Home pregnancy test strips were one of the first commercially available LFIA microfluidic devices which tested for human chorionic gonadotropin (hCG)[39]. A typical LIFA test strip is represented in Fig. 2.5. It consists of several overlapping components made of various materials. These components include a sample pad, a conjugate pad, a nitrocellulose membrane, an absorbent pad and backing pad. The conjugate pad is modified with a particle – usually colloidal gold. The nitrocellulose membrane contains immobilised proteins which make up the test and control lines. A sample is placed onto the sample pad where it travels to the conjugate pad which contains a dried conjugate particle. The sample re-mobilises the dried particle and the analyte and the particle interact as they travel onto the nitrocellulose membrane which contains the immobilised proteins and the control and test lines. Any excess reagents will be collected by the absorbent pad. Depending on the type of analyte being tested a direct or indirect assay can be used. Direct assays are used for larger analytes such as hCG, or human immunodeficiency virus (HIV). For direct assays a positive result is indicated by the presence of the test line as well as the control line[40].
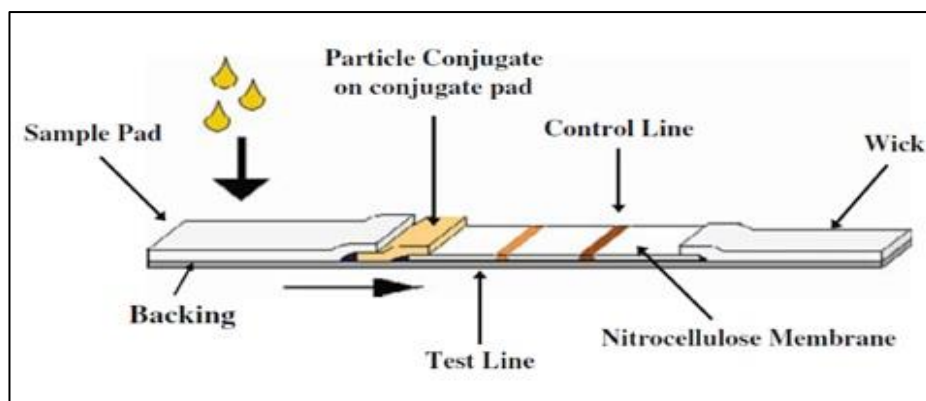
Figure 2. 5: Representative schematic of a typical LFIA test strip[40]

2.8 Optofluidics

Optofluidics or "fluidic optics" is the integration of both optical and fluidic devices onto a single platform. Optofluidic devices most frequently consist of an optical component coupled to a microfluidic platform or a fluidic component that is coupled to a micro-photonic platform[41]. They fundamentally aim at manipulating fluids and light at the microscale and exploiting their interactions to create highly versatile systems[42].

The term "optofluidic" was coined in the early 2000's and referred to a device that integrated both optical and fluidic components on the same platform. The research was supported by DARPA similar to research projects that were conducted into microfluidic devices in the early 1990s[9,43]. Without the advances and understanding of fluidic behaviours at the micro scale, the integration of both optics and fluidics would not have been possible.

Optofluidic devices can be broadly classified into 3 major areas based on their structure and mechanism as described by Psaltis et el[44].

1. Structured solid-liquid hybrids in which the optical properties of both media are relevant. In this case the waveguides are solid and the fluidic channels are liquid examples include an optofluidic microscope (OFM)[45] and zero-mode waveguide sensors[46].

24

2. Complete fluid-based systems, where the optical properties of the fluid are relevant. Both the waveguide and channel are liquid, an example being an optical waveguide where both the core and cladding are liquid – termed an L^2 waveguide[47].

3. Colloid based systems in which the manipulation of solid particles in liquid or by using the unique optical properties of colloidal solutions, form the basis of the optofluidic device. Examples include; colloidal photonic crystals[48].

They can also be classed into 3 categories by their overall purpose as described by Sinton et el[49],

1. Optofluidic light sources that employ fluids as their gain medium (dye lasers).

2. Optical devices that employ fluids to tune or configure optical responses.

3. Fluidic sensors that employ photonic structures.

2.9. Applications of optofluidics

The combination of both an optical and microfluidic component onto a single device, has enabled the exploitation of each field to open up a wide range of applications for these devices. Optofluidic devices have a broad range of different application from photonics, sensing and imaging to healthcare, food and energy. The integration of microfluidics into photonic devices provides a way to tune and reconfigure microphotonic devices at the micrometre scale, a property they lack on their own. Microfluidics also offers a wealth of different ways to control microphotonic devices, laminar flows can transport various nanostructures or species that have desired optical properties efficiently[42]. Optofluidic devices are well suited in particular for biological or chemical analysis and detection in extremely small volumes because of the integration of sample preparation and delivery with the analytical mechanism[50]. This integration of microfluidics into an optofluidic

device enables the exploitation of a number of unique characteristics for biological or chemical analysis. Many optical mechanisms can also be exploited individually or in combination to generate a sensing signal, such as refractive index change, fluorescence, Raman scattering, absorption and polarisation modification. The integration of optical and microfluidics components has also had a great benefit for biosensors, optofluidic biosensors include resonators[51], photonic crystals[52,53] and surface plasmon resonators[43]. The Nano-photonics centre at the University of Cambridge have developed photonic crystals for use in chemical sensing[53].

Within medical diagnostics, optofluidic diagnostic systems can give medical professionals the tools to help people with various diseases in developing countries, such as malaria[54].

2.10 Biosensors

A biosensor can be defined as an analytical device that incorporates a biological sensing element (or bio-receptor) which is connected to a transducer for detection of a specific analyte (Fig. 2.5). The biological recognition element binds to the specific analyte being studied and can be an antibody, antigen, DNA, proteins, enzymes, organelles, etc[55]. A transducer element, which can be optical, electrochemical, piezoelectric, thermal or electric, transforms the signal from the interaction between the specific analyte and bioreceptor into a measurable signal and finally a display device, which is responsible for displaying the analytical results in a manner that is user friendly[56].
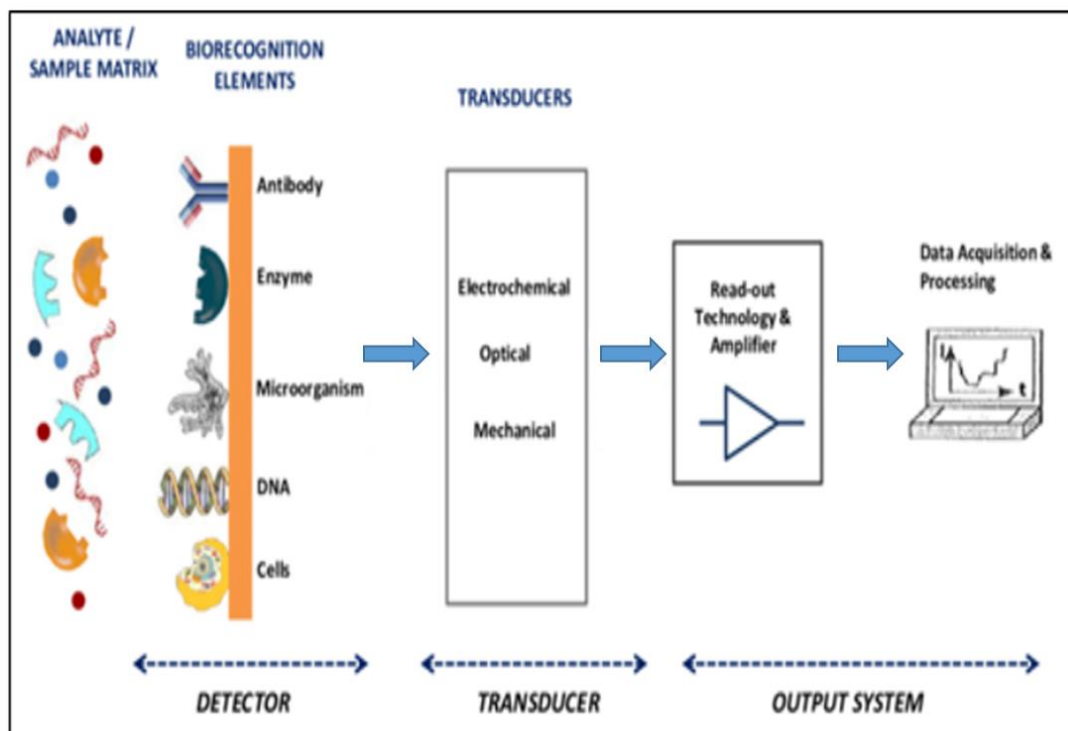
Figure 2. 6: Schematic of the components of a biosensor

2.10.1 History of Biosensors

Clarke and Lyons described one of the first biosensors, for the determination of glucose in 1962. These biosensors were often called enzyme electrodes. It was first patented in 1970 and in 1974 was marketed by the Yellow Stone Instrument Company[57], and was the first commercially available biosensor. The biosensor was based on the fact that the enzyme glucose oxidase catalyses glucose to gluconic acid. Oxygen was used as the oxidising agent and its consumption was followed by the electrochemical reduction at a platinum electrode [57].

Another early biosensor, originally developed by Guilbault and Montalo in 1969, was for the determination of urea, one of the major components of urine. A very simple biosensor for the determination of dopamine was first described in 1985 by Sidwell and Rechnitz[58]. They demonstrated that a banana could be used for the determination of dopamine. Wang

27

and Lin also demonstrated the determination of dopamine using a mixed plant-tissue based bio-electrode in 1988[59].

Over the last few decades, advancements in micro and nanofabrication have led to the miniaturisation of several analytical techniques and the integration of methods such as mass spectroscopy with traditional separation techniques. From these advancements integrated biosensors have been developed that bring together several different operations such as sensing, purification, sample extraction etc., onto a single platform[1].

2.10.2 Types of Biosensors

Biosensors can be grouped or classified according to their biological or transduction elements. Biosensors were originally classed into two categories:

1. Microarray type biosensors that included cantilever or field effect devices with the detection method bases on mechanical changes brought about by the adsorption of target molecules to the sensing elements (cantilever biosensors) or changes in biomolecular charges (field effect devices).

2. Microfluidic and nanofluidic sensors that involved the manipulation of small volumes of fluids which lead to an optical method for detection[1].

Biological recognition elements include antibodies, micro-organisms, organelles, enzymes and biological tissue. Transduction elements include electrochemical, optical, plasmonic, thermal, piezo electric and magnetic devices. Depending on the event that is detected by the biosensor they can be described as catalytic or affinity-based biosensors. Affinity based biosensors operate as a function of either the semi-permanent or permanent binding between both the bio-recognition element and the analyte[60]. When the event detected is the binding interaction between the analyte and the sensing element the biosensor instrument is referred to as an affinity sensor. Affinity based biosensors include

immunosensors- binding between antibodies and antigens, nucleic acid biosensors-binding between the probe and its complementary nucleic acid, and aptameric based biosensors- binding between a ligand and a synthetic oligonucleotide receptor. The type of physiochemical change resulting from a particular sensing event will determine the method of transduction used[60]. Catalytic based biosensors work on the impermanent interaction between the analyte and the bio-recognition element, which involves a chemical reaction which forms a product which is easily detectable. Catalytic biosensor includes cell-based, enzymatic and catalytically active polynucleotide biosensors. These biosensors are very useful for trace analysis.

2.10.2.1 Optical Sensors

Optical biosensors are among the most commonly researched biosensors. They exploit the photometric properties of the bio-recognition elements used. Optical biosensors produce an optical signal which is directly proportional to the concentration of the analyte. They utilise a wide range of bio-recognition elements including- enzymes, antibodies, antigens, nucleic acids and biological tissues[61]. They are highly sensitive and selective and can be cost-effective. Optical biosensors can be broadly classified into two groups, according to their detection method – label-based and label-free detection[62]. In label-based sensors, the bio-recognition molecule or the target molecule is labelled with a fluorescent tag, usually a dye such as Cy5, which will indicate the strength of the interaction between the target molecule and the bio-recognition element via the fluorescence of the particular label used[62]. Therefore label-based detection can also be referred to as fluorescent based detection. The optical signal generated from these sensors is generally via a fluorescent, luminescent or colorimetric method. Examples of biosensors which utilise label-based detection include- DNA, aptameric, quantum dots[63] and fluorescence resonance energy transfer (FRET) based sensors.

In label free sensors, the target molecules are not labelled or altered in any way and are detected via their interaction with the transducer. There are many detection methods for label free optical detection including Raman scattering and optical index change detection. Surface plasmon resonance-based detection devices are common in label-free biosensor areas and are discussed hereafter.

2.10.2.1.1 Surface Plasmon Resonance Devices

Surface plasmon resonance (SPR) biosensor devices use surface plasmons to measure the bio-molecular interactions that occur at the surface of a sensor. The first reported SPR biosensor was by Liedberg et al in 1983 for gas sensing and bio-sensing using various anitbodies[64]. SPR is often used in label free affinity bio-sensing. Surface plasmons are generated at the surface of a metal and a dieletric medium, when the metal surface is illuminated with transverse magnetic polarised light at a specific angle known as the resonance angle[61]. Surface plasmons are measured by monitoring the angle or wavelength at which the energy is transferred. This is observed as a "dip" in the intensity of the reflected light. There are 4 methods to excite the SPR, waveguide coupling, prism coupling, fibre optical coupling and grating coupling. Prism coupling is by far the most common method. The changes in the wave vector of the surface plasmon that is generated at the surface of the sensor is proportional to the concentration of biomolecules affecting the surface optical properties. The operating principle of a SPR device is shown below. It typically consists of an optical detector- which measures the shift in light intensity, a sensor chip with a metallic surface- usually gold, and a layer which enables the immobilisation of ligands, and an integrated fluidics systems which allows for a flow through operation of the device[61]. SPR is an extremely versatile technique and has been employed for a variety of process including environmental monitoring for pesticides[65],

heavy metals and chemical analysis . A detailed review of SPR sensors are given by J.Homola[63].
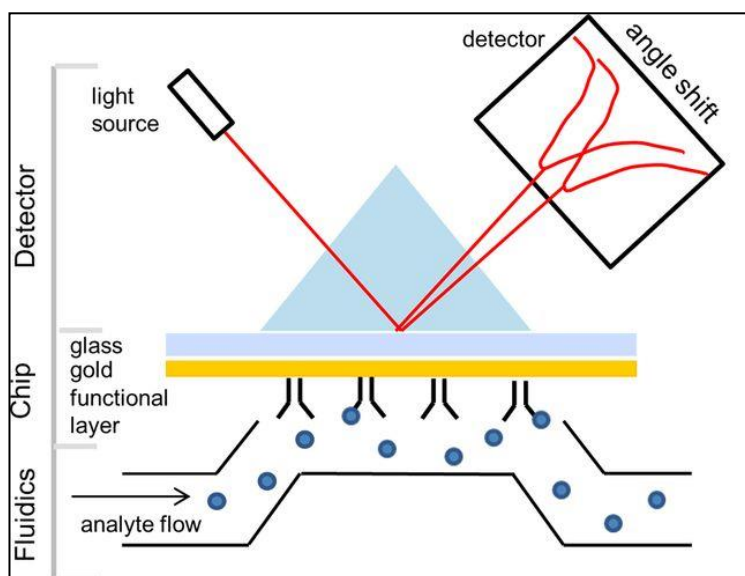
Figure 2. 7: Operating principle of an SPR device[61]

2.10.3 Biosensor Fabrication Methods

2.10.3.1 Bottom-up Methods

In biosensor device fabrication, bottom-up methods rely on the manipulation of materials to build systems one block at a time [1]. Most bottom-up methods are very specific to certain applications. Self-assembly methods can be used to develop polymer structures based on phase separation, or for the formation of monolayers enabling surface modifications. Other methods include pick and place approaches which make use of optical tweezers or atomic force microscopes.

2.10.3.2 Top-down Methods

Top down methods of fabricating biosensor devices involve using conventional and advanced material machining techniques. Top down methods are derived from the more common methods for bulk silicon and glass processing, which remain the more common

methods for the fabrication of biosensor devices[1]. Various lithographic such as UV, electron-beam and nano-imprinting are used to define the channels or other features in the device, which are then etched to form the actual features. UV-lithography or photolithography is one of the most common methods for the fabrication of features within these devices. The polarity of the photoresist will determine the definition of the features. With positive photoresists, the exposed areas are dissolved when placed in a suitable developing solvent. For negative photoresist, the unexposed areas are dissolved when placed in a suitable developing solvent. UV-lithography is frequently used in the fabrication of micro/nanofluidic based biosensor devices, fluidic channels, and Si nanowires[66], and has been discussed in detail in section 2.5.1 above. Although UV-lithography is a cost-effective method for the fabrication of biosensors, problems often arise with uneven photoresist coverage when patterning hierarchical structures. Alterations to the spin step of the photoresist or the use of detachment lithography have been shown to resolve this issue[67].

2.11 Applications of Biosensors

Biosensors have a wide range of applications due the variety and type of biosensor devices available, either commercially or in research. Biomedical diagnostics is one of the major driving forces in relation to the research and development of biosensors. Biosensors have applications in tissue engineering for DNA[68] and nucleic acids[69] . In the food industry, for the monitoring of bacteria including *Listeria monocytogenes*- a bacteria that is found in processed meat and raw milk and *Escherichia coli*-a bacteria that is found in the intestines of both animals and humans and can cause food poisoning[70,71]. Biosensors have also found application in the food industry for the detection of fungal pathogens. They are also used in environmental monitoring of heavy metals like lead,

copper, cadmium, nickel, tin and mercury among other metals[72,73]. Other applications are the detection and monitoring of pesticides, polychlorinated biphenyls (PCBs), nitrogen compounds and microbes and for biochemical oxygen demands (BODs). A more in depth review of the most recent applications of biosensors has been published by J.Ali et al.[74], and M.Parkiha[55]. Within the agri-food sector, the commercialisation of biosensors for food quality and safety, process control and intelligent food packaging have been developed[75]. Companies involved in the commercialisation of biosensors within this sector include; Gwent Sensor Group Ltd, Yellow Springs Instruments and Universal Sesnors, to name but a few. A detailed review of commercially available biosensors within this sector has been published by A.Antonacci et al.[75].

More recently the integration of biosensors into microfluidic devices has become more common, in particular towards POC diagnostics, with the aim of improving the diagnostic capability of a given biosensor. One of the biggest commercially available POC biosensors is for the monitoring of blood glucose for patients with diabetes[76]. A novel glucose biosensor integrated into a microfluidic chip was developed by Hou et al. and reported an increase in the detection of glucose compared to conventional glucose sensors[77]. Urea sensors have also benefited from the integration with microfluidic devices to improve the detection of urea via the co-immobilisation of urease and glutamate dehydrogenase onto a titania–zirconia nanocomposite and integrated into a mediator free microfluidic sensor as reported by Srivastara.S et al[78].

2.12 Sol-gel Materials- Background

The sol-gel process is a liquid phase technique that can be used to prepare bulk metal oxides such as glasses, ceramics and fibres at ambient temperatures. The process involves two steps- the hydrolysis of an inorganic precursor to form a sol, and the subsequent condensation or gelling to form a gel. A sol is suspension of colloidal solid particles within a liquid that is said to be stable. A gel is a porous, 3-dimensional interconnected solid network that expands throughout a liquid in a stable fashion. The gel network structure depends upon both the shape and size of the sol particles[79]. Colloidal gels consist of a solid network of colloidal sol particles, polymeric gels consist of a solid network of sub-colloidal chemical units[80]. Depending on the solvents used, sol-gel process can be divided into two categories- aqueous sol-gel and non-aqueous sol-gel processes[79]. Aqueous sol-gel chemistry is often more complex because of the reactions that can take place between the metal oxide precursors and water[79]. Non-aqueous sol-gel chemistry involves the conversion of a precursor in the presence of an organic solvent and without the presence of water. For this reason, the list of molecular precursors is longer than that of aqueous chemistry and includes not only inorganic metal salts and metal alkoxides, but also metal acetates and metal acetylacetonates. Non-aqueous processes have not gained as much popularity as their aqueous counterparts. The many varied end materials that are possible by means of aqueous sol-gel chemistry include thin films, dense ceramics, fibres, porous aerogels and glasses to name but a few. The advantages of low temperature processing and the chemical inertness of sol-gel materials make them attractive materials for many different applications: antifogging systems for glass surfaces, anticorrosion coatings for metals and most recently as thin films for microfabrication.
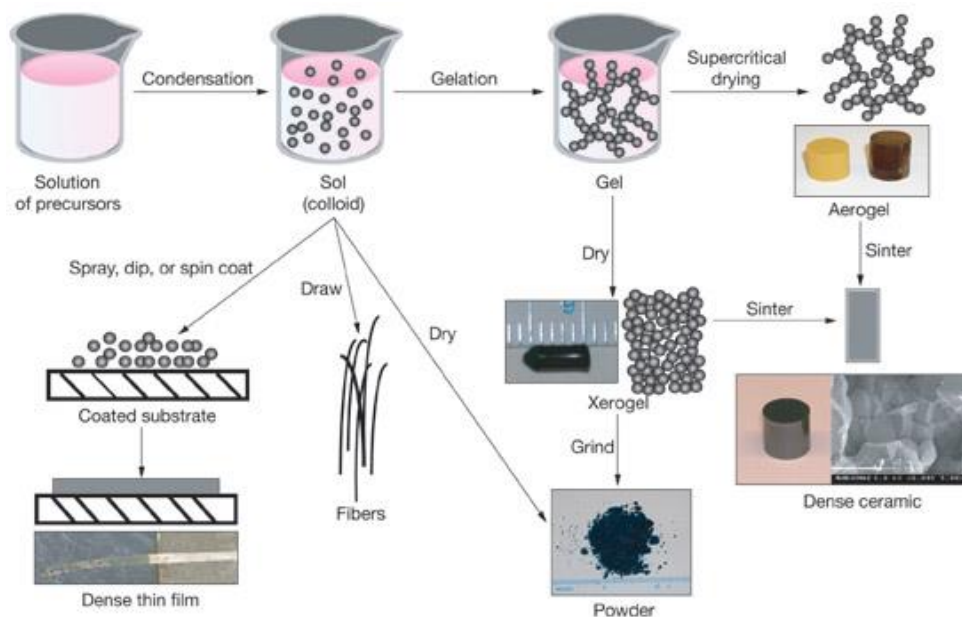
Figure 2. 8: Schematic of the sol-gel process[81]

2.12.1 History of Sol-gel Materials

The discovery of sol-gel materials can be traced back to Ebelman around 1845. He realised that a sample of silicon tetrachloride ($SiCl_4$), once exposed to the atmosphere hardened over a period of months into a glasslike material[82]. During the 1930's, Geffcken recognised that alkoxides could be used for the preparation of oxide films. This process was subsequently developed in Germany by the Schott glass company. At the time there were two working theories on the structure of sols. The first theory regarded the sol-gel as a solid network structure with continuous porosity. Work done by Graham helped supported this theory. He demonstrated that water in a silica gel could be exchanged for an organic solvent. Another competing theory at the time, regarded the gel as an emulsion, or as a coagulated sol with each particle surrounded by a layer of bound water. It was work carried out by Hurd, during the 1930's, that contributed to the theory of the silica sol being a solid network structure becoming widely accepted. He was able to show that a sol must consist of a polymeric skeleton of silicic acid, where a continuous liquid phase is enclosed[83]. In 1932, Kristler developed the first aerogel. He was interested in

35

studying the structure and demonstrating the existence of the solid skeleton of the sol-gel. Around the same time, mineralogists became interested in the use of sols and gels for the preparation of homogenous powders for phase equilibrium studies. Roy later popularised this method in the ceramics community. During the late 1930s and early 1940's antireflection coatings, and binders for inorganic materials were developed. By the early 1960's the sol-gel technique was being used to prepare several metal colloids to form ceramics at ambient temperatures. Hybrid sol-gel materials began to appear during the 1980's and quickly started to be used in the fabrication of materials for optical, electrical, mechanical, and biomedical applications[84].

$$\begin{array}{c} OH \\ | \\ HO-Si-OH \\ | \\ OH \end{array}$$
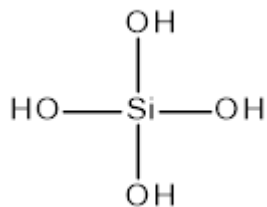
Figure 2.3: Structure of silicic acid

2.12.2 The Sol-gel Process

The sol-gel chemistry process can be defined as a bottom up approach for the synthesis of nanomaterials. The starting materials used in the aqueous sol-gel process include molecular precursors such as organic metal alkoxides or inorganic metal salts. These molecular precursors undergo a series of hydrolysis and condensation reactions to form metal oxopolymers, which will eventually form a colloidal sol. Organic metal alkoxides are among the most common molecular precursors used in the synthesis of sol-gels. This is due to their reactivity and the wide variety of metals available. They have the general formula: $M(OR)_z$, where M is a metal and R is an alkyl group. Some of these metals such as Ti, Si and Zr are available commercially at low costs[79]. These metal alkoxides will be converted into an inorganic polymer network via both hydrolysis and

36

condensation reactions. The hydrolysis of an alkoxide group is shown below in equation 1.

The hydrolysis of the alkoxide occurs in 3 steps.

1. The nucleophilic attack of the metal M, by the oxygen atom of the water molecule

2. The transfer of a proton from the water to an OR group of the metal

3. The resulting ROH molecule is released

$$M - OR + H_2O \rightarrow M - OH + ROH \quad \text{Equation.1}$$
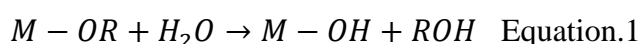
The resulting reactive alkoxide species can then undergo condensation reactions to form the inorganic polymer sol-gel network. Two different reactions can occur depending on the chemical species involved. Oxolation- the condensation reaction between two hydroxylated metal species leading to the release of water, and alkoxolation- the reaction between a hydroxide and alkoxide species leading to the release of alcohol[85].

The reactivity of metal alkoxides including transition metal alkoxides is due in part to the electronegativity of the metal atom. They react readily in the presence of water and without the need for a catalyst. Therefore, the hydrolysis and condensation reactions must be controlled using chemical additives such as chelating agents. Silicon alkoxide have a low electrophilicity and are quite stable against hydrolysis. Hence silicon alkoxide precursors must undergo hydrolysis and condensation reactions in the presence of a catalyst- either an acid or a base to speed up the rate of reaction[85].

Both acid and base catalysts will influence the overall structure of the final condensed sol-gel material. For acid catalysed systems more linear structures are formed and will proceed via SN1 nucleophilic substitution reactions (scheme 2.1). For this reason, the hydrolysis and condensation of the polymer network generally proceeds faster than for base catalysed systems. Base catalysed systems generally undergo SN2 type nucleophilic substitution reactions (scheme 2.2). Under acid-catalysed systems the final gel network

tends to be much more chain like than base-catalysed systems which tend to form highly condensed branch like networks. The reason being that reactions are favoured at terminal Si atoms for base catalysed systems and at centralised Si atoms for acid catalysed systems[86].
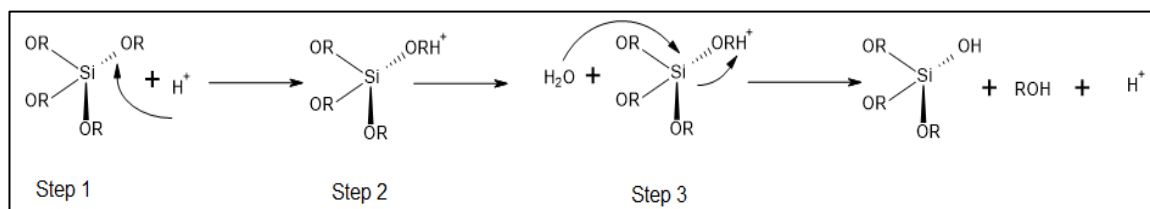
Scheme 2. 2: Mechanism for S_N1 nucleophilic substitution reaction
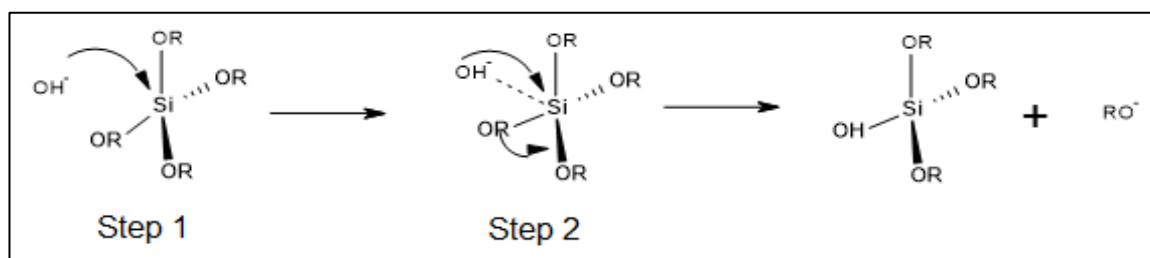
Scheme 2. 3: Mechanism for S_N2 nucleophilic substitution reaction

2.12.3 Hybrid Sol-gel Materials

Hybrid inorganic organic sol-gel materials are another class of sol-gel materials that are composed of both an organic silicate network and an inorganic network. Hybrid materials can be divided into two classes or groups, Class I and II depending on their chemical interactions. These two classes were first described in the early 90's by Sanchez and Ribot[85]. Class I hybrid materials include systems where organic molecules, oligomers or polymers are embedded into an inorganic network. The materials are synthesised by the hydrolysis and condensation of the inorganic compound to form the inorganic network, in the presence of the organic compound or by the polymerisation of the organic monomers in porous inorganic hosts. Weak type interactions between the hosting network and the entrapped species are present. These systems are based on Van der Waals , H-

bonding and electrostatic interactions[87]. Common examples of Class I hybrid material include organic dyes or biomolecules which are incorporated into porous sol-gel matrixes. Class II hybrid materials are composed of materials where the organic and inorganic species are covalently bonded. A schematic representation of both classes of materials is shown in Fig. 2.9.
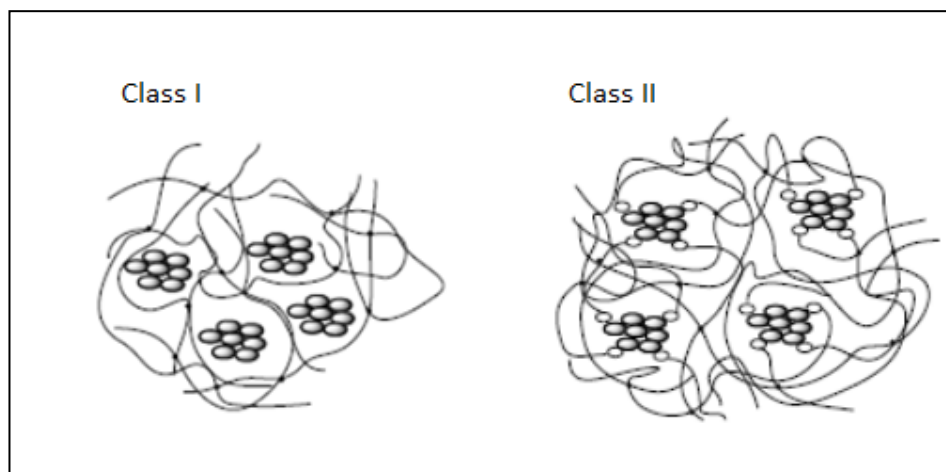
Figure 2. 9: Schematic representation of class I and class II hybrid materials[88]

Organically modified silicates (ORMOSILs) are a family of organic-inorganic materials that can be used in the synthesis of class II hybrid sol-gel materials. Ormosils are derived from tetra functional alkoxysilanes e.g. TEOS, and as such have at least one alkoxide functionality. TEOS is one of the most reported sol-gel precursors and is mostly employed as a network former in the formation of silicate nano porous hybrids[89]. MTEOS, ETEOS and PTEOS are all hybrid silicates with varying substituted alkyl chain lengths. Similarly, to TEOS, these materials can form a silicate-based network. They have all been used as precursors in the fabrication of oxygen sensor films[90]. The alkyl chain length of the precursors can also alter the textural and surface properties of the final materials[91]. GPTMS, MPTS and APTES are all used as silane coupling agents, albeit with very different functionalities. GPTMS contains an epoxy ring and is one of the most widely used hybrid precursors for the synthesis of hybrid sol-gel materials[92]. It has been used for

the fabrication of superhydrophilic coatings for polymer substrates[92] and a hybrid sol-gel material based on GPTMS has been synthesised for use in microfabrication processes [4]. MPTS contains a reactive thiol tail and is commonly used as a coating for the protection of metal surfaces for corrosion prevention[93]. APTES is a silane based ormosil containing an amine functionality and is also used as an adhesion promotor. MAPTMS is used as a crosslinker and the first UV curable hybrid sol –gel materials were based on MAPTMS due to is photo-reactivity capabilities[88]. Table 2.1 summarises the most commonly used ORMOSILs in the preparation of hybrid sol-gel materials.

Chemical Name	Molecular Formula	Abbreviation	Structure
Tetraethylorthosilicate	$C_8H_{20}O_4Si$	TEOS	
Methyltriethoxysilane	$C_7H_{18}O_3Si$	MTEOS	
Ethyltriethoxysilane	$C_8H_{20}O_3Si$	ETEOS	
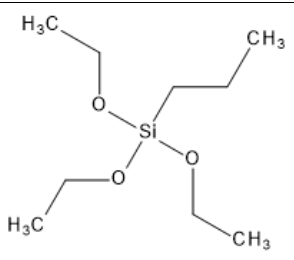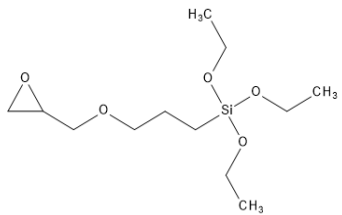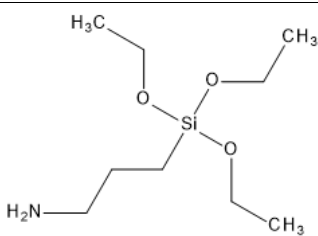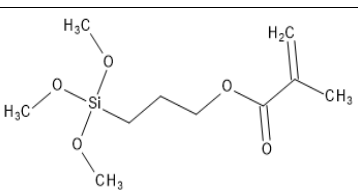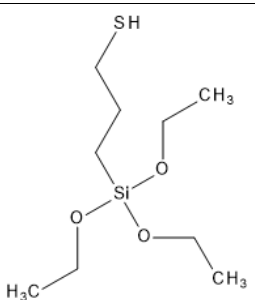
Propyltriethoxysilane	$C_9H_{22}O_3Si$	PTEOS	
3-Glycidoxypropyltriethoxysilane	$C_9H_{20}O_5Si$	GPTMS	
3-Aminopropyltriethoxysilane	$C_6H_{17}NO_3Si$	APTES	
3-Methacryloxypropyltrimethoxysilane	$C_{10}H_{20}O_5Si$	MAPTMS	
Mercaptopropyltriethoxysilane	$C_9H_{22}O_3SSi$	MPTS	

Table 2. 1: Chemical name, abbreviation, molecular formula and structure of some
commonly used ORMOSILS

2.13 Applications of Hybrid Sol-Gel Materials

Hybrid sol-gel materials have a wide range of applications including optical, biomedical, sensing and microfabrication. They also have a wide range of industrial applications as protective coatings for metals and plastics particularly in the aerospace [94] and automotive industries. This wide variety of applications is due in part to the exploitation of various different properties including their mechanical, optical, barrier and electrical properties. Many of the protective coatings that have been developed have exploited either the mechanical properties of the materials, for the development of abrasion resistant coatings for the protection of plastics[95] or their barrier properties, for the development of anti-corrosion coatings for the protection of metals [96].

Apart from these industrial applications, hybrid materials have been used in the development and fabrication of various biosensor platforms- including an optical based platform for use in medical diagnostics[2]. A sol-gel based water vapour sensor incorporating optical waveguides was developed by Skdrla et al.[97]. By incorporating an indicator (erythrosine B) within a porous sol-gel layer and integrated with optical waveguides fabricated from a hybrid silicate/titanium sol-gel material, the detection of water vapour at low ppm concentrations was possible.

A wave-guide based photonic sol-gel sensor for the detection of biofilm formation was reported Elmaghrum et al.[98]. The sensor platform was fabricated using a silicate/zirconate hybrid sol-gel material. By using this platform, it was possible to detect, within the first 10 minutes of sensing test, the formation of a biofilm.

Sol-gel based materials have also found applications in the biomedical field. This is due the tunability of the materials both in their chemistries, which allows control over their size, porosity and morphology[99]. These materials have been used as antimicrobial

bioactive glass materials[100], and as antibacterial coatings for biomaterials when doped with silver ions as reported by Jaiswal et al.[101].

3 Experimental and Fabrication Techniques

Introduction

This chapter outlines the experimental and fabrication techniques employed throughout this work. As the project is multidisciplinary in nature, for clarity the characterisation and fabrication techniques are divided into 4 separate sections;

3.1 Surface characterisation techniques

3.2 Materials characterisation techniques

3.3 Fabrication techniques

3.4 Photomask Design and Fabrication

3.5 Optical properties characterisation techniques

3.1 Surface Characterisation Techniques

The surface characterisation techniques that are used throughout this work are, contact angle measurements, stylus profilometry and optical microscopy. These techniques are employed to investigate the wettability of the sol-gel coatings and the dimensions and morphologies of fabricated coatings and micro-structured sensor platforms.

3.1.1 Contact Angle Measurements

The contact angle technique is used to identify the affinity of a liquid to a surface. The most common study is to identify the hydrophilic or hydrophobic affinity of a surface to water[102]. Other applications include oleophobic characterisation, namely the affinity of a surface for a given oily liquid[103].

The principle of the technique consists of a depositing a drop of a liquid, usually at a microliter level, on a flat surface and measuring the angle formed by the intersection of the liquid solid interface and the liquid vapour interfaces. This angle is defined as the

contact angle (CA). The intersection between all 3 of these interfaces is called the triple point[102]. The CA of a liquid can be represented mathematically by the Young Equation:

$$\gamma_{LG} cos\theta_\gamma + \gamma_{SL} = \gamma_{SG}$$

Where γ_{SG}, γ_{SL} and γ_{LG} are the solid gas, the solid liquid and the liquid gas interfacial tensions respectively and θ_γ is the contact angle. The CA is the degree of wetting of the liquid to the solids surface. When θ=0 there is complete wetting of the surface. Depending on the surface being investigated there are several different techniques that can be used to measure the contact angle. Sessile drop and captive bubble both use optical tensiometry whereas the Whilhemy Plate method uses force tensiometry to measure the contact angle of a particular liquid drop.

For the purposes of this work the sessile or static drop method was used to measure the contact angles of the coatings. Contact angle measurement provide quantitative data on the interfacial energy between a liquid drop and a solid surface. It is also an indirect method to investigate the surface properties of a coating. Specifically, the hydrophilicity and /or hydrophobicity of a coating. If the contact angle is greater than 90° the surface is said to be hydrophobic, similarly if the contact angle is less than 90° the surface is said to be hydrophilic. The most common liquid used is water. A schematic of hydrophilic and hydrophobic contact angles is shown in Fig. 3.1.

Water CAs were measured using the static sessile drop method on the developed hybrid sol-gel coatings. The measurements were taken using deionized water under ambient conditions using an electronic syringe. The measurements were taken using 2 different contact angle goniometers – FTA200 First Ten Angstroms and a Dataphysics OCA Contact Angle (Fig. 3.2). This was for convenience as both instruments were in different locations. Uniform droplets of 5.00 μl of deionised water were dropped onto the surface of the coatings and allowed to stabilise for 10 seconds before digital images of the droplets

were recorded. The images were then analysed using FTA32 Video 2.0 software and SCA 20 software. 6 contact angle measurements were taken for each sample and the average measurement was calculated.
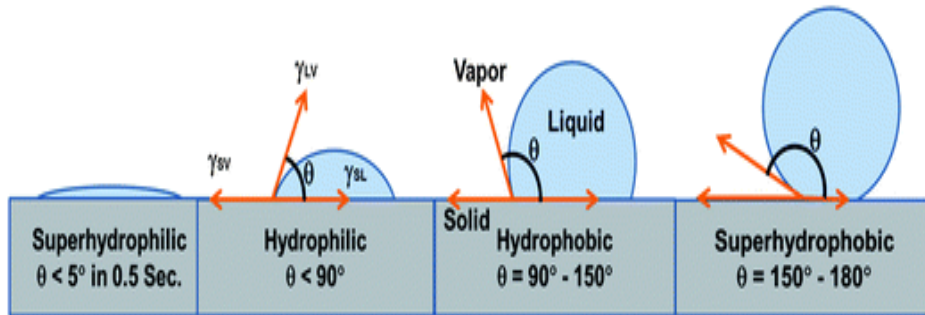
Figure 3. 1 : Schematic of superhydrophilic to superhydrophobic water contact angles[104]
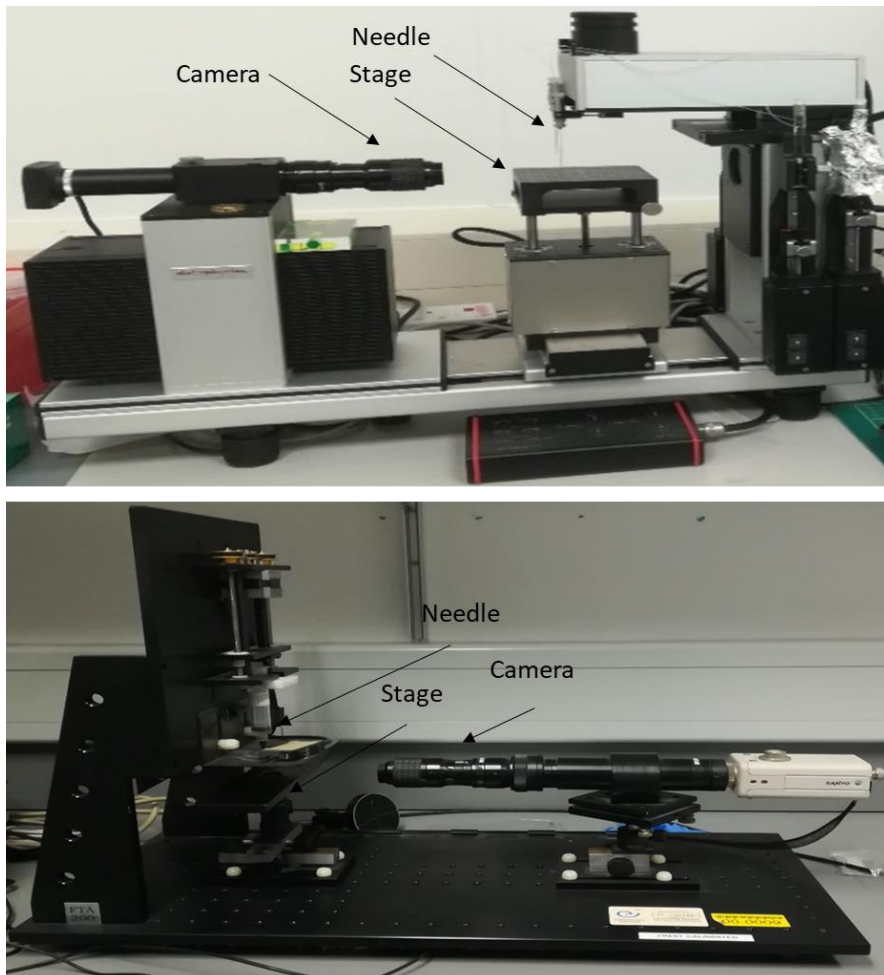
Figure 3. 2: Dataphysics OCA 20 Contact Angle goniometer (top), FTA 200 First Ten Angstroms Contact Angle Goniometer (bottom)

3.1.2 Stylus Profilometry

Contact based stylus profilometry is a technique employed to measure the surface topography of a material including surface roughness. One early application of the stylus profilometer was the use of a Talysurf 1 which was used in the film industry to measure optics[105]. Two common technologies that are used to control the stylus stability or mobility are based on the Linear Variable Differential Transformer (LVDT) and the Phase Grating Interferometer (PGI)[105].

LVDT is the most commonly used technology to control the stylus. It involves taking measurements electromechanically by moving the sample beneath the stylus. The high precision stage moves beneath the stylus via user programmed scan lengths, speeds and stylus force. The stylus is mechanically coupled to the core of the LVDT. As the stage moves, the stylus moves over the sample surface.

The tip of the stylus is a very important factor to consider when choosing the stylus system to use. As the tip is constantly in contact with the surface to be measured it is therefore essential to know as much information about the tip dimensions as possible. The tip needs to avoid as much wear as possible and so hard materials such as diamond are used. The diameter, stylus force and rate of scanning are also critical factors to ensure that the measurement data is correct and there is no damage done to either the stylus tip or the sample[105]. The operating principle of a stylus profilometer can be seen in Fig. 3.3 below.

The step height of the microfluidic channels, sensing spots, pillars and wicking zone of the biosensor platform were investigated using a Bruker DektakXT stylus profilometer (Fig. 3.4). Care was taken not to touch the stylus tip when changing between samples. As the stylus tip made contact with the surface of the samples it was important to ensure they were clean and free of dirt/debris before measurements were carried out. Measurements

were carried out in the Nano-Bioanalytical Research Facility (NRF) in Dublin City University (DCU). The parameters used are outlined in table 3.1 below.

Scan Type	Standard Scan-single acquisition
Profile	Hills and Valleys
Scan Range	$65.5\ \mu m$
Stylus Type	$2.5 \mu m$ radius
Stylus Force	3mg
Length	$6000\ \mu m$
Duration	30 seconds

Table 3. 1: Dektak XT parameters
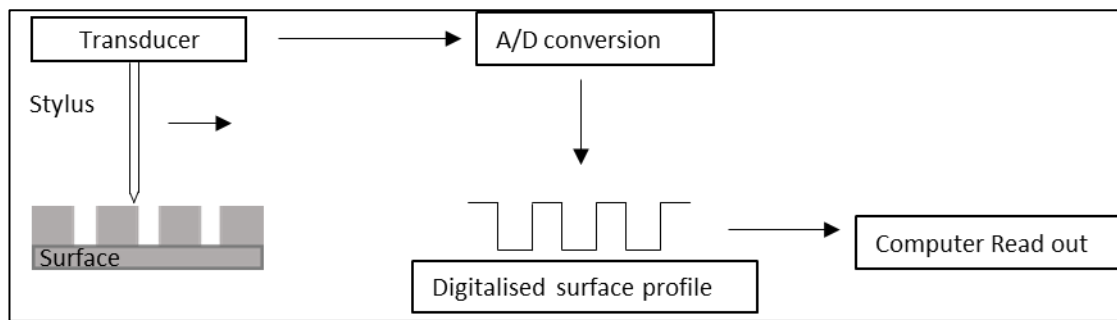
Figure 3. 3: Operating Principle of Stylus Profilometer

Figure 3. 4: Bruker DektakXT

3.1.3 Optical Microscopy

Microscopy is the technique of using a microscope to view samples which cannot be seen unaided by the naked eye. Optical microscopy uses visible and UV light with a system of lenses to magnify an image of small samples. Optical microscopes are the oldest design of microscope and used photographic film to capture an image. Purely digital microscopes now use a charge coupled device (CCD) camera in place of a traditional eyepiece to capture images that are then displayed on a computer screen[106]. However, the principle of basic light microscopy plays a major role in the collection of reliable microscope images for digital analysis. The objective lens selected is a major factor in collecting successful optical images. A schematic of a light microscope is shown in Fig 3.5.

The biosensor platform and the double split waveguide structures were imaged using a Keyence VHX digital microscope (Fig. 3.6). The fluid flow within the biosensor platform was also visualised using the Keyence VHX digital microscope. This system was used in the NRF in DCU.
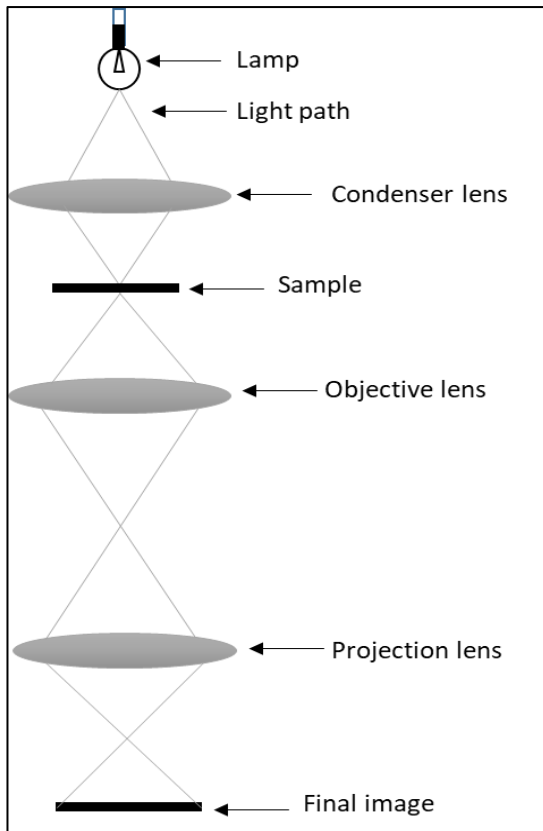
Figure 3. 5: Schematic of a light microscope
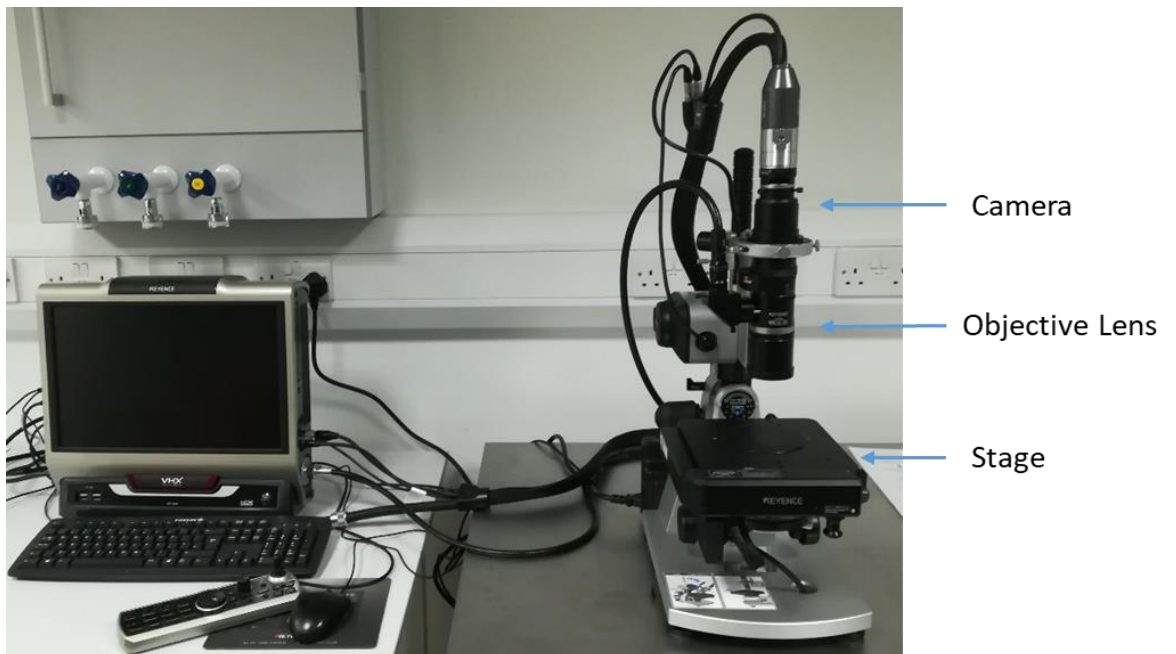
Figure 3. 6: Keyence VHX Digital Microscope

3.2 Materials Characterisation Techniques

The materials characterisation techniques that are used throughout this work and will be further discussed below are, dynamic lights scattering (DLS), differential scanning calorimetery (DSC), Fourier-Transfrom infrared spectroscopy (FTIR), [29] silicon nuclear magnetic resonance spectroscopy (^{29}Si-NMR), scanning electron microscopy/energy dispersive x-ray microscopy (SEM/EDX) and x-ray photoelectrcon spectroscopy (XPS). These characterisation techniques will be employed to investigate the structure, composition and thermal properties of the materials.

3.2.1 Dynamic Light Scattering (DLS)

Dynamic light scattering (DLS) is a technique used in chemistry, biochemistry and physics to study the time dependent fluctuations in the intensity of scattered light due to particles in solution. It is also called quasi-electric light scattering (QELS) or photon correlation spectroscopy (PCS)[107]. These fluctuations are known as Brownian motion. By processing the fluctuations of the intensity of scattered light, the size distribution and the zeta potential of the particles can be determined. It is important to note that small particles will diffuse faster than larger particles in a system undergoing Brownian motion[108]. DLS also allows determination of the size distribution of the particles and the diffusion coefficient. It is a non-destructive technique and is an extremely popular technique used in the characterisation of polymer solutions and colloidal suspensions. The fluctuation of scattering intensity of different sized particles is shown below in Fig. 3.7.

In our study, the particle size of the materials was investigated using a Malvern Nano Zs instrument (Fig.3.9). However, to avoid scattering and to achieve a system where particles are in a quasi-isolated environment (Fig. 3.8), the liquid sol-gel materials were diluted in

isopropanol (IPA) in a ratio of 95:5 %v/v, IPA : sol and filtered using a 0.45 µm Whatman syringe filter prior to each run. This filtration step is essential to eliminate contaminating particles that may originate from the environment as the experiments are performed in a non-clean-room laboratory.
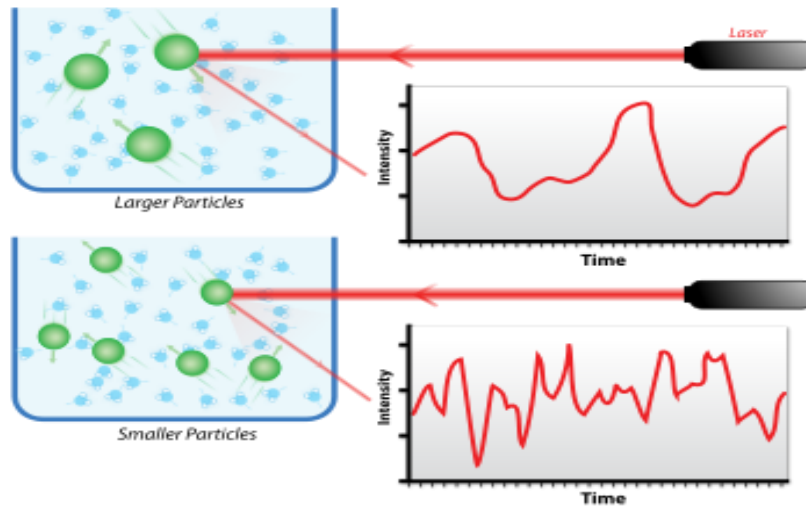
Figure 3. 7: Time dependent fluctuations of intensity of scattered light due to different size particles[109]
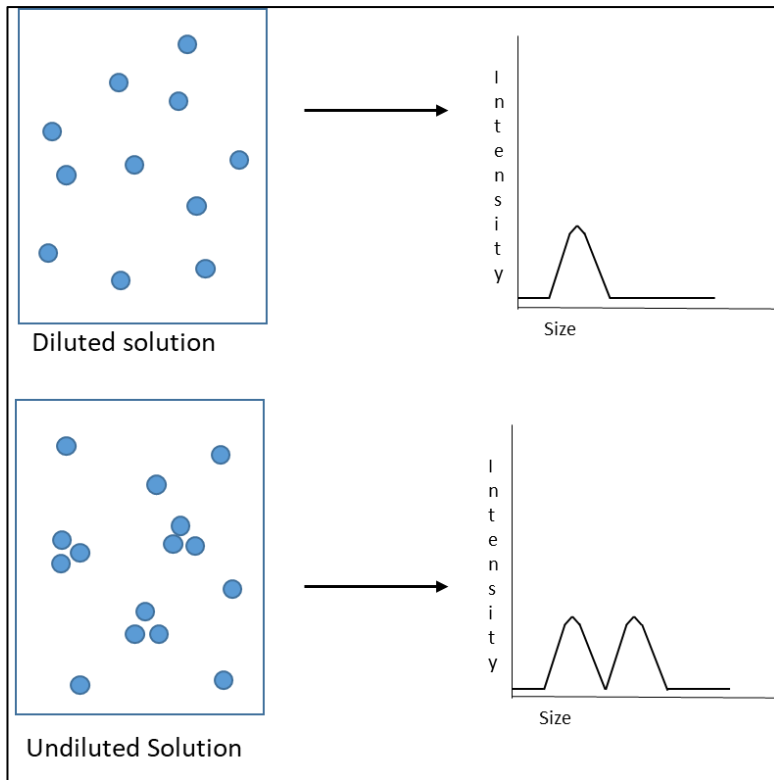
Figure 3. 8: Effect of dilution on the sol-gel particle size using DLS
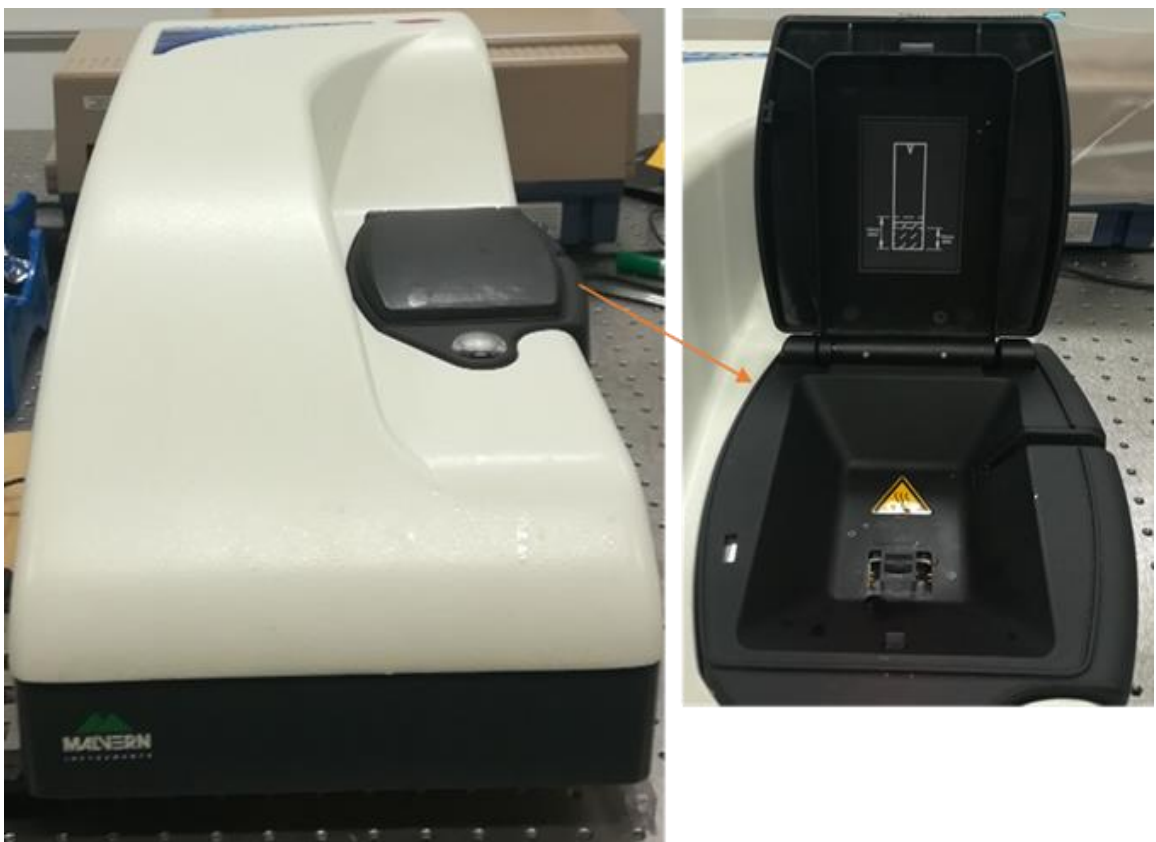
Figure 3. 9: Malvern Nano Zetasizer

53

3.2.2 Differential Scanning Calorimetry (DSC)

Differential scanning calorimetry is a thermal analytical technique employed to determine the thermal exchange (enthalpy and specific heat) of a material with its environment as function of an applied temperature against a reference sample. There are two types of DSC setups currently available including heat-flux and power compensation. In power-compensated DSC, both the sample and reference material are maintained at the same temperature, and are enclosed in separate furnaces[110]. In heat-flux DSC, also known as calorimetric differential thermogravimetric analysis (DTA), the sample and reference material are placed in similar holders on separate thermal conducting bases and are enclosed in a single furnace. Both the sample and reference are connected via thermocouples. A schematic of both a heat-flux DSC and a power compensated DSC are shown below in Fig. 3.10. Heat -flux DSC was used for this work.
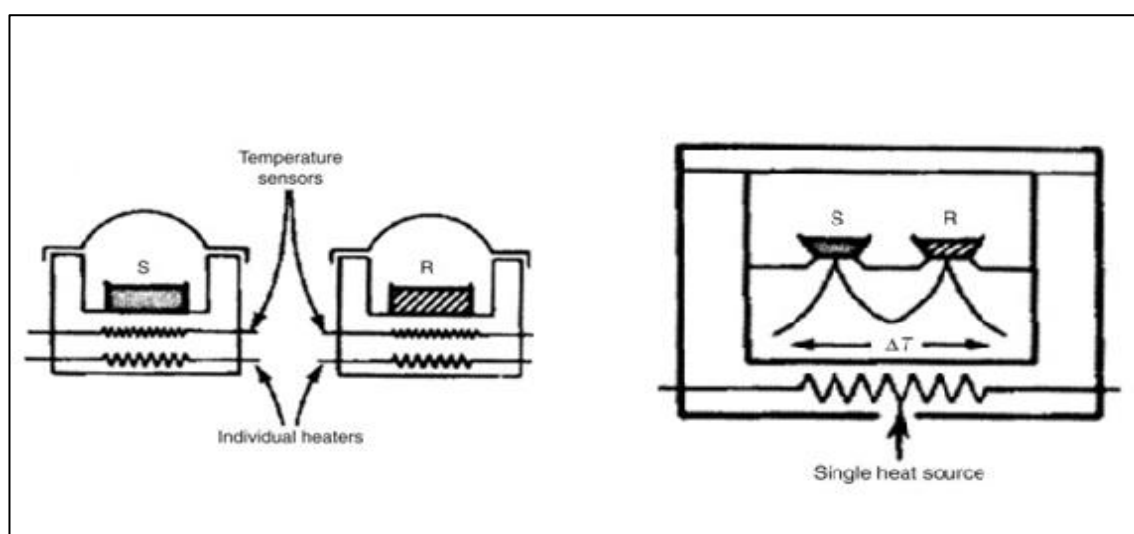
Figure 3. 10: Classical apparatus for : Heat –flux DSC (right) and power compensated DSC (left) (S= sample, R=reference)[111]

In power compensated DSC endothermic responses in the material are represented as being positive, above the baseline whereas in heat flux DSC the opposite is true, as the temperature of the sample lags behind the temperature of the reference, endothermic

54

responses are below the baseline and therefore negative. A schematic of a typical curve for heat-flux DSC is shown below in Fig. 3.11. As previously mentioned in heat flux DSC endothermic peaks are below the baseline and represented as negative i.e. downward peaks.

The thermal behaviour of the liquid sol-gel materials over a specific temperature range were investigated using DSC. 10 μl of sol were pipetted into an aluminium pan and placed in the chamber. Measurements were carried out using a Shimadzu DSC QC instrument (Fig. 3.12) under an air atmosphere and a heating rate of 5°C/min between 25 and 300°C.
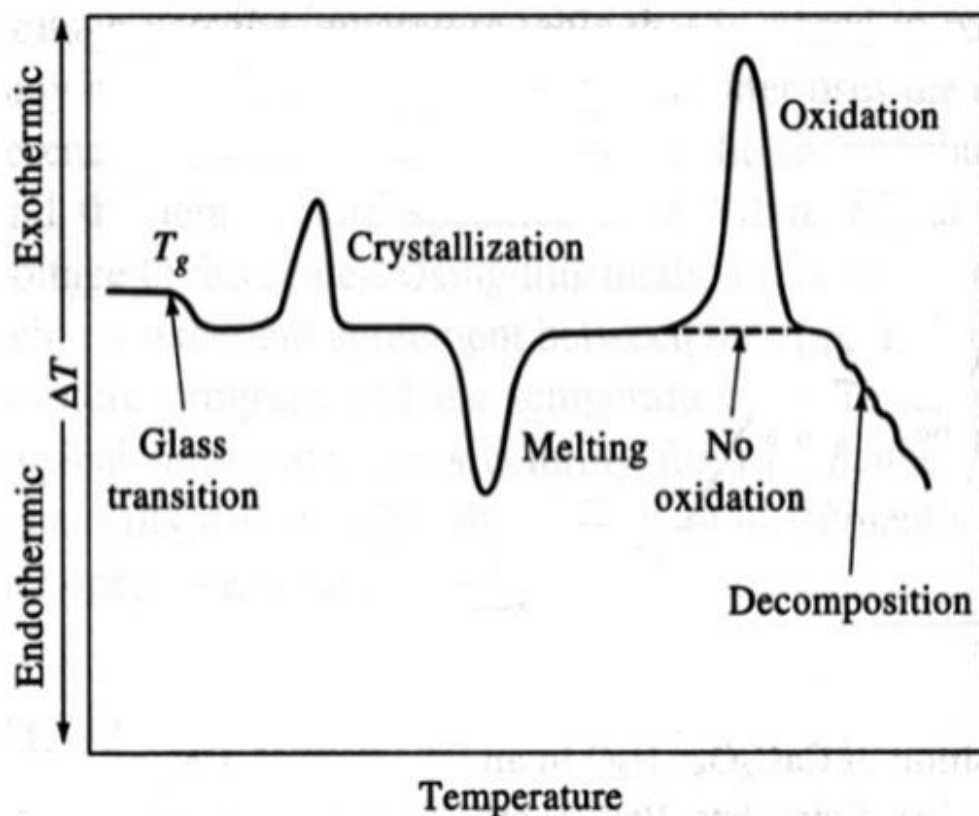
Figure 3. 11: Typical heat-flux DSC curve[112]

Figure 3. 12: Shimadzu DSC

3.2.3 Fourier-Transform Infrared Spectroscopy (FTIR)

Fourier-Transform Infrared (FTIR) spectroscopy is an analytical technique that is used to characterise the absorption of a material in the $400 - 4000$ cm^{-1}. Infrared spectra are exploited to identify the chemical groups present in a given material and as such is a technique of choice in materials science and chemistry for the identification of both inorganic and organic molecules. Samples can be in almost any form including liquids, gases and solids. It can also be used in the analysis of both bulk and thin films[113], and the experiments can be run in transmission or reflection modes, the latest being called Attenuated total reflectance (ATR) mode. The principle of FTIR consists of measuring the amount of infrared light absorbed by a molecule. It is commonly used in organic and inorganic chemistry to determine the different functional groups in a molecule or compound. Interferometers are optical devices that are used for the controlled generation

of an interferogram. One of the oldest and most common interferometers used today is the Michelson interferometer, shown below in Fig. 3.13. It consists of an IR source, a beam splitter and two mirrors-one stationary and one movable. Radiation from the IR source is passed through a beam splitter, where it is divided into two different optical paths. Both mirrors are aligned so that the light waves can reflect in a direction that allows for their recombination at the beam splitter. One path of light is reflected onto a fixed mirror and the second path is reflected onto a moveable mirror. The movable mirror is able to move forward and backwards along it axes. The distance the light travels if it is reflected towards the movable mirror is therefore constantly changing, whereas the distance the light travels towards the stationary mirror is of a fixed length. The resulting measurement that is obtained is called an interferogram, which is a plot of the light intensity vs optical path difference. This interferogram is then converted into a spectrum via Fourier transformation.

In our study, the FTIR in the reflection ATR configuration is employed to investigate the different vibrational modes of the chemical species within the sol-gel coatings. The FTIR spectra of all coatings were obtained using a Perkin Elmer GX instrument (Fig. 3.14) within the $650 - 4000$ cm^{-1} spectral range. 8 scans were acquired per spectra.
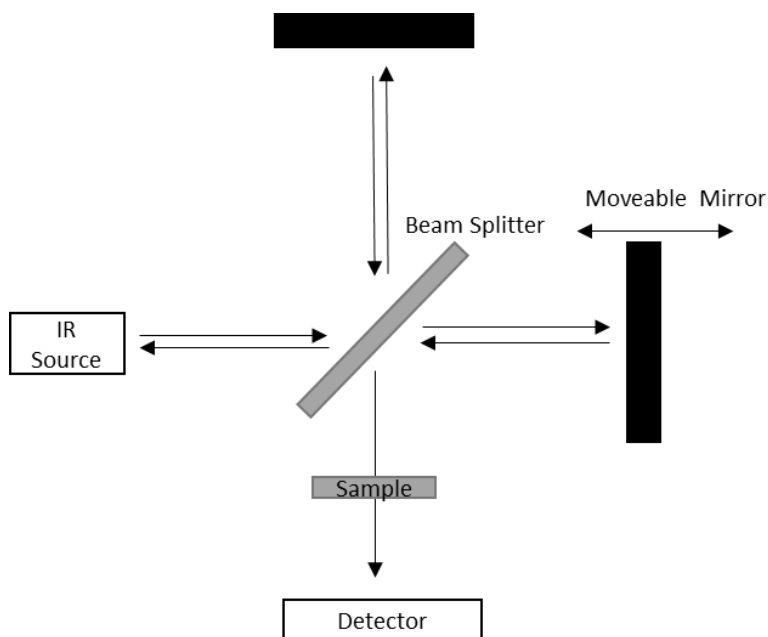
Figure 3. 13: Michelson Interferometer
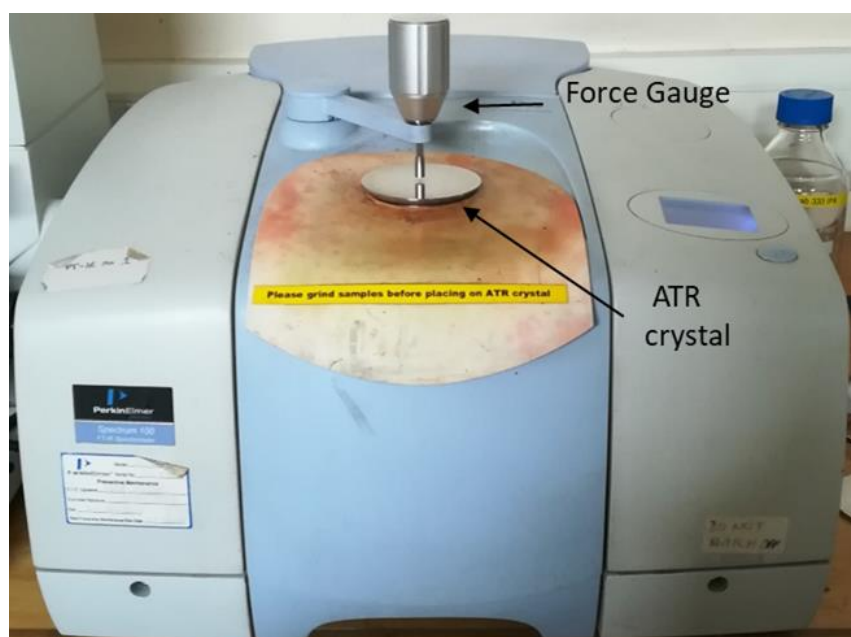
Figure 3. 14: Perkin Elmer Spectrum 100 FTIR/ATR Spectrometer

3.2.4 ^{29} Silicon Nuclear Magnetic Resonance Spectroscopy (^{29}Si-NMR)

Nuclear magnetic resonance (NMR) is a physical phenomenon that relies on the interaction of the atomic nuclei of certain isotopes with a static magnetic field. It was first experimentally observed by two different research groups at Stanford and Harvard

Universities in 1945 and published in 1946[114]. Common active NMR nuclei include ^{1}H, ^{13}C, ^{15}N and ^{29}Si. The technique can be used to study the chemical, physical and biological processes in materials.

Silicon nuclear magnetic resonance spectroscopy is a powerful technique for the quantitative study of the silicate-based sol-gel processes, namely the hydrolysis and condensation reactions of the reactive organoalkoxysilanes. Of the 3 naturally occurring isotopes of silicon- ^{28}Si (92.21%), ^{29}Si (4.90%) and ^{30}Si (3.09%). ^{29}Si is the only naturally occurring isotope of silicon that has a spin of a ½ and therefore a magnetic moment[115]. The receptivity of ^{29}Si (how easily it can be detected) is 3.6×10^{-4}, compared to ^{1}H. Therefore, it can be characterised as a magnetically diluted isotope of medium sensitivity. The gyromagnetic ratio of Si is negative, since the spin and magnetic moment of the isotope are antiparallel.

There are several problems that arise with measuring a ^{29}Si-NMR spectrum. The majority of the construction materials for both the probe head and tube consist of Si containing materials such as glass and ceramics, this can lead to a broad background scattering. One method to correct this issue is to use population pulse transfer programs such as a distortionless enhancement by polarization transfer (DEPT) or insensitive nuclei enhancement by polarization transfer (INEPT). These techniques are used if the silicon atoms are coupling to protons. A DEPT program uses a polarization transfer from one nucleus to another, usually proton to carbon or another X nucleus, to increase the signal strength of the X nucleus. An INEPT pulse sequence was used for this work.

^{29}Si-NMR was used to investigate the rate of hydrolysis on the liquid sol-gel materials at room temperature. A Bruker Avance II 400 MHz spectrometer was used (Fig. 3.15). An INEPTRD pulse sequence was used to record the NMR spectra. Deuterated dimethylsulfoxide (DMSO) was used as a lock solvent.
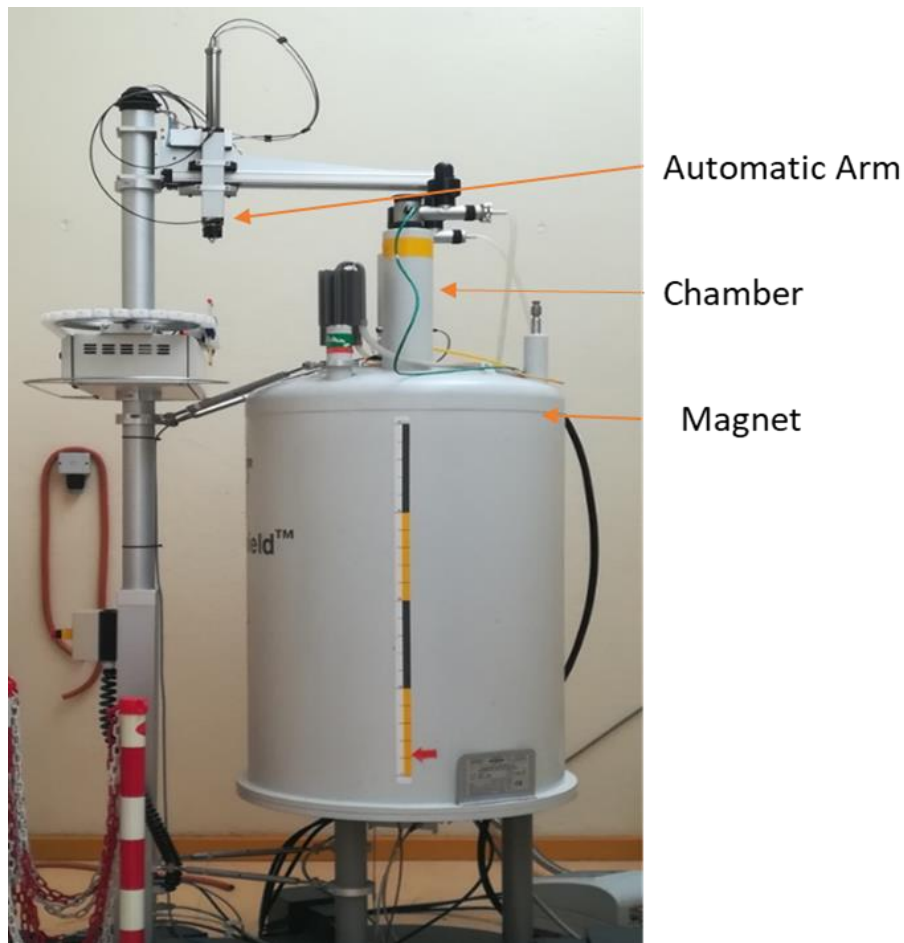
Figure 3. 15: Bruker Avance II 400 MHz Spectrometer

3.2.5 Scanning Electron Microscopy (SEM) / Energy dispersive x-ray microscopy (EDX)

Scanning electron microscopy is a versatile technique for the analysis of both the microstructure morphology and chemical composition of an object or sample. It uses high energy electrons to generate a high-resolution image. It consists of an electron gun and a system of condenser lenses to focus the electrons onto the sample. The electron gun in an SEM is operated between 1000 and 30000 volts and is a heated filament that provides a source of electrons for the probing beam. Image formation is dependent on the acquisition of signals produced from interaction between the electron beam and the sample. They can be classified as elastic interactions or inelastic interactions. Elastic interactions are the

result of deflection without energy exchange of the incident electrons by the atomic nucleus or the outer shell electrons of the sample. Inelastic interactions are the result of a variety of different interactions between the incident electrons and the electrons and atoms of the sample. They lead to substantial energy being transferred to the atoms. This excitation leads to the generation of secondary electrons which can be used to generate an image of the sample[116]. The schematic diagram of an SEM is sketched in Fig. 3.16.
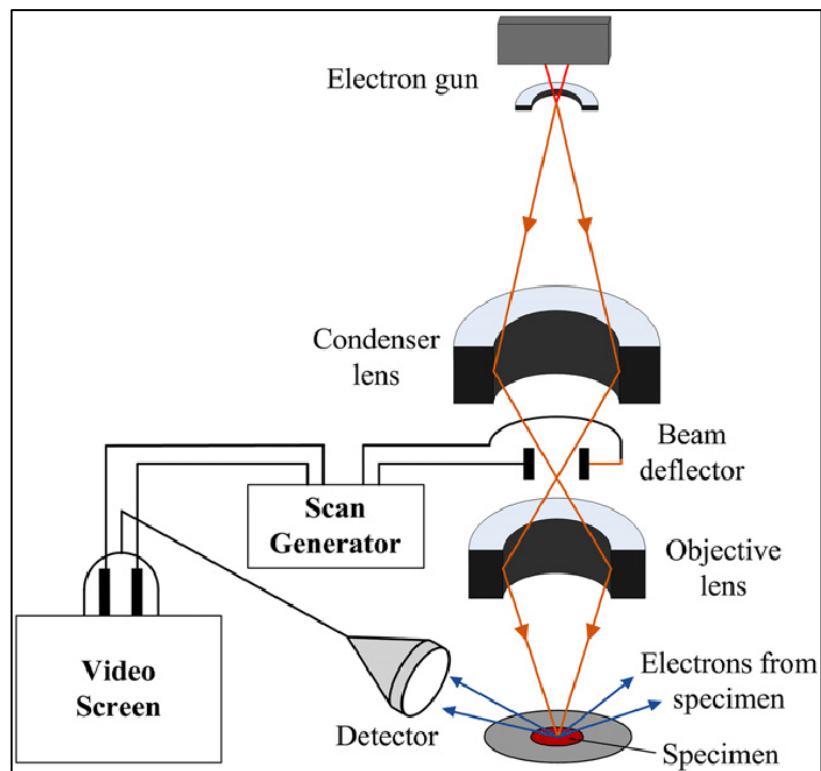
Figure 3. 16: Schematic diagram of an SEM [117]

Energy dispersive X-ray (EDX) spectroscopy is an analytical technique that is used for the identification of the chemical composition of the surface of a sample. It is very often coupled with SEM imaging. In EDX, an electron beam is focused onto a sample using an electron microscope. This interaction causes electrons to be displaced in the sample, these scattered electrons are then converted into an image via a detector. X-rays which are characteristic of a particular element are also generated[118]. The x-rays produced are

analysed and presented as a spectrum rather than an image, similar to XPS analysis (Fig. 3.17). The spectrum consists of a series of peaks with each peak representing a particular element[119].

SEM images and EDX analyses were recorded employing a Hitachi SU-70 SEM (Fig. 3.18), using an accelerating voltage of 5 keV for SEM images and 20 keV for EDX analyses.

Samples coated onto Si wafers were cleaved and sputter coated with 6.1 nm of platinum/palladium coating using a Cressington 208HR sputter coater to reduce the charge of the samples.

Element	Weight %	Atomic %
Zn	50.0	54.7
Se	50.0	45.3
Total	100.0	100.0
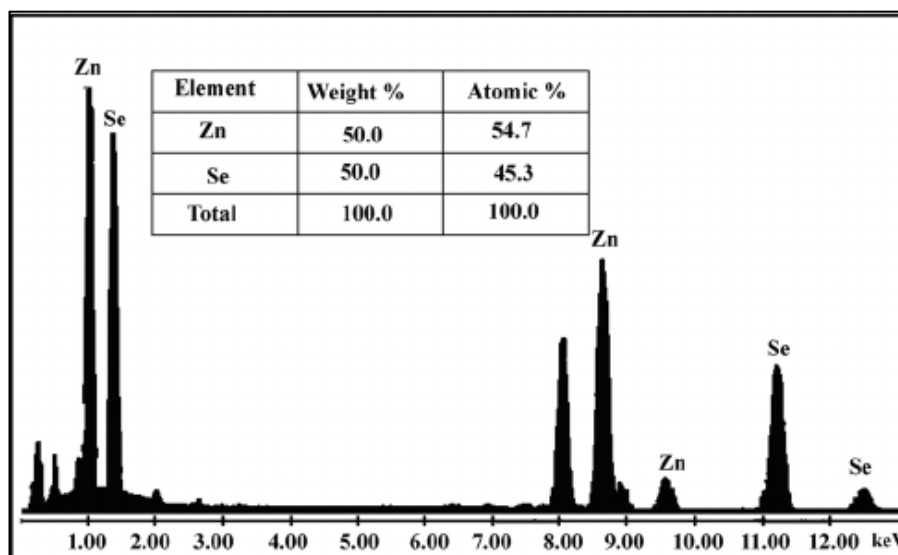
Figure 3. 17: EDX elemental analysis spectrum of ZnSe powder [120]

Figure 3. 18: Hitachi SU-70 SEM/EDX

3.2.6 X-ray photoelectron spectroscopy (XPS)

X-ray Photoelectron Spectroscopy (XPS), sometimes called electron spectroscopy for chemical analysis (ESCA), is a quantitative surface analysis technique that measures the surface elemental composition of a material[121]. It is one of the most widely used surface analysis techniques owing to the wide range of materials that can be analysed and can provide valuable quantitative data and information about the chemical state of the surface of the materials that are being studied. The technique has its origins in the photoelectric effect, first discovered by Hertz in 1887[122]. Samples are placed in under ultra -vacuum (a pressure lower than 10^{-8} Torr) and can be used to obtain both qualitative and quantitative data. The average analysis depth is 5nm. The sample is exposed to a beam of x-rays,

which excites electrons near the surface of the sample. The kinetic energy emitted from these photoelectrons can be measured and related to the binding energy of the different electrons emitted from the surface of the sample. The chemical composition of the surface of the sample can be obtained with a detection limit of 0.1% of the atoms in the analysed sample area[123]. The generation of photoelectrons from the surface of a sample is sketched in Fig. 3.19.

XPS analysis was carried out using a VG Microtech electron spectrometer (Fig. 3.20) at a base pressure of 1×10^{-9} mbar. The photoelectrons were excited with a conventional Mg Kα (hν = 1253.6 eV) x-ray source and an electron energy analyser operating at 20 eV pass energy, yielding an overall resolution of 1.2 eV. The analysis was carried out by Dr Rob O'Connor in the School of Physical Sciences in DCU.
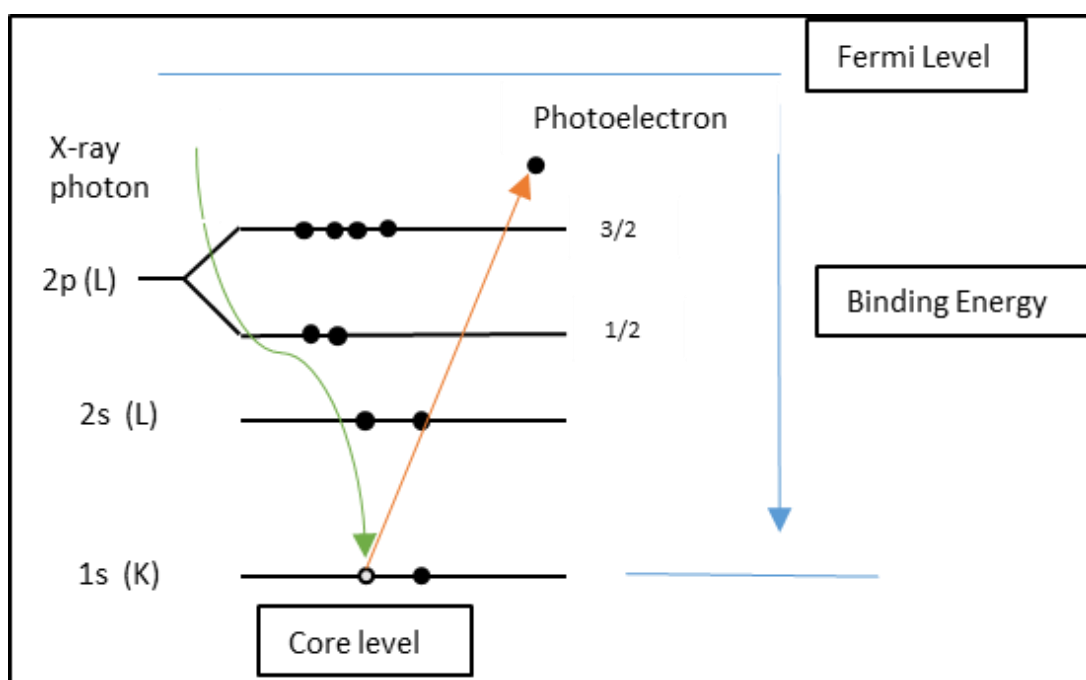
Figure 3. 19: Schematic of the generation of photoelectron for XPS
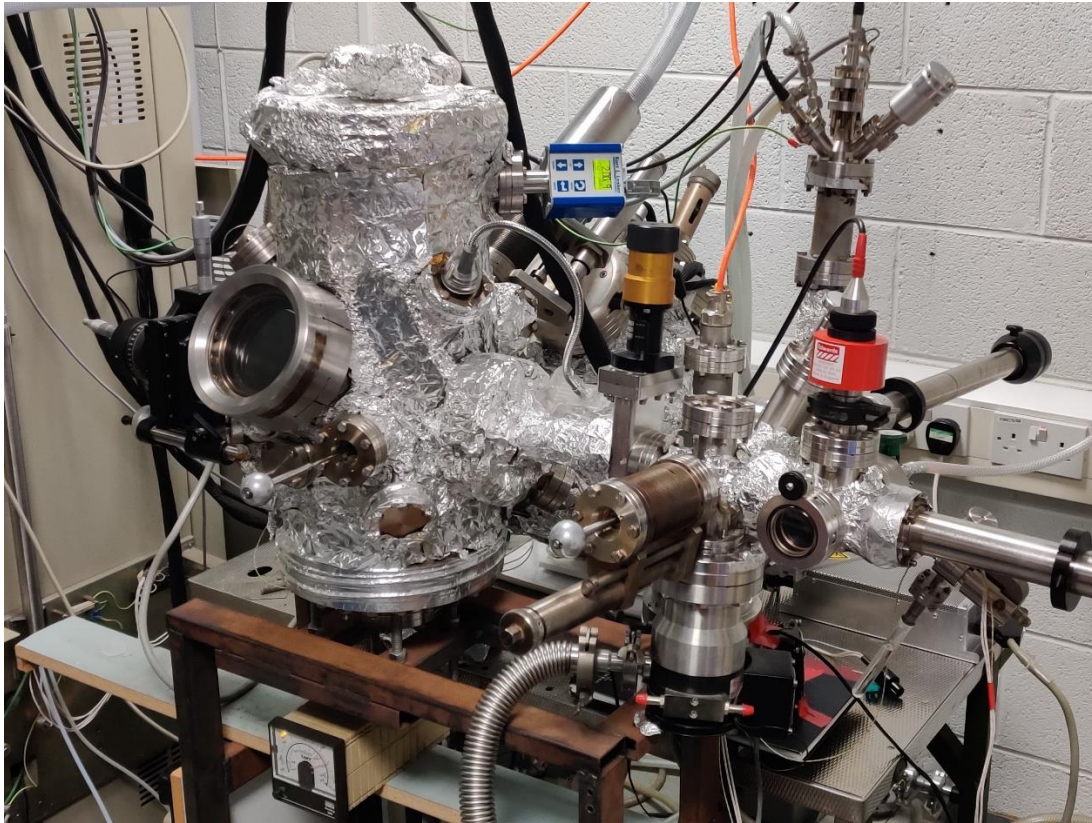
Figure 3. 20: VG Microtech Electron Spectrometer

3.3 Fabrication Techniques

The fabrication of the photomask used for the microstructuration of the microfluidic and optofluidic platforms will be discussed. The coating of the sol-gel and the sensor platforms fabrication process employed throughout this work will also be discussed.

3.3.1 Coating Fabrication-Background

Films and coatings are one of the earliest commercial uses of sol-gel processing. They offer many advantages including control of surface area, pore size and microstructure. Very little raw material is used, and they can be processed in a rapid and cost-effective manner. The fabrication also allows for the coating of irregularly shaped and very large surfaces. There are various processes for fabricating thin films. These include dip-coating, spin-coating and spray-coating[124]. As the sol-gel ages its viscosity can affect its

deposition and thickness. Therefore, for reproducibility reasons thin films and coatings should be deposited at constant viscosities which can be adjusted and controlled through dilution with appropriate solvents[124]. For this work the sol-gel coatings were fabricated 24 hours after the sol-gel synthesis. This was to control the particle size and viscosity of the material.

3.3.2 Spin-Coating

Spin-coating is a technique whereby a thin film is deposited on a substrate by means of centrifugal forces. In the field of microfluidics it is considered an additive technique for the deposition of thin films and is one of the most common deposition techniques in the fabrication of microfluidic devices[28]. Although the process can be in performed in a single rotation step, spin-coating is usually performed in a multi-step process and can be broken into 4 main stages: deposition, spin-up, spin off and evaporation (Fig. 3.21). After the liquid to be coated is deposited onto the substrate, it is spread to, and eventually off the substrate by centripetal acceleration, leaving a thin film of the liquid behind. The final thickness of the coating is dependent upon several parameters including the viscosity of the liquid, drying rate and the spin speed (initial, acceleration and final). Longer spin times and higher spin speeds will give, in general, a thinner coating.

The prepared sol-gel materials were filtered using a 0.45 μm nylon syringe filter prior to use. 1.5 ml of material was then deposited onto glass microscope slides or AA2024 aluminium panels by spin coating at a 1000 rpm to achieve micron-scale thicknesses. The glass and aluminium substrates were cleaned with IPA prior to use and air dried. The fabricated coatings were then cured at different temperatures in the range 100 -150℃ in an oven for 1 hour. All sol-gel coatings were fabricated 24 hours after fabrication of the final sol-gel material.

For the fabrication of the biosensor and optofluidic platforms, and samples for RI measurements, sol -gel materials were deposited onto test grade 4" silica wafers. As there were slight variations to the process for both the biosensor and optofluidic platforms, the specific fabrication methods will be discussed in chapters 9 and 10. A Laurell spin coater was used to fabricate both platforms (Fig. 3.22).

1. Deposition   2.Spin up   3. Spin off   4. Evaporation
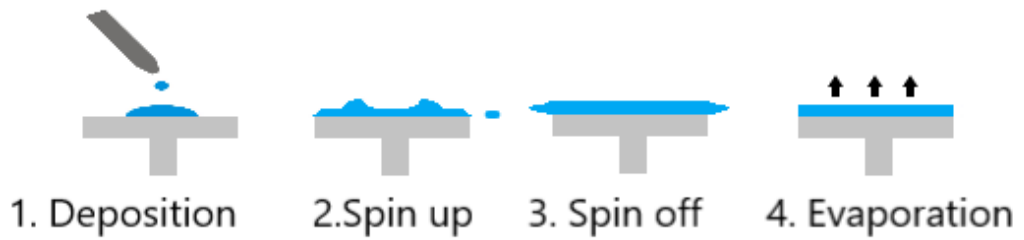
Figure 3. 21: Schematic of Spin coating process

Figure 3. 22: Laurell WS 650 MZ Spin Coater

3.3.2 Dip Coating

Dip coating is a common technique used in the fabrication of thin films and coatings.

Coatings are formed by immersing a substrate into a liquid and withdrawing it at a

controlled speed, this is done in controlled atmospheric and temperature conditions[125].

For sol gel materials, the evaporation of the solvent is controlled by the atmosphere and

the subsequent destabilisation of the sol by the evaporation of the solvents leads to the

gelation process and the thin film formation due to the small particle size of the sol. The

withdrawal speed, viscosity of the liquid and the solid content all control the final coating

thickness. The sequential dip coating process is shown below in Fig. 3.23.

The prepared sol-gel materials were filtered using a 0.45µm nylon syringe prior to use. They were then deposited onto aluminium panels. Prior to use the aluminium panels were cleaned with IPA and air dried. The dip speed to was set to 40mm/min, this was to achieve coatings of micron scale thickness. The fabricated coatings were then cured at different temperatures in the range of 100-180°C in an oven for 1 hour.   All sol-gel coatings were fabricated 24 hours after fabrication of the final sol-gel material. A Bungard RDC 21-K dip coater was used for the fabrication of the coatings (Fig. 3.24).

Dipping   Wet layer formation   Solvent evaporation
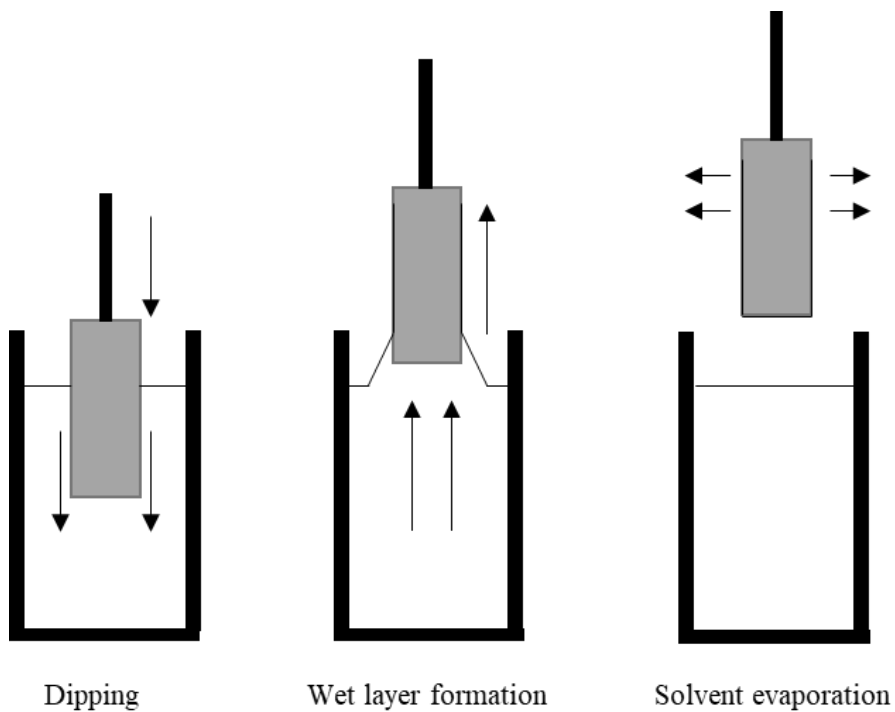
Figure 3. 23: Schematic of dip coating process

Figure 3. 24: Bungard RDC 21-K Dip coater

3.4 Photomask Design and Fabrication

In order to fabricate any microfluidic patterns or structures, a photomask is used to transfer the patterns to the photoresist via UV exposure. A photomask is a square plate of either glass or quartz, depending on the type of UV radiation being used, that is covered in a patterned layer of opaque material. This material can either be an emulsion, iron oxide or chromium. The mask substrate material, wavelength of UV radiation used and the methods of mask fabrication will affect the type of material used[32,126]. Photomasks are generally designed using computer programs such as computer aided design (CAD). The geometric patterns that can be created from CAD files can vary depending on different parameters such as minimum feature size and tolerance.

The biosensor platform and linear micro-channels were designed using AutoCAD 2018 software. The linear microchannel photomasks were fabricated onto 5" square glass plates with a layer of chromium. The biosensor platforms were fabricated onto 4" square soda lime glass plates with a layer of chromium. They consisted of a circular inlet with y-split micro-channels, sensor spots, and a wicking zone, containing colourless circular spots which would form micro-pillars within the wicking zone. Both photomasks were fabricated by JD photo tools and can be seen in Fig. 3.25.

Base Material	Soda Lime Glass (0.063"-1mm)
Resolution	Class 4 – 500 dpi
Smallest Feature	75 microns
Polarity	Positive, right reading, chrome down

Table 3. 2: Parameters for the photomask fabrication
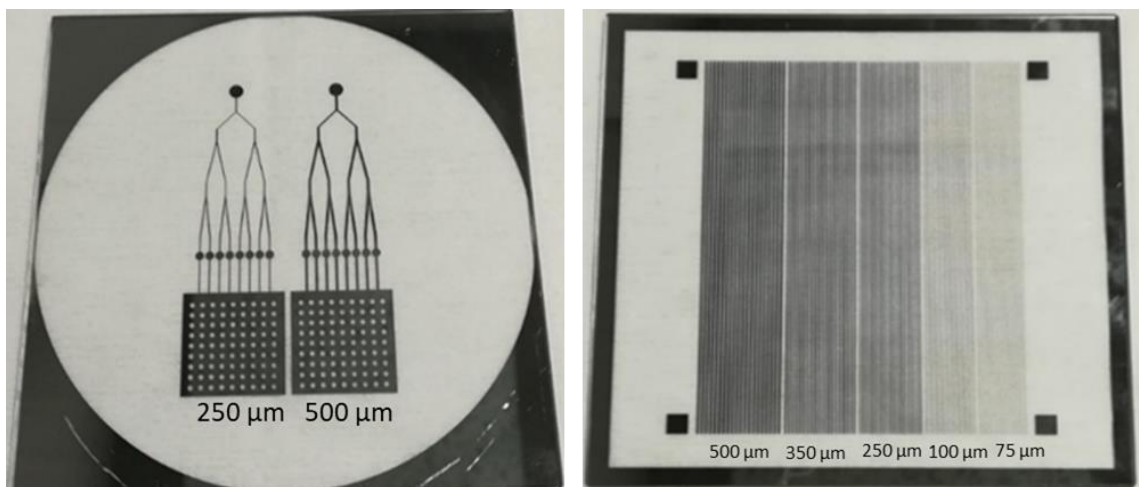
Figure 3. 25: Microfluidic biosensor (left), and linear microchannel photomasks (right)

3.5 Optical Techniques

The optical techniques that will be used include prism coupling refractometry, UV-vis and fluorescence spectroscopy. The optical waveguide set-up and the sensing applications of the optofluidic platform are also discussed.

3.5.1 Prism-Coupling Refractometry

Prism-coupling refractometry is an optical technique that can be used to measure the refractive index (η) and film thickness (W) of dielectric thin films[127]. The principal behind this method is as follows. A laser beam strikes the base of a high refractive index prism and is reflected onto a photodetector. The coupling of this light to the prism base is governed by the angle of incidence θ [127]. This angle determines the phase velocity in the x direction and thus the mode angles. The film to be measured is brought into contact with the prism via a pneumatically operated coupling head, so the film and the prism are separated by an air gap (of no more then 100-200 nm). At certain values of θ, called mode angles, photons move from the base of the prism across the air gap into the film and cause optical propagations. These propagations cause a subsequent sharp drop in the intensity of the light that is striking the photodetector. If this intensity is plotted against θ, a characteristic spectrum is obtained (Fig. 3.26). Two modes can be used to measure the RI of thin films- transverse electric (TE) and transverse magnetic (TM). These modes refer to the linear polarisation of the laser beam. An optical TE mode propagates in the film with its electric field lying in the transverse plane (perpendicular to the propagation direction). For a TM mode, the magnetic field lies in the transverse plane. Due to planar waveguide anisotropy, TE and TM modes exhibit effective indices differences. Due to film index and thickness dependence, the effective indices associated with propagation angles are used to solve for these optogeometrical properties.

The sol-gel materials were spin coated onto 4" Si wafers at a spin speed of 900 rpm. This was to ensure coatings thickness of ~6 microns. The coatings were then placed in an oven at 100℃ for 10 minutes to ensure both the stabilisation of the coatings and that they were also "touch dry". The Si wafers were then cleaved into 4 and subjected to varying UV irradiation times- 50, 100, 250, 500 and 650s respectively. Before measurements were

taken the rotary table was referenced and the gain was adjusted to ~0.8mA. The samples were then loaded with the coating facing the prism. A pneumatically operated coupling head is used to hold the sample in place. Once a coupling spot (Fig. 3.27) was present, and the red laser beam was in contact with the spot, measurements were run. The following parameters (Table 3.3) were used to measure the RI and thickness of the sol gel coatings. The RI measurements for each coating was measured as well **for** as a sample without any UV irradiation. The refractive index and thickness of the sol gel coatings was taken simultaneously using a Metricon 2010 /M Prism Coupler (Fig.3.28).
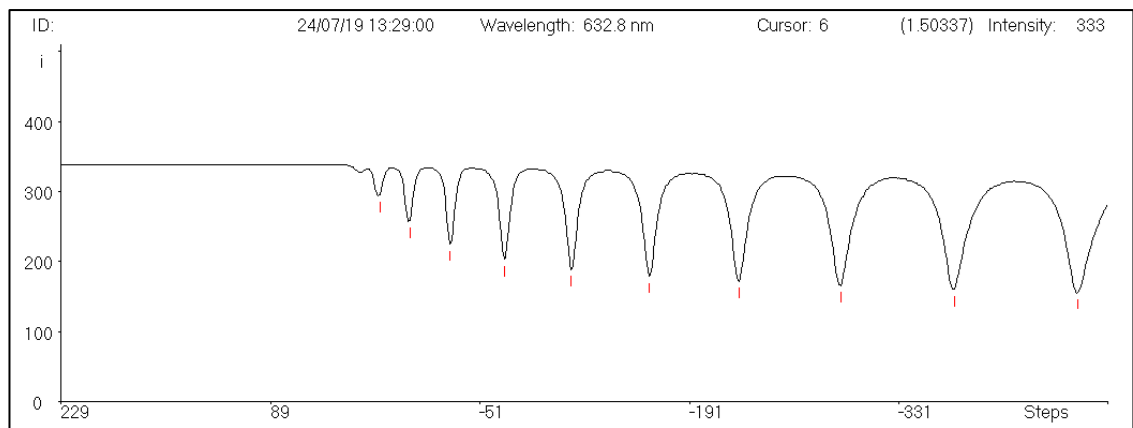
Figure 3. 26: Characteristic mode angle spectrum
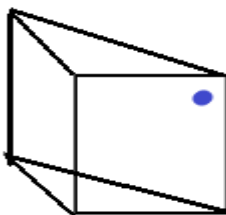
Figure 3. 27: Coupling Spot

73

Parameter	
Prism Index	<1.8
Mode	TE
Laser Wavelength	633 nm
Laser Type	HeNe
Substrate RI	3.4
Measuring Type	Single Film

Table 3. 3: Metricon 2010 parameters
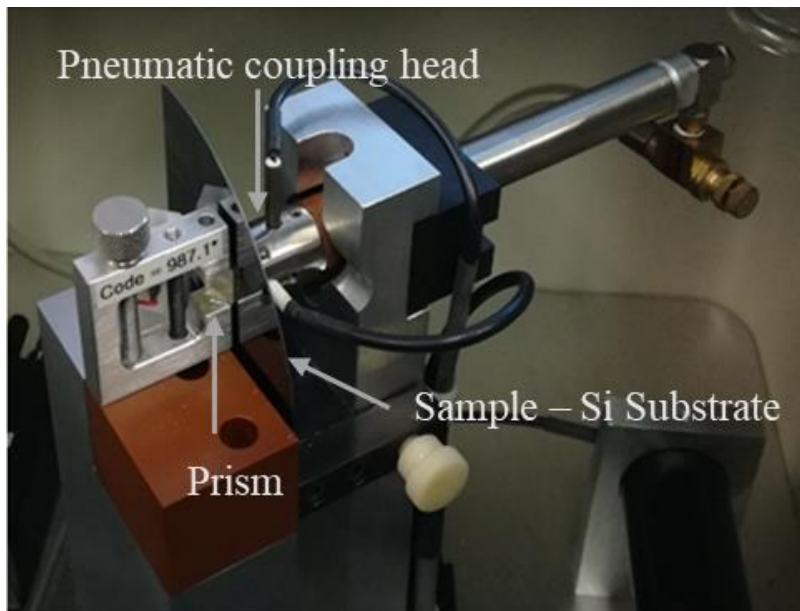
Figure 3. 28: Metricon 2010 Prism and Pneumatic coupling head

3.5.2 UV-Vis spectroscopy

Ultraviolet-visible (UV-Vis) absorption spectroscopy is an optical/spectroscopy characterisation technique that is primarily used to identify the absorption of a material in the 400 – 700 nm spectral region. It measures the absorption of light due to electronic transition in a sample (usually a chromophore), either in the UV (200 – 400 nm) or the visible (400 - 700 nm) region of the electromagnetic spectrum[128]. It can also be used as

an analytical technique to determine the concentration of an analyte dispersed in a transparent solvent in the UV-Vis. One of the most important mathematical equations is the Beer Lambert law which forms the mathematical-physical basis for the light absorption measurements on both liquid and gaseous samples (eqt 1).

$$A = \log I_0/I = \varepsilon l c = \alpha c \qquad \text{Equation 1}$$

Where the absorbance (A) is related to the incident light (I_0) and transmitted intensity of light (I), the concentration of solution (c), path length (l), absorption coefficient (α) and molar absorptivity (ε) of the sample. Absorbance can be experimentally determined as Io and I will be known, and α is wavelength dependent.

A schematic of a typical spectrometer is sketched in Fig. 3.29. The intensity of light is measured by a photodiode or photomultiplier tube and is measured without and with a sample between the light source and the detector. If the sample absorbs light within the given wavelength range, this is translated as a drop in the intensity of the transmitted light. The intensity of the transmitted light is then plotted as a function of wavelength, to give an absorption spectrum of the sample[128].

Both samples were run from 200-700 nm using PMMA cuvettes. The spectra were acquired using a Perkin Elmer Spectrometer (Fig. 3.30), the fluorescein sodium and Atto 633 dye dissolved in water can be seen in Fig. 3.31.
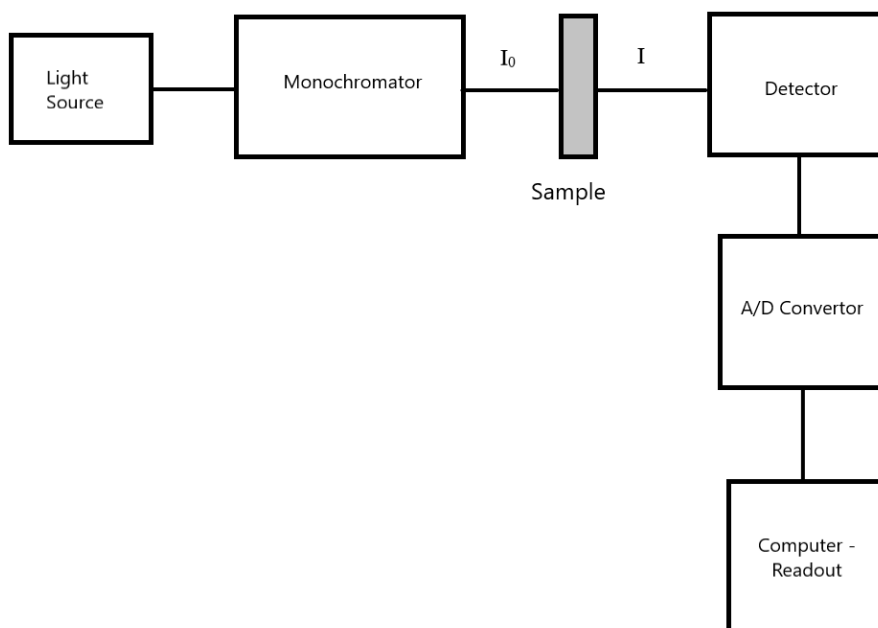
Figure 3. 29: Schematic of a typical UV spectrometer

Figure 3. 30: Perkin Elmer Spectrometer
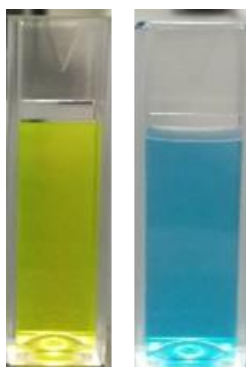
Figure 3. 31: Fluorescein sodium (left) and Atto 633 (right) dissolved in water

3.5.3 Fluorescence Spectroscopy

Fluorescence or photoluminescence spectroscopy is another electromagnetic spectroscopic technique that measures the emission of a sample following an optical excitation. The principle is similar to absorption spectroscopy, as both techniques involve the measurement of electronic transitions in their initial and final states couples by the electrical dipole operator.

Fluorescence spectroscopy is a zero-background experimental technique, meaning that if there is no photoluminescence present then no signal is detected. This, consequently makes it a much more sensitive technique than UV spectroscopy[128].

Several components of a spectrofluorometer, sketched in Fig. 3.32, are similar to a UV-Vis spectrometer including the light source, sample cuvette and detector. The detection of light is where the difference occurs. Light emitted from the sample rather than the transmitted light is detected. A specific wavelength of light is selected from a light source by an excitation monochromator and directed towards the sample of interest. Light emitted from the sample is collected by an emission monochromator and detected by a photodetector. The signal is then converted by an A/D convertor to a digital signal and the intensity of fluorescent light is plotted as a function of the wavelength of light emitted from the sample.

In this work, the emission spectra were recorded using a Perkin Elmer SS 55 Luminescence Spectrometer, as shown in Fig. 3.33. Excitation wavelengths were selected depending on the employed dyes and are discussed in Chapter 10. A wavelength range of 400 – 800 nm was used for fluoroscein sodium and 600 – 800 nm for Atto 633.
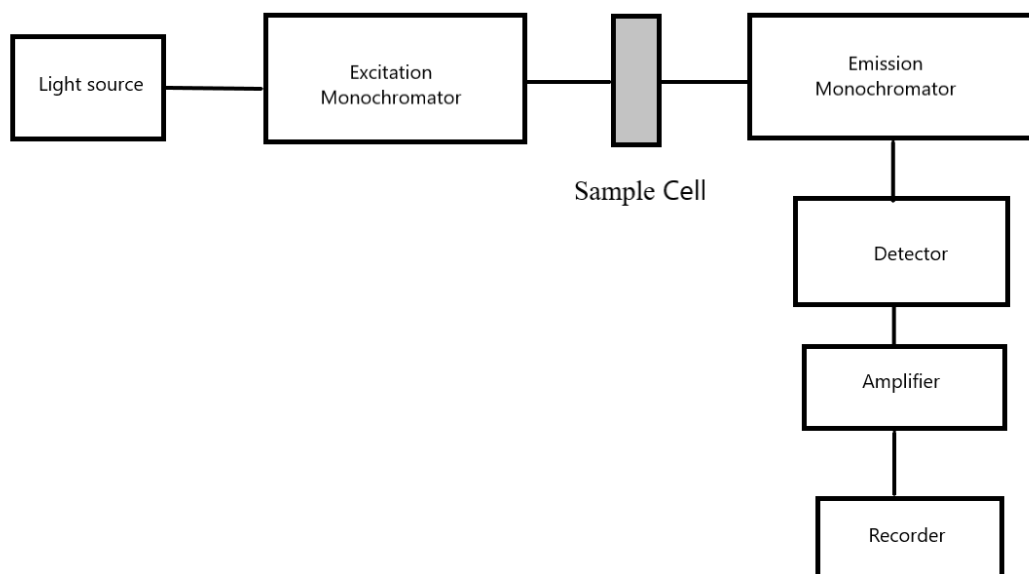
Figure 3. 32: Schematic of a typical fluorimeter

Figure 3. 33: Perkin Elmer Luminescence Spectrometer

3.5.4 Waveguide Optical Set-up

A waveguide can be described as any structure used for guiding the flow of electromagnetic waves in a direction parallel to its axis and confining these waves to a region within the core or adjacent to its surfaces. An optical waveguide can be classed according to its mode structure – multimode or single mode, their geometry or RI distribution[129]. Optical waveguides consist of the core- a high index material and the cladding- a low index material which surrounds the core. The most obvious examples of optical waveguides are optical fibres, which are currently widely used in the telecommunications systems[130], as sketched in Fig. 3.34.
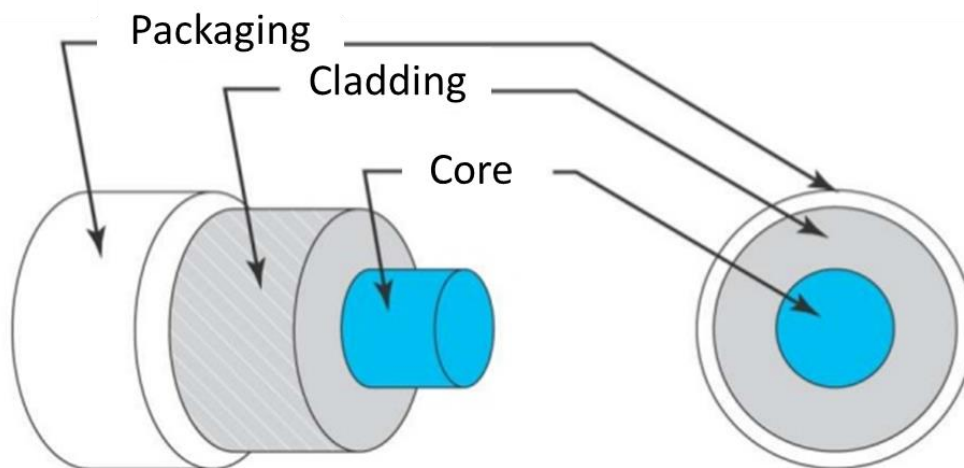
Figure 3. 34: Structure of a typical optical fibre

The transverse profile of an optical waveguides di-electric constant determines its characteristics. Waveguides can be further classed into planar or 2-D waveguides and non-planar or 3-D waveguides depending on the transverse direction of the optical confinement.

Planar waveguides-Optical confinement in one transverse direction where the core is confined within the cladding in one direction only.

Non-planar waveguides- 2- dimensional transverse optical confinement and the core is surrounded by the cladding in all transverse directions[129].

The optical waveguides that will be fabricated in chapter 10 of this work can be classed as planar waveguides.

In order to determine if the propagation of light through the waveguides was indeed occurring and if the waveguides had been fabricated correctly, they were coupled to an optical fibre and tested using a red laser diode in the visible region with a wavelength of 635 nm. This work was carried out with the help and guidance of Dr Arun Mallick of the Photonic Research Group in TU Dublin.

The waveguides were coupled to a single mode optical fibre using a 635 nm laser line at an intensity of 2.5 mW. To ensure the output from the waveguides was visible it was magnified using a x10 objective lens. The optical set up used can be seen in Fig. 3.35.
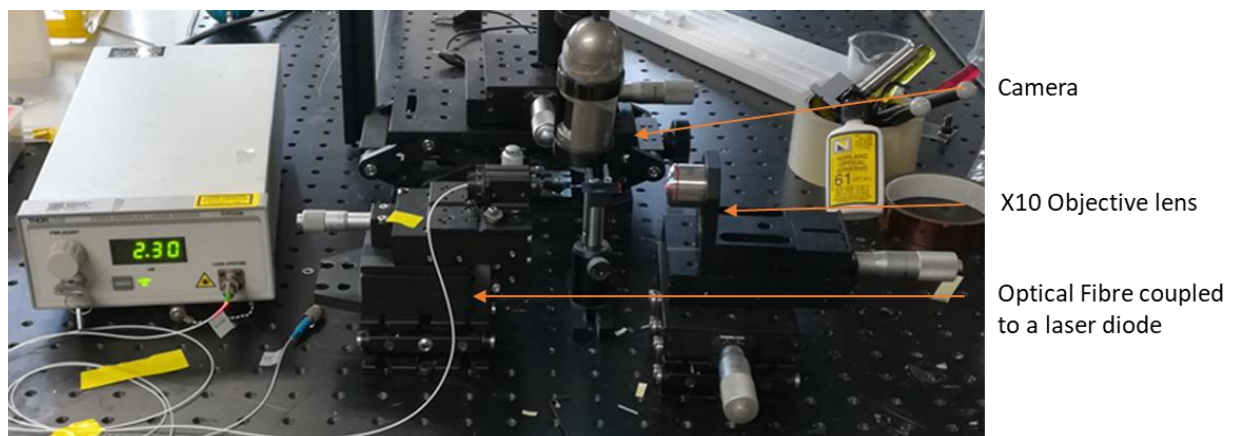
Figure 3. 35: Optical set up for waveguide testing

3.5.5 Optofluidic Platform

The optofluidic platform will be fabricated via the integration of a microfluidic sensor platform and optical waveguides. The procedure for testing both the optical sensing and bio-sensing applications of the platform are discussed in more detail below.

3.5.5.1 Optical Sensing Application

In order to ensure the optofluidic platform was indeed functional, the platform was tested with the help of the industrial and engineering optics (IEO) group in the FOCAS Institute in TU Dublin. Two different laser lines were used – a green laser line at 532 nm (Verdi G series 5W) and a red laser line at 635 nm (Uniphase He/Ne laser).

To assess the sensing performance of the optofluidic platform, the green laser was aligned with the waveguides within the optofluidic platform. The fluorescence of fluorescein sodium was assessed. 0.5 μl of the dye was dropped onto the platform closest to the output of the waveguide. 3 concentrations of the fluorescein dye were used, A) 6.6×10^{-3}g/ml, B) 1.65×10^{-4}g/ml and C) 1.65×10^{-5}g/ml. The power of the laser was set to 0.20 W and 0.10 W. The fluorescence of each dye was captured using a spectral analyser (Avantas AvaSpec-2048) with a broad band light source guided by a fibre optic cable. Each concentration of dye was monitored for a total of 5 minutes. The spectral analyser was placed directly above the dye to capture the fluorescence.

The procedure was repeated using the Atto 633 dye. As this dye absorbed in the red region of the spectrum, a red laser line of 635 nm was used to excite the dye. Two concentrations of the Atto 633 dye were used, A) 1.2×10^{-5} g/ml and B) 1.2×10^{-6} g/ml. The intensity of the laser was 0.1 mW. A spectrum was also taken of the output of the light from the waveguides without any of the dye present. A schematic of the optical set up is shown in Fig.3.36 and of the sensor platform set up in Fig. 3.37.
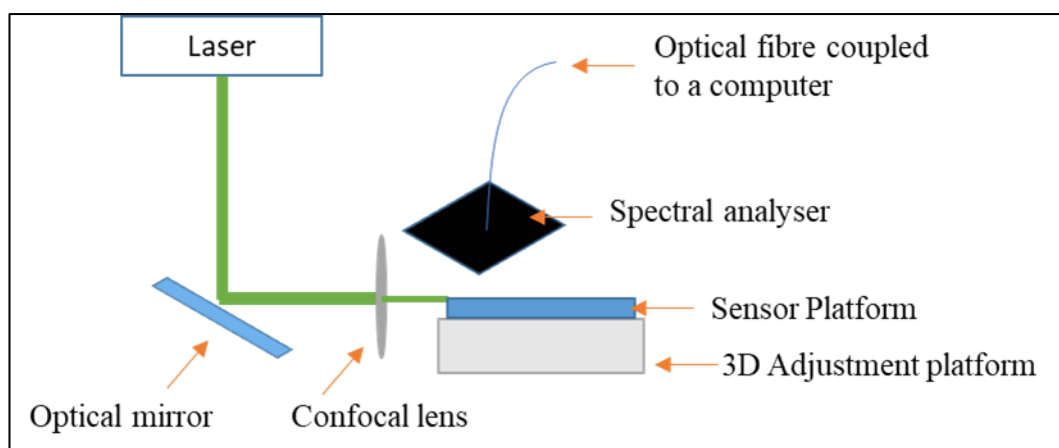
Figure 3. 36: Schematic of the optical set up used for the fluorescence studies
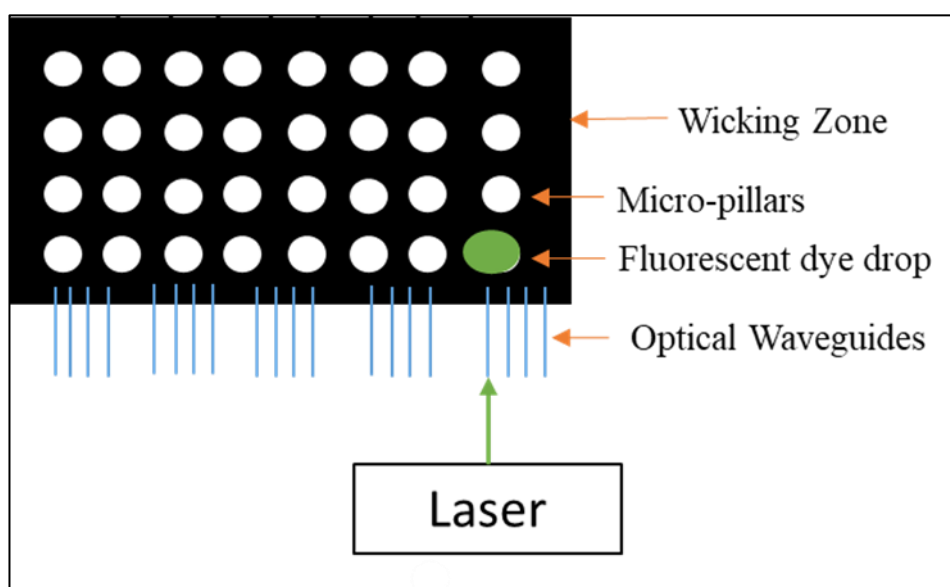
Figure 3. 37: Schematic of the sensor platform with the location of the fluorescent dye

3.5.5.2. Bio-sensing Application

The bio-technology protocol established to demonstrate the applicability of the developed optofluidic device as a sensing platform is sketched in Fig. 3.38. As the sensor platform was first functionalised with a 5% APTES solution, 1-Ethyl-3-(3-dimethylaminopropyl)-carbodiimide (EDC) / N-hydroxysuccinimide (NHS) coupling chemistry was used to bind the primary antibody to the functionalised surface of the sensor platform via the primary amine on the APTES silane. EDC is a water-soluble cross-linking agent that is used to

form amide bonds between carbonyl and amine groups. As EDC is not fully stable in water, due to the oxygen atoms acting as nucleophiles and inactivating the EDC, NHS is used to improve its stability[131]. The structure of both compounds are shown below in Table 3.4 and the reaction scheme for the EDC/NHS coupling chemistry with the primary amine of the functionalised sensor platform is shown below in Fig. 3.39. The reaction schematic for the surface functionalisation of the sensor platform with APTES is shown below in Fig. 3.40. As the 5% APTES wash is made using a 10 % v/v of water, the ethoxy groups on the APTES molecule will be hydrolysed before binding to the sol-gel surface via possible electrostatic interactions and / or hydrogen bonding[132].

In order to assess the optofluidic platforms suitability as a biosensor using an immuno-fluorescence technique, a primary antibody-mouse IgG and a fluorescently labelled secondary antibody- anti-mouse IgG labelled with CF 555 were used.

The platform was first functionalised using a dilute APTES wash at a 5 % concentration, the chemical equation of which is shown in Fig x. In order to ensure the primary antibody was bound to the surface of the sol, EDC/NHS coupling chemistry was carried out. The IgG was reconstituted into a 1 mg/ml concentration, by dissolving 5.5 mg of IgG for 15 minutes in 5 ml of phosphate buffer solution (PBS). 1.12 mg of EDC was dissolved in 1 ml of PBS, and 1.06 mg of NHS was dissolved in 1 ml of PBS to ensure both compounds were in excess in relation to the antibody concentration. The EDC was then added to the antibody followed by the NHS. 5 µl of this mixture was then pipetted onto specific areas of the optofluidic platform close to the output of the waveguides. This was left to bind to the surface by diffusion for 2 hours before being washed with PBS 3 times to remove any excess unbound primary antibody. 5 concentrations of the secondary antibody were made, 500,200,100,50 and 10 µg/ml from a stock solution of 2 mg/ml. 5 µl of each concentration were pipetted onto corresponding functionalised spot with the primary antibody and left

to bind for 2 hours before being rinsed with PBS 3 times. A blank was also prepared on the same platform. The blank was used to identify any non-specific binding that may occur of the primary antibody to the platform itself. The primary antibody was prepared without using EDC/NHS coupling chemistry and so should not have been bound to the optofluidic platform. 5 µl of the reconstituted IgG primary antibody was pipetted onto a specific area of the optofluidic platform close to the output of the waveguides. This was left to bind to the surface by diffusion for 2 hours before being washed with PBS 3 times. 5 µl of the highest concentration of the secondary antibody (500µg/ml) was pipetted onto the corresponding area that had been not been functionalised via the EDC/NHS coupling chemistry. Again, this was left to bind for 2 hours before being washed 3 times with PBS.

Chemical Name	Molecular Formula	Abbreviation	Structure
1-Ethyl-3-(3-dimethylaminopropyl)-carbodiimide	$C_8H_{17}N_3$	EDC	
N-hydroxysuccinimide	$C_4H_5NO_3$	NHS	

Table 3.4: Chemical name, molecular formula, common abbreviation and structure of

the coupling agents used
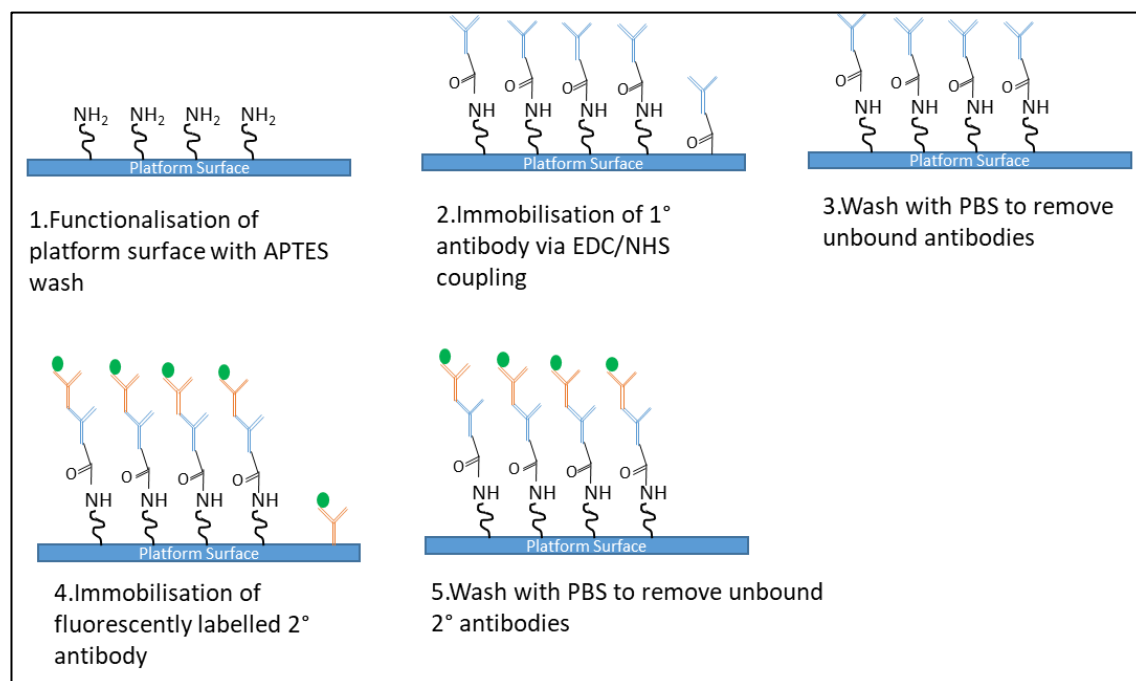
Figure 3. 38: Representation of the biotechnological protocol employed in the sensing

testing of the optofluidic device
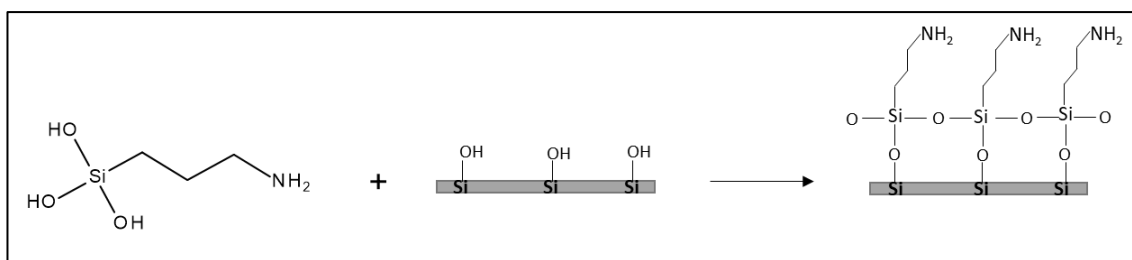
Figure 3. 39: Reaction schematic of the surface functionalisation of the sol-gel surface with partially hydrolysed APTES from the 5% APTES wash
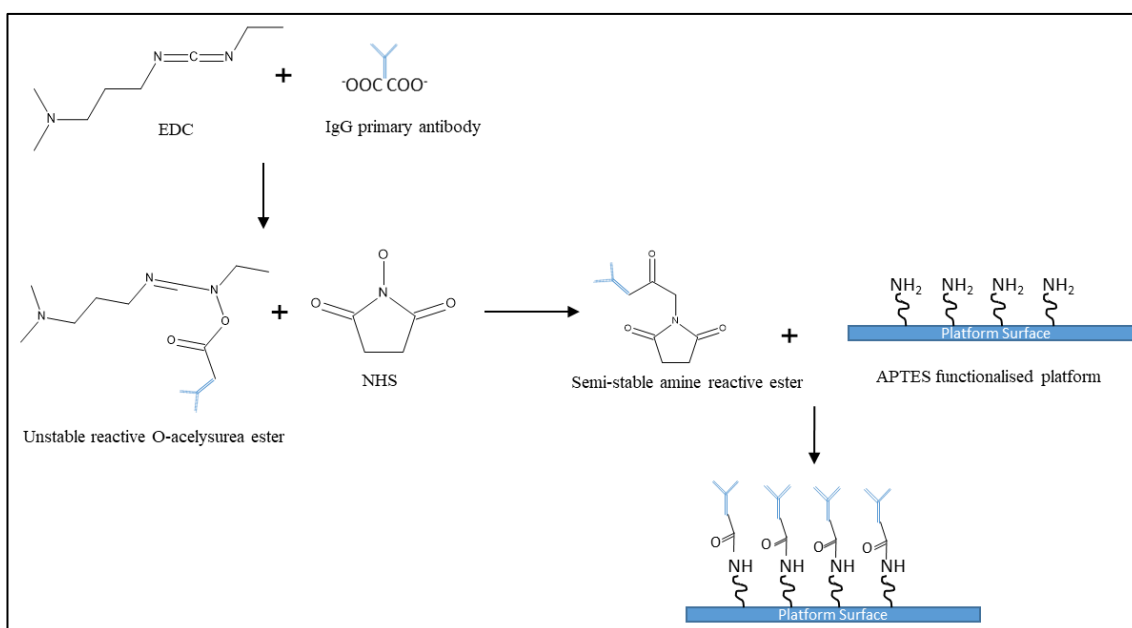
Figure 3. 40: Reaction scheme for the EDC/NHS coupling chemistry with the primary amine of the APTES functionalised platform

4 Development and Characterisation of a Reference Photo-curable Hybrid Sol-gel material.

4.1 Introduction

This chapter is concerned with the development and characterisation of a reference hybrid sol-gel material that will serve as a guideline throughout this work for the development of materials with improved properties. The design of the reference material must take into consideration the processing fabrication conditions and the final properties needed. Indeed, as the overall application of the material will be towards microfabrication of microfluidic platforms employing a photolithographic process, the first condition to consider is **photo-reactivity upon UV-irradiation**. The material needs to **enable fabrication of homogeneous coatings** with minimum mechanical properties achievable **at low-curing temperatures**, ideally at room-temperature. The material will also need to exhibit **good mechanical resistance** and a **high surface energy** to enable the flow of liquids within the microfluidic platform.

The literature review performed on the state-of-the-art has identified a number of potential materials including methacrylate[5] and epoxy-based[4] sol-gel systems. Although both systems may be employed for our objectives, the choice towards the use of methacrylate-based sol-gel was performed, due to the higher chemical resistance of these chemistries in comparison with the epoxies.

The hybrid sol-gel system that has been chosen to be investigated employs an organosilane, MAPTMS and a transition metal complex formed from the chelation of zirconium (IV) propoxide (ZPO) and methacrylic acid (MAAH). The photo-reactivity of the sol-gel material is due, in part to the MAPTMS precursor. It contains a methacrylic group that enables free radical polymerisation upon irradiation with UV light when

combined with a suitable photo-initiator. The chelating agent-MAAH, also contains a polymerisable methacrylic group that further enables radical polymerisation. A variety of photo- initiators can be used to ensure the photo-reactivity of the material, such as Irgacure 369, 184 and 819. For this work, Irgacure 184 has been chosen due to its stability within zirconium based sol-gel matrixes[133]. The chemical structures for each starting material have been presented in Table 4.1 below. The formulation for the reference sol-gel material is shown in Table 4.2. The volumes of reagents used to synthesis ~48 ml of sol are shown in table 4.3 below. This volume was scaled up depending on the volume of sol needed.

This system has been studied previously in the fabrication of microfluidic platforms for bio-sensing[2], and in the development of waveguides and integrated microfluidics[5]. However, optimisation of its structure to achieve a high-surface energy has not been performed. Neither strategies for its further improvement were proposed.

In this chapter we will develop this material and try to understand its structural and morphological aspects and correlate them to the surface properties.

The sol-gel will be characterised, first during its synthesis using ^{29}Si-NMR, as a liquid sol-gel to determine its particle size and thermal properties via DLS and DSC and finally as a thin coating to determine its structure and wetting properties employing FTIR and contact angle measurements.

4.2 Materials Preparation

The synthesis of the sol-gel matrix is based on a stable and homogenous sol formulation, obtained from the mixture of an organically modified silicate precursor, 3-methacryloxypropyltrimethoxysilane (MAPTMS, Assay 99 wt. % in methanol, Sigma Aldrich) and an organically modified zirconium complex, which was prepared from the

chelation of zirconium (IV) n-propoxide (ZPO, Assay 70 wt. % in propanol, Sigma Aldrich) with methacrylic acid (MAAH, Assay >98 wt. %, Sigma Aldrich). The mechanisms for the hydrolysis and condensation reactions of the sol-gel material have already been discussed in section 2.12.2 and more detailed information can be found in articles[86,134–136].

As shown in Fig. 4.1, the photo-curable sol-gel material was synthesised in a 4 step-process:

1. The parallel pre-hydrolysis of the MAPTMS and the complexation of the ZPO with MAAH, used as the chelating agent. (Scheme 4.1 and 4.2)

2. The addition of the pre-hydrolysed alkoxysilane within the network of the chelated zirconium complex. (Scheme 4.3)

3. The final hydrolysis of the silicate/zirconium sol. (Scheme 4.4)

4. The addition of a photo-initiator in order to enable the sol-gel materials to be photo patterned, using a standard photolithography process. (Scheme 4.5)

MAPTMS is pre-hydrolysed using an aqueous HNO_3 0.1M solution in a 1:0.25 molar ratio. MAPTMS (28.70 ml) was pipetted into a 100 ml plastic beaker and HNO3 (1.6 ml) was added under constant stirring in the fumehood. As MAPTMS is immiscible with water, HNO_3 was added slowly to the MAPTMS until the production of methanol was sufficient to ensure miscibility between all species in solution. In parallel, ZPO was chelated using MAAH in a 1:1 molar ratio, in order to reduce the reactivity of the ZPO and to form a zirconium propoxide methacrylate complex. MAAH (2.58 ml) was added to a 100 ml plastic beaker containing ZPO (13.54 ml) under constant stirring in the fumehood. Both these reactions were performed simultaneously and allowed to stir for 45 minutes. The partially hydrolysed MAPTMS was then added dropwise to the chelated zirconium complex and left to react for a further 5 minutes under constant stirring. After

this, the second hydrolysis was carried out by adding deionised water (2.44 ml) dropwise to the now silicate/zirconium pre-sol. The synthesis was carried under ambient conditions. The sol was then left to stir for 24 hours before being used. The initial concentration of MAPTMS: ZPO was at fixed in a ratio of 80:20 mol %. In the first development, we decided to fix the theoretical hydrolysis degree at 50% as it was found to be a good compromise between solution viscosity, stability and coatability. The theoretical hydrolysis degree is calculated against the total methoxy groups of the sol gel material, in this case 5 methoxy groups- 3 from the MAPTMS precursor and 2 from the zirconium propoxide precursor. The theoretical hydrolysis degree is then calculated from the overall hydrolysis degree (100%) whilst taking into account the partial hydrolysis of the MAPTMS, to calculate the moles of water needed for the second hydrolysis to give the desired final hydrolysis degree of the material.

In order to make the sol-gel material photo-reactive, a photo-initiator (PI) was added prior to use. The photo-initiator used was 1-Hydroxycylohexyl-1-phenyl methanone, commonly referred to as Irgacure 184 (Irgacure-184, BASF, Germany). The concentration was fixed to 5 mol % with respect to the methacrylate groups of the MAPTMS. The PI was added to the final sol and left to stir for 1 hour prior to use to ensure full dispersion.
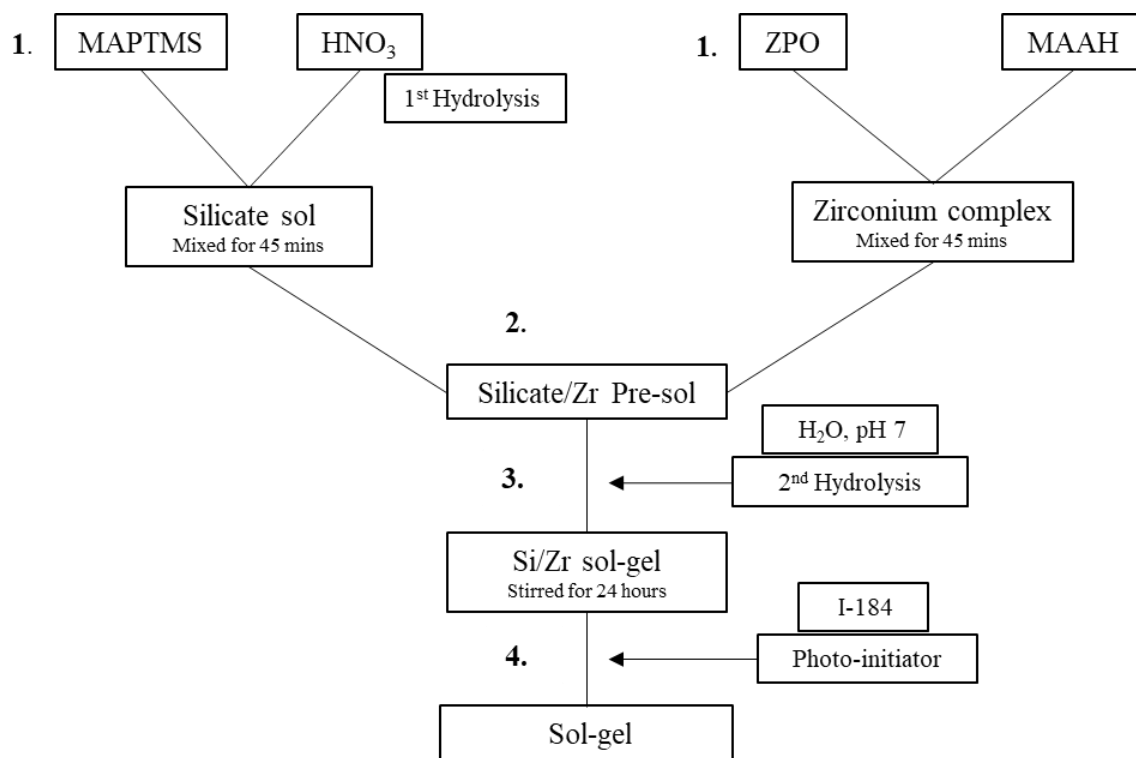
Figure 4. 1: Flow chart for the synthesis of the reference hybrid sol-gel material
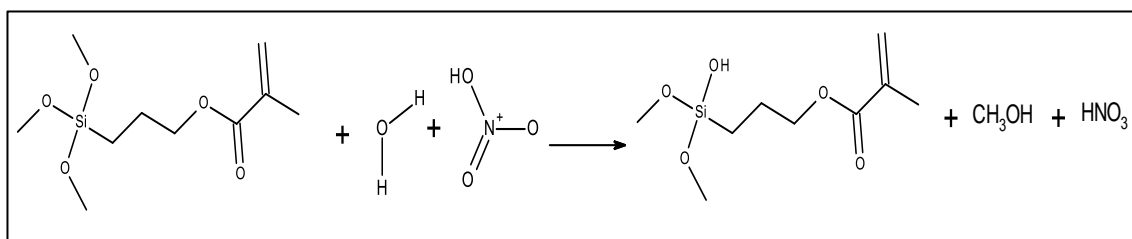
Scheme 4. 1: Reaction scheme of acid catalysed hydrolysis of MAPTMS with nitric
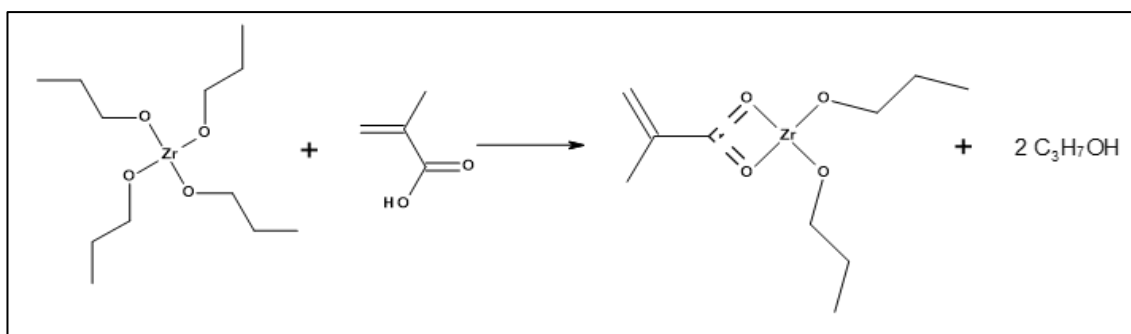
acid

Scheme 4. 2: Reaction scheme for the chelation of zirconium (IV) propoxide with methacrylic acid
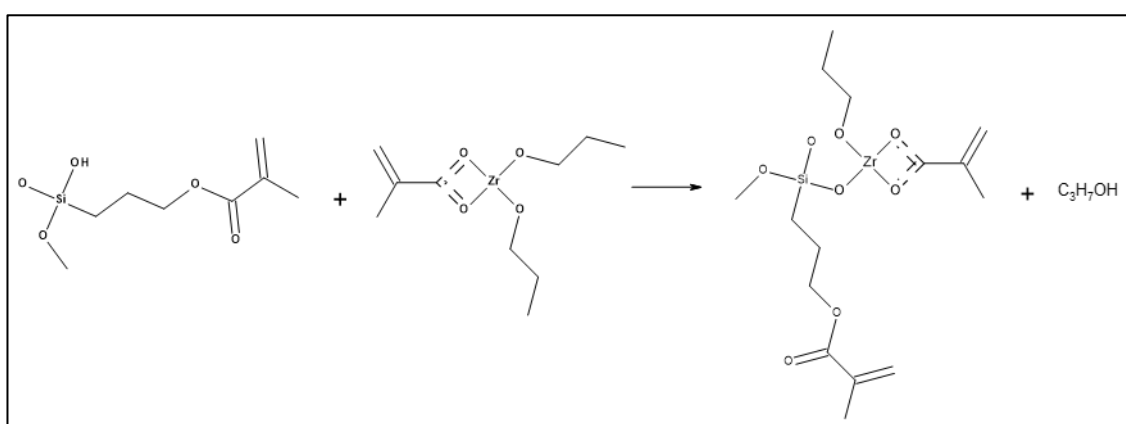
Scheme 4. 3: Reaction scheme for the condensation of the zirconium complex with the pre-hydrolysed MAPTMS
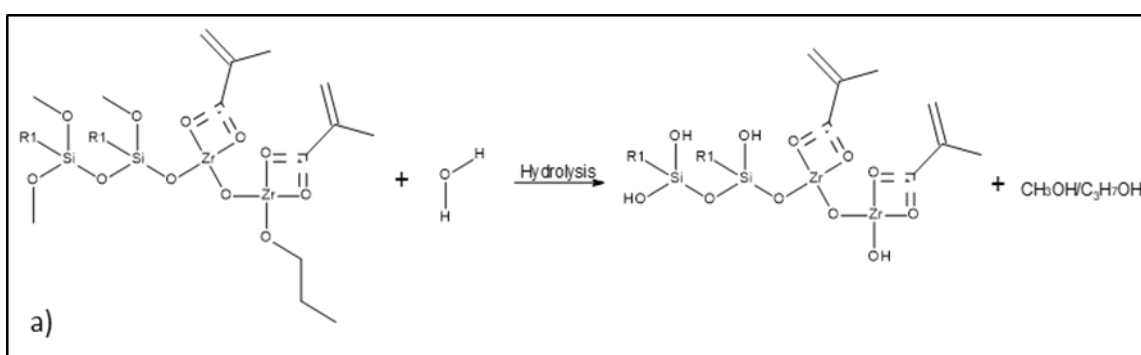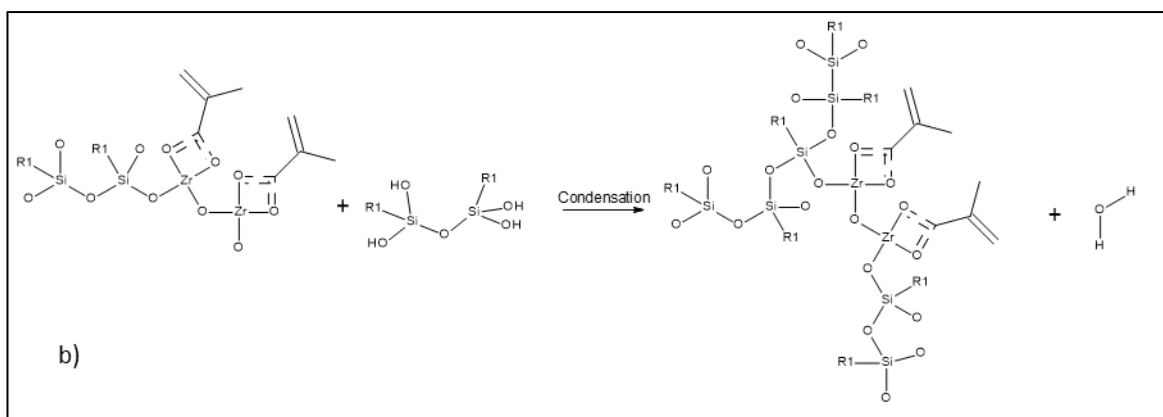
Scheme 4. 4: Reaction scheme for a) the final hydrolysis of the silicate/zirconium sol

and b) the subsequent condensation with a silanol group
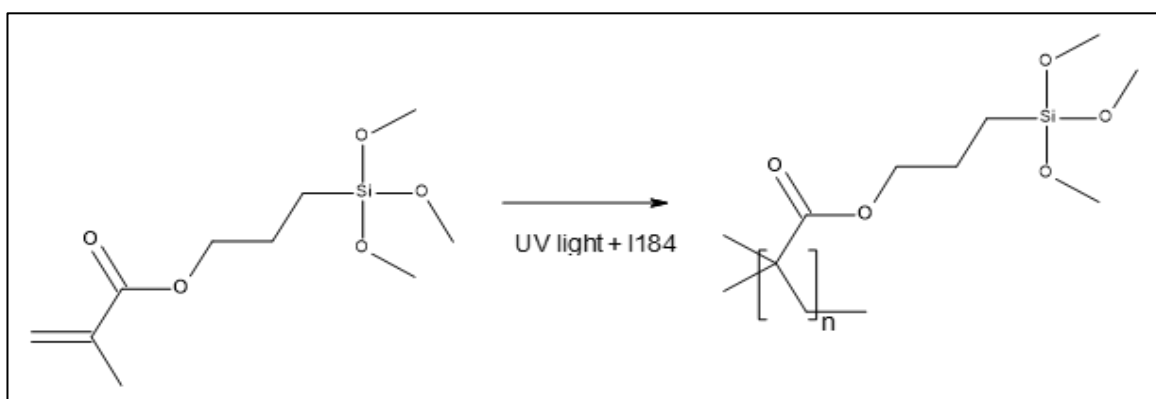
Scheme 4. 5: Reaction scheme for the UV photopolymerisation of methacrylate group

of the MAPTMS

Chemical Name	Abbreviation	Formula	Structure
3-(trimethoxysilyl)propyl methacrylate	MAPTMS	$C_{10}H_{20}O_5Si$	
Zirconium (IV) Propoxide	ZPO	$C_{12}H_{28}O_4Zr$	
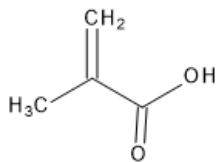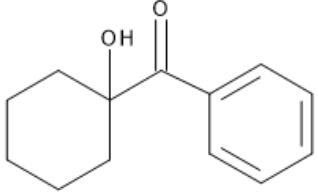
Methacrylic Acid	MAAH	$C_4H_6O_2$	

Table 4. 1: Chemical name, abbreviation, formula and structure of the sol-gel precursors

and photo-initiator used in the synthesis of the sol material

1-Hydroxycyclohexyl-1-phenyl methanone (Irgacure 184)	I-184	$C_{13}H_{16}O_2$	

MAPTMS (mol. %)	ZPO /MAAH (mol. %)	Theoretical Hydrolysis Degree against total alkoxide groups (%)
80	20	50

Table 4. 2: Formulation of Reference hybrid material

Material	Volume (ml)
MAPTMS	28.7
ZPO	13.54
MAAH	2.58
HNO_3	1.6
H_2O	2.44

Table 4. 3: Volume of reagents used to make 48 ml of sol

4.3 Results and Discussion

4.3.1 Particle size analysis

The particle size and distribution of the reference material was measured using DLS over a 4-day period, starting 24 hours after fabrication of the sol-gel material. The main objective behind this characterisation is to identify the possible agglomeration behaviour and sol stability within this period in order to define the adequate coating processing period to achieve coatings with similar particle size. Therefore, any differences observed in terms of structures, surface properties could be only assigned to the chemistries and not to the structure of the particle or the fabrication process.

As shown in Fig. 4.2, all spectra exhibit a single distribution band ranging from 1.2 to 20 nm, which is centred between 3 and 4 nm. Overall there is very little particle growth over the 4-day period and the sol has reached its maximum peak after 2 days of ageing. The distribution band is centred at 3.6 nm after 24 hours of ageing and increases to 4.18 nm after 48 hours where it remains stable up to 4 days after ageing. Another relevant observation is the clear broadening of the distribution bands with ageing. In order to better estimate the broadening of the distribution bands, the full width at half maximum (FWHM) has been measured and plotted along with the maximum peak distribution in Fig. 4.3. The FWHM values range from 4.0 nm after 24 hours to 5.4 nm after 3 days of ageing.

At this stage, it is impossible to clearly explain the aggregation mechanism as the DLS technique can only give an indication on particle sizes and distributions. Nevertheless, the materials being sol-gel reactive, it is likely that the aggregation mechanism involves condensation reactions between silanol groups (scheme 4.6), silanol and methoxysilane groups (scheme 4.7), silanol and zirconium propoxide or hydroxide groups (scheme 4.8, 4.9), zirconium hydroxide groups (scheme 4.10) and zirconium hydroxide and zirconium

95

propoxide groups (scheme 4.11). The results of these condensation reactions are siloxane and/or silicon/zirconium oxide groups. However, ^{29}Si-NMR and FTIR characterisations will be performed in the following sections to provide a better understanding of the chemical reactions taking place during the sol-gel synthesis and ageing process.
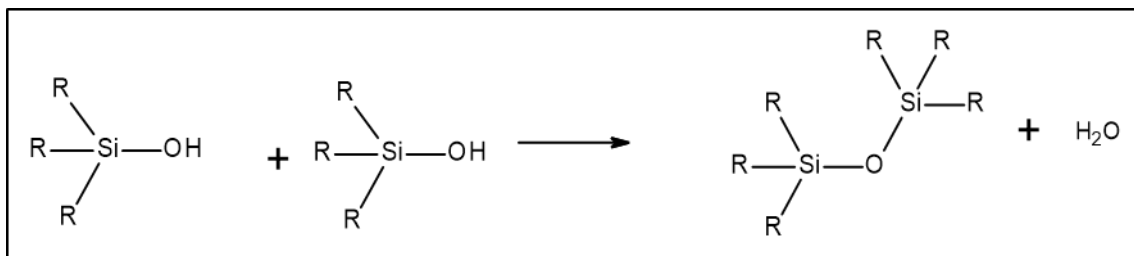
Scheme 4. 6: Condensation reaction between silanol groups
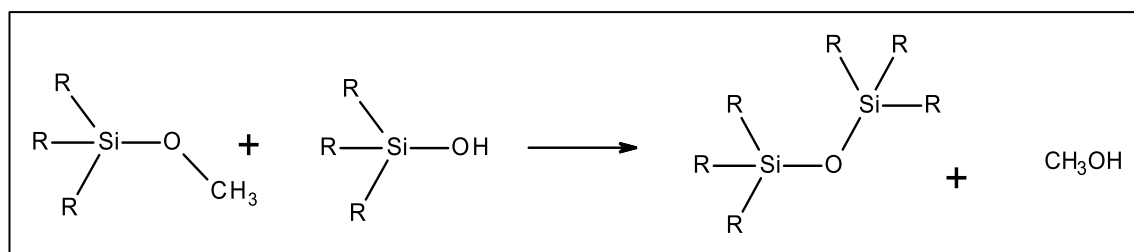
Scheme 4. 7: Condensation reaction between silanol and methoxy silane groups
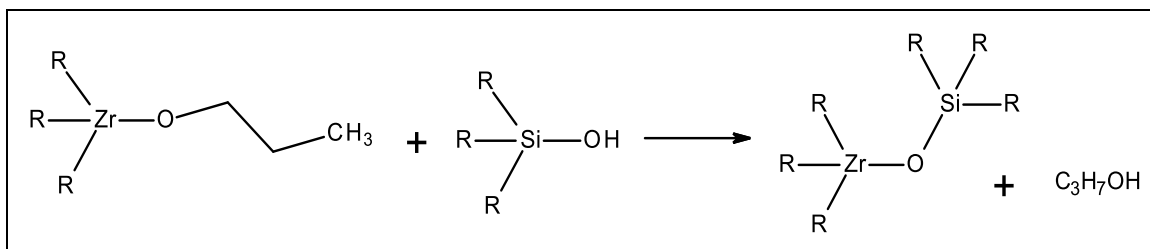
Scheme 4. 8: Condensation reactions between zirconium propoxide and silanol groups
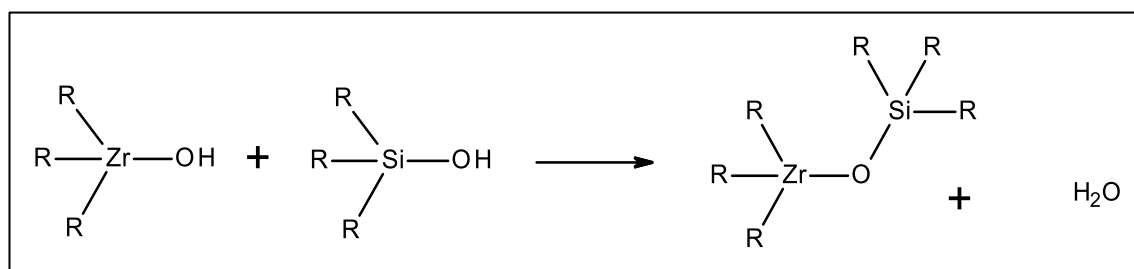
Scheme 4. 9: Condensation reactions between zirconium hydroxide and silonol groups
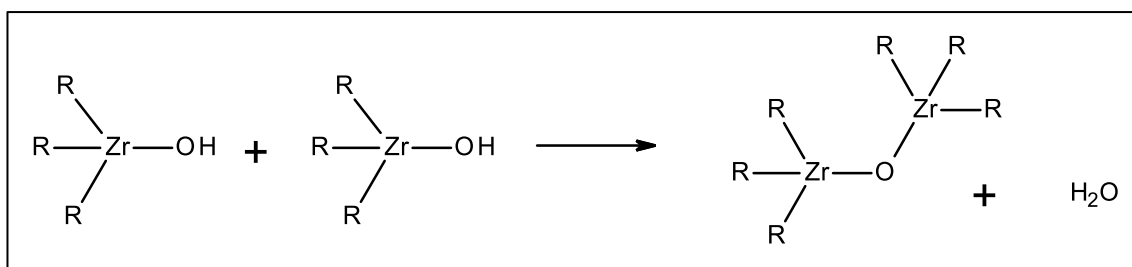
Scheme 4. 10: Condensation reactions between zirconium hydroxide groups
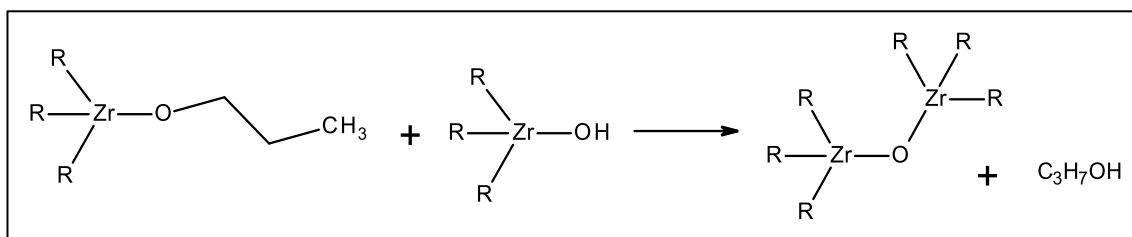
Scheme 4. 11: Condensation reactions between zirconium propoxide and zirconium

hydroxide groups
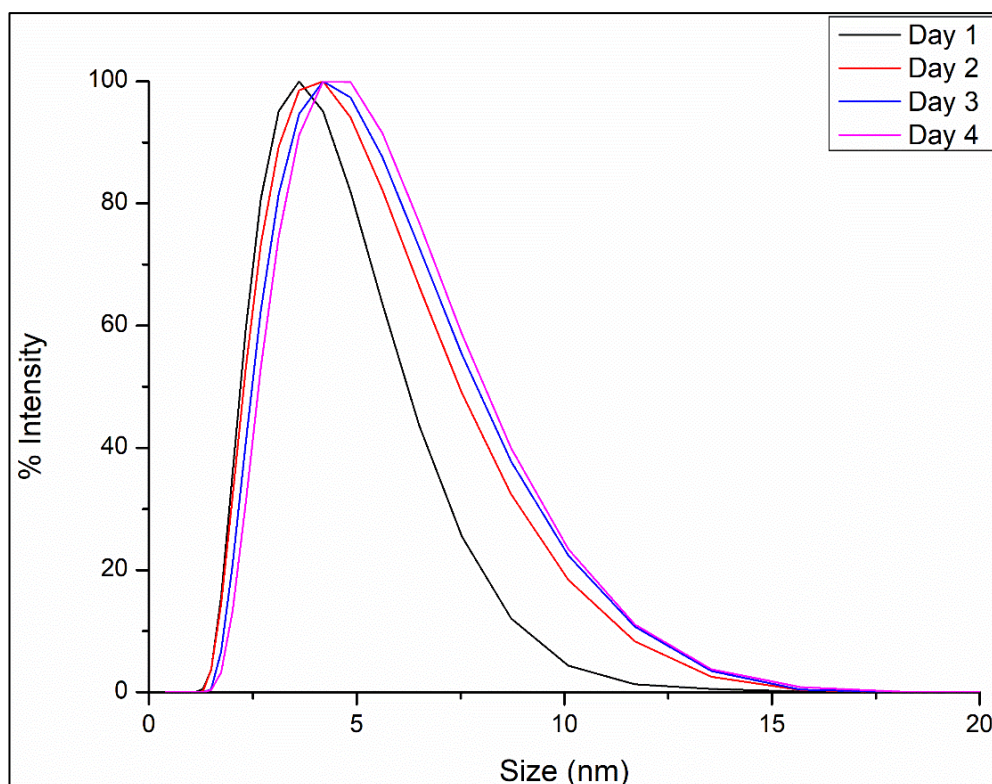
Figure 4. 2: DLS spectra of the reference material over time
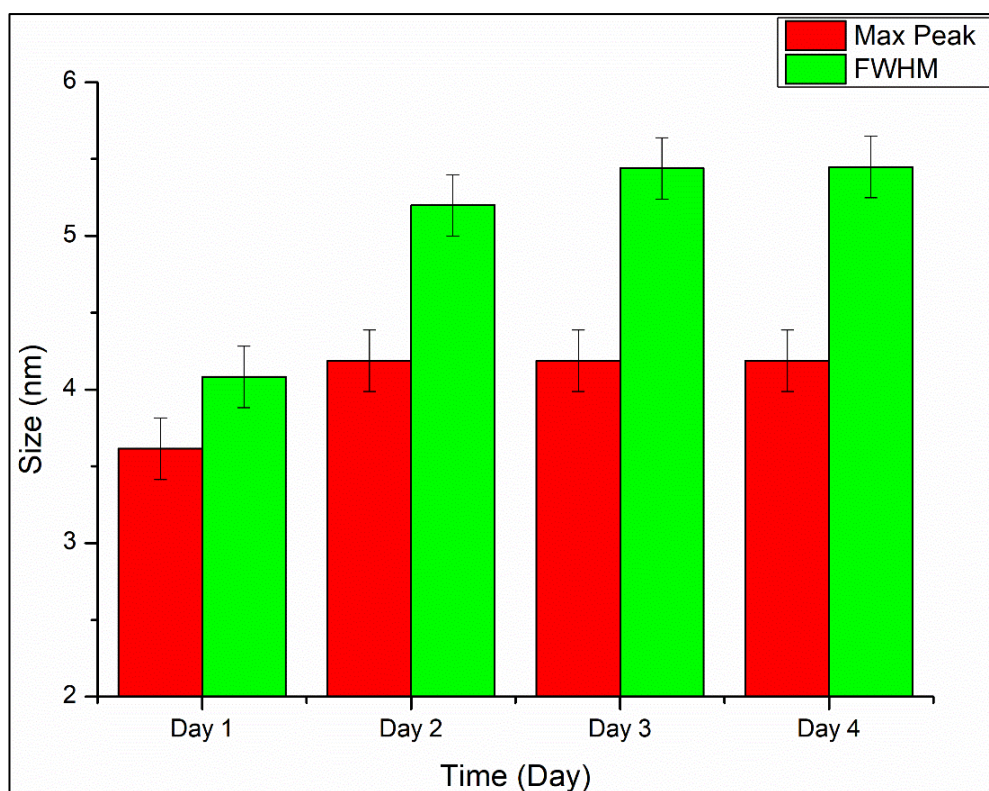
Figure 4. 3: FWHM and max peak measurements for the reference material

4.3.2 Contact Angle Measurements

The surface properties of the reference material were characterised using static water contact CA measurements on coatings which were deposited on glass substrates via spin coating and cured at various temperatures in the range $100 - 150°C$. The goal of varying the curing temperature is to identify if the fabrication process influences the surface properties and if this is case in what proportions this occurs. The CA values were taken once the samples were removed from the oven and left to cool. The CA values as a function of time were not recorded. As represented in Fig. 4.4, it is observed that as the curing temperature increases, a decrease of the contact angle can be seen from $71°$ for the sample cured at 100 °C to $61°$ for the sample cured at $130°C$. Interestingly, further increase of the curing temperature up to 150 °C does not provoke any change of the CA outside of the error measurements (+/- 0.15-0.55). This signifies that most of the physico-

chemical phenomena involving the surface modification take place at temperatures between 100 and 150°C. At this stage, one can conclude on the significant effect of the curing temperature on the surface properties of reference material which may be cause by an increase in surface hydroxyl groups, however the identification of the occurring physico-chemical process would need to be investigated by FTIR spectroscopy to identify any evolution of the structure.

Importantly, these results show that, in our investigations into the development of hydrophilic hybrid sol-gel surfaces, the curing conditions must be fully considered and can play a significant role in tailoring the surface properties.
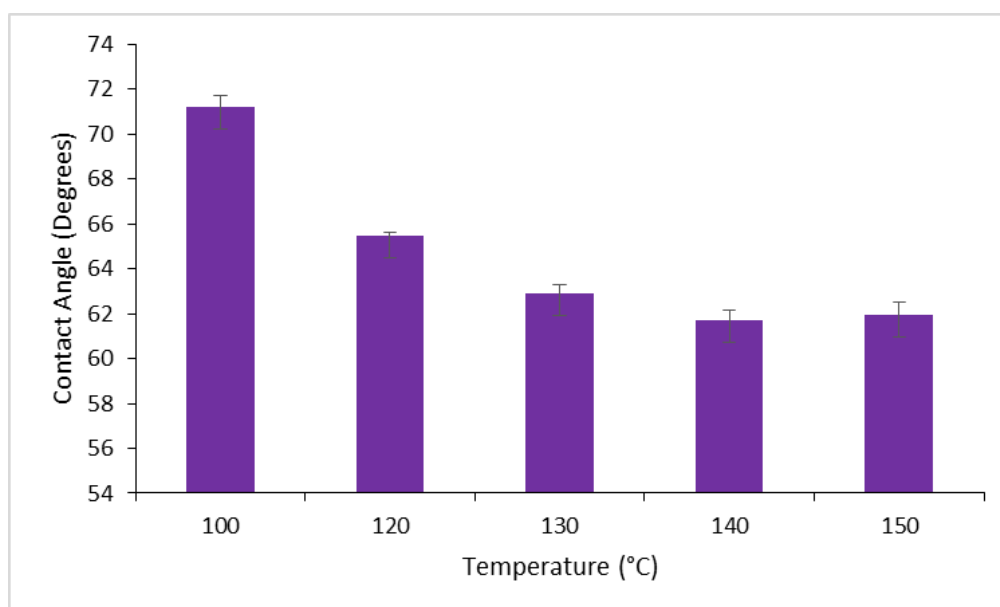
Figure 4. 4: CA measurements vs temperature for the reference material, n = 3 (number of separate samples measured)

4.3.3 FTIR Analysis

FTIR analysis was performed on the reference material which was deposited as coatings on glass substrates and cured at 100, 120, 130, 140 and 150°C. The spectra were recorded in the range of 650-4000 cm^{-1} and are represented in Fig. 4.5. All absorption bands have been attributed based on previous references[137–142] . The broad band located in the range

800–1200 cm^{-1} is characteristic of the silicate network resulting mainly from the superimposition of the silanol (Si–OH, 850 cm^{-1}) stretches, Si–O–Si (890 and 1010–1050 cm^{-1}) and Si–O–Zr vibrations (940 cm^{-1}). The band observed at 1170 cm^{-1} symbolises the stretching of the Si–O–C contained in the methoxy-silane groups of the MAPTMS. The Zr–OH and Zr–O–C bonds composing the zirconium complex are in the region 1300–1650 cm^{-1}. The Zr–MAAH complex possesses two peaks around 1635 and 1533 cm^{-1}, which can be attributed to the symmetric (vs) and asymmetric stretching (vas) vibrations of the carboxylic group (COO$^-$), respectively. With a Δv (COO$^-$) value of 102 cm^{-1}, the chelate can be said to be bidentate[143]. The bands located at 1730, 2800, 3000 and 3200 cm^{-1} are due to the C–O (stretching), C–H (stretching) and residual Si–OH and Zr–OH groups (stretching), respectively.

The sol-gel material exhibits similar chemical vibrations for each curing temperature. In order to identify the effect of the curing temperature on the hybrid sol-gel structure, including the condensation of the inorganic network and the alteration of the hydroxyl groups that are responsible for the surface properties of the material, it is important to focus on the characteristic absorption bands of the inorganic network of the material. Therefore, we will concentrate our analysis in the 800 – 1250 cm^{-1} spectral region, where the silicate and combined silicate/zirconate species are known to absorb, as shown in Fig. 4.6.

In Fig. 4.6 it can be observed that the bands assigned to the Si-O-C groups located at 815 and 1170 cm^{-1}, which are due to the unreacted methoxy-silane groups, are progressively decreasing as the curing temperature increases. Owing to these results, it is obvious that the increase of the curing temperature provokes the conversion of the methoxy-silane groups into higher condensed siloxane bonds along with the formation of silanol groups. Furthermore, as these phenomena are taking place at temperatures up to 130°C, with

stagnation from 130 to 150°C, this signifies that the hydroxylation process and the condensation of the inorganic network are reaching their maximum at 130°C. Indeed, the decrease of the CA can be correlated to the hydroxylation process as identified here. **Therefore, we can conclude that the surface properties of the reference hybrid sol-gel material can be tailored by the control of the curing process, which is essentially due to the thermally activated residual methoxy-silane groups, as represented in Fig. 4.7.**
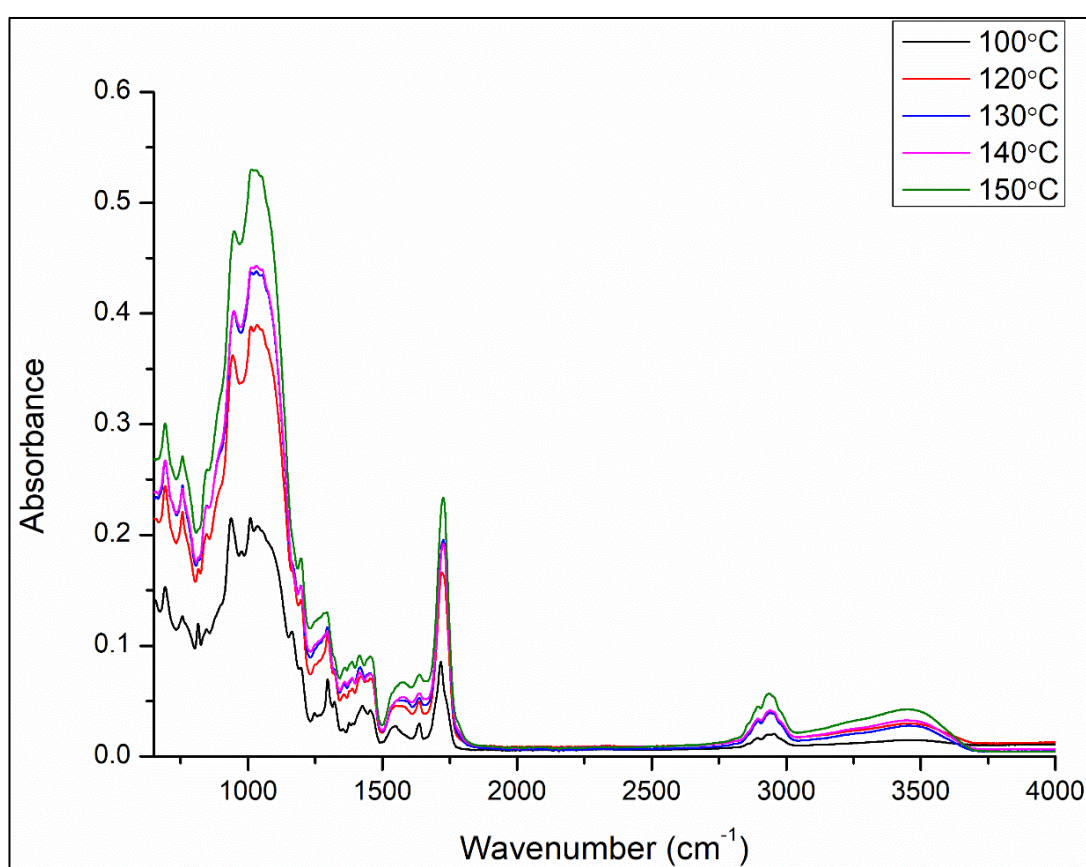
Figure 4. 5: FTIR spectrum all materials from 650-4000 cm^{-1}
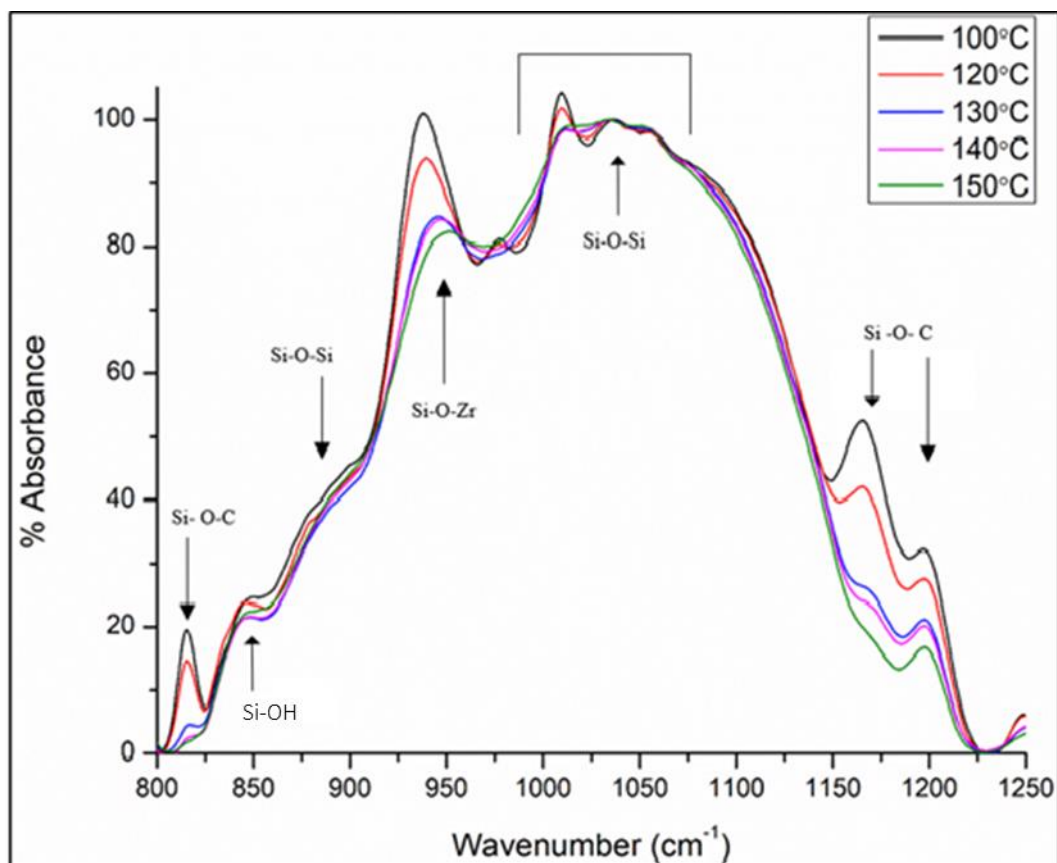
Figure 4. 6: FTIR spectra of the reference material in the range of 800 – 1250 cm^{-1}
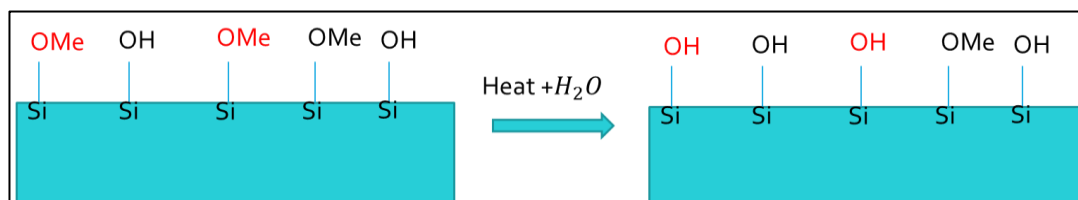
Figure 4. 7: Schematic of proposed hypothesis for the curing effect on the surface properties of the reference sol-gel coating

4.3.4 ^{29} Si-NMR Analysis

Liquid state ^{29}Si-NMR was used to follow the evolution of the silicate network during the synthesis of the sol-gel material and up to 24 hours of ageing, corresponding to the deposition time of the sol-gel materials as coatings, prior to micro-processing. ^{29}Si-NMR spectra were taken at 5 different stages throughout the synthesis, in the pure organosilane

precursor (MAPTMS), during the pre-hydrolysis of the MAPTMS with nitric acid (solution A), after addition of the zirconium complex with the MAPTMS solution (solution B), 30 minutes after the final hydrolysis (solution C), and finally 24 hours after the sol-gel has been synthesised (Sol-gel). Fig. 4.8 represents the ^{29}Si-NMR spectra recorded for the above mentioned preparation stages. T_n notation is used in ^{29}Si-NMR to describe the number of siloxane bonds (Si-O-Si) formed in a silicon atom in the materials. As MAPTMS contains three reactive methoxide groups that can convert into siloxane bonds, there are 4 different T_n species (T_0, T_1, T_2 and T_3) where n is equal to the number of bridging Si-O-Si bonds within the organosilane[144]. The concentration of each of the 4 T species T_0, T_1, T_2 and T_3 are plotted Fig. 4.9 below. The chemical shift range for each T species has been presented in Table 4.3.

The pure MAPTMS precursor exhibits a single sharp peak at -42.6ppm within the T_0 range which indicates that the MAPTMS is un-hydrolysed and contains no bridging Si-O-Si bonds, thus free of any impurity. Solution A exhibits T_0, T_1, and T_2 species in relative concentrations of 51.41, 44.52, and 4.06 % respectively. This presence of T_1 species within the solution indicates that the MAPTMS precursor has undergone hydrolysis and condensation reactions and contains at least one bridging Si-O-Si bond. For solution B, all 4 T species are present in concentrations of 46.34, 26.31, 24.18, and 2.60 % for T_0, T_1, T_2 and T_3 species, respectively. The presence of all 4 T species indicates that the introduction of the zirconium complex within the sol-gel matrix may play a role in the condensation of the material. As the zirconium complex would be more reactive than the MAPTMS[85], this increase in reactivity may account for the increase in the condensation of the material from solution A to B. For solution C, the T_0 species have disappeared, which indicates that the MAPTMS precursor has been fully hydrolysed. T_1, T_2 and T_3 species are present in ratios of 18.23, 50.91, and 30.85 % respectively. For the

final sol-gel material, T_1, T_2 and T_3 species are present in the material in concentrations of 2.40, 39.11 and 58.47 % respectively. It is clear that there has been a dramatic decrease in the T_1 species for the increase of T_3 species, indicating that an ageing of 24 hours of favours the formation of highly condensed T_3 silicate species.

As the ^{29}Si-NMR study was carried out on the liquid sol and is still a liquid after 24 hours of ageing, the results cannot be directly correlated with the FTIR data or the CA data – which is performed on solid cured coatings, as the liquid state and solid cured state of the sol-gel material are not identical and differ due to the thermal condensation of the materials.

Structure	Chemical Shift Range (ppm)	Notation
$RSi(OH)_3$	-40 to -48	T_0
$RSi(OH)_2OSi$	-49 to -55	T_1
$RSi(OH)(OSi)_2$	-56 to -63	T_2
$RSi(OSi)_3$	-64 to -73	T_3

Table 4. 4: Structure, chemical shift range and notation for ^{29}Si-NMR
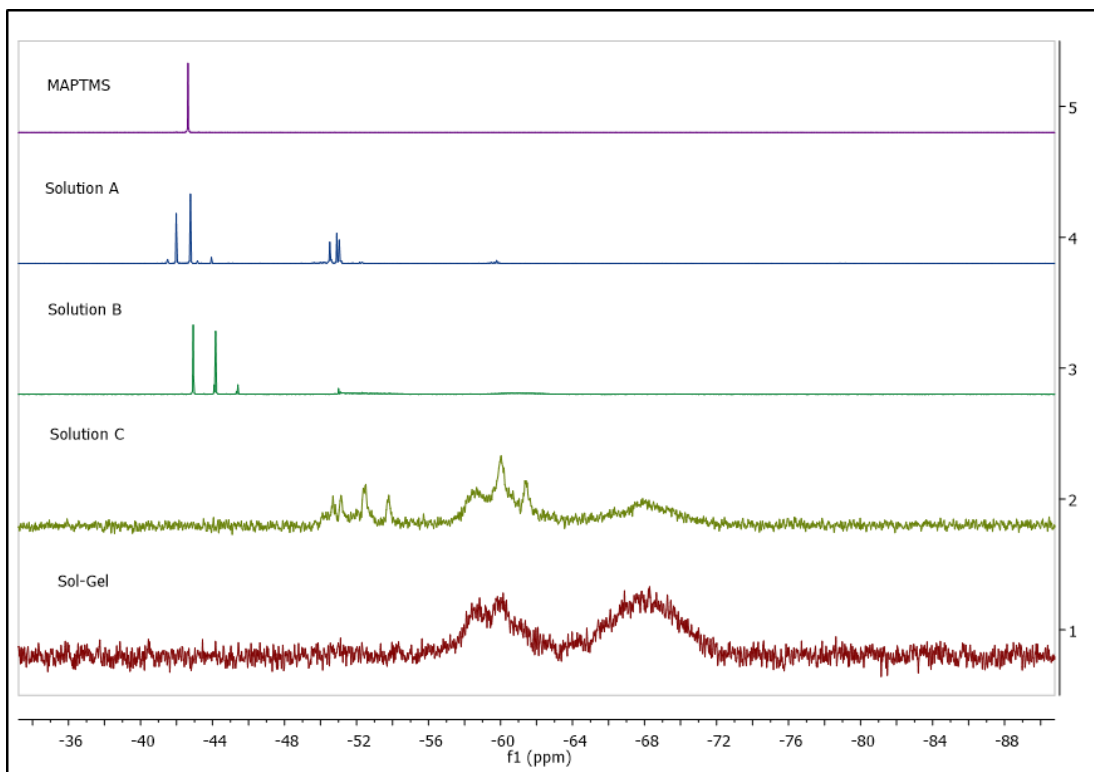
Figure 4. 8: Liquid state ^{29} Si-NMR for the reference material at 5 different synthesis stages
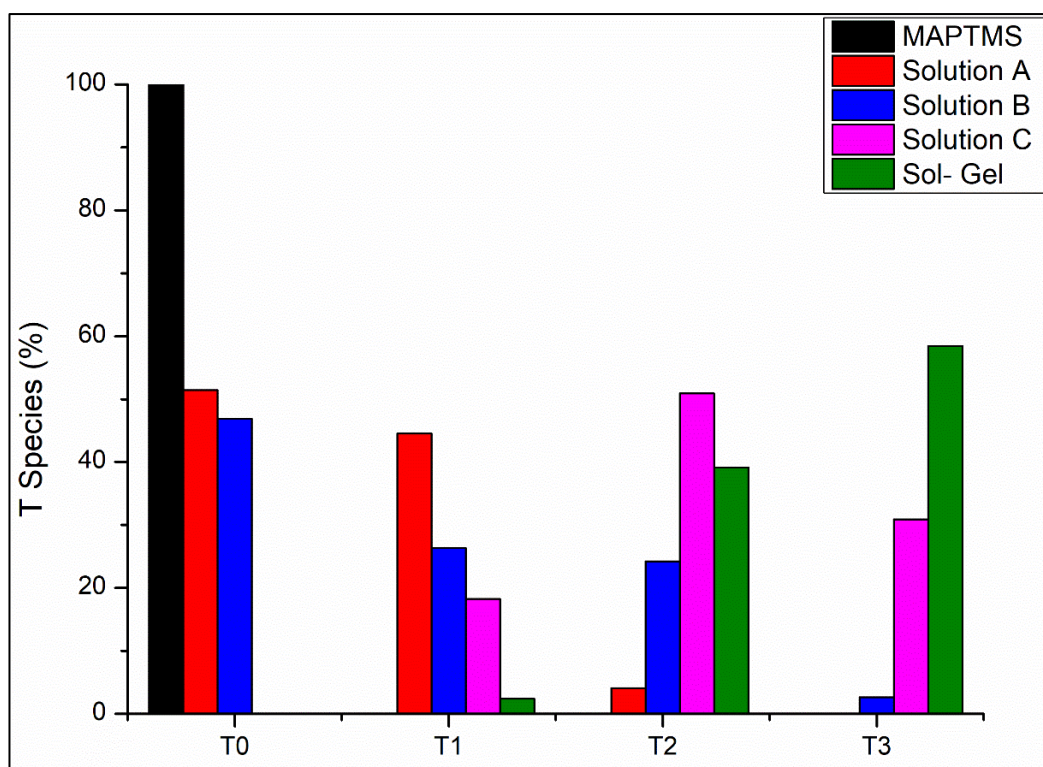
Figure 4. 9: T species concentration for the reference material at 5 different synthesis stages, n=3

The ^{29}Si-NMR clearly highlights the effect of the transition metal on the condensation of the silicate species, thus forming microstructures with denser morphologies. However, if the content of silicate species can be identified by the ^{29}Si-NMR, it is not possible to quantify the evolution of the silanol groups, primarily responsible for the surface properties of the coatings. Therefore, for this, the FTIR is the only conclusive structural characterisation technique.

4.3.5 Thermal Analysis

DSC analysis was performed on the liquid sol-gel material from 25 – 300°C to identify the thermal behaviour of the material including solvent evaporation, glass transition and possible degradation of the material, as well as to identify the optimum curing working temperature of the material. As shown in Fig. 4.10, the spectrum exhibits three thermal

zones namely, 25 – 100 ℃, 100 – 170℃ and above 170℃. These thermal zones represent the evaporation of volatile solvents, including free and entrapped solvents (methanol, propanol and residual water) within the sol-gel network, the condensation of the material and the glass transition phase of the material, respectively. The presence of the solvent endothermic band centred at 39℃ is due to the MAPTMS and ZPO precursors that contain 2 and 70 wt. % of methanol and 2-propanol, respectively. In addition, the sol-gel process involves hydrolysis and condensation reactions of the MAPTMS and ZPO precursor that also contribute to the in-situ production of methanol and 2-propanol. The condensation band observed between 100 and 170℃ shows a negative slope due to the thermally catalysed condensation reactions (as demonstrated by the FTIR results) that also contributes to the formation of solvents. The exothermic peak at 185℃ is characteristic of the glass transition temperature (Tg) of sol-gel materials. More precisely, it represents the full solidification point of the sol-gel material. Therefore, from these results one can conclude that our reference material still undergoes thermally activated condensation reactions at up to 185℃, which constitutes the maximum condensation point of the material. Both the CA and IR samples were tested up to a maximum temperature of 150 ℃ here but the working temperature would be much lower around 120-130 °C and thermal degradation is evident above temperatures of 150°C.
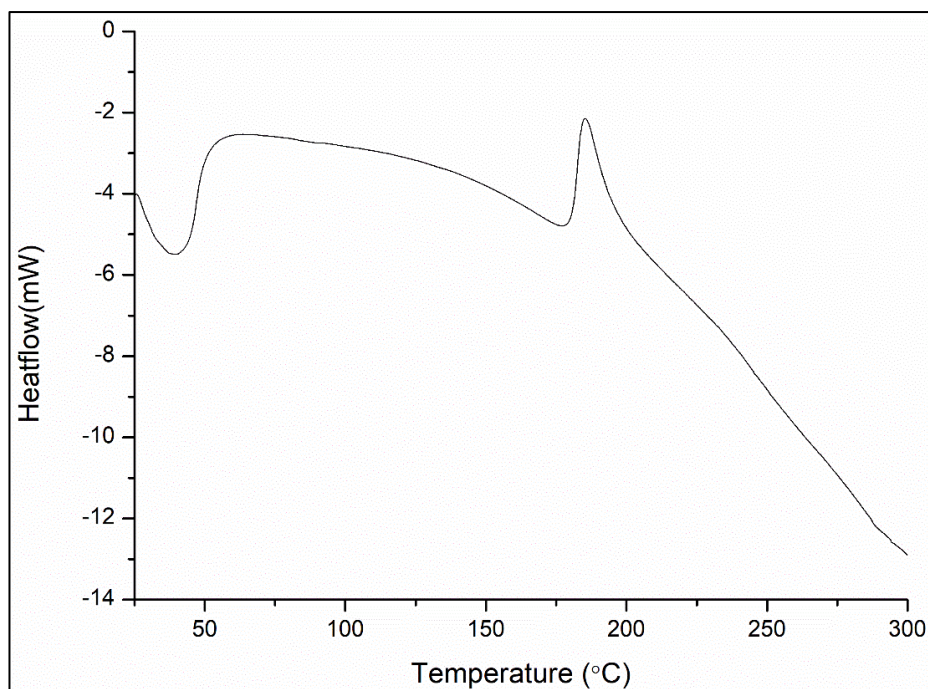
Figure 4. 10: DSC spectra of the reference sol-gel material

4.4 Microstructuration

In this section, the microstructuration ability of the developed material will be investigated. The reference material as described above contains MAPTMS and MAAH, which contains methacrylate groups that can potentially be photo-reactive in the presence of free radicals. For this purpose, 5 mol % Irgacure 184 has been added to the sol-gel material and left to stir for 1 hour before use. The microstructuration process employed is a standard mask-photolithography process that involves 4 main steps as illustrated in Fig. 4.11 and has been used previously to fabricate microstructures.
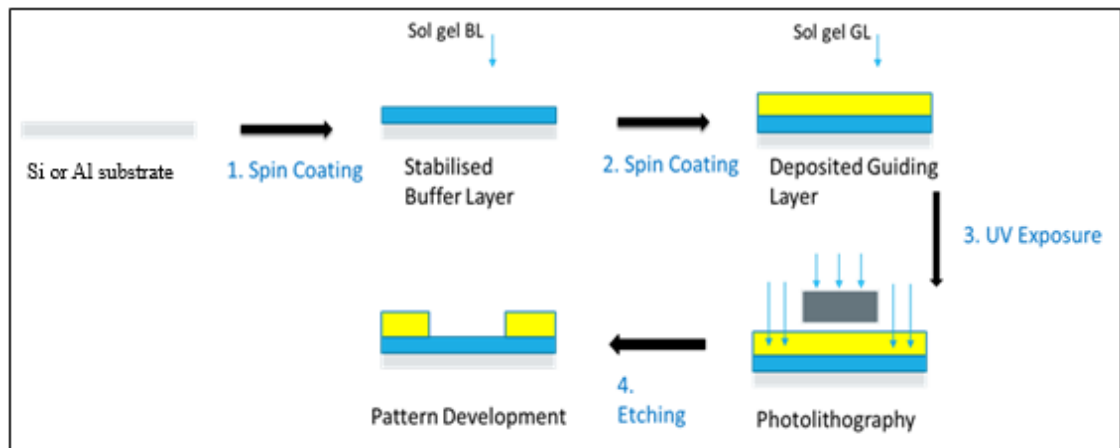
Figure 4. 11: Microchannel photolithography process

This process involved four main steps starting with a bare substrate material. This initial proof of the microstructuration ability of the reference material was performed using AA2024-T3 aluminium alloy as a substrate. However, silicon wafers would be more adequate in the optimisation phase of this project due to their cleaving ability especially for cross-section observations.

Step 1: The aluminium substrate was coated with the first layer of the reference sol-gel material (as synthesised in section 4.2) and fully thermally stabilised. This 1st sol-gel layers is referred to as the buffer layer (BL) and will form the bottom of the microfluidic channels. The BL was dip coated onto the aluminium substrate at a dip speed of 40 mm/min and cured at 120℃ for 1 hour. Under these conditions, the layer was found to be insoluble in the alcoholic solvents used to develop the microfluidic channels in the subsequent process steps, suggesting the thermal curing process enabled the creation of enough condensation reactions and fully stable chemical bonds to fully thermally stabilise the material.

Step 2: The reference material was deposited on the BL and partially thermally stabilised at a temperature of 100°C for 10 min. This 2nd sol-gel layer is referred to as the guiding layer (GL). Under these conditions, the coating was found to be `touch dry` while being

fully soluble in alcoholic solvents. This is essential to avoid loss of matter, when the GL is in contact with the photomask, while still allowing for the development of photo-patterned microstructures.

Step 3: Having allowed the substrate to cool to room temperature, microfluidic channels were patterned by exposure to UV light from a mask aligner (KUB, KLOE) and through a photomask. A UV exposure time of 250 s was employed to yield a high-fidelity image.

Step 4: The pattern was developed by etching the UV exposed GL in 2-propanol, gently agitating the substrate in a petri dish of the solvent for 20 s, followed by drying in an oven at 100°C for 10 min. As the sol-gel is itself a negative photoresist, the area that was unexposed to UV light will be dissolved away. As the BL was fully thermally stabilised it should not undergo polymerisation reactions and therefore will not be affected by the etching step.

With these fabrication conditions, micro-channels were successfully fabricated as shown in the SEM image in Fig. 4.12. In this figure three zones can be observed: (1) a densified zone of about 488 μm, (2) an intermediate zone comprised between 50 and 80 μm and (3) the channel itself of about 100 microns. The intermediate zone may be the result of over irradiation of zone 1 or it may be sol debris from the etching process. Therefore, processing parameters to achieve exact mask patterns on the photo-reactive sol-gel material will need to be optimised.

Importantly, these initial fabrications demonstrate the ability of the developed reference material to be photo-patterned and enabled the fabrication of well-defined micro-channels, which we aim to further optimise in the next sections.
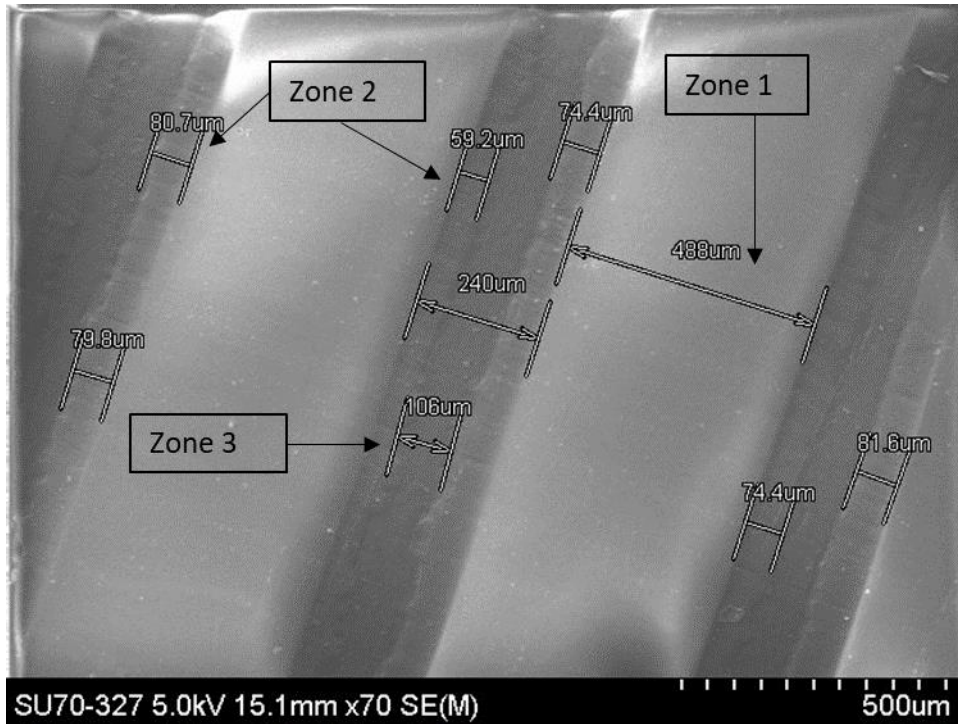
Figure 4. 12: SEM image of a microchannel fabricated by mask UV-lithography

4.5 Conclusion

This chapter focused on the development and characterisation of a reference photo-curable hybrid sol-gel material. The particle size analysis showed a single size distribution band centred at 3.6 nm and that a homogenous material was formed after 24 hours. Further ageing showed significant increase of both particle size and distribution, which were explained by the agglomeration of both small and large particles characterised at up to 48 hours of ageing. The CA measurements found that as the curing temperature increased, the CA values decreased up to 130 °C and then remained stable up to 150 °C, due to condensation of the inorganic network along with the formation of Si-OH groups as corroborated by the FTIR results. A CA angle decrease of 10° was achieved by the alteration of the curing temperature to reach 61°, for samples cured at 130°C and above. This result needed to be explained by the structural evolution of the material as characterised by FTIR spectroscopy. Indeed, the FTIR analyses demonstrated the

occurrence of a dual phenomenon taking place as function of the applied curing temperature, namely the condensation of the inorganic network along with the formation of silanol (Si-OH) groups, attributed to the hydroxylation of the residual methoxy-silane (Si-O-C) groups, which were resulting from the under-stoichiometric hydrolysis employed in the sol-gel synthesis. Correlation between the CA measurements and FTIR analyses demonstrated that the thermally activated condensation and hydroxylation process takes is optimum at 130°C. More importantly, these results showed that the surface properties of the reference sol-gel material can be tailored by the applied thermal curing of the fabricated coatings. ^{29}Si-NMR analysis gave an indication of the hydrolysis and condensation reactions throughout the synthesis of the sol-gel material. It showed that that after 24 hours the so-gel materials favoured the formation of the higher condensed T_2 and T_3 species with very little T_1 species present in the material. DSC analysis identified the thermal behaviour of the material, with condensation reactions identified at temperatures above 100°C, thus confirming FTIR results, and a full stabilisation temperature of the material noted at 185°C. The sol-gel material was also shown to be micro-structurable using a standard photolithography process. Channel widths of ~100 microns were achieved as seen by the SEM images. As this was an initial proof of concept further optimisation is needed.

This chapter has highlighted the relationship between the structure of the sol-gel coatings and the effect of the curing temperature. This result will be further explored in the following chapters. The following 3 chapters will investigate separate chemical routes of altering the reference hybrid sol-gel material chosen for this work. The alteration of the zirconium content and the degree of hydrolysis will be investigated. The fabrication of core shell nanoparticle materials will also be explored with the aims of improving the wettability of the coatings for the use in

microfluidic applications. The microstructuration of the sol-gel material will be further explored in chapter 9.

5 Influence of the transition metal on the structure and surface properties of the hybrid sol-gel materials.

5.1 Introduction

Having successfully developed the reference material in chapter 4, this chapter will concentrate on investing the effect of the concentration of each of the employed precursors on both the structure and surface properties of the reference hybrid sol-gel material. To better understand the effect of the structure on the wetting properties of the coatings, the relative content of the silicon and zirconium precursors will be altered while keeping the sol-gel synthesis and coatings fabrication conditions identical so that the only effect of the precursors content may be identified on the structure and surface properties of the coatings.

The properties of the hybrid sol-gel materials will be characterized employing Fourier transform infrared spectroscopy (FTIR), silicon nuclear resonance spectroscopy (^{29}Si-NMR), and scanning electron microscopy/energy dispersive X-Ray spectroscopy (SEM/EDX). The wettability will be identified by contact angle measurements. The thermal properties will be characterized by differential scanning calorimetry (DSC), while the particle size and distribution of the materials will be characterized by dynamic light scattering (DLS).

5.2 Materials Preparation

As previously described in chapter 4, the reference sol-gel material is composed of an organically modified silica precursor (MAPTMS) and an organically modified zirconium complex (ZPO). As this chapter is concerned with the effect of the zirconium concentration on the structure and wettability of the hybrid coatings, the ZPO

concentration has been varied from 1 to 30 mol%, as summarised in Table 5.1 below. The theoretical hydrolysis degree has been fixed at 50% against the total reactive alkoxide groups. As photo-curable materials were not needed for this work, the photo-initiator was not added to the final sol-gel material. The synthesis of these new series of materials is the same as previously described in detail in section 4.2. The volumes used to make ~48 ml of each material is shown in table 5.2. The material volumes were scaled up as necessary.

Material	Theoretical Hydrolysis Degree (%)	MAPTMS: ZPO: MAAH (Mol %)
A	50%	99:1:1
B	50%	95:5:5
C	50%	90:10:10
D	50%	80:20:20
E	50%	70:30:30

Table 5. 1: Material formulations

Reagent	Material A Vol (ml)	Material B Vol (ml)	Material C Vol (ml)	Material D Vol (ml)	Material E Vol (ml)
MAPTMS	28.70	28.70	28.70	28.70	28.70
ZPO	0.54	2.83	6.01	13.54	23.50
MAAH	0.104	0.544	1.148	2.58	4.46
HNO$_3$	1.6	1.6	1.6	1.6	1.60
H$_2$O	1.692	1.23	2.00	2.44	3.00

Table 5. 2: Volumes of reagents for each material

5.3 Results and Discussion

5.3.1 Particle Size Analysis

The particle size of the materials was recorded using DLS 24 hours after fabrication and are shown in Fig. 5.1. It can be seen that each material exhibits a single size distribution band ranging typically from 0.5-20 nm. Two main differences are observed: (1) the maximum size of the various materials and (2) the widths of the bands between the minimum and maximum size for each material. To get a better understanding of the evolution of the particle sizes of the materials, the maximum peak position and the full width at half maximum (FWHM) of each band are plotted in Fig. 5.2

It can be observed that the increase of the ZPO concentration provokes a progressive increase in both the max peak of the distribution band and the FWHM, suggesting that the transition metal has an active role on the particles growth and size distribution. Interestingly, the increase of both parameters is consistent for all materials. For materials A-C, the particle size ranges between 1.7 and 2.7 nm, and between 3.6 and 5.6 nm for materials D and E. The FWHM has the same tendency with values varying from 2 to 3.2 nm for materials A to C, and values from 5 to 7.2 nm for materials D and E.

In addition to the particle size increase, this also indicates that the zirconium increases the particles heterogeneity. To understand these results, an insight into the effect the zirconium complex has on the silica network is needed. It has been demonstrated in similar materials that the Zr can act as a catalyst of the condensation of the reactive silanol and silicon alkoxide, enabling the formation of fully condensed inorganic networks[138].

Although DLS analysis can provide an insight into the particle size and distribution of the materials it cannot provide an insight into the structure of the sol-gel materials. Therefore, FTIR will be employed in the following section to investigate the structural evolution of

the materials and conclude on the effect of the zirconium complex onto the condensation of the inorganic network, thus possibly further explaining the DLS results discussed here.
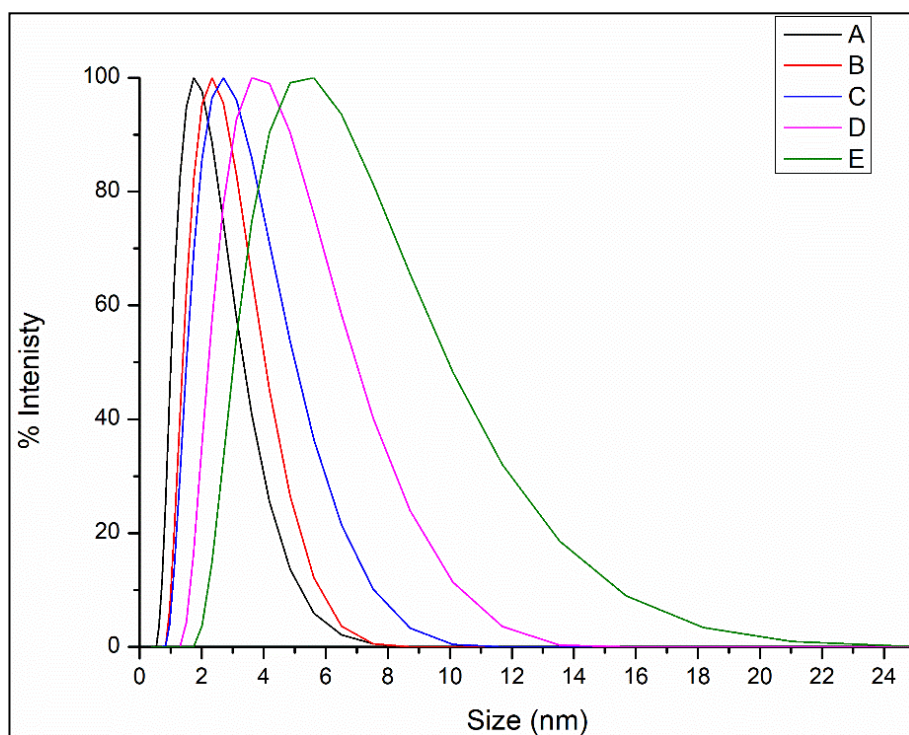
Figure 5. 1: DLS spectra for all materials 24 hours after fabrication
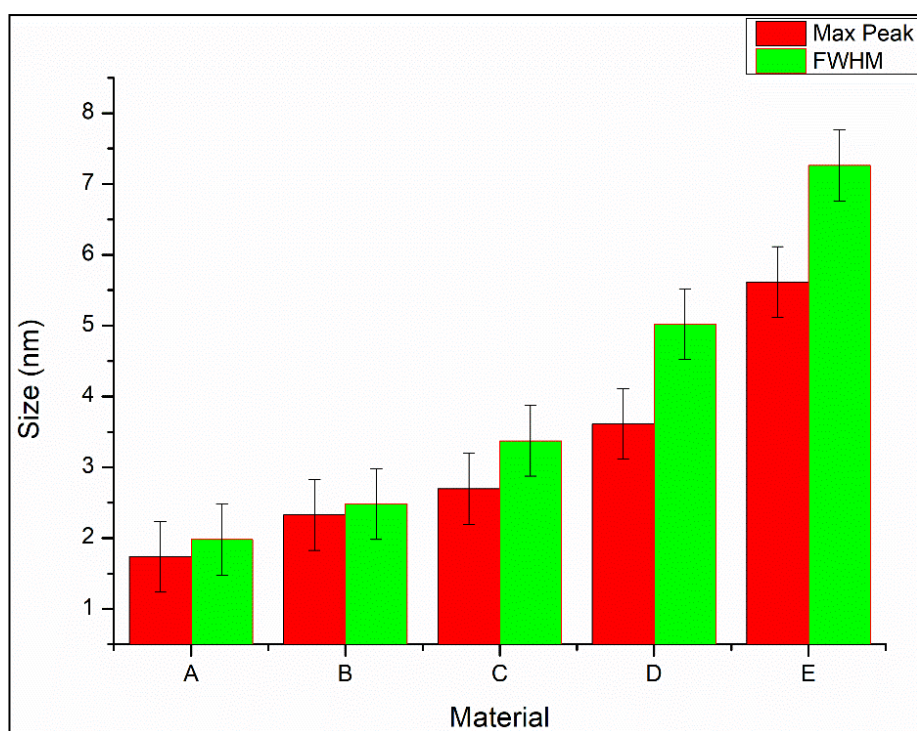
Figure 5. 2: FWHM and max peak for all materials 24 hours after fabrication

5.3.2 Contact Angle Measurements

Static water contact angle measurements were performed on all sol-gel coatings. The contact angle measurement of all materials were investigated and the average contact angle was plotted as a function of temperature. The CA measurements for this series of materials is pictured in Fig. 5.3 below. Two behaviours can be observed depending on the curing temperature. At 100°C, materials containing 1 to 20 % ZPO exhibit a CA close to 67°, whereas the material containing 30 % ZPO has a slightly higher CA value of 70°. As the temperature increases to 120°C it can be seen that an opposite tendency is observed with samples containing a high content of ZPO exhibiting lower CA values than those that contain lower % ZPO content. Interestingly, except for material A, all other materials show a stagnation of their CA value from a curing temperature of 130°C. Unlike the other materials, material A shows an increase of the CA from 130 to 150°C. These observations clearly signify that the content of zirconium plays a role in the surface properties of the materials. The hypothesis to explain this behaviour for material A can be in relation with the formation of hydrophilic species at up to 130°C with a conversion of these hydrophilic species into hydrophobic groups for temperatures greater than 130°C. However, this variation can only be possible if the morphology of the materials is dramatically different from low to high ZPO concentrations, therefore enabling conversion of hydrophilic to hydrophobic species being more favourable at low ZPO concentration. In other words, this phenomenon would be possible if material A exhibits a higher porosity than other materials, therefore having the ability to be hydrophilised at temperatures lower than 130°C and hydrophobised at higher temperatures. This would mean that the surface properties would be governed by the occurrence of a competition between a hydrophilisation process at low temperatures and a hydrophobisation process taking place at higher temperatures, likely due to the conversion of hydroxyl groups into oxide groups.

In order to confirm or disconfirm this hypothesis, FTIR analyses of the evolution of the inorganic groups are required.
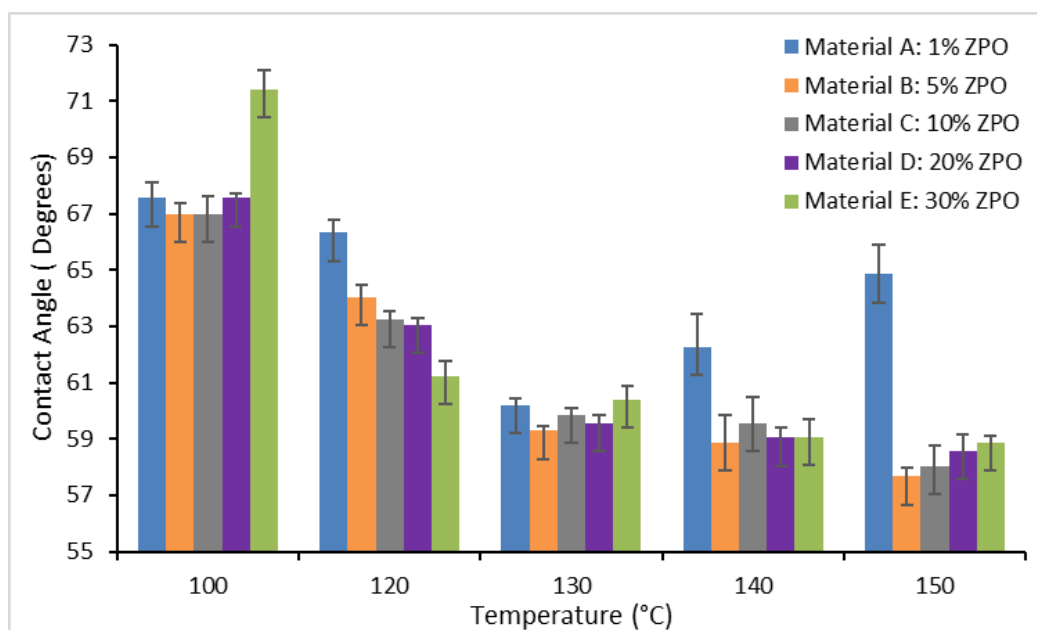
Figure 5. 3: CA measurement vs temperature for all materials with varying [ZPO]

5.3.3 FTIR Analysis

The recorded FTIR spectra for all materials were found to exhibit similar chemical vibrations and peak positions, as shown in Fig. 5. 4 (samples cured at 100ºC). This is due to the formation of the same chemical groups because of a uniform preparation process, the only difference being the MAPTMS/ZPO ratio. To identify the effects of the curing temperature and material formulations on the reactivity and condensation of the inorganic network, it is important to focus on the characteristic absorption bands of the inorganic backbone of the materials. For this reason, the absorption bands in the range $800 – 1250$ cm^{-1} were investigated, as shown in Fig. 5.5. In the previous study[145], it was found that, for a curing temperature of 120ºC, the ZPO content significantly affects the absorption in the $800 – 1250$ cm^{-1} range, but here the effect of the curing temperature is investigated in the domain of temperatures usually required for fully stabilizing hybrid sol-gel coatings, from 100 to 150ºC. The absorption bands were attributed according to the results of

119

previous studies[137,138,140,141,146,147]. For material A, it can be observed that the Si-O-Si symmetric stretching band located at 815 cm^{-1} and the Si-O-C symmetric stretching bands located at 1170 and 1200 cm^{-1} decrease when the curing temperature increases. In parallel, the broad band located in the range $1000 - 1100$ cm^{-1} and related to the asymmetric stretching of the Si-O-Si bonds is seen to shrink from the high energy vibrations as the curing temperature increases. Actually, this band is composed itself by the superimposition of five sub-bands located at 1010, 1030, 1055, 1070 and 1090 cm^{-1}. According to Lerot and Low[139], the band located at 1090 cm^{-1} is attributed to siloxane units located at the interface between tetrahedral and octahedral units, whereas the lower energy bands would relate to siloxane units at the interface between tetrahedral units. From this reference, one can suppose that in our system, in this spectral region, the high-energy vibrations would represent the siloxane bonds with a more structured network whereas the lower ones would be related to a more disordered network. Therefore, the decrease of the intensities of the bands with higher energy indicates the formation of a network with a lower connectivity, probably with a higher porous morphology. This hypothesis is supported by the intensity decrease of the symmetric stretching of the Si-O-Zr bond located at 940 cm^{-1}. Finally, although the intensity of the band related to the symmetric vibration of the Si-OH group located at 890 cm^{-1} is seen to decrease, its relative intensity against the Si-O-Si groups (815 and $1000 - 1150$ cm^{-1}) is found to be the highest for the sample cured at 130 ºC. This supports the CA measurements where the sample cured at 130℃ was found to be the most hydrophilic sample for material A. In summary, for material A, the increase of the curing temperature provokes the formation of hydrophilic silanol groups at up to 130℃. Above 130℃, the coatings tend to form hydrophobic siloxane groups with increasing amorphous character of the inorganic network.

For materials B to E, the bands related to the symmetric siloxane (815 cm^{-1}) and residual alkoxysilane (1175 cm^{-1}) groups are seen to decrease as the curing temperature increases. The relative intensity of the silanol (840 cm^{-1}) groups against the symmetric siloxane stretching increases as the concentration of the zirconium precursor increases, suggesting that the zirconium atom favours the formation of hydrophilic Si-OH groups. The shrinkage of the asymmetric siloxane vibrations bands (1000 – 1150 cm^{-1}), which was identified for material A, is not observed for materials B to D and the opposite effect is observed for material E. The progressive increase of the zirconium content minimises the decrease of the Si-O-Zr band located at 940 cm^{-1}, suggesting the formation of more stable structures. Therefore, one can conclude that the zirconium precursor favours the formation of highly condensed silicate species, resulting in a more condensed network. Finally, these results indicate that the incorporation of the transition metal favours the formation of denser materials, thus limiting the further condensation process observed in material A, and the subsequent contact angle increase. However, to better identify the effect of the zirconium incorporation on the morphology of the silicate network and its subsequent consequences on the wetting capabilities of the coatings, we propose to perform ^{29}Si-NMR analyses of the materials investigated here. Importantly, this would enable us to confirm or disconfirm the competition between the hydroxylation and condensation processes discussed in this section.
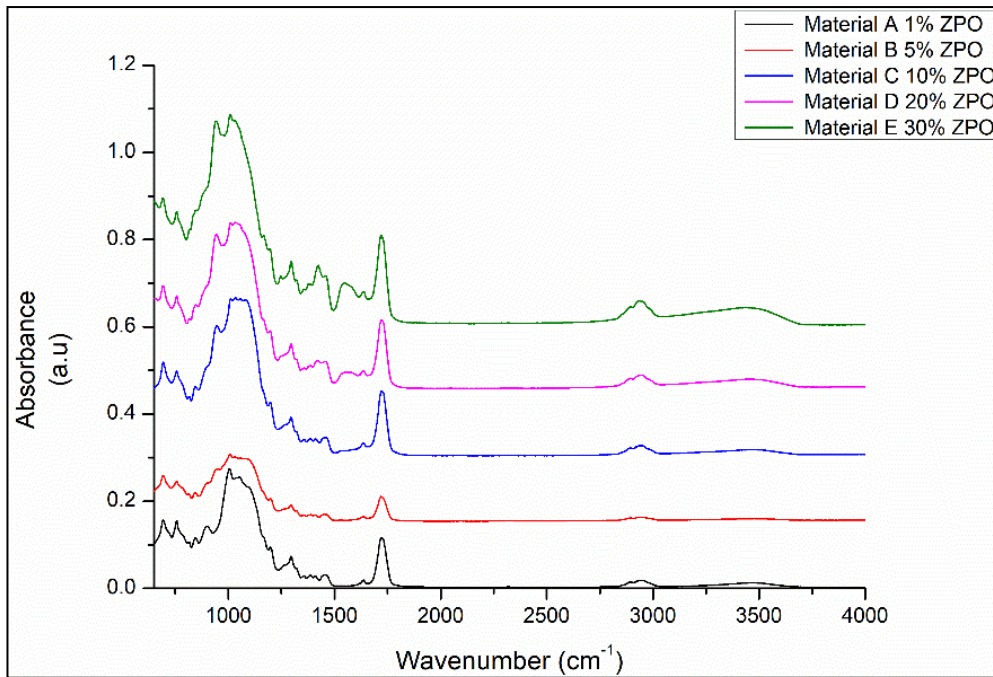
Figure 5. 4: FTIR spectra for all materials in the range of 650-4000 cm^{-1}
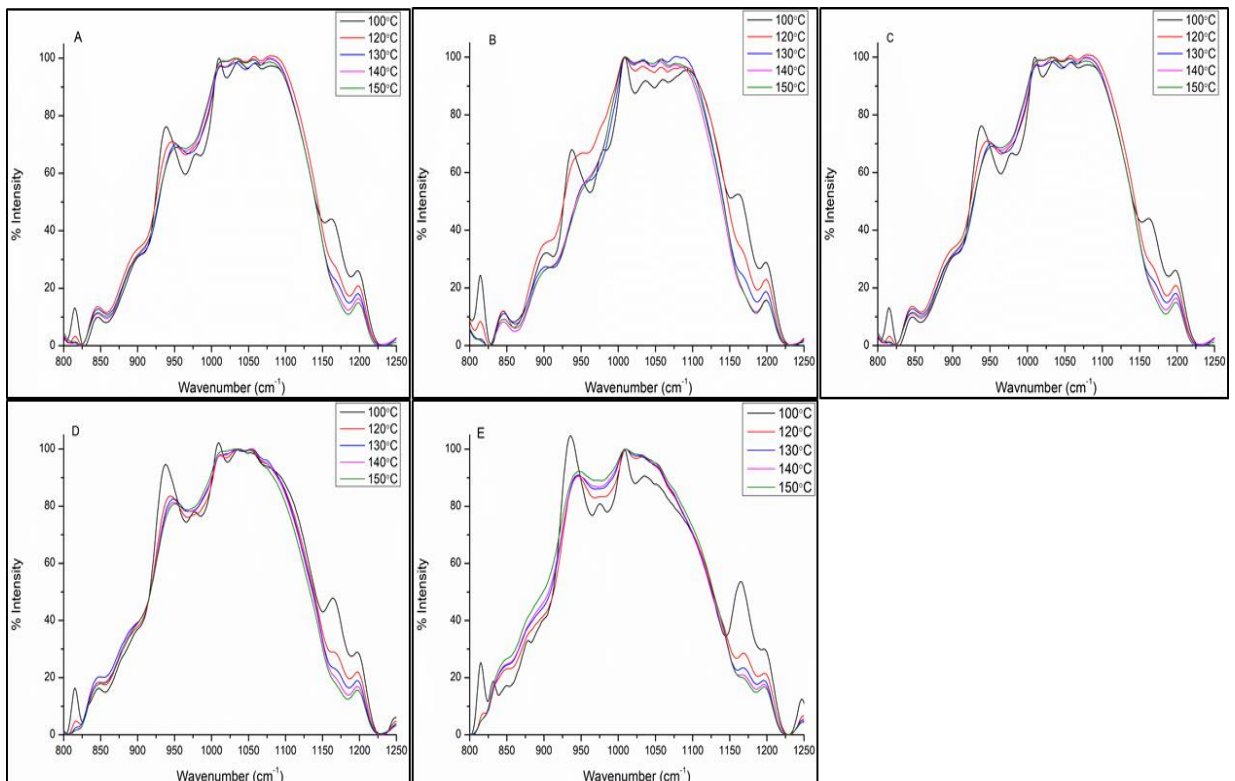
Figure 5. 5: FTIR spectra of all materials for all curing temperatures in the range 800-1250 cm^{-1}

5.3.4 ^{29}Si-NMR Analysis

^{29}Si-NMR spectra were recorded for all materials 24 hours after fabrication and are shown in Fig. 5.7 below. A spectrum of the precursor MAPTMS was also recorded and is represented in Fig. 5.6 below and exhibits a single sharp peak at -42.6ppm. The presence of the different chemical shifts in the T_0, T_1, T_2 and T_3 regions of the spectra correspond to the different degrees of condensation of the silicon atom contained in the MAPTMS. Firstly, it can be noted that no T_0 species are observed for any material, suggesting that all silicon atoms have formed at least one siloxane bond. However, it does not mean that all alkoxide groups have reacted as each silicon atom contains three reactive alkoxide groups. In order to better appreciate the evolution of the different T species for each material, the different chemical shifts have been integrated and their relative proportions plotted in Fig. 5.8. T_1 species are present in all materials at a % ratio of 32.2, 4.8, 2.7, 3.5 and 13.3% respectively. T_2 species are present at a % ratio of 50.0, 50.3, 45.2, 42.4, and 44.2% respectively. The most condensed species T_3 is present in concentrations of 17.1, 44.8, 52.0, 54.0, and 42.4% respectively. The increase of the T_3 species at the expense of both the T_2 and T_1 species suggests that the materials are forming more condensed networks with increasing ZPO concentration up to 20%. For material E with a ZPO concentration of 30% there is a dramatic increase in the concentration of T_1 species with a decrease in the T_3 species. This suggests that the network favours the formation of T_1 silicate species at ZPO concentrations of 30%. This may be due to the steric hindrance of the zirconium complex.
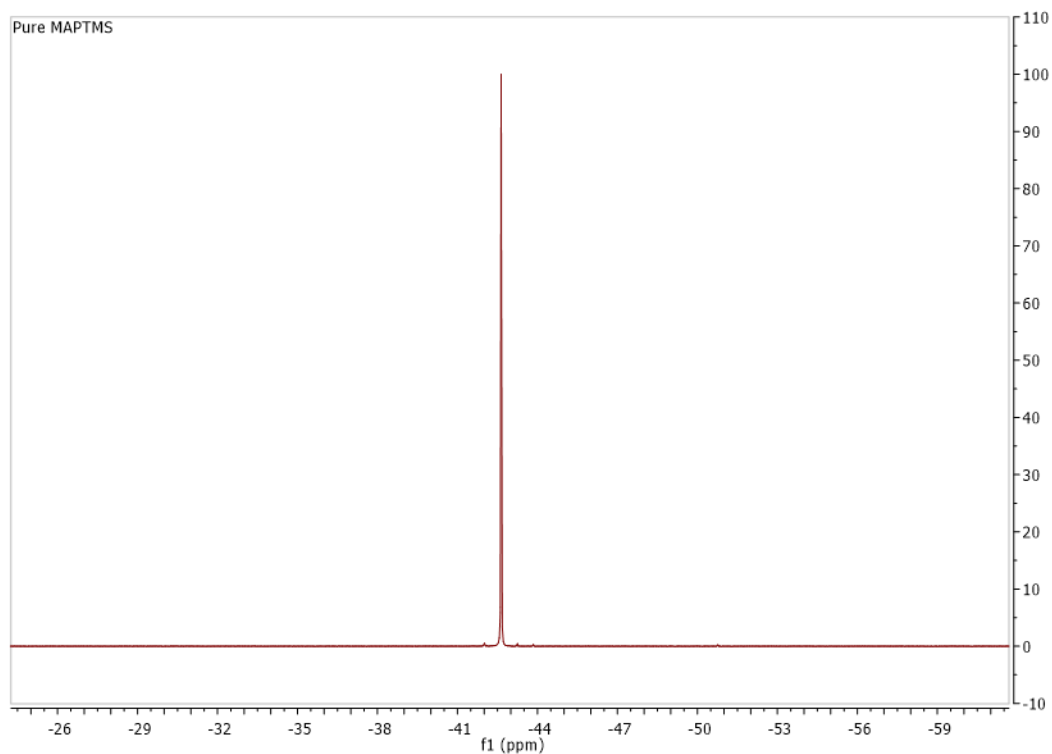
Figure 5. 6: ^{29}Si-NMR spectra of the MAPTMS precursor with a peak at -42.6 ppm
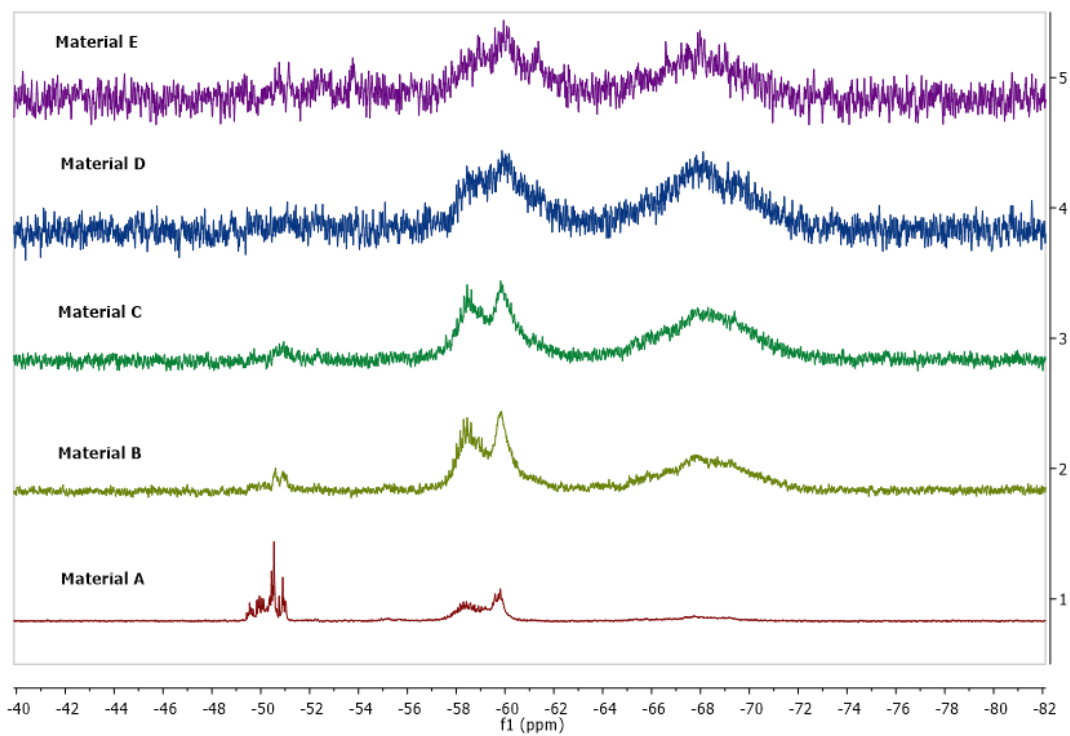
Figure 5. 7: NMR spectra of all materials
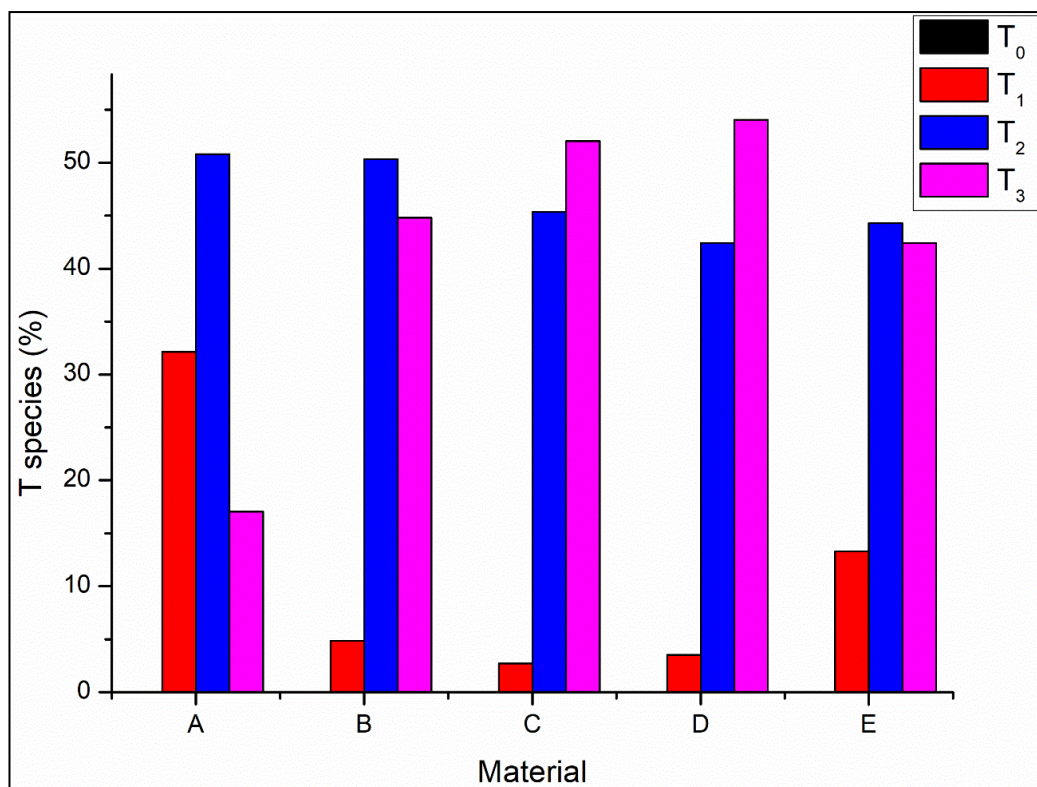
Figure 5. 8: T species concentration for all materials

5.3.5 Thermal Analysis

DSC was performed on all sols (liquid sol-gel materials) to determine their thermal behaviour and to identify the optimum working temperature of the sol-gel material. The thermal behaviour of materials A-E are represented below in Fig. 5.9. There are three different areas of thermal behaviour that can be observed, between 25-70°C, between 100°C and 170°C and above 170°C. These thermal zones correspond to the evaporation of volatile solvents, the condensation of the materials and the glass transition phase of the materials respectively. The large broad endothermic band between 25-70 °C is due to the evaporation of free volatile solvents within the hybrid network formed during the sol-gel synthesis or from the precursor materials. The endothermic band shifts to higher temperatures with increasing zirconium content, this may be due to a higher degree of entrapped solvents in the sol-gel network. Similar behaviour has been reported for Sn

doped ZrO_2 samples which were prepared by sol-gel methods[148]. The exothermic band between 160 and 190°C is due to the glass transition phase (Tg) or the full solidification point of the sol-gel materials. It can be noted that the Tg for materials B to E can be seen at 194, 194, 185 and 199°C, respectively. Material A, exhibits two exothermic bands in the region of 171 and 192°C, which may be due to the occurrence of two different phases within the material due to the low content of ZPO, as previously observed in similar materials[145]. Apart from materials C and D, an additional exothermic band located above 200°C is present for the other materials, translating structural heterogeneity, probably due to the presence of hybrid nanoparticle populations with different structures, thus with different thermal behaviors. The most plausible explanation to the likely heterogeneity can be explained by the capability of the silicate network to host the zirconium complex in a homogeneous manner within its backbone. At low zirconium concentrations (materials A and B), the sol-gel network may be primarily composed of silicate species with some local inclusions of zirconium species. At the highest zirconium content (material E), the silicate network may not be able to host the whole content of zirconium species, thus leading to some rich zirconium nanoparticles populations. According to this explanation, the integration of the zirconium complex in the silicate network is optimum in materials C and D.
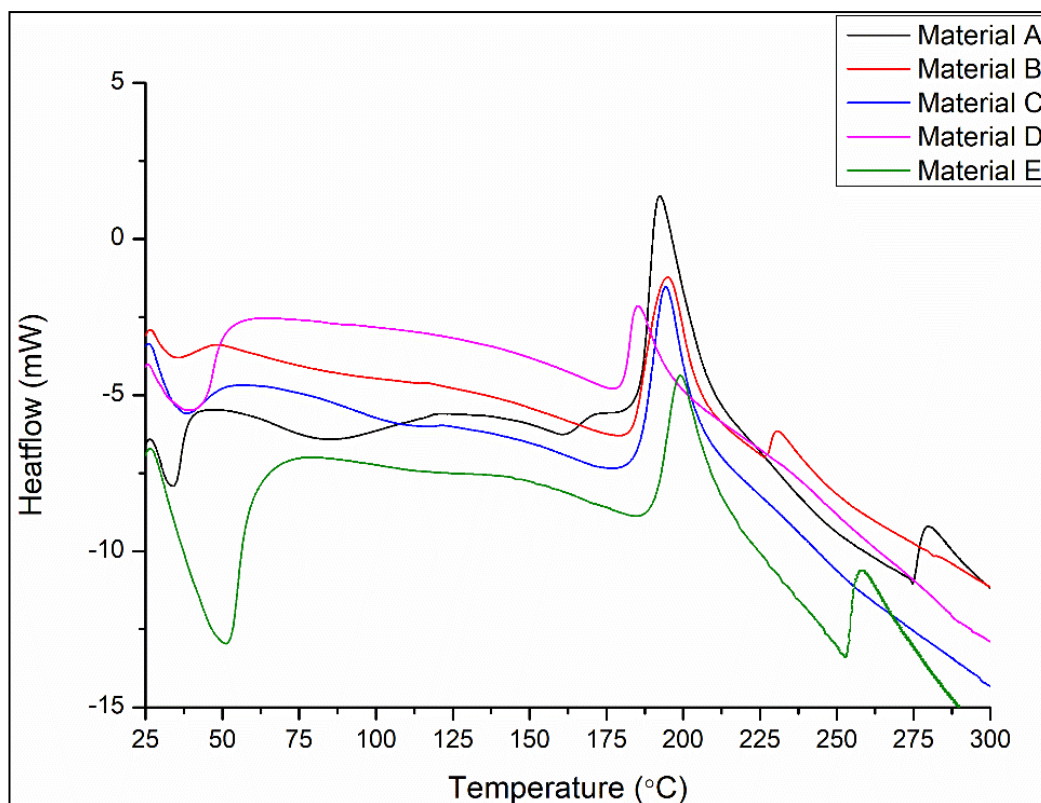
Figure 5. 9: DSC spectra for all materials

5.3.6 SEM/ EDX Analysis

The SEM images of cross-sectioned samples were recorded to identify the coating homogeneity and thicknesses, as well as adhesion on the glass substrate for all materials. All samples show homogenous coatings with thicknesses in the range of $4.8 – 6.0 \ \mu m$ (+/- $0.5 \ \mu m$), as seen in Fig. 5.10. Although the sample preparation involved mechanical cleaving of the substrate in order to enable cross-section analysis on a sharp interface, no delamination of the coatings from the glass substrate was observed, demonstrating a strong adhesion of the sol-gel materials with the glass substrate. As the glass substrate surface contains silanol groups, it is likely that they will undergo inorganic condensation with the residual uncondensed silanol and alkoxysilane groups of the sols to form strong siloxane bonds, thus explaining the strong adhesion of the hybrid sol-gel coating onto the substrate. Apart from the stripes observed on the cross-section, which are due to the

127

propagation of the cleaving defects of the glass substrate, the coating is found to be smooth and uniformly distributed on the substrate, suggesting a highly homogeneous material.

EDX analysis of the materials was also carried out. The main elements that were investigated were C, Si, O and Zr. The overall % of each element was plotted as a function of chemical composition of the materials and is shown in Fig. 5.11. A representative EDX image for material A is shown in Fig. 5.12 below. There is a linear increase in the concentration of Zr at the expense of the Si concentration within the materials as the Zr content increases from 1-30%. With material E exhibiting the highest concentration of Zr a 32.8%. This analysis further supports the theory and corroborates the DLS analysis, that the zirconium is inserted within the organic backbone of the material. There is also a decrease in the concentration of both C and O as the Zr concentration increases from materials A –E.
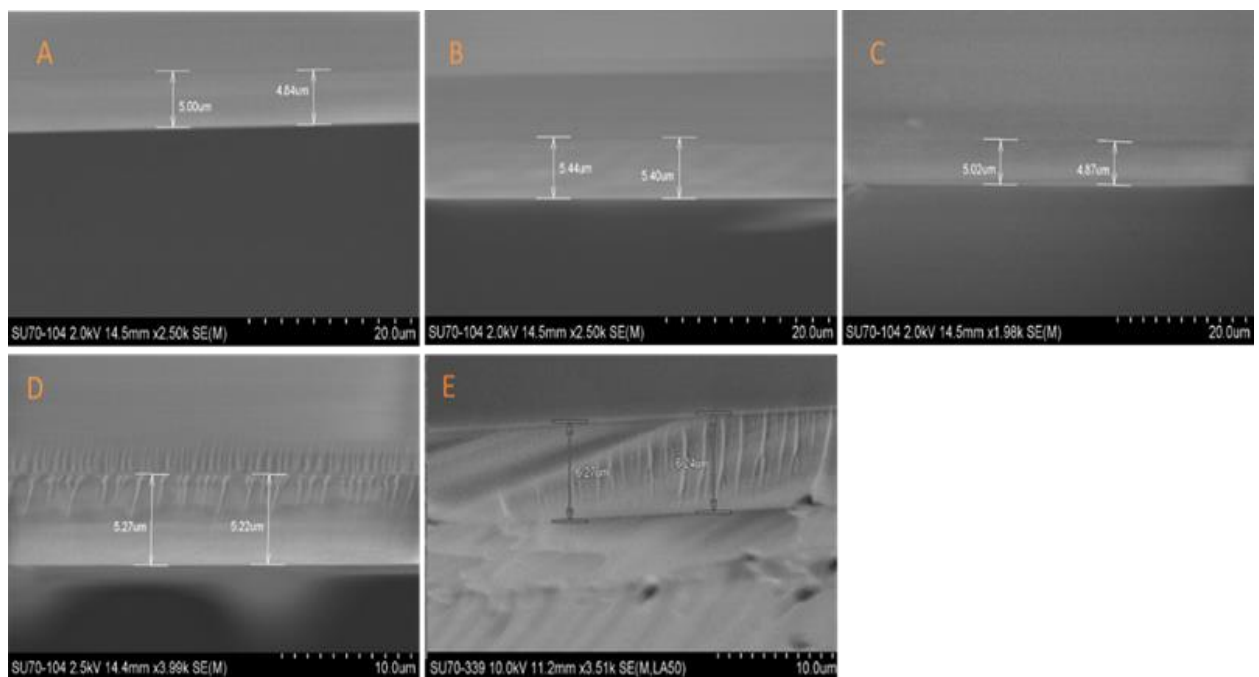
Figure 5. 10: SEM image of all materials A-E
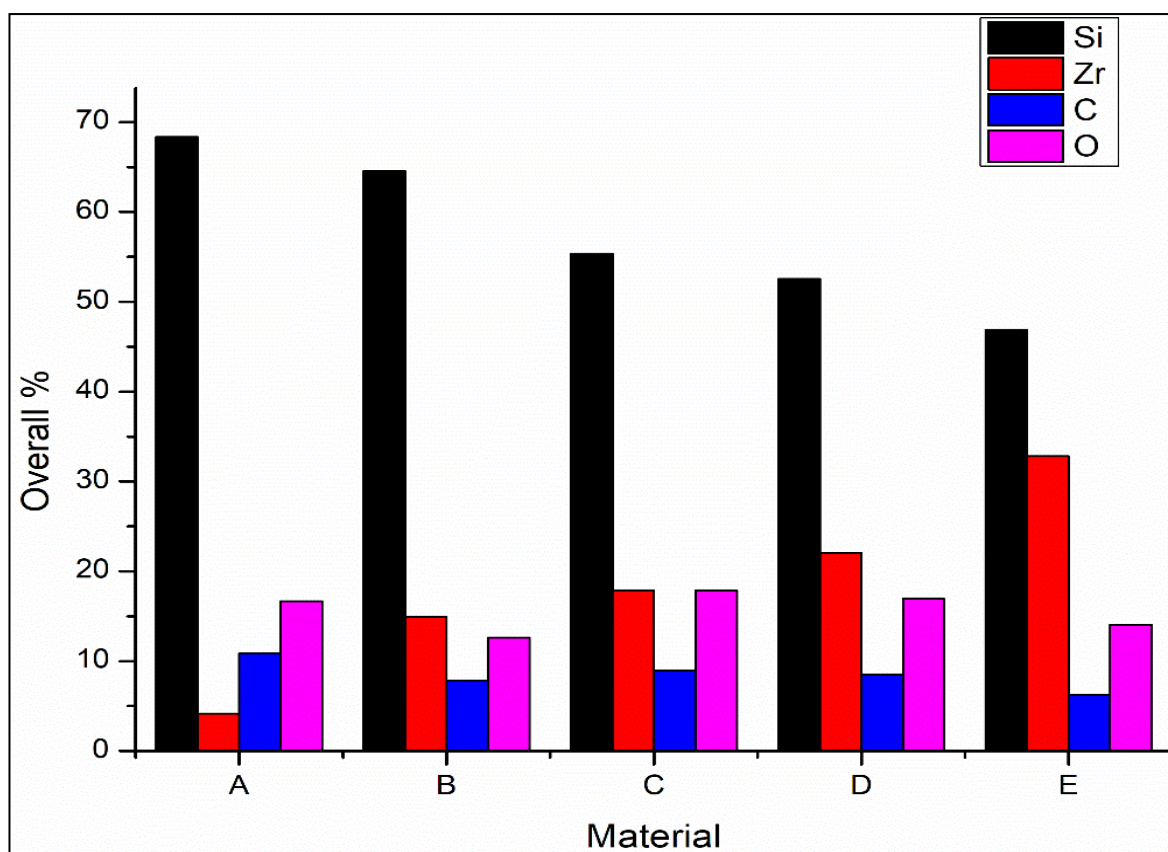
Figure 5. 11: Percentage concentrations of Si, Zr, C and O within materials A-E
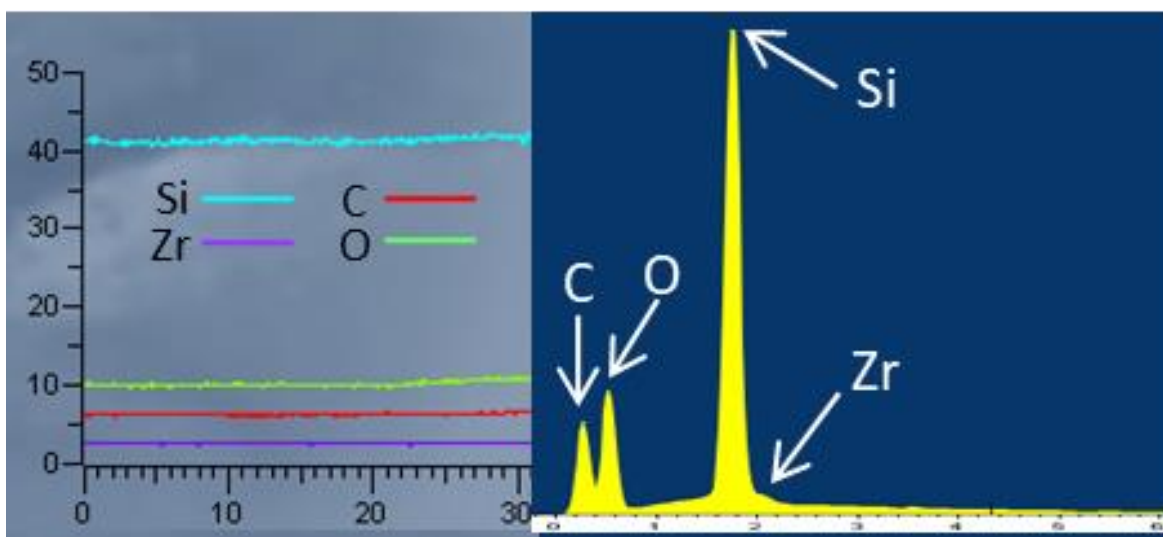
Figure 5. 12: EDX spectra for material A

5.4 Conclusion

This chapter focused on the influence of the transition metal concentration on both the

surface properties and structure of the sol-gel material deposited onto glass substrates.

The developed materials were thoroughly characterised by FTIR, SEM/EDX, DSC and ^{29}Si-NMR, DLS and the wetting properties were identified by CA measurements. DLS analysis showed that the particle size and FWHM of the materials increase with an increase in the zirconium content within the materials. FTIR analysis showed that the curing temperature provokes the condensation of the silicate network at the expenses of the Si-O-Zr and Si-OH groups. However, this phenomenon is decreasing as the content of zirconium increases, suggesting the zirconium precursor minimises the progression of the silicate network probably by the formation of a rigid network in the liquid phase. Indeed, ^{29}Si-NMR characterisations have supported this hypothesis by showing that highly condensed silicate species are formed in the liquid phase when the content of zirconium increases. From the cross-section SEM observation, the prepared coatings are found to be uniformly deposited onto the glass substrate with thicknesses ranging from 4.8-6.2 μm (± 0.5μm). Elemental analysis of the coatings shows that there is an increase in the overall zirconium content of the materials with a decrease in the Si concentration. Wettability analysis showed that all coatings exhibit a progressive decrease of their CA values at up to 130°C, a similar trend previously seen with the reference material. Above 130°C, the sample containing 1% zirconium content exhibits an increase of its CA value, while coatings containing a minimum of 5 % of zirconium maintain a stable CA value. Therefore, when corroborating the structural and wettability analyses it has become evident that the transition metal minimises thermal condensation of the silicate network, thus enabling stabilisation of the wetting properties at higher hydrophilic values.

To our knowledge, the control of the wettability of hybrid coatings by curing process and transition metal incorporation within a silicate network is a fundamentally new result in the physico-chemistry of hybrid sol-gel materials. Importantly the work in this chapter has demonstrated that a range of formulations with zirconium contents

of 5% and higher and with a minimum curing temperature of 130℃ can be used to further optimise the surface properties of the materials. The next chapter will focus on the alteration of the hydrolysis degree in conjunction with a range of zirconium concentrations.

6 Influence of the hydrolysis degree on the structure and surface properties of the reference sol-gel material

6.1 Introduction

As described in the previous sections, the sol-gel process employed in the materials development of this work involves both hydrolysis and condensation reactions of the inorganic alkoxide groups of the precursors. The hydrolysis reactions being the key step in the formation of the reactive hydroxide groups that are responsible for the formation of inorganic networks via the subsequent and often parallel occurrence of condensation reactions. Residual uncondensed hydroxide groups are the main source of hydrophilic species responsible for the high surface energy of hybrid sol-gel coatings. Therefore, investigations on the effect of the hydrolysis degree on the structure and surface properties of the reference materials is studied in this chapter. In addition to the effect this parameter may have on the surface properties, it will be essential to investigate its impact on the structure of the materials prepared with various contents of organosilane against the transition metal complex. This study may enable us to better understand the physicochemical phenomena governing the formation of hybrid sol-gel materials composed of both organosilanes and transition metal complexes. In order to do this, four different theoretical hydrolysis degrees (25, 50, 75 and 100%) of five materials containing each one a zirconium complex concentration (1, 5, 10, 20 and 30%) will be prepared and investigated. By hydrolysis degree it is meant the content of water against the total reactive alkoxide groups.

The prepared materials will be coated on an aluminium substrate, cured at various temperatures ranging from 100 to 180°C to form coatings and will undergo DLS, FTIR, ^{29}SiNMR, DSC and wettability analysis. In order to identify solely the effect of the

hydrolysis degree on the hybrid sol-gel coatings, each series of samples will focus on varying only the overall hydrolysis degree, keeping the concentration of the zirconium complex constant.

6.2 Materials Preparation

The materials were prepared as per the synthetic route previously described in section 4.2, the only difference being the hydrolysis ratio, which was varied from 25 – 100% and the zirconium complex which was varied from 1 – 30 mol %. All other parameters were kept constant to avoid multiple simultaneous variations and clearly identify only the hydrolysis parameter on the surface properties and structures of the hybrid sol-gel materials. In order to synthesis the hybrid sol-gel coatings used throughout this work- the liquid sol-gel materials were cured at varying temperature to form a solid sol-gel coating. A flow chart for the synthesis of the materials is shown in Fig. 6.1 and the material formulations are presented in Table 6.1 The volumes used to make ~48 ml of each material in series1 is shown below in table 6.2. The hydrolysis degree is a theoretical hydrolysis degree which is calculated against the total reactive methoxy groups of the sol-gel. As we are interested in studying hybrid sol-gel materials for use in microfabrication applications, there would be no need to include the study of a purely silicate sol for comparison purposes.
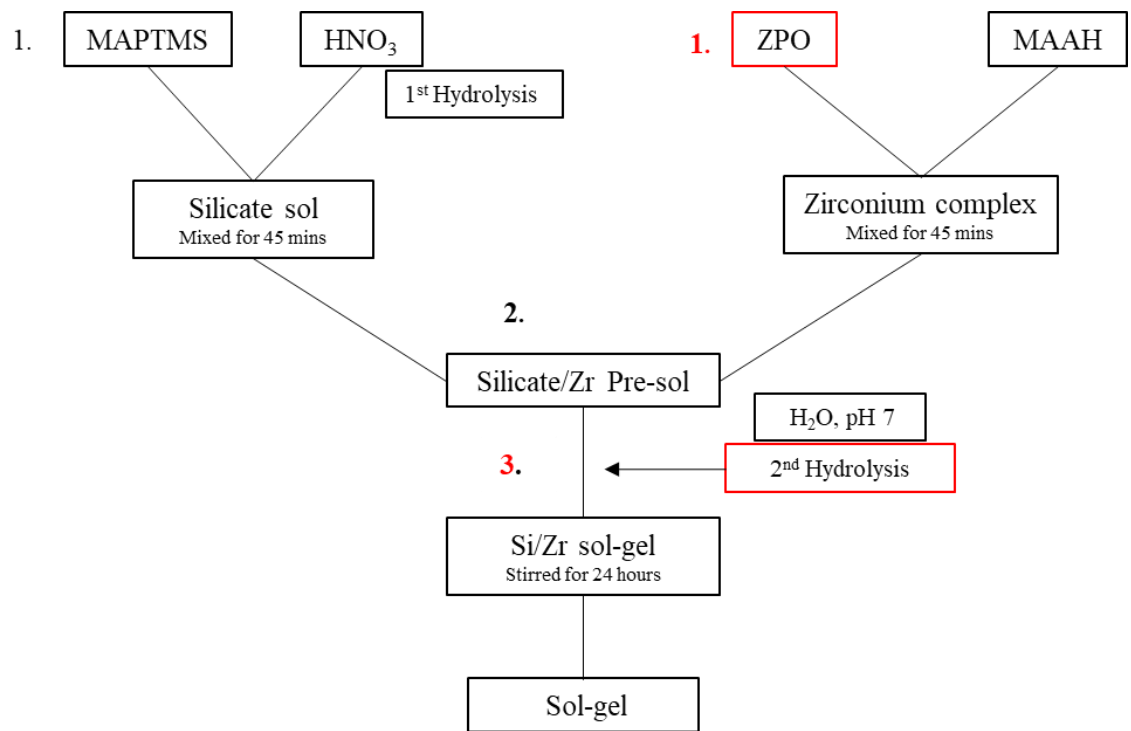
Figure 6. 1: Flow chart for the synthesis of the sol-gel material

Sample	Series	Hydrolysis Degree (against total reactive alkoxide groups)	MAPTMS: ZPO: MAAH (mol %)
A1	1	25	99:1:1
B1	1	50	99:1:1
C1	1	75	99:1:1
D1	1	100	99:1:1
A2	2	25	95:5:5
B2	2	50	95:5:5
C2	2	75	95:5:5
D2	2	100	95:5:5
A3	2	25	90:10:10
B3	3	50	90:10:10
C3	3	75	90:10:10
D3	3	100	90:10:10
A4	4	25	80:20:20
B4	4	50	80:20:20
C4	4	75	80:20:20
D4	4	100	80:20:20
A5	5	25	70:30:30
B5	5	50	70:30:30
C5	5	75	70:30:30
D5	5	100	70:30:30

Table 6. 1: Material Formulations for the hydrolysis degree study

Reagent	Sample A 1 Vol (ml)	Sample B1 Vol (ml)	Sample C1 Vol (ml)	Sample D1 Vol (ml)
MAPTMS	28.70	28.70	28.70	28.70
ZPO	0.57	0.57	0.57	0.57
MAAH	0.10	0.10	0.10	0.10
HNO_3	1.6	1.6	1.6	1.6
H_2O	0.046	1.69	3.34	4.98

Table 6. 2: Volumes used for synthesis of the materials in series 1

6.3: Results and Discussion

6.3.1 Particle Size Analysis

As with the previous studies proposed in Chapters 4 and 5, the particle sizes and distribution of the newly developed materials were recorded 24 hours after fabrication and are shown in Fig. 6.2. It can be seen that all materials show the presence of a single band located in the range 0.5 – 20 nm. However, it can be observed that both the maximum peak and the distribution of the bands can significantly be influenced by the hydrolysis degree (HD). To determine the overall broadening of the peaks and to get a better understanding of the dispersion of the sol-gel nanoparticles, the FWHM is represented in Fig. 6.3.

For series 1 as the HD increases from 25 – 100 % there is a progressive increase in the FWHM. For series 2, the opposite behaviour can be seen, as the HD increases there is a decrease in the FWHM from 25-75 % HD and a slight increase for 100 % HD. Series 3, a similar trend can be observed albeit more pronounced. Series 4, there is little variation in the FWHM regardless of the HD suggesting that this series of materials is the most

stable in terms of size distribution. Series 5, there is a significant increase of 33% for the FWHM from 25-50% HD. It can then be seen that there is a progressive decrease in the FWHM from 50-100% HD for the materials prepared with 30% zirconium content. These results suggest that the zirconium content as well as the HD play a role in the reactivity of the materials and in the particle growth. The above trends suggest that at contents of ZPO below 5%, the HD has a greater effect on the reactivity of the materials and the growth of the particles. Whereas the opposite effect is seen with materials containing intermediate concentrations of ZPO between 5-10 %. The particle growth decreases with increasing HD up to 75 % suggesting that the incorporation of transition metal within the silica network limits the growth the particles. The most stable formulation seems to be synthesised with concentration of 20% ZPO. There is little variation in the broadening of the distribution band and no change in the max peak of the particles. For series 5, it can be noted that at a HD of 25-50% there is an increase in the particle growth and then a subsequent decrease from 50-100% HD. Again this suggests that at lower HDs there is greater reactivity of the materials and particle growth.

DLS analysis showed that regardless of the HD and ZPO content, the sol-gel materials are composed of nanoparticle populations not greater than 25 nm with the vast majority in the range 1 – 10 nm. Although it showed variations relying on the HDs and ZPO content, DLS is not powerful enough to provide information on the molecular structure of the materials. For this purpose, the following sections will deal with;

1. ^{29}Si-NMR analysis to provide a picture of the silicon environment and give a better indication of the reactivity and molecular structure of the silicon network

2. FTIR analysis to provide indications on the condensation degree of the silicate and zirconium species

By corroborating the ^{29}Si-NMR and FTIR results along with the contact angle characterisations it may be possible to better estimate the impact of the chemical alterations performed in this chapter and establish relationships existing between:

1. The HD and the structure of the materials

2. The HD and the wetting properties

3. The HD and ZPO content on the structure and wetting properties.

With these results, the effect of the HD may be further clarified.
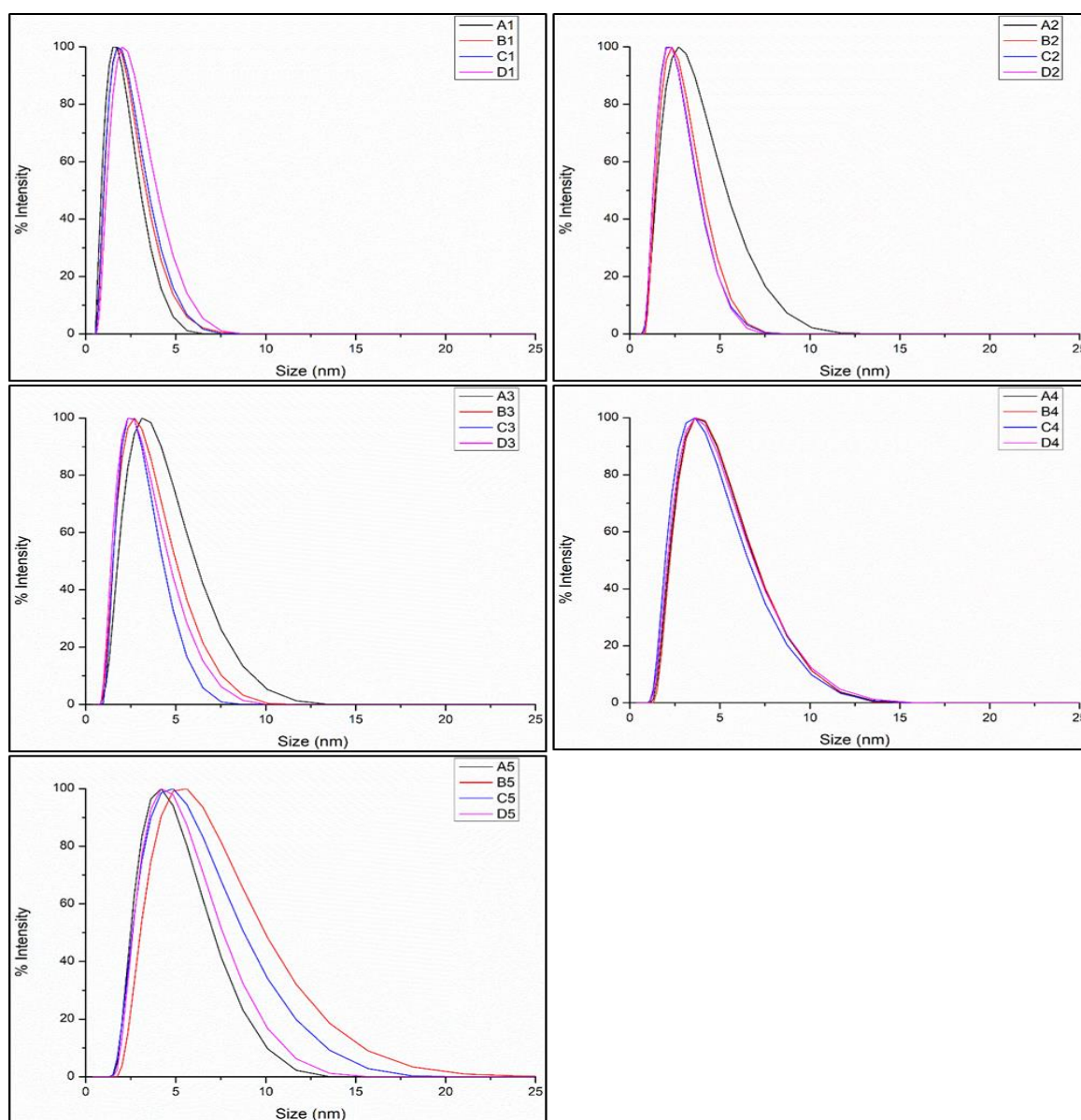
Figure 6. 2: DLS spectra for all materials 24 hours after fabrication
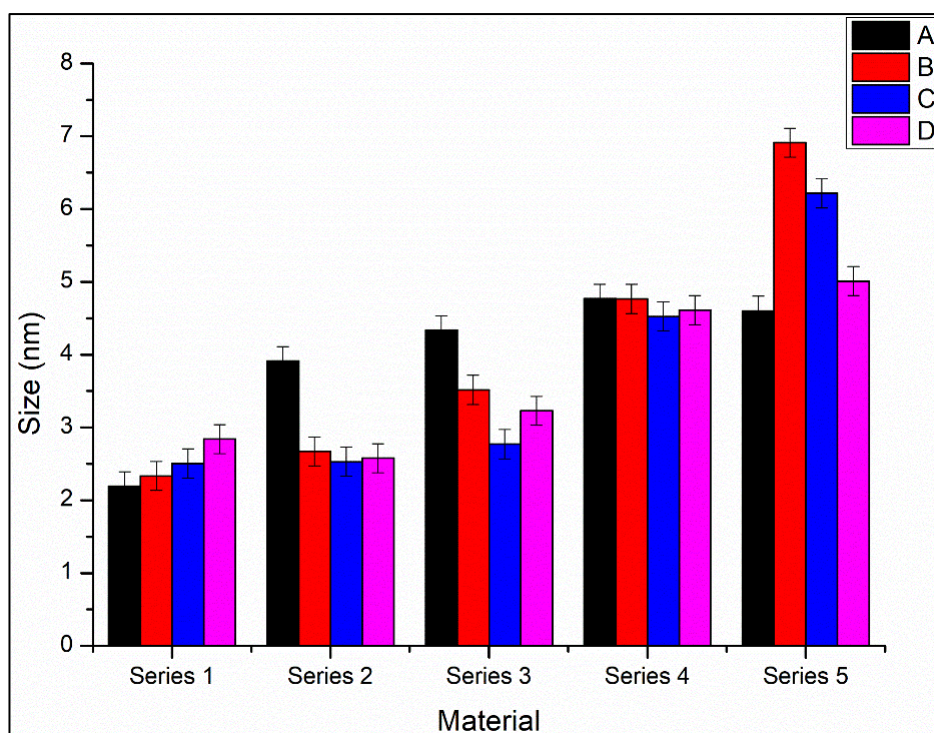
Figure 6. 3: FWHM for all materials, n=3 (number of repeat analyses)

6.3.2 Contact Angle Measurements

Static water CA measurements were taken for all materials in series 1 – 5 and the average corresponding CA values are represented below in Fig. 6.1 – 6.5. The HDs that were investigated were 25, 50, 75 and 100% and the ZPO concentration used were 1, 5, 10, 20 and 30%. The materials were deposited on aluminium substrates via dip coating and subsequently cured at temperatures of 100, 120, 140, 160 and 180℃ for one hour. For a better comparison of the effect of the hydrolysis degree and curing temperature, each series of materials will be analysed separately.

Series 1:

Material D is not represented due to de-wetting of the coating. It can be observed that depending on the HD two behaviours are taking place depending on the curing temperature. The sample prepared with the lowest hydrolysis degree (25%), shows an increase of the CA value from 68 to 73° from 100 to 120℃. The CA is seen to decrease

to 70° at a curing of 140℃ with a further increase at 160 and 180℃ with CA values of 71° and 77° , respectively. On the contrary, the samples prepared at higher HD of 50 and 75% are progressively observed to exhibit decreasing CA values up to 160°C, with values of 57° and 53°, for materials B1 and C1, respectively. However, at a curing temperature of 180°C, both samples show an increase of the CA values recorded at 61 and 56°. From these results, it is evident that for series 1 the increase of HD favours the formation of more hydrophilic surfaces. However, the increase of the CA value for the sample prepared at 25% HD proves that in addition to the hydroxylation process identified previously an additional structural effect is taking place, which also contributes to the surface properties of the materials. Although at this stage it would be difficult to clearly identify this effect, it is likely associated to the ZPO content, which either favours the hydroxylation or minimises the condensation of the residual silanol species, responsible for the hydrophilic character of the materials. Both phenomena are also possible but would need to be further investigated by structural characterisations such as FTIR and ^{29}Si-NMR which will be discussed in the following sections.
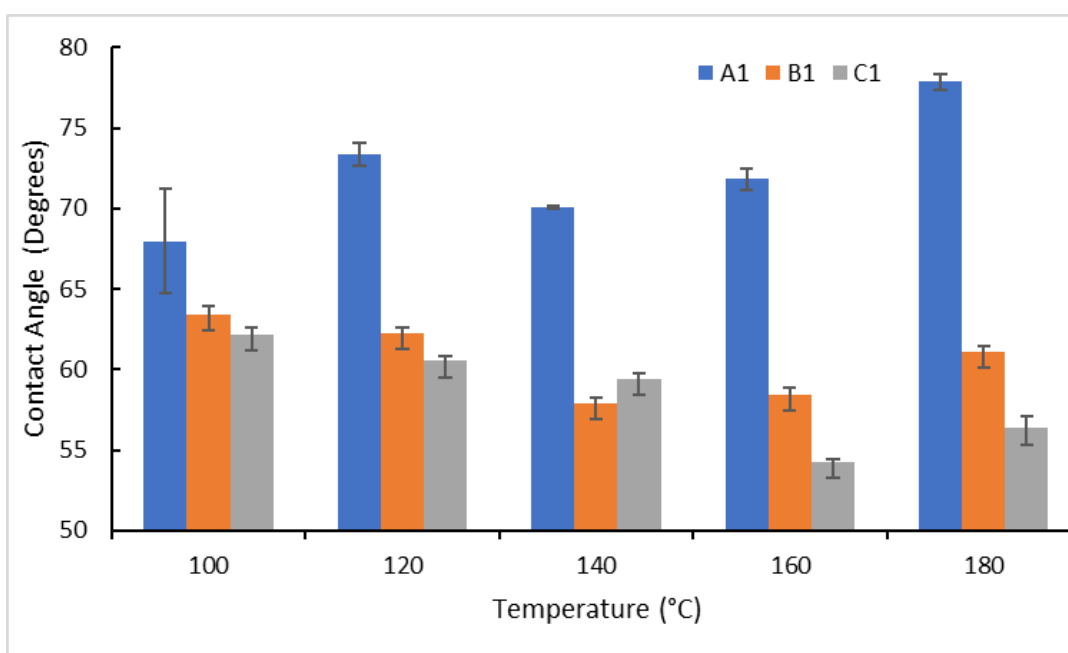
Figure 6. 4: CA values for materials A1-C1 for Series 1, n=3

140

For samples prepared with the lowest hydrolysis degree of 25%, material A2, a progressive decrease can be seen in the CA values up to 120℃ from 66-62° with the stabilisation of the values up to 140℃. At 160℃ , the CA value increase to 67°, with a subsequent decrease for 180℃ to give a final CA value of 65°. For samples prepared with a HD of 50%, a progressive decrease of the CA values can be seen from 100-140℃, with a stabilisation of the CA value up to 160℃ and then a further decrease at 180℃ to give a CA value of 59°. For the samples prepared with a hydrolysis degree of 75%, material C3, a progressive decrease in the CA values from 62-57° can be seen for curing temperatures between 100-160℃. At 180℃, a significant increase in the CA value for material C3 is evident with a final value of 63°. Samples prepared with the highest hydrolysis of 100%, material D2, exhibit an increase in their CA values from 57-61°, between 100-120°C and then a progressive decrease from 140-180°C with a final CA value of 56°. It is expected that the thermal curing of the sol-gel materials will increase the condensation of the silicate network (Si-O-Si) and therefore may decrease the silanol groups (Si-OH) within the network, although it may not decrease the concentration of surface Si-OH groups as evident by the these results.

It is clear from these results that an increase in curing temperature and hydrolysis degree provokes an increase in the hydrophilicity of the surface of the coatings. This increase in the surface hydroxyl groups and expected condensation of the silicate network may be reflected in the FTIR results which will be discussed in the following sections.
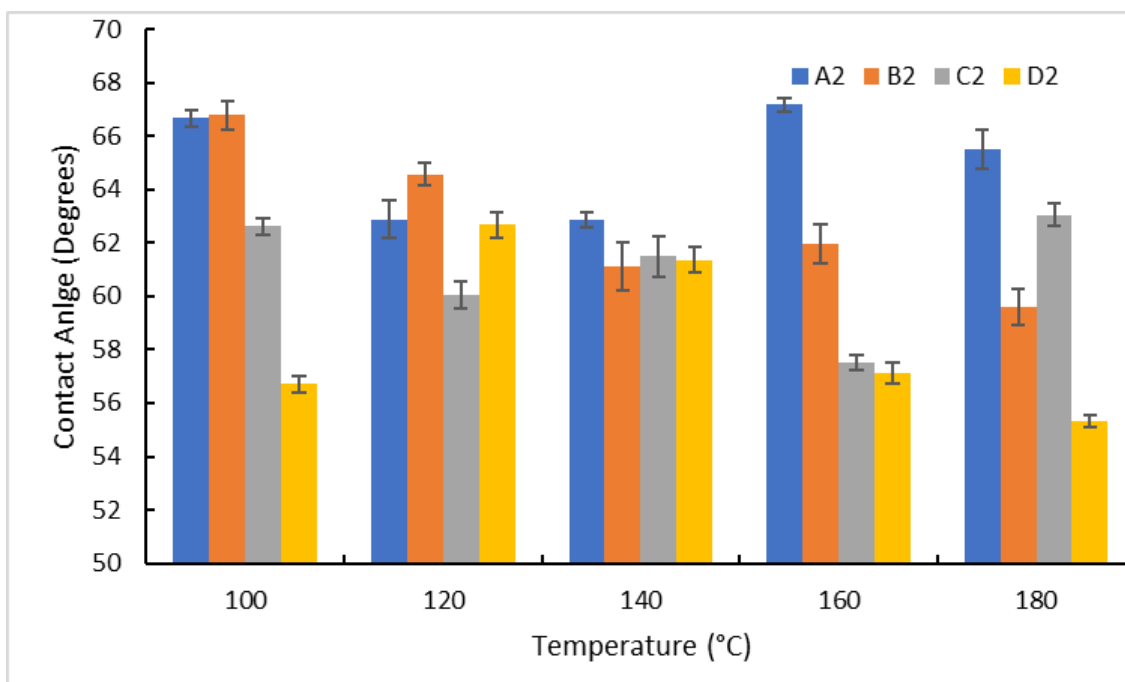
Figure 6. 5: CA values for all materials A2-D2 in Series 2, n=3

Series 3:

It can be observed that at 100°C, the CA values are situated between 66-64° with material A 3 exhibiting the highest value at 66°. All materials exhibit a decrease of their CA values up to 140°C, with the lowest value being 55° for material B3. There is a further decrease of the CA value for material B3 from 160-180°C to give a final CA of 54°. For material D3 the CA value stabilises at 140°C. There is a significant increase in the CA values from 59-65° for material A3 and from 55-63° for material C3 between 160-180°C. It is evident that for samples prepared with the highest HD of 100%, the increase in the hydroxylation of the coatings is favoured from curing temperatures of 120°C and above, which is evident by the continued decrease in CA values, from 62° at 120℃ to 55° for the sample cured at 180℃.
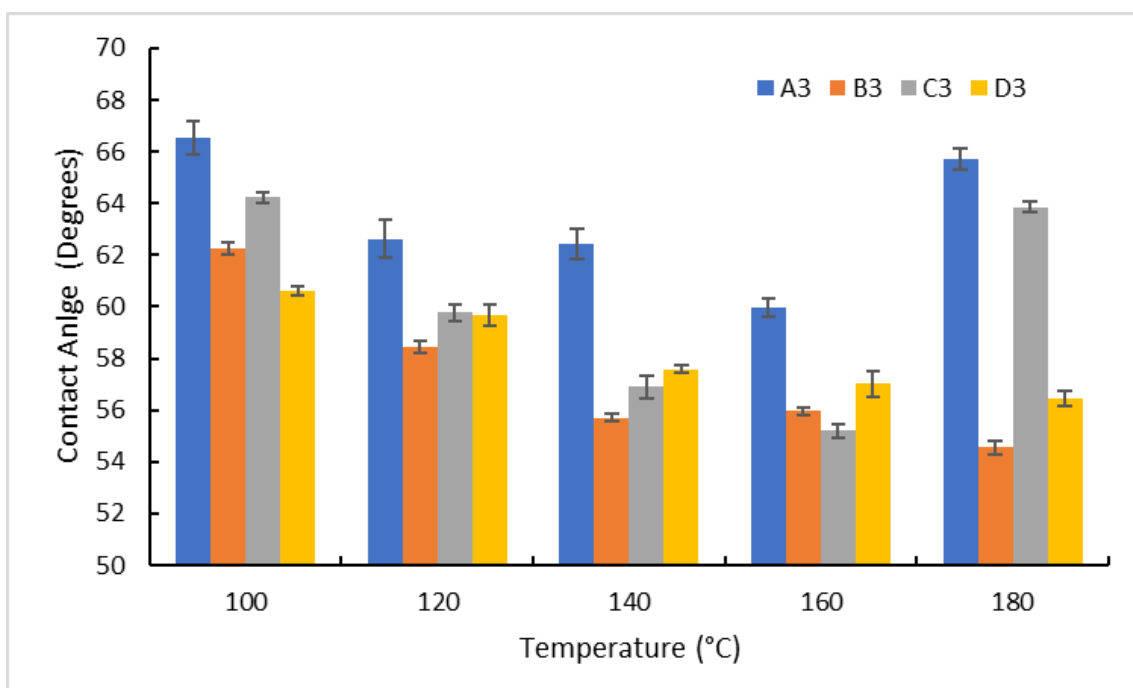
Figure 6. 6: CA values for materials B3-D3 for Series 3, n=3

Series 4:

At a curing temperature of 100°C all samples exhibit a CA value comprised between 62 and 64°. All materials show a progressive decrease of the CA up to 140°C. At 160°C, the CA is seen to further decrease for the material prepared with the highest hydrolysis degree of 100% with a value of 55°, while it is observed to increase for the other series to reach a value of 57°. At 180°C, unlike materials A4 and C4, which are found to show a stable CA, material D4 shows a significant increase of its CA to attain 60°, demonstrating that this material is more sensitive to higher curing temperatures. The CA value for material B3 is seen to decrease to 54°. A possible explanation to the different trends observed here may be due to the formation of a more favourable structure. As the CA value was found to be the lowest at 140°C, the significant increase of the CA value for material D4 at 180°C is probably due to the presence of a higher content of surface hydroxyl groups that may require higher energies to polycondense and form hydrophobic species. Indeed, for

143

materials A4 to C4 a lower content of hydroxyl groups probably located at further distances may not have as high a polycondensation potential, thus explaining the stability of their CA values between 160 and 180°C. This possible phenomenon is sketched in Fig. 6.9. Nevertheless, if this hypothesis is valid it may be reflected in the FTIR and ^{29}Si-NMR results, which will be undertaken in the following sections.
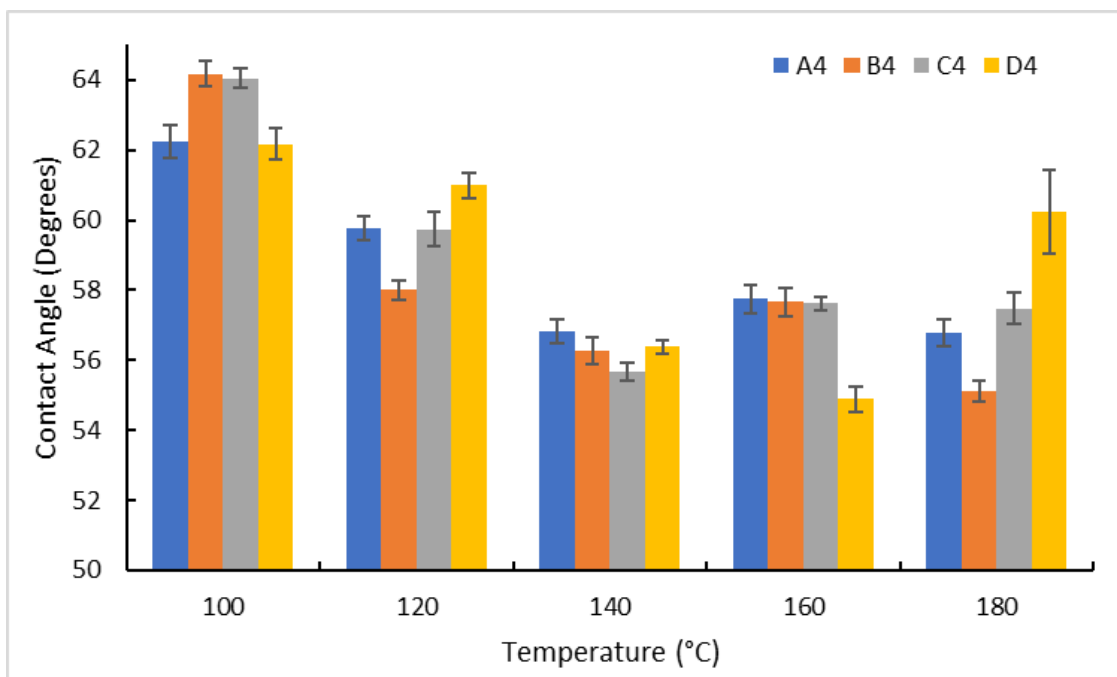
Figure 6. 7: CA values for materials A4-D4 in Series 4, n=3

Series 5:

At 100 °C, the CA values are between 70 and 63° with the most hydrophilic material being D5. There is a progressive decrease in the CA values for all materials up to 120°C. The CA values can be seen to further decrease for materials A5 and B5 but remains stable for material D5 from 140 to 160°C respectively. It can be observed that from 160-180°C for materials A5 and D5 there is a significant increase in their CA values from 56-67° and from 58-64° respectively. The CA values for materials B5 and C5 are seen to stabilise from 160°C. A possible explanation for the behaviour of material A5 and D5 may be due to the structure of the materials, similar to the phenomenon proposed for

materials in series 4. For material A the high ZPO % and low hydrolysis rate may be responsible for the increase in hydrophobicity of the surface of the coatings. The increase in the CA value for material D5 may be due to the presence of a higher concentration of surface hydroxyl groups similar to material D4. Again, the FTIR and ^{29}Si-NMR may give more insight into the possible phenomena occurring for these particular materials.
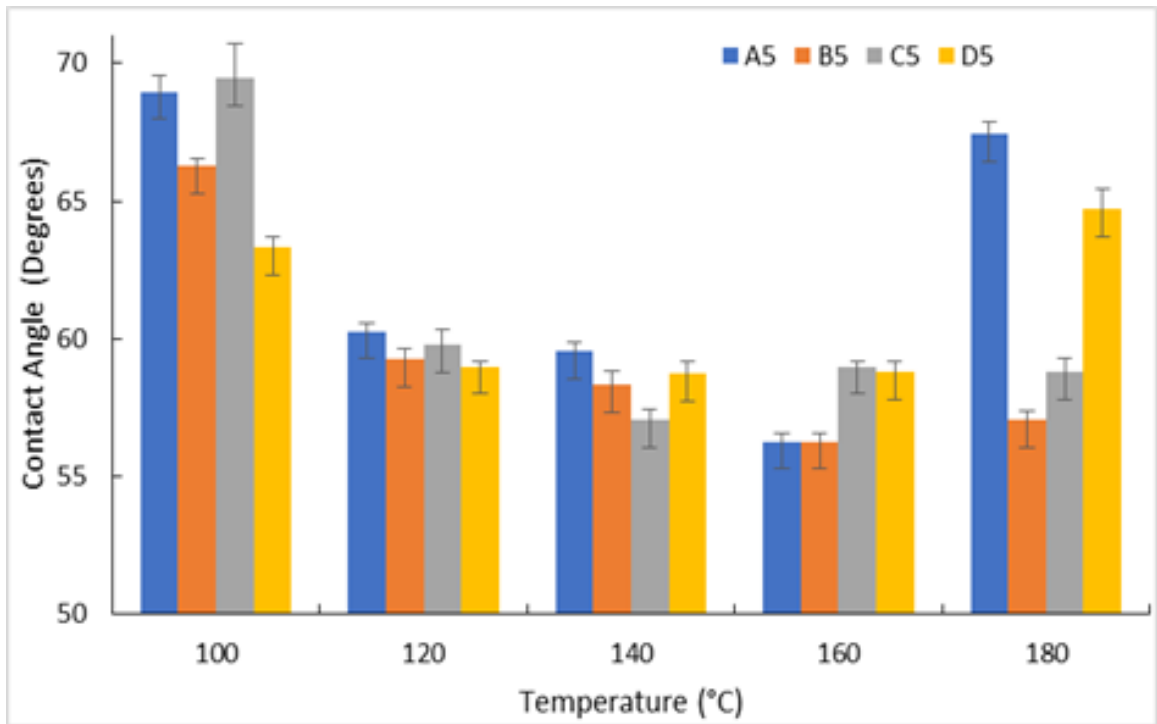
Figure 6. 8: CA values for materials A5-D5 in Series 5, n=3
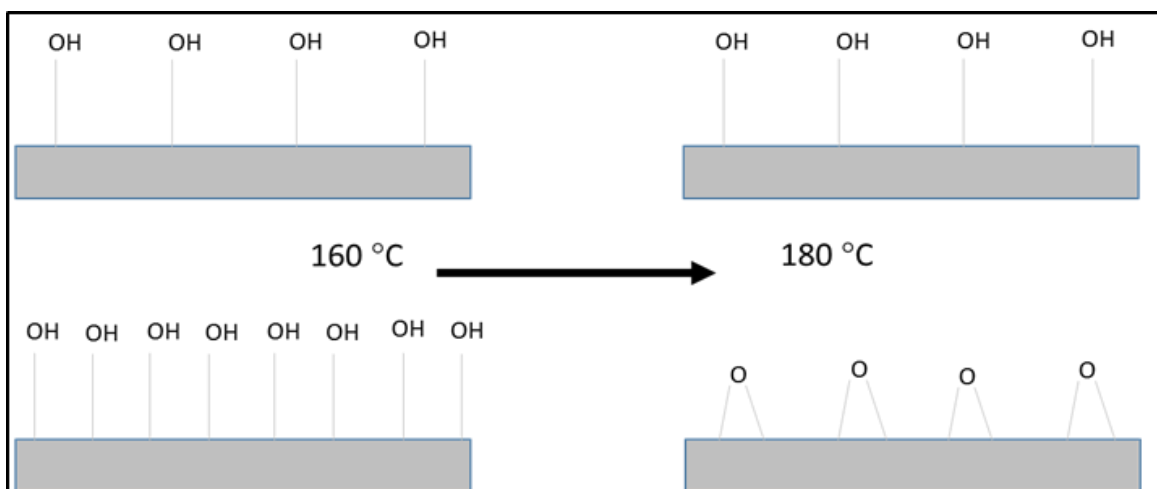
Figure 6. 9: Surface hydroxylation hypothesis for CA behaviour

In summary, an increase in HD provokes a decrease in the CA values and favours the formation of hydrophilic surface coatings with increasing curing temperature. With the exception of material A1 where an increase in the CA measurements can be seen. It is also worth noting that for materials C2, A3, D3, D4, A5 and D5 a significant increase in the CA measurements and hydrophobicity of the coatings can be seen from 160 – 180℃. A possible explanation for this behaviour has been presented in Fig. 6.9. As the CA measurements are an indirect method to characterise the structure of the materials, FTIR and ^{29}Si-NMR may give a better insight into effect of the ZPO on the network and the effect of the HD and will aid in confirming or disconfirming the hypothesis proposed here for the CA behaviour of the coatings.

6.3.3 FTIR Analysis

The FTIR spectra for all materials in series 1 – 5 are represented in Fig. 6.10 – 6.14 below. To identify the effect of the hydrolysis degree on the reactivity and condensation of the materials it is important to focus on the inorganic network namely on the siloxane and the silicon zirconium oxide moeities of the materials. All absorption bands have been attributed to previous references[137–141] and have also been previously described in sections 4.3 and 5.3, respectively. Therefore FTIR analyses will be concentrated in the 800 – 1250 cm^{-1} spectral range. More specifically, the vibrational groups of interests are as follows:

Vibrational group	Vibration name	Wavenumber (cm^{-1})
Si-OH	Silanol	850
Si-O-Zr	Silicon/Zirconium oxide	950
Si-O-Si	Siloxane	1000 – 1100
Si-O-CH_3	Methoxysilane	1170

Table 6. 3: Vibrational groups of interest within 800-1250cm^{-1} region

Series 1

<u>Silanol vibration</u> – Except for the 100ºC cured samples, all other curing temperatures clearly show a similar trend in the evolution of the silanol vibration located at 850 cm^{-1}. For a given curing temprature, the intensity of this band is progressively increasing as the HD increases, demonstrating the occurrence of the hydrolyis reaction. Interestingly this band remains clearly defined for the highest curing temperature, suggesting the presence of hydrophilic Si-OH species.

<u>Siloxane vibrations</u> – The siloxane vibrational bands located in the range 1000 – 1150 cm^{-1}, which are associated to the asymmetric stretching of the Si-O-Si bonds are present in all materials of series 1, indicating the effective formation of the silicate backbone of the sol-gel materials. However, two observations can be made. First, for curing temperatures 100 – 160ºC, it can be seen that the increase of the HD provokes an increase of the high-energy siloxane bonds located from 1050 to 1150 cm^{-1}, while maintaining a high absorption in the low-energy siloxane bonds (1000 – 1050 cm^{-1}). Second, for the highest curing temperature, unlike the other samples, the sample with the lowest HD forms only high-energy siloxane bonds with the disappearance of low-energy siloxane bonds.

Methoxy-silane vibrations – The intensity of the methoxsilane groups genereally are seen to decrease with the increase of the HD and curing tempeture. This suggests that hydrolysis reactions are taking place with the increase of HD and that for a given HD the increase of the curing temperature converts these groups either in Si-OH or Si-O-Si groups. According to the above analysis, as the Si-OH groups is not increasing with the curing temperature it is likely that these groups are converted into siloxane species.

Silicon/Zirconium oxide – The Si-O-Zr bond is generally seen to decrease with the increase of the curing temperature and fully disappears from 140ºC. This means that at low zirconium concentrations, it is likely that this bond would be converted into other inorganic species, such as Si-O-Si (as suggested by the above analysis), Zr-OH or Zr-O-Zr groups. Because of the low ZPO content, it is likely that the zirconium would preferentially form Zr-OH groups.
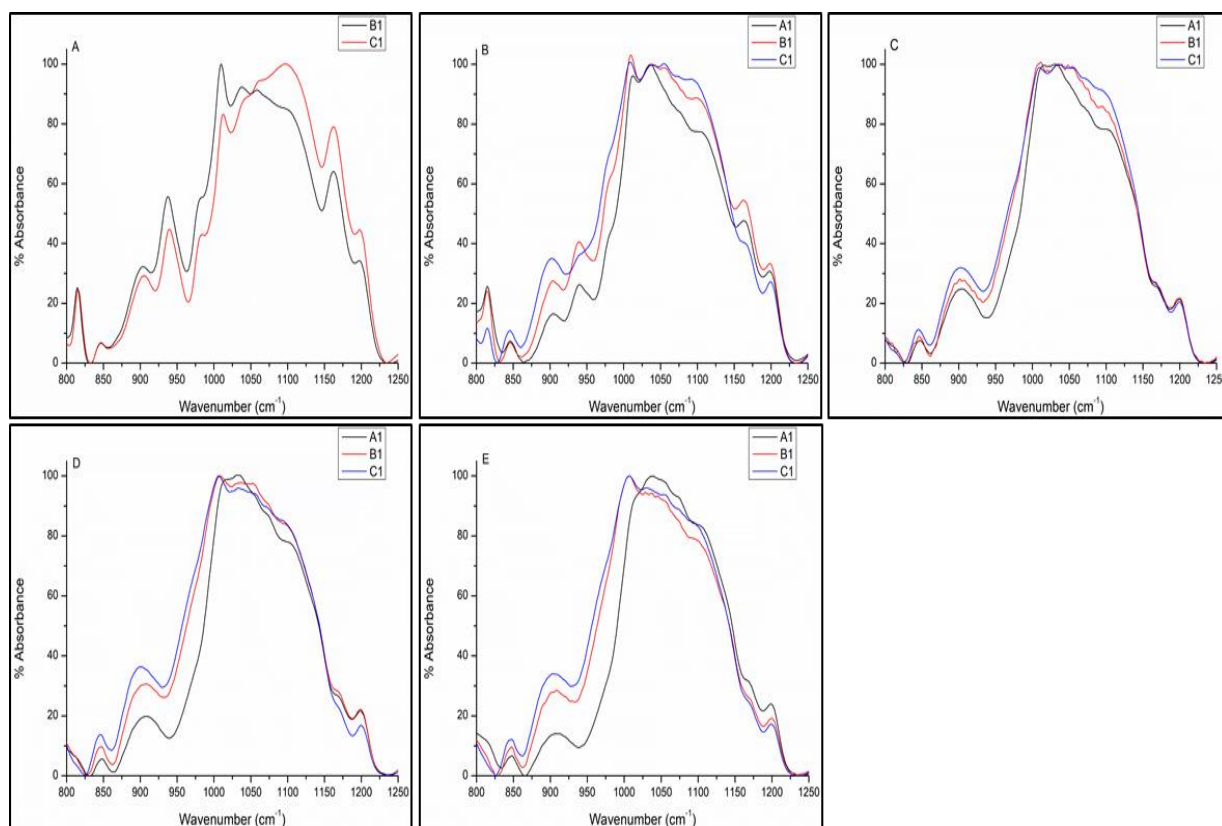
Figure 6. 10: FTIR Spectra for Series 1; A) 100°C, B) 120°C,C) 140°C, D) 160°C, E) 180°C

Series 2

Silanol vibrations - At a curing temperature of 100ºC, the silanol vibration is decreasing with the increase of HD. For the curing temperatures 120 – 180ºC, the opposite effect is observed. This suggests that the curing temperature favours the formation of silanol groups regardless of the HD.

Siloxane vibrations – Simirlary to Series 1, the increase of HD provokes the formation of high-enegry siloxane groups with no significant alteration of the low-energy silicate species.

Methoxy-silane vibrations – They are inconsistent for 100 and 120℃, suggesting the occurrence of competitive chemical reactions. In comparison with series 1, the increase of the zicornium content may be responsible for hydrolysis competition between the two sol-gel reactive centres (Si and Zr). For temperatures greater than 120℃, it can be seen that the intensity of the methoxy-silane vibration is decreasing regardless of the HD. Importantly, it has completely disappeared for the 180℃ curing temperature. This clearly shows that the curing temperature favours the reactivity of the residual alkoxide groups, as previously identified for series 1.

Silicon/Zirconium oxide – Similarly to the methoxy-silane vibration, the Si-O-Zr bond is favoured by the lowest HD and low curing temperature. From 140ºC, this band has fully disappeared for the lowest HD but is still present in the other materials. Therefore, the increase of the curing temperature favours the formation of Si-O-Zr species when the HD is at least 50%.
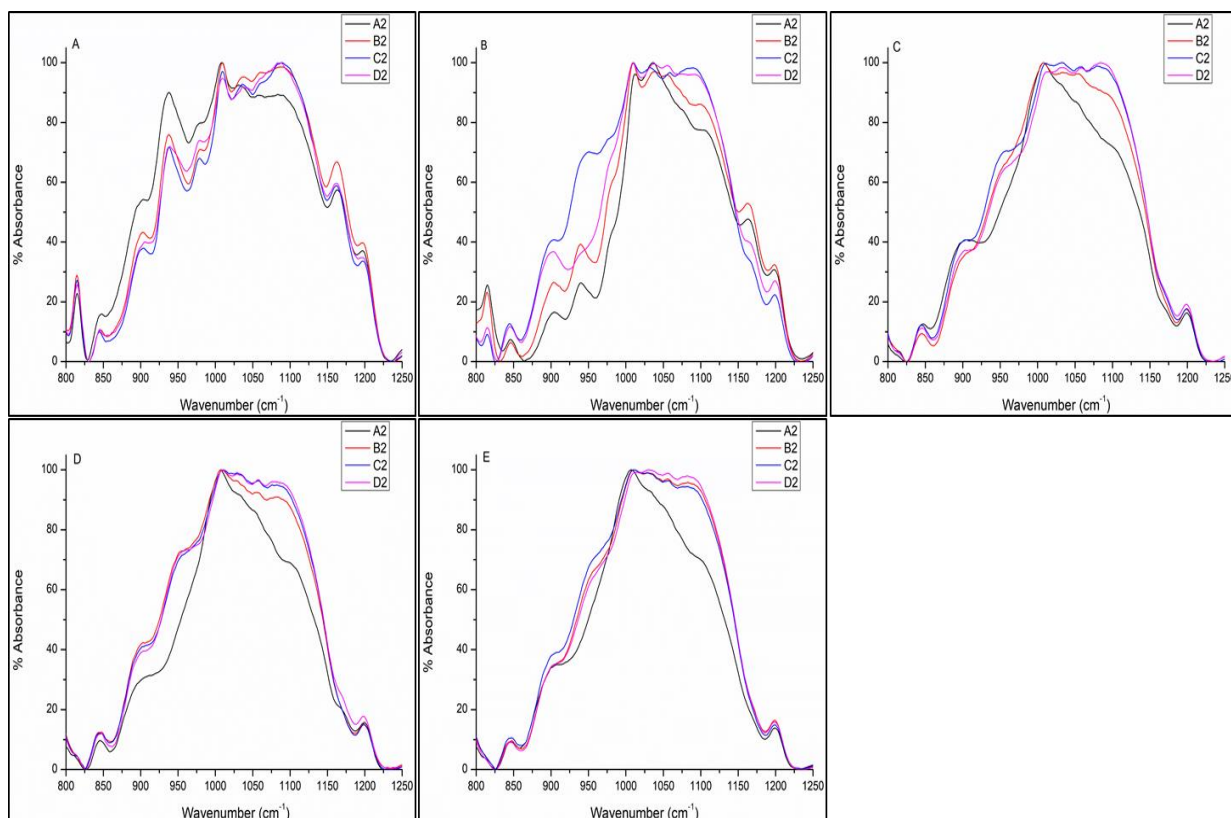
Figure 6. 11: FTIR Spectra for Series 2: A) 100°C, B) 120°C, C) 140°C, D) 160°C, E) 180°C

Series 3

Silanol vibration – The intensity of the silanol groups is generally higher for the lowest HD, regardless of the curing temperature. This is an opposite phenomon than the one observed for series 1 and 2. This clearly shows that the increase of HD catalyses the formation of other species than Si-OH and confirm the competition in the hydrolysis reactions between the sol-gel reactive centres, which would seem to be dominated by the Zr complex.

Siloxane vibrations – Similarly to series 1 and 2 the increase of the HD increases the formation of high – energy siloxane bonds ($1050 – 1150$ cm^{-1}).

Methoxy-silane vibrations – The intensity of the Si-O-CH$_3$ groups is the highest for the samples prepared with the lowest HD for the curing temperatures $100 – 140$ºC. This would make sense as the more watter is added, the more of the reactive groups should be

150

consumed. Again, regardless the HD, the Si-O-CH$_3$ decreases as the curing temperature increases further confirming the thermal catalysis of the Si-OCH$_3$ groups into different inorganic species.

Silicon/Zirconium oxide – The Si-O-Zr bonds is seen to decrease when the curing temperature is increased. It also seen to decrease with the increase of HD. Importantly, this band is decreasing with the increase of zirconium content for the benefit of the formation of Si-O-Si bonds. This clearly suggests that the Si-O-Zr bonds is less stable than the Si-O-Si bonds.
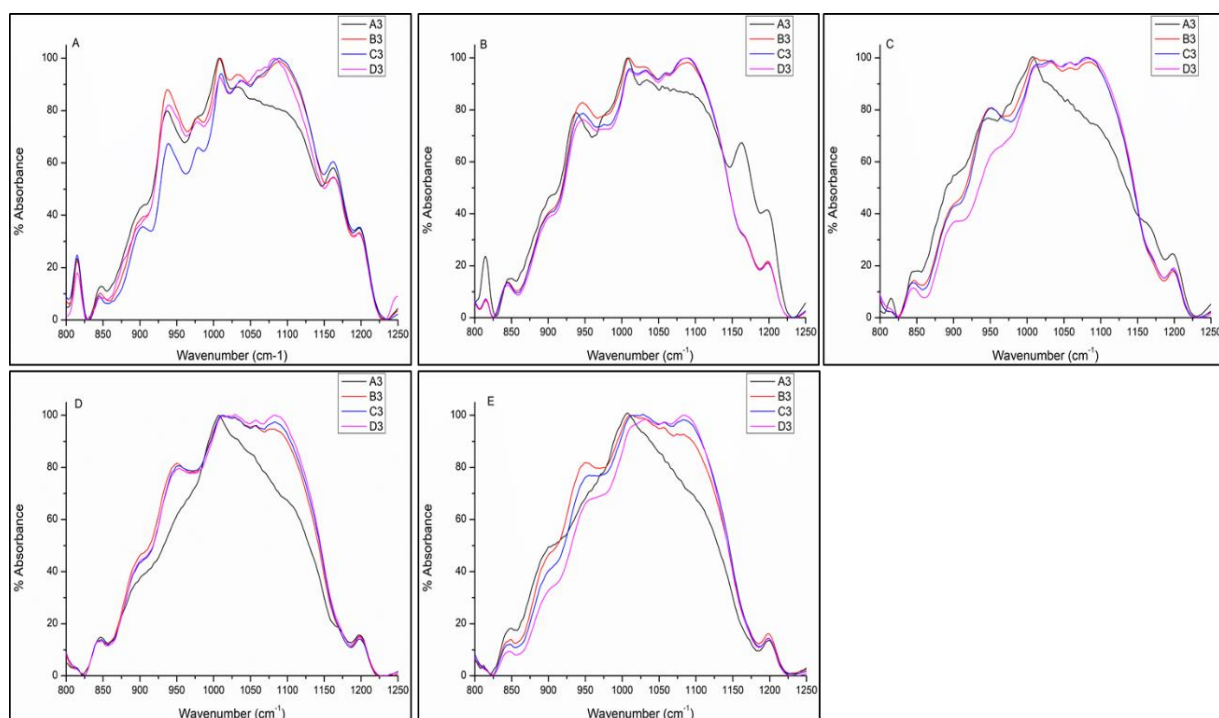
Figure 6. 12: FTIR Spectra for Series 3: A) 100°C, B) 120°C, C) 140°C, D) 160°C ,E) 180°C

Series 4

Silanol vibration – The Si-OH groups are decreasing as the HD increases regardless of the curing temperature and zirconium content. Although this effect was slightly observed for series 3, it was absent in series 1 and 2, confirming the competition of the two reacive

151

centres on the hydrolysis reactions and that the hydrolsyis is preferentially occuring on the zirocnioum atom.

Siloxane vibrations – Although the low –energy siloxane bonds (1000 – 1050 cm^{-1}) show similar intensities for all materials, the high energy vibrations appear to be less favoured for the low HD. This means that at this zirconium content, the primary factor influencing the condensation of the siloxane bonds is the HD.

Methoxy-silane vibrations – The Si-O-CH$_3$ are primarily impacted by the curing temperature with a full disappearance from a curing temperature of 160°C. Importantly, in comparison with the previous series, the decrease is more pronouced for the low HD and lower temperatures. This suggests that the zirconium acts as a catalyst for the reactivity of the Si-O-CH$_3$ groups. As the Si-OH groups are seen to decrease the most likely catalysis of the Si-O-CH$_3$ groups would be from siloxane bonds.

Silicon/Zirconium oxide – The increase of the HD tends to decrease the intensity of the Si-O-Zr bond, translating the formation of Si-O-Si species. The same trend is observed when the curing temperature is increased, further suggesting the instability of the Si-O-Zr bond in comparison with the siloxane bonds.
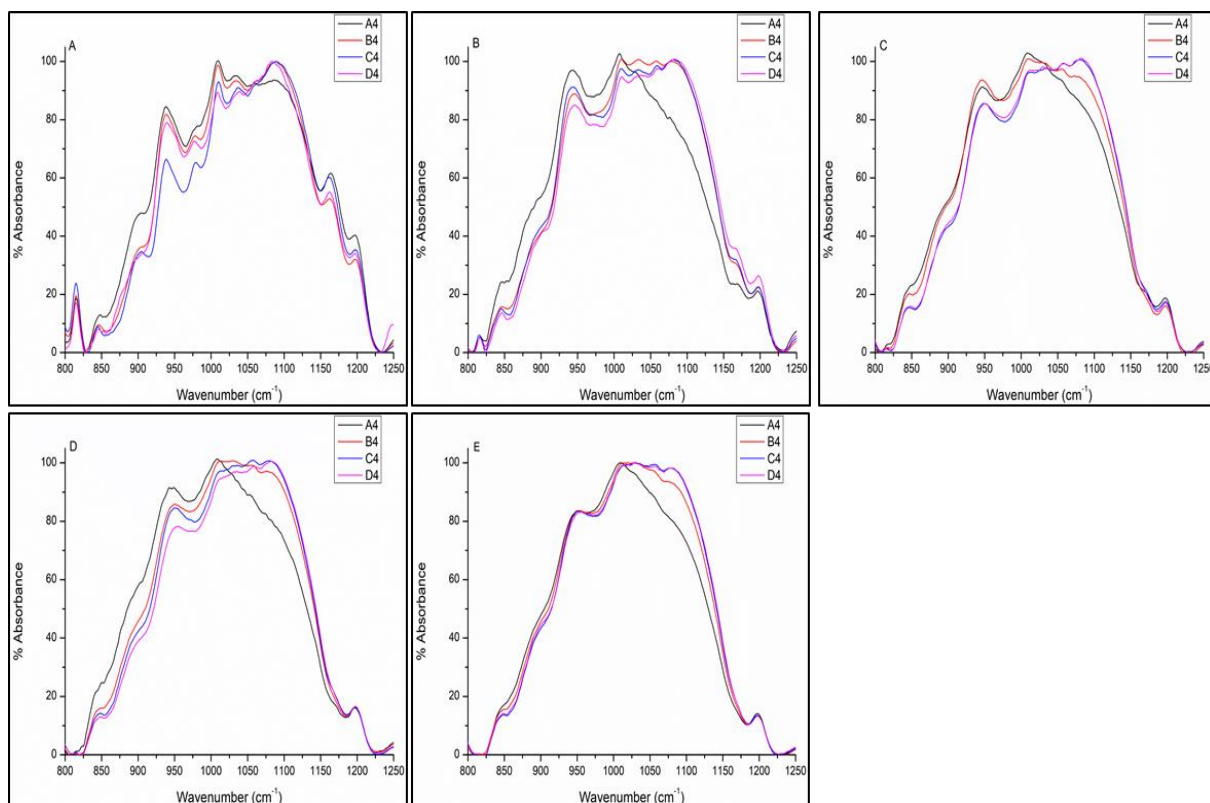
Figure 6. 13: FTIR Spectra for Series 4: A) 100°C, B) 120°C,C) 140°C, D) 160°C, E) 180°C

Series 5

Silanol vibration – Similarly to series 3 and 4, the intensity of the Si-OH bonds decreases as the HD increases, further confirming that the zirconium atom is the most reactive centre. Again, this band is also seen to decrease as the curing temperature increases, suggesting the occurrence of condensation reactions.

Siloxane vibrations – The high-energy siloxane bonds are seen to increase as the HD increases with the highest intensities observed for the 75 and 100 % HDs. From 120°C, the effect of the curing temperature is negligible as for series 3 and 4, suggesting the main impact on the formation of siloxane bonds is the zirconoum content.

Methoxy-silane vibrations – The Si-O-CH$_3$ groups are mainly effected by the curing temperature that provokes their disappearance from 140°C.

153

<u>Silicon/Zirconium oxide</u> – Unlike the other series, the Si-O-Zr bonds remain at high intensity regardless of the curing temperature. Nevertheless, a decrease of their intensity is observed for the highest curing temperatures (160 and 180°C), suggesting their conversion into other reactive species, probably as siloxane bonds.
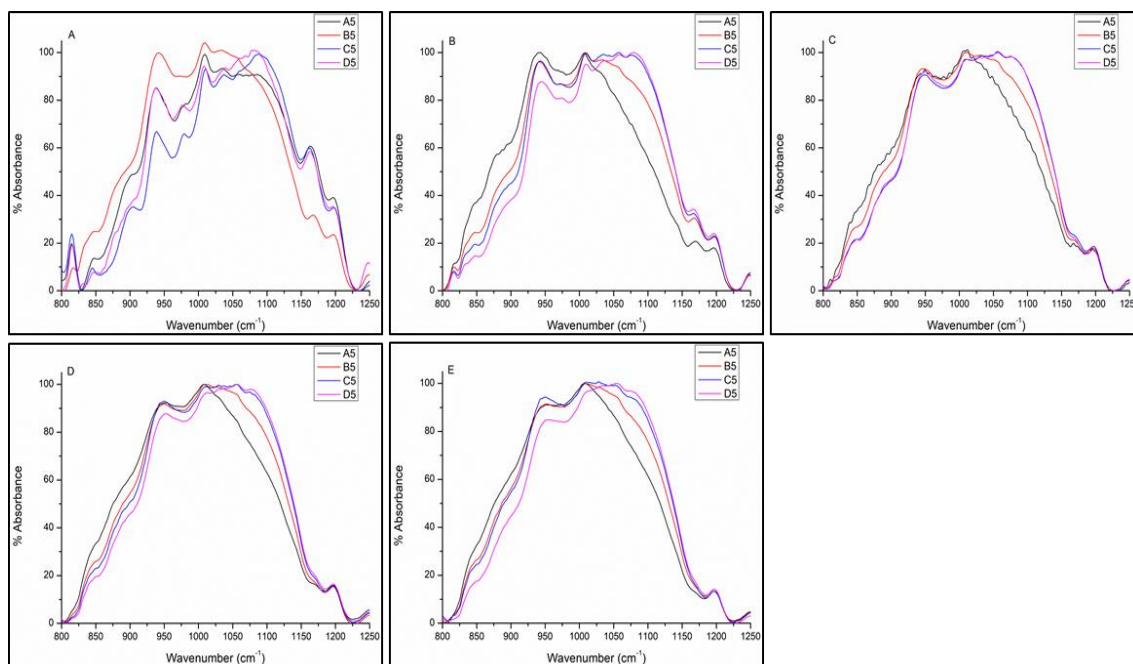
Figure 6. 14: FTIR Spectra for Series 5: A) 100°C, B) 120°C, C) 140°C, D) 160°C, E) 180°C

From these results it can be summarised that the condensation of the materials is thermally catalysed and an increase in hydrolysis degree favours more condensed systems as seen by the increase in intensity of the high energy siloxane bonds above 1010 cm^{-1}.

Also, by corroborating the contact angle (section 6.3.2) and FTIR results, the decrease of the silanol concentration cannot support the hydroxylation process we proposed in Fig. 6.9.

Therefore, the only physico-chemical phenomenon that is occurring can only be the formation of Zr-OH bonds. This is supported by the fact that the Si-O-Zr bonds are decreasing as the curing temperature increases with a parallel decrease and increase of the silanol and siloxane bonds. Finally, the hydrophilicity is provided by:

1. **The Si-OH groups for the low zirconium contents**

2. **The Zr-OH for the high zirconium contents.**

A structure of the sol-gel system is proposed in Fig. 6.15 below.

To further understand the results presented here, ^{29}Si-NMR will be discussed in the following section.
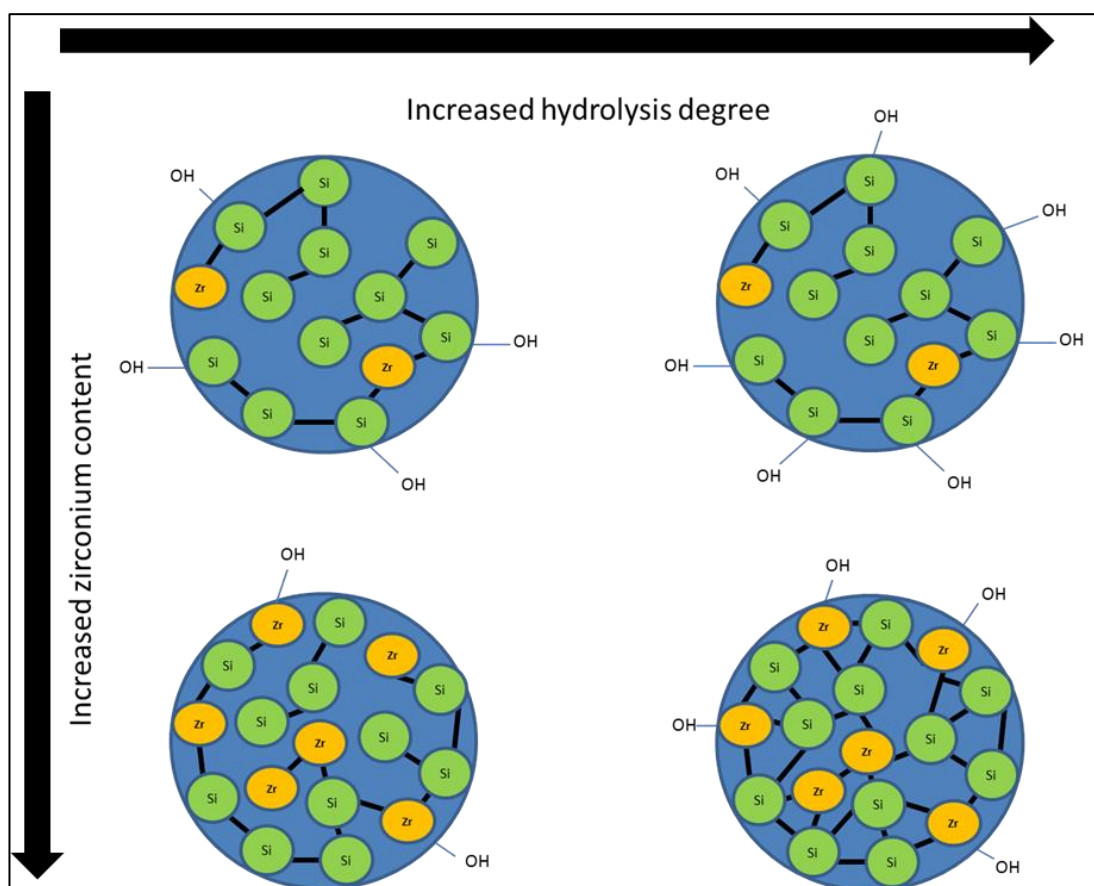
Figure 6. 15: Proposed structure of the sol-gel system at low and high zirconium contents

6.3.4 ^{29}Si-NMR Analysis

^{29}Si-NMR spectra were recorded for all materials in series 1-5 and are presented in Fig. 6.16. For a better quantification of the different T species present in the materials, the signals were integrated and are represented in Fig. 6.17 for series 1 to 5, respectively.

It can be observed that T_0 species are present only at the lowest hydrolysis degree (materials A1-A5), in concentrations of 8.9, 28.7, 21.0, 23.9 and 23.2 %, respectively. It can be observed that as the HD increases the T_1 species located between -49 to -55ppm decrease and are not present in the any of the materials with a HD of 75 and 100%, with the exception of materials in series 1 (1% ZPO concentration) and material D2 (5% ZPO concentration). It is also worth noting that as both the HD and zirconium content increases there is a significant increase in the signal to noise ratio of the spectra (Fig. 6.12). This may be due to the increase in the densification of the silicate network and overlapping of the magnetic responses of silicon nuclei in similar configurations. As the HD increases for series 1, there is an increase in the content of T_2 species with increasing hydrolysis degree, with the highest concentration being 57.08% for material D3. A similar trend can be noted for series 2-4. As the hydrolysis degree increases up to 50%, the ratio of T_2 species also increases, from 50-75% there is a decrease in T_2 species and from 75-100%, a further increase can be seen. Interestingly the highest concentration of T_2 species for series 2-4 can be found in material B with a hydrolysis degree of 50% and a ratio of 50.79, 44.34 and 41.83% respectively. For series 5 it can be seen that as the hydrolysis degree increases up to 50% , the concentration of T_2 species increases up to 44.60% for material B5. As the hydrolysis degree increases from 50 -100% there is a decrease in the concentration of T_2 species. Regarding the evolution of T_3 species a similar set of behaviours can be seen for the materials. For series 1-4, the content of T_3 species within the materials increases with an increase in hydrolysis degree up to 75%, with a slight decrease from 75-100%, which does not exceed 4.5%. For series 5, which contains the highest content of ZPO, the T_3 species increases with increasing hydrolysis degree up to 100%.

The signal for the pure MAPTMS precursor is located at -42.64 ppm. However, for materials A1-A5 we can observe multiple signals for the T_0 species. This indicates that there are unreacted MAPTMS molecules present within the materials. A possible explanation for this may be that the MAPTMS is unable to hydrolyse fully due to an insufficient water content or that the MAPTMS molecules have become entrapped within the already formed nanoparticles and remain un-hydrolysed. Material A1 contains 3 T_0 signals located at -42.00, -42.72 and -44.95 ppm. Material A2 contains 5 T_0 signals located at -42.03, -42.64, -43.89, -45.14, and -45.09 ppm. Material A3 exhibits 4 T_0 signals located at -41.96, -42.58, -43.84 and -45.09 ppm. Both material A4 and A5 exhibit 4 nearly identical T_0 signals at -42.73, -43.98,-45.22, -46.46 ppm and -42.76, -44.01, -45.25 and -46.49 ppm, respectively. This suggests that both materials are composed of particles with nearly identical morphologies.

It can be observed that for each series of materials, the concentration of T_3 silicate species increases in concentration up to a hydrolysis degree of 100% for series 1 and 5 and up to a hydrolysis degree of 75% for series 2-4 with a decrease for the materials with the highest hydrolysis degree of 100%. This increase in the T_3 species may be explained by the increase in reactive silanol groups which undergo condensation reactions to form more condensed silicate species, due to the increase in the quantity of water within the sol-gel network. For series 2-4, it can be noted that as the T_3 species decrease the T_2 species increases in concentration. Series 4 and 5 show the highest concentration of T_3 groups for material C4 and D5 respectively. It can also be noted that materials A1-A5 are the only materials with unreacted T_0 groups present in the ^{29}Si-NMR spectra. These materials also have the highest concentration of T_1 groups. This may be due to low degree of hydrolysis and ZPO content. It can also be noted that T_1 species are present for materials with a hydrolysis degree of 25-50% only regardless of ZPO concentration. It

can also be noted that there is an increase in T_1 species and a decrease in T_3 species for the materials- which indicates that at ZPO concentrations of 30 %, condensation of the network is hindered and the formation of T_1 species is favoured. This may be due to steric hindrance form the zirconium. Therefore these results show that the condensation of the sol-gel network can be controlled by controlling both the hydrolysis degree and ZPO concentration.

In summary, the formation of condensed species is favoured by the increase of the HD or the increase of ZPO content, as identified by FTIR analysis. Importantly the absence of T_0 species in series 1 to 5 for materials B-D, further confirms that the hydrophilic properties cannot be ascribed to Si-OH groups and are therefore <u>confirmed to be attributed to Zr-OH groups</u>.
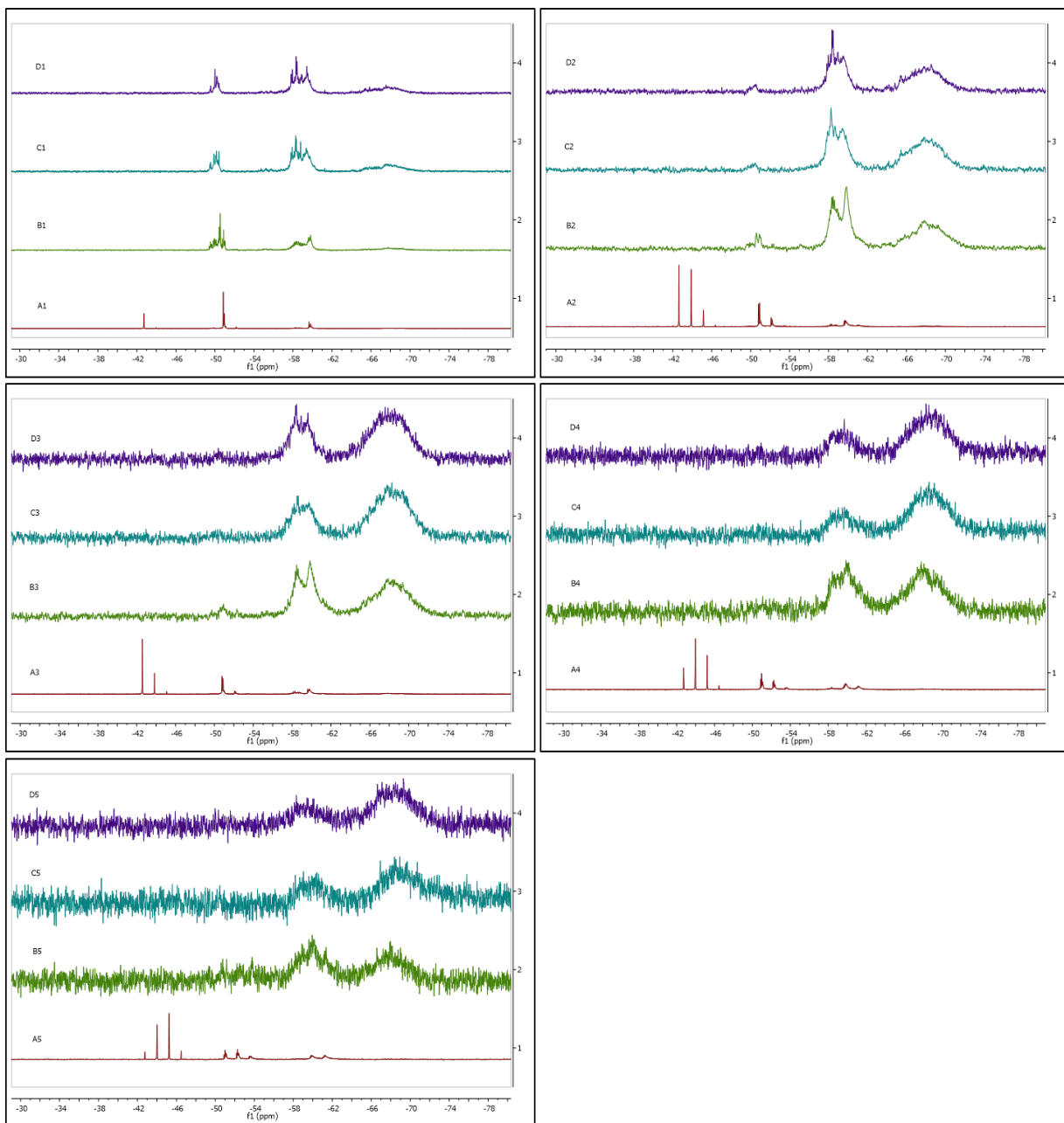
Figure 6. 16: ^{29}Si-NMR spectra for all materials in Series 1-5
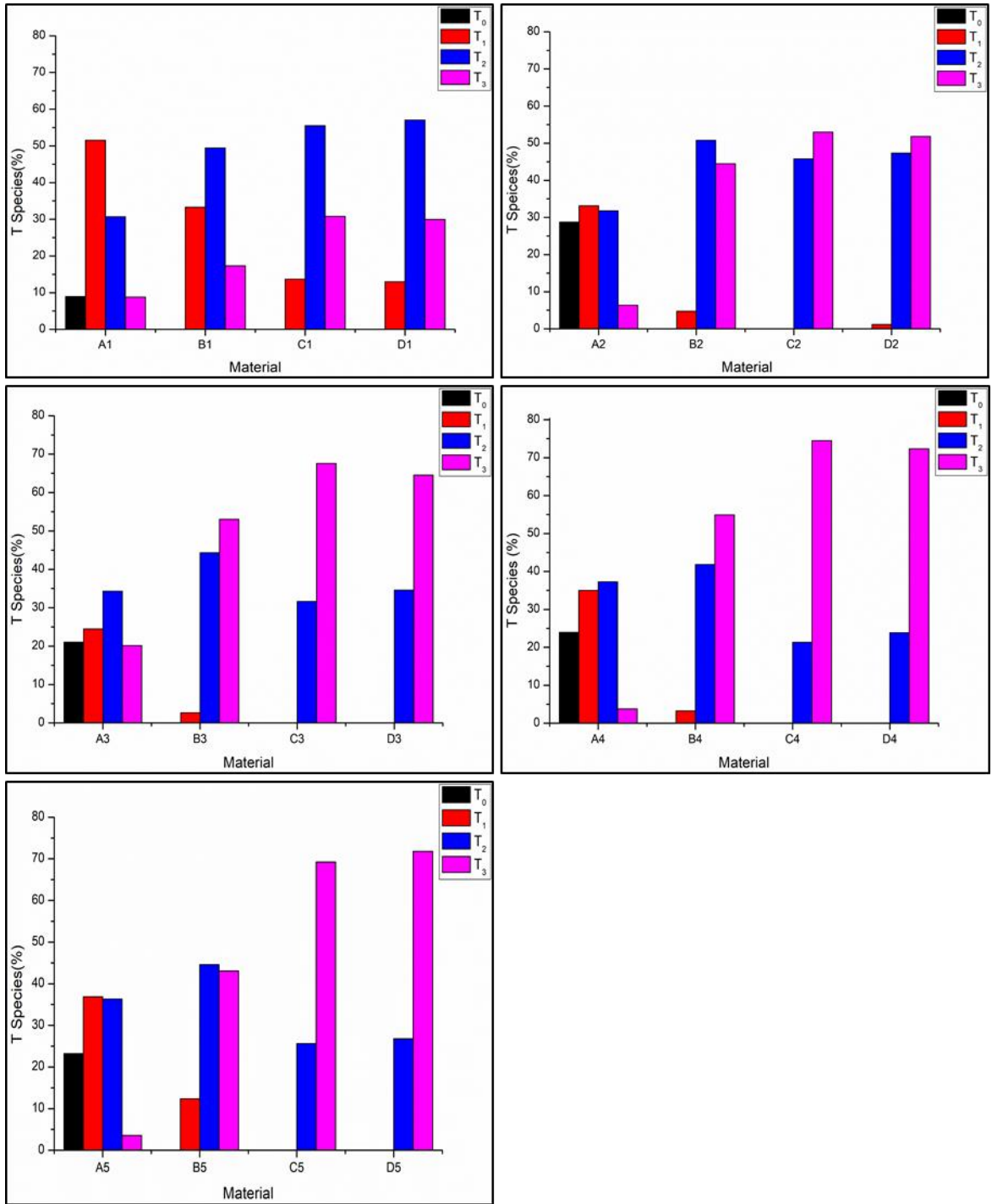
Figure 6. 17: T species evolution for all materials in Series 1-5

6.3.5 Thermal Analysis

The thermal behaviour of the liquid sol-gel materials was analysed using DSC and is shown below for all materials in series 1-5 in Fig. 6.18. There are three different areas of thermal behaviour that can be observed, between 20-60℃, between 100℃ and 170℃ and above 170℃. These thermal zones correspond to the evaporation of volatile solvents, the condensation of the materials and the glass transition phase of the materials, respectively. Any exothermic bands above 200℃ are due to the thermal decomposition of the materials. The large broad endothermic band between 20 – 60℃ is due to the evaporation of entrapped volatile solvents within the silicate network, methanol and propanol, which are formed during the sol-gel synthesis or from the precursor materials. It can be observed that the endothermic band increases with increasing HD up to 75% for series 1-4, respectively. This suggests that as the HD increases, the amount of solvent entrapment within the network of these materials also increases. For the materials with a HD of a 100% the endothermic band is slightly smaller for all materials except material D5 which also contains a zirconium content of 30%. There is also an increasing shift towards higher temperatures with increasing hydrolysis degree for all materials in series 1-3 and for materials A4-C4 in series 4 respectively with temperatures shifts of 10, 10.3 and 14.5℃ respectively for series 1-3. For the materials in series 4 there was an overall temperature shift of 12.85℃. For series 5 there is a temperature shift towards lower temperatures from material A5 to B5 and a shift towards higher temperatures for materials B5-D5 with an overall shift of 17℃. This behaviour may be due to a higher content of hydrophilic species of Si-OH and Zr-OH within the sol-gel network. The exothermic bands located between 170 and 190℃ can be associated with the glass transition temperature of the materials, and represents the full solidification of the materials. Overall the Tg of the materials decreases as the ZPO content increases within a range of 10℃ up to series 4. It can also

161

be noted that the Tg of the materials increases with increasing hydrolysis degree from 25-50%, remains unchanged up to 75% and decreases for 100% for series 1 and 2. The opposite behaviour is observed for the materials in series 3. For the materials in series 4, the Tg increases from 25-50%, and then decreases from 50-100%. The Tg remains stable from 25-50% and increases from 50-75% and then remains stable up to 100% for the materials in series 5. The explanation for this behaviour is likely due to the condensation process of the sol-gel nanoparticles and the surface reactivity of the materials in the liquid phase. For material B5 there are two exothermic bands located at 179 and 193℃ respectively. These two bands may indicate the occurrence of two different phases within the material. As seen previously in both structural characterisations of the materials increasing the hydrolysis degree provokes the formation of sol-gel systems which are more condensed. This would lead to less reactive groups (namely hydroxyl groups), on the surface of the sol-gel nanoparticles.

In summary, these results show that the HD has an effect on the thermal properties when the ZPO concentration is greater than 10%, confirming the role of the zirconium atom on the condensation process of the silicate network, as previously concluded from the FTIR and ^{29}Si-NMR.
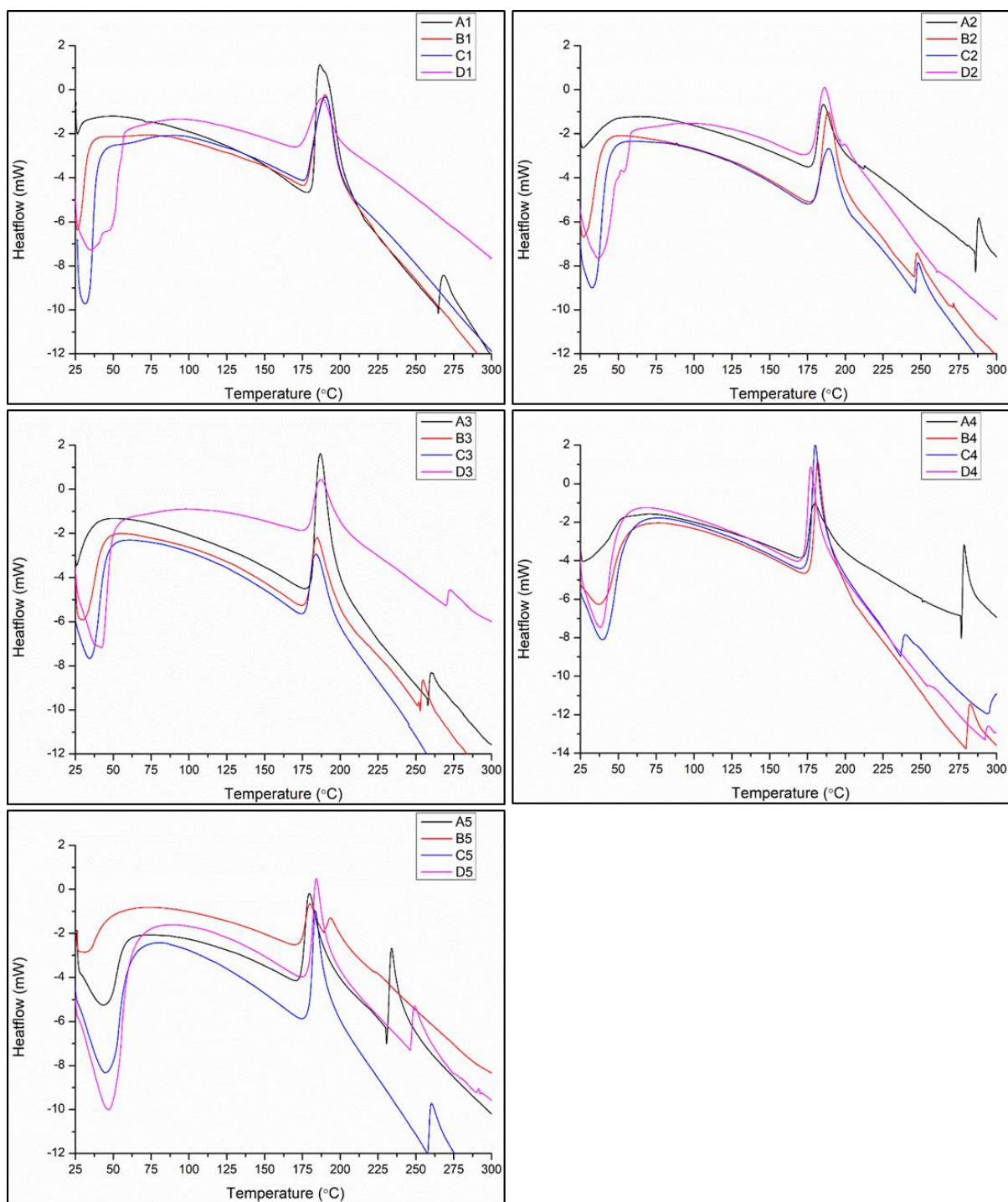
Figure 6. 18: DSC spectra for all materials in Series 1-5

6.4 Conclusion

This chapter focused on the influence of the hydrolysis degree on the surface properties

and structure of the sol-gel network with the objective to identifying the species

163

responsible for the hydrophilic properties of the coatings. The structure of the sol-gel materials was also altered by varying the concentration of ZPO along with the curing temperatures of the coatings. The effects of varying these parameters on the structure and surface properties of the sol-gel materials were investigated and characterised using DLS, CA measurements, FTIR, DSC, and ^{29}Si-NMR. The DLS results showed that both the hydrolysis degree and ZPO content control the reactivity of the materials and the particle growth. From the CA results it was seen that as the hydrolysis degree increases the CA decreases and becomes more hydrophilic in nature. It was also noted that for materials with ZPO concentrations of 10% and above there is an increase in the hydrophobicity of the materials from 160 – 180℃ for C3, D3, D4, A5 and D5. Both the FTIR and ^{29}Si-NMR results show that an increase in the hydrolysis degree leads to the formation of more condensed materials. The thermal analysis confirmed that it is possible to control the condensation of the sol-gel network by varying the hydrolysis degree and ZPO concentration.

In summary, it was found that the HD, zirconium content and curing temperature play a role in condensation of the materials. Although the HD plays a role in increasing the overall wettability of coatings- which is an important factor to consider for microfluidic applications, it was found that there was little variation in the wettability of the coatings after 50% hydrolysis, for temperatures between 120 – 140 ℃. Importantly, the structural characterisations demonstrated that the wettability is primarily due to the Zr-OH groups. The next chapter will focus on functionalising the surface of the zirconium modified silicate sol-gel nanoparticles to fabricate functional core-shell nanoparticles employing a variety of functional alkoxysilanes.

7 Surface modification of the reference material: Development of Core Shell based sol-gel coatings

7.1 Introduction

In the previous chapters, the effects of the relative content of the reactive sol-gel precursors and their hydrolysis conditions were investigated. In this chapter we will concentrate on investigating strategies to functionalise the surface of the reference material during its preparation. One strategy we have identified consists of the incorporation of functional alkoxysilanes that can bind at the surface of the sol-gel nanoparticles via inorganic condensation so that their surface properties can be altered due to the organic pendant group of the introduced functional silane, thus forming core-shell based sol-gel nanoparticle coatings. The aim of this strategy would be to investigate a number of functional silanes, each one of them containing a specific organic functionality which will potentially enable the increase of the hydrophilicity of the final microstructured sol-gel coating. The functional alkoxysilanes are incorporated when the initial sol-gel network has been formed and therefore the silanes should bind to the surface of the sol-gel nanoparticles rather than being incorporated into the sol-gel network. The selected alkoxysilanes used to functionalise the surface of the sol-gel nanoparticles are tetra-ethylorthosilicate (TEOS), 3-glycidyloxypropyltrimethoxysilane (GPTMS), 3-aminopropyltriethoxysilane (APTES) and vinyltriethoxysilane (VTES) and their structure structures are presented in Table 7.1. APTES, GPTMS and VTES are commonly used as silane coupling agents (also called adhesion promoters) and have been used as surface modifiers for silica nanoparticles in previous studies for underfill applications[149]. Therefore, we believe that if they can effectively bind at the surface of

the sol-gel nanoparticles, functional core-shell nanoparticles coatings can be formed with

likely effects on the wetting properties of the final coatings.
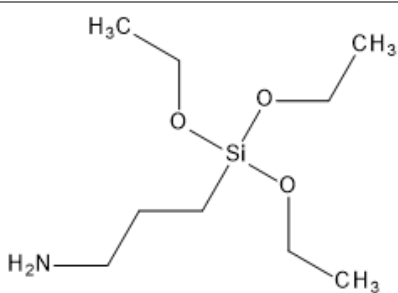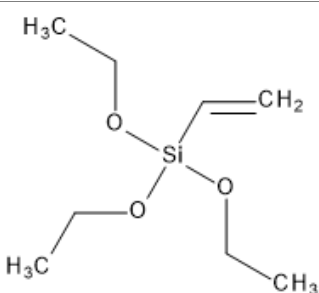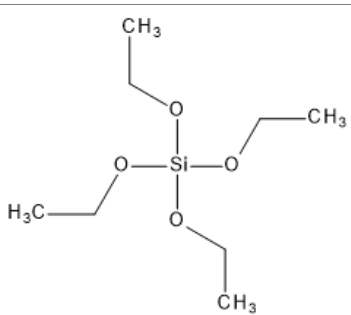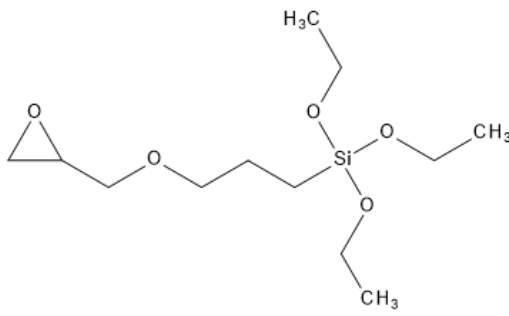
Chemical Name	Abbreviation	Molecular Formula	Structure
(3-Aminopropyl) triethoxysilane	APTES	$C_9H_{23}NO_3Si$	
Vinyl triethoxysilane	VTES	$C_8H_{18}O_3Si$	
Tetra ethylorthosilicate	TEOS	$C_8H_{20}O_4Si$	
(3-Glycidyloxypropyl) trimethoxysilane	GPTMS	$C_9H_{20}O_5Si$	

Table 7. 1: Chemical name, abbreviation,formula and structure of the selected

functional alkoxysilanes

7.2 Materials Preparation

The reference sol-gel material was synthesised as in chapter 4 with the ZPO concentration fixed at 20% and the hydrolysis degree fixed at 50%, and functionalised with the above-mentioned 4 alkoxysilanes, 24 hours after synthesis. A mother batch of the reference material was prepared as described in section 4.2 and divided into 4 equal volumes in 4 separate 100 ml beakers to which the functional alkoxysilanes were added. The concentration of the alkoxysilanes used were 1, 5, 10 and 20 mol% against the methoxy groups of the MAPTMS. Each concentration of alkoxysilane was added to equal volumes of the mother batch sol-gel material under constant stirring and the prepared materials were stirred for 1 hour before use. The synthesis was carried out under ambient conditions. A flow chart of the synthesis of the core-shell based sol-gel materials is shown in Fig. 7.1. The material formulations and volumes of alkoxysilane used to synthesise each sample are presented in table 7.2.

As the alkoxysilanes were added after the sol-gel network has already formed, in theory the functional silane should bind to the outside of the nanoparticle rather than being incorporated within the network, via the occurrence of inorganic condensation reactions between their alkoxy groups and the residual hydroxyl groups located at the surface of the nanoparticles. A schematic of the fabrication of the core-shell nanoparticles can be seen in Fig. 7.2. The following surface, structural and thermal characterisations will aim at identifying the chemical reactions taking place and their effect on the surface properties of the materials.

Functional Alkoxysilane	Concentration (% against total methoxy groups)	Mother-batch formulation (MAPTMS:ZPO:MAAH)	Volume of alkoxysilane used per 10.55g of sol Vol (ml)
APTES	1	80:20:20	0.083
APTES	5	80:20:20	0.42
APTES	10	80:20:20	0.83
APTES	20	80:20:20	1.67
GPTMS	1	80:20:20	0.056
GPTMS	5	80:20:20	0.28
GPTMS	10	80:20:20	0.56
GPTMS	20	80:20:20	1.13
TEOS	1	80:20:20	0.057
TEOS	5	80:20:20	0.28
TEOS	10	80:20:20	0.57
TEOS	20	80:20:20	1.14
VTES	1	80:20:20	0.054
VTES	5	80:20:20	0.27
VTES	10	80:20:20	0.54
VTES	20	80:20:20	1.079

Table 7. 2: Material Formulations for functionalised alkoxysilane study
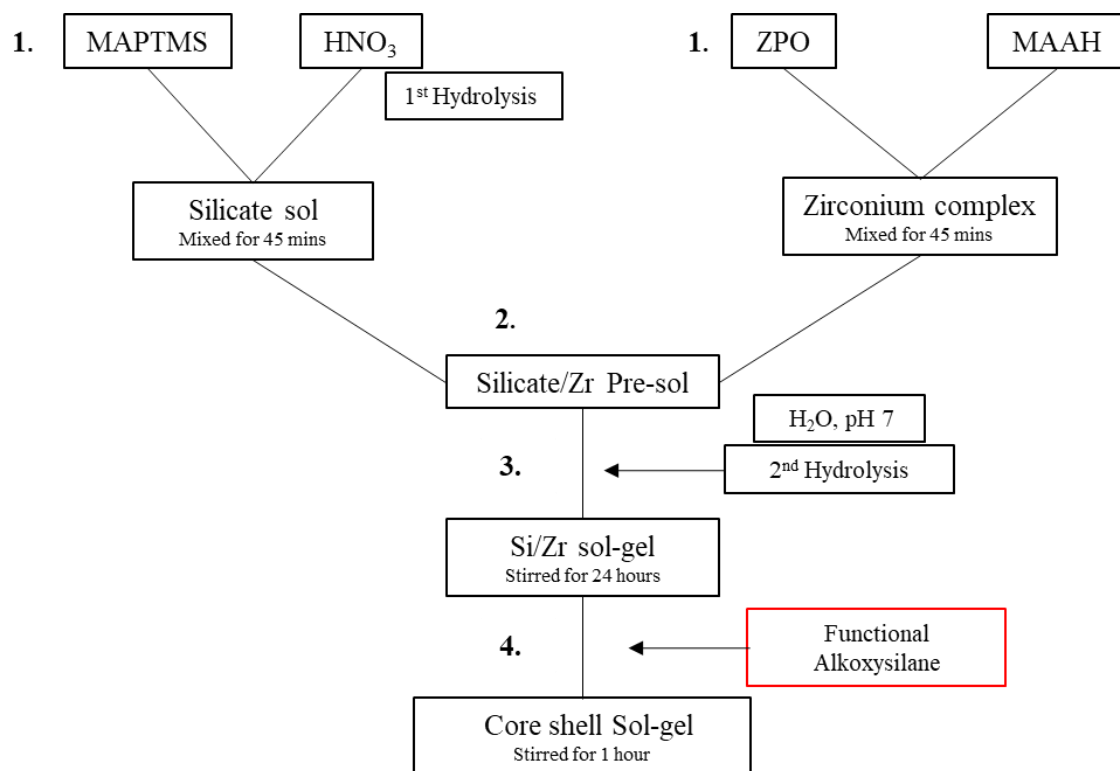
Figure 7. 1: Flow chart for the synthesis of core shell sol-gel materials
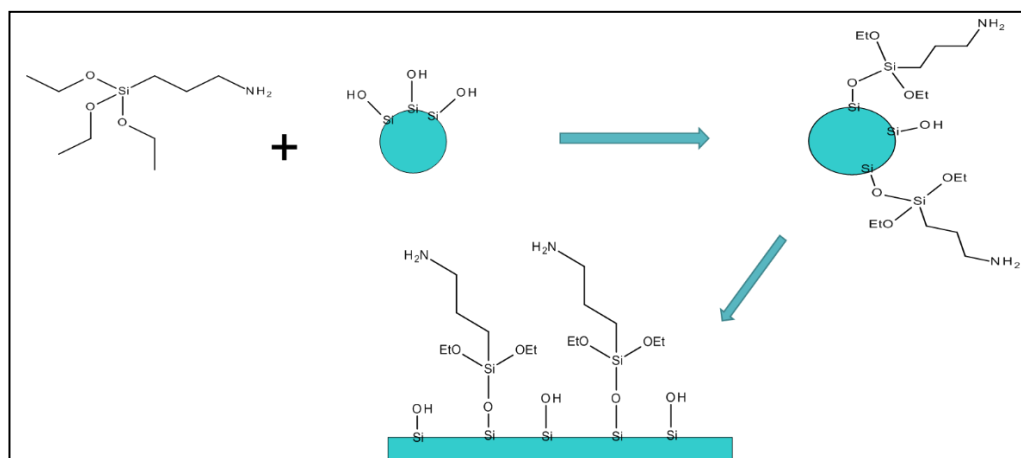
Figure 7. 2: Schematic of the fabrication of core-shell sol-gel materials (example with APTES as surface modifier)

7.3 Results and Discussion

7.3.1 Particle Size Analysis

The particle sizes for all materials 24 hours after preparation are represented in Fig. 7.3. Firstly, it can be observed that all spectra exhibit a single distribution band in the 0 – 20 nm range, regardless of the concentration of the functional alkoxysilane. Secondly, the reference material modified with 1% of functional silanes shows no variation of the maximum particle size located at 4 nm. For the other concentrations of functional silanes, it is observed that the maximum particle size fluctuates around 4 nm with a fluctuation value of 1 nm, which is considered to be the error measurement of the spectrometer. Therefore, from the analysis of the maximum particle size, it can be concluded that the addition of the functional silane does not significantly alter the particle size of the materials. However, to better estimate the effect of the silane modifiers on the distribution of the particles, the full width at half maximum (FWHM) for all spectra has been measured and represented in Fig. 7.4. It can be observed from the DLS data that no significant alteration of the particle distribution is evident with the exception of the material functionalised with APTES at concentrations of 1 and 20%, which would indicate a tendency to accelerate the aggregation process, probably of small particles with larger particles. The particle size analysis does not provide structural information on the sol-gel materials. For this analysis, FTIR spectroscopy will be performed and discussed in detail.
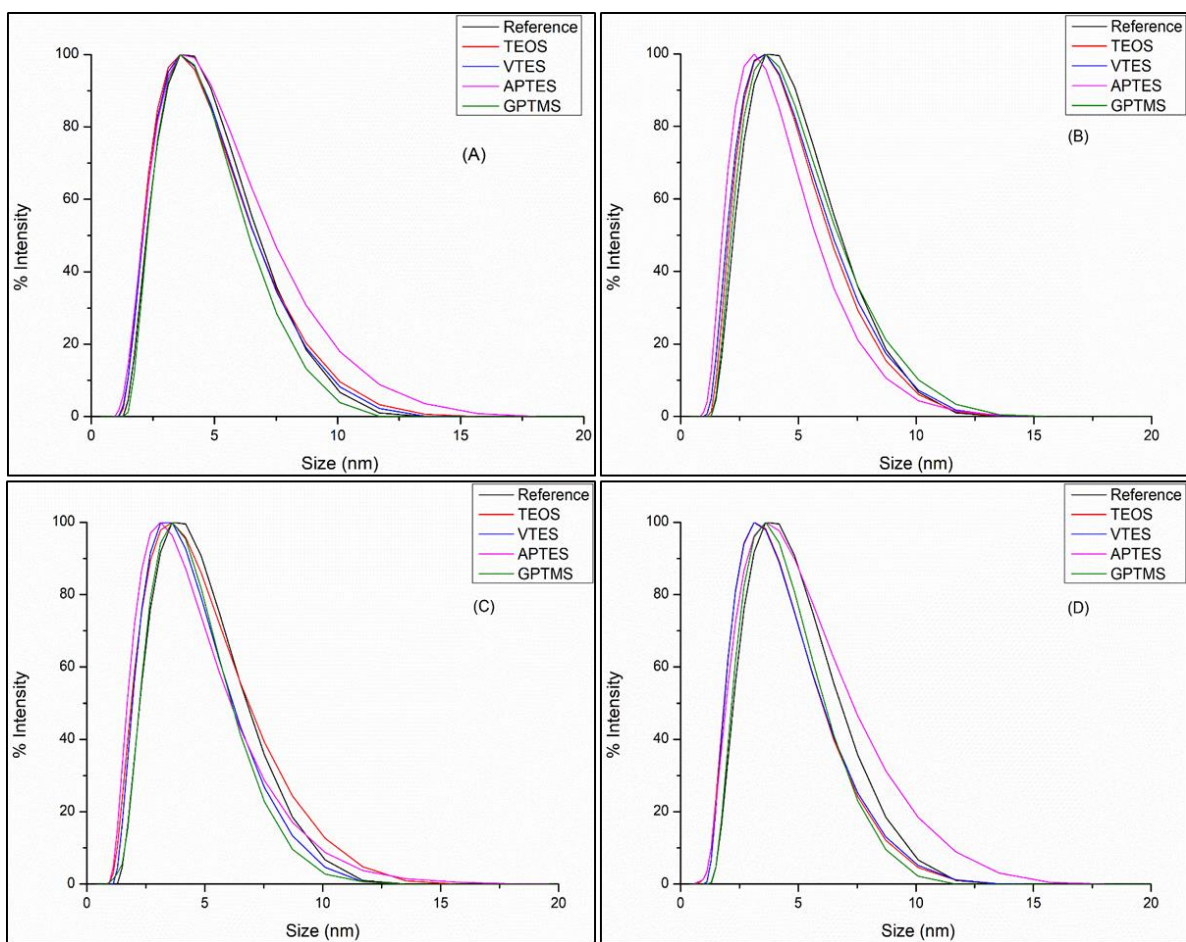
Figure 7. 3: DLS measurements for all functional silane modified materials after 24 hours of ageing: A) 1%, B) 5%, C), 10% and D) 20% concentration
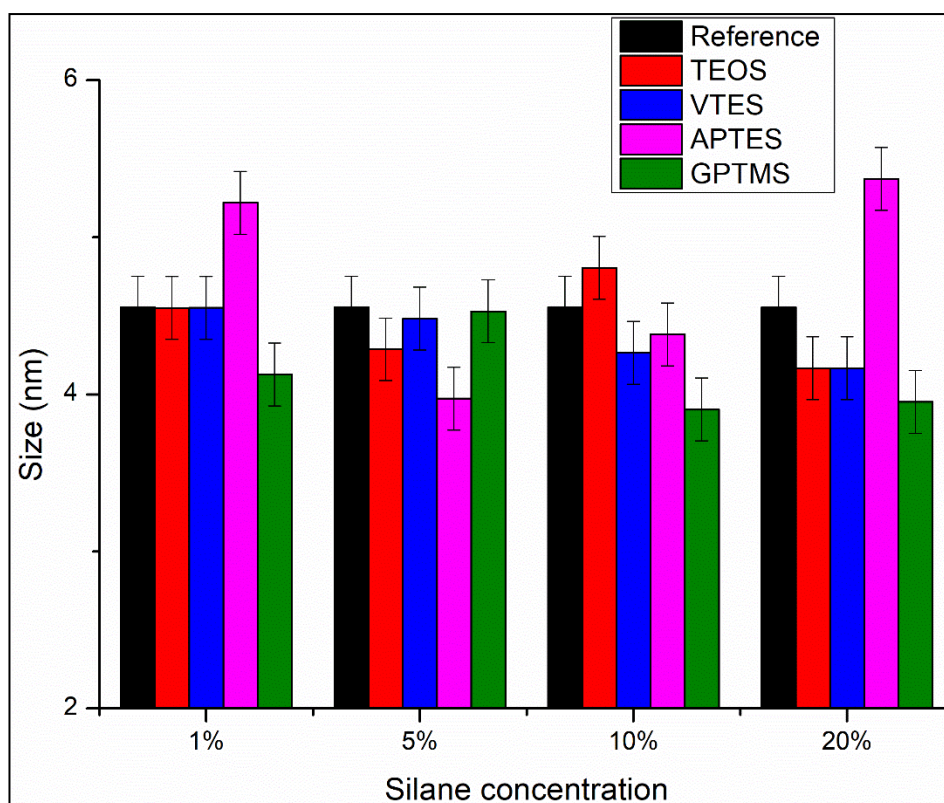
Figure 7. 4: Full width at half maximum (FWHM) for all functional silane modified materials

7.3.2 Contact Angle Measurements

Static water contact angle (CA) measurements were performed on the prepared coatings for each of the 4 concentrations (1, 5, 10 and 20%) of functional silane. Contact angles were measured on 6 different areas of the coatings and the average values for all materials at a given concentration are represented in Fig. 7.7.

Depending on the employed functional silane and its concentration, the CA values are seen to vary differently with the curing temperature. At 1%, TEOS is found to exhibit a constant CA value in the range 67 – 69°, regardless of the curing temperature. At 5%, TEOS shows a slight increase of CA from 65 to 68° from 100 to 140°C, with a stabilisation of the CA between 140 and 150°C. However, for concentrations of 10 and 20%, the opposite tendency is observed with decrease of the CA values from 68 to 66°

and from 71 to 66°, for the 10 and 20% concentrations, respectively. When comparing the TEOS effect with the reference material, it can be seen that regardless of the TEOS content, the main factor governing the wettability is the curing temperature. When the coatings are cured at 100℃, the introduction of TEOS decreases the CA values. However, when the coatings are cured at temperatures of 120℃, or higher, the TEOS increases the CA values of the coatings, suggesting the formation of hydrophobic moieties. At this stage, one can speculate that at 100℃, the TEOS maintains most of its hydrophilic ethoxysilane groups when linked to the surface of the nanoparticles, wheras when the curing is increased to higher temperatures these ethoxysilane groups could be converted into hydrophobic siloxane groups, as sketched in Fig. 7.5. This point would need to be analysed by FT-IR in the following section.
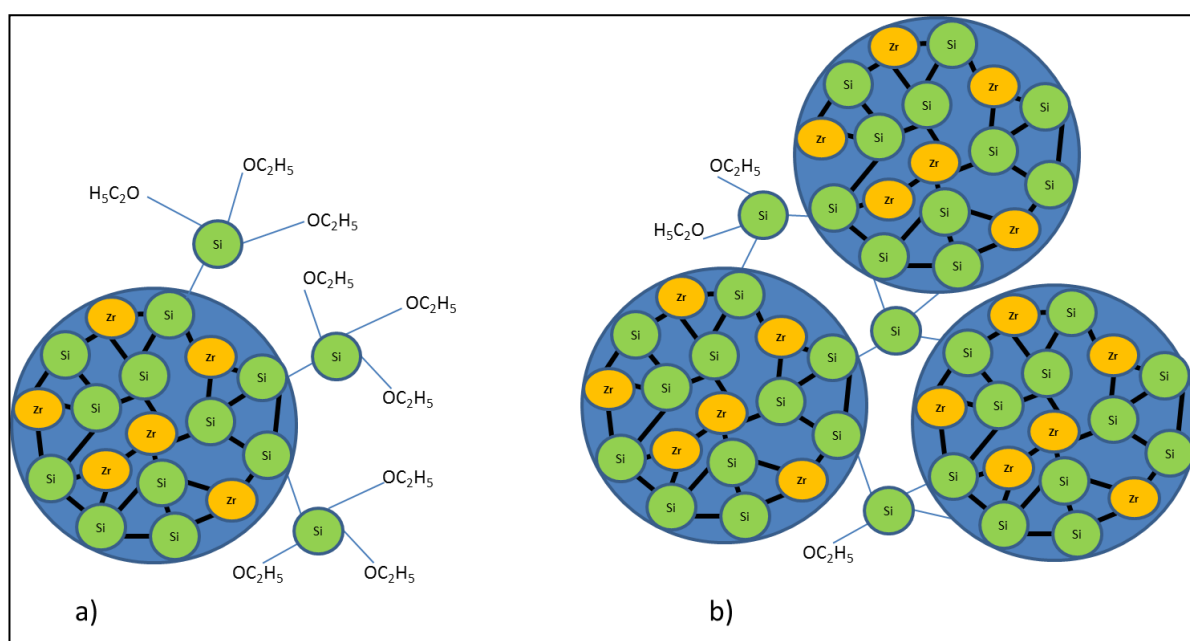
Figure 7. 5: Schematic representation of TEOS a) at the surface of sol-gel nanoparticles at low temperatures and b) crosslinked at higher curing temperatures

For all concentrations of GPTMS, the CA values are seen to progressively decrease to a value comprised between 58 and 60° with increasing temperatures up to 130℃. The CA value is then stable for temperatures up to 150℃. A very similar behaviour is observed

for VTES however with lower and higher CA values recorded at 1% concentration for temperatures of 140 and 150℃ in comparison with GPTMS. This suggests that GPTMS and VTES have similar effects on the structure of the reference nanoparticles, likely the formation of thermally stable cores as shown in Fig. 7.6.
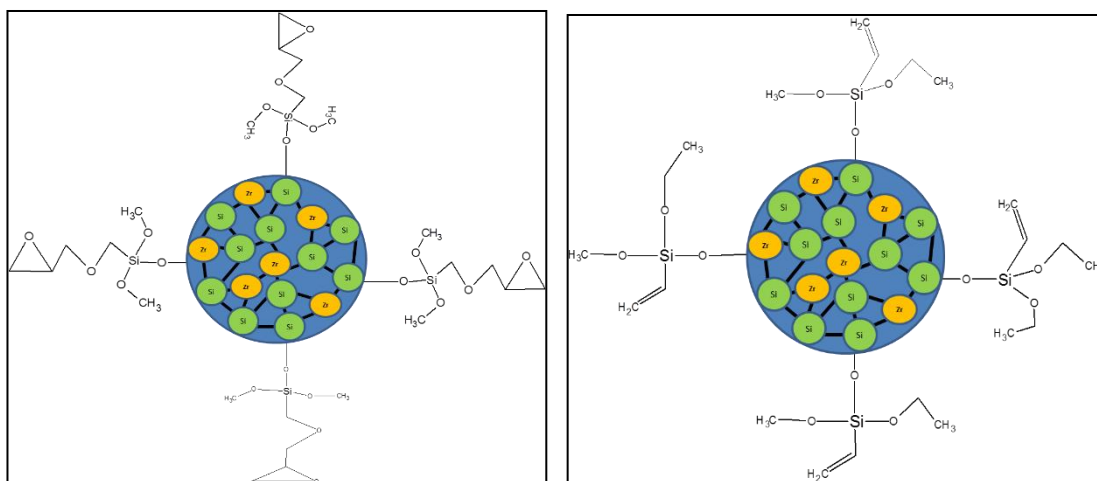
Figure 7. 6 Schematic representation of the effect of GPTMS (left) and VTES (right) on the formation of stable sol –gel nanoparticles

Of the 4 investigated functional silanes, APTES is the silane that shows the strongest variations in the CA values depending on its concentration and curing temperature. Indeed, at 1% concentration, while VTES and GPTMS are found to have CA values that stagnate from 130℃, APTES is shown to further decrease at 140 and 150℃ to reach a CA value of 52°, the lowest value recorded for all samples in this study. In comparison with the reference material, this recorded CA value represents a decrease of 20 and 11°, for curing temperature of 100 and 150℃, respectively. For concentrations of 5 and 10%, the CA values are comparable to those recorded for VTES and GPTMS. However, the CA values are clearly higher (between 63 and 65°) and close to those recorded with TEOS as a modifier, for the materials prepared with a concentration of 10 and 20%. This clearly suggests that for a given curing temperature, the reactivity of APTES is influenced by its concentration. Unlike the three other silanes, which only have one sol-gel reactive site on

their alkoxy group, APTES contains an amino group that may react with organic or inorganic species to form urea or complexes with transition metals (Fig. 7.8), thus explaining the variation observed here. The characterisation of the formed groups will be undertaken using FTIR spectroscopy in the following section.

If at this stage, one can conclude on the effect of the functional silane on the CA value of the reference material with the likely the formation of core-shell particles. However, it is difficult to determine the exact physico-chemical phenomena that can explain the observed behaviours. FT-IR analyses will be undertaken for this specific objective.
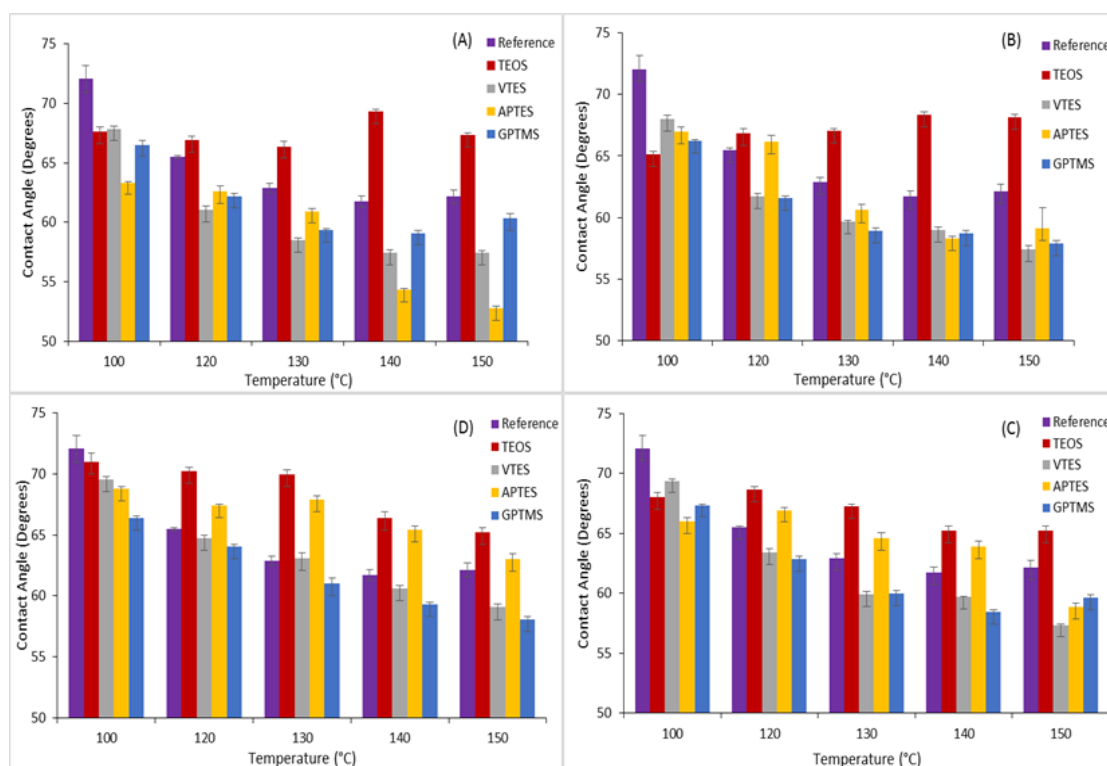
Figure 7. 7: CA measurements vs temperature for all materials A) 1%, B) 5%, C) 10% and D) 20% concentration of functional silanes
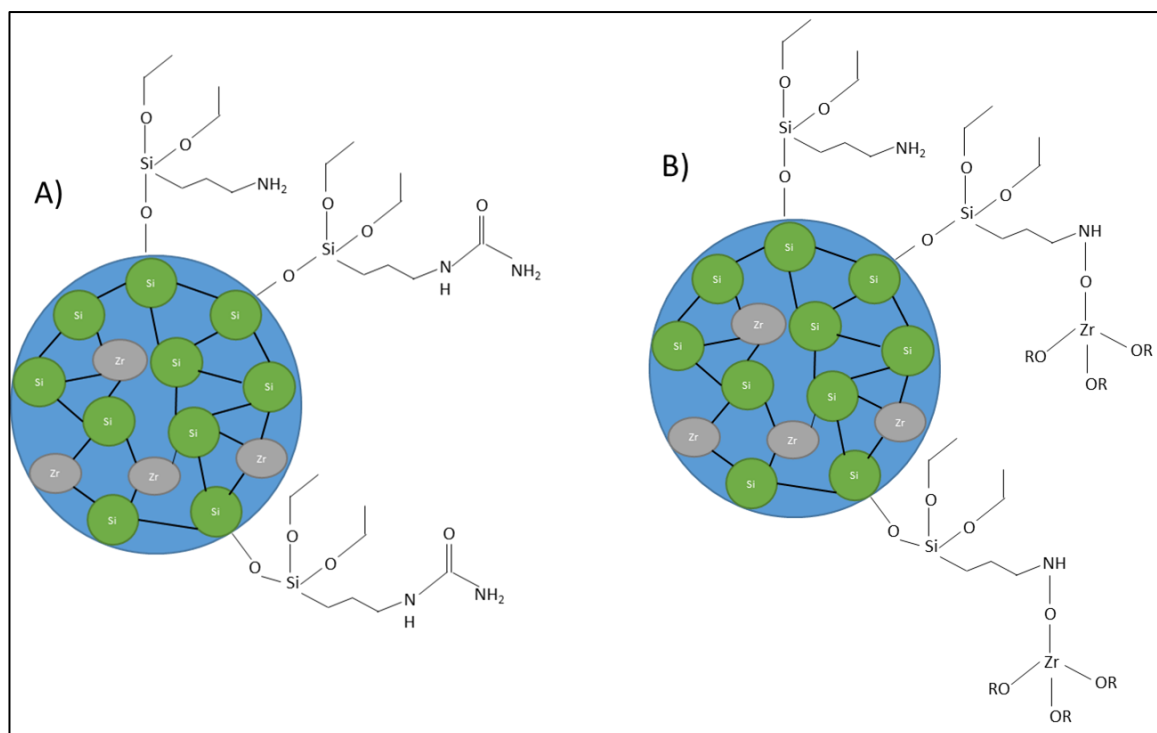
Figure 7. 8: Schematic representation of the possible reaction of APTES with inorganic species to form A) urea or B) transition metal complexes

7.3.3 FTIR

The FTIR spectra recorded for the reference material modified with the four functional silanes at concentrations of 1, 5, 10 and 20 % and cured at temperatures of 100, 130 and 150°C are displayed in Fig. 7.9. The analysis was focused on the $800 - 1250$ cm^{-1} spectral range in order to identify the effect of the materials formulations and curing process on the condensation of the materials so that correlation between the structure and the surface properties as well as the thermal properties may be made. It can be observed that all spectra exhibit the vibrations identified in the reference materials, namely Si-O-C (810 and 1170 cm^{-1}), Si-OH (840 cm^{-1}), Si-O-Si (880 and $1000 - 1100$ cm^{-1}) and Si-O-Zr (940 cm^{-1}). Although the large band located in the $1000 - 1100$ cm^{-1} spectral range represents the asymmetric siloxanes vibrations, in this region four superimposed bands can be distinguished at 1010, 1030, 1055 and 1090 cm^{-1}. Lerot and Low were the first to identify

these four bands in purely inorganic silicate materials[139]. In this reference, the band located at 1090 cm^{-1} was attributed to the stretching vibration of the Si-O-Si groups located at the interface between tetrahedral and octahedral units (called silicon apical oxide units), whereas the three other bands (1010, 1030 and 1055cm^{-1}) were assigned to stretching vibrations of siloxane bonds within symmetrical tetrahedral units, requiring less vibration energy than those located at 1090 cm^{-1}. Based on this reference study, in our work, the band located at 1090 cm^{-1} represents the formation of high energy siloxane bonds originating from the aggregation of nanostructures of different sizes and possibly different densities. The bands located at 1010, 1030 and 1055 cm^{-1} represent siloxane bonds within networks of lower connectivity. It is important to note that as the wavenumber of the vibration increases, the energy of the bond also increases symbolising a more connected network. Therefore, the band located at 1010 cm^{-1} would represent a siloxane network with a lower degree of connectivity than the band located at 1030 cm^{-1}, itself representing a network of a lower degree of connectivity than the band located at 1055 cm^{-1}.

It can be observed that at 100℃, apart from APTES, all other modifiers provoke the decrease of the Si-O-Zr bond along with the decrease of the high energy siloxane bond initially observed in the reference material at 1080 cm^{-1}. In addition, the intensity of the lowest energy siloxane bond is observed at the same intensity. This clearly means that the siloxane network is weakened as the content of 3 silane modifiers (GPTMS, VTES and TEOS) increase. As the content of silane modifiers increase, the content of Si-O-C bonds should also increase but interestingly the opposite effect is observed with a tendency towards a slight decrease of the vibration of these bonds. These results demonstrate that at 100℃, GPTMS, VTES and TEOS silanes are preferentially reacting with the residual Si-OH groups of the reference sol-gel material. Finally, as the silanes are effectively

reacting with the residual Si-OH groups and that the high energy siloxane bonds are decreased, this demonstrates that GPTMS, VTES and TEOS are definitely anchored at the surface of the nanoparticle, thus forming core-shell nanoparticles.

For APTES, unlike the three other functional silanes, the intensity of the Si-O-Zr bond increases along with a significant decrease of all siloxane bonds. This proves that APTES exhibits a greater affinity to Zr-OH groups than silanol groups. Transition metal oxides such as Zr-OH have much higher reactivity than Si-OH which is a considered a neutral nucleophile as shown by Schanez et al.[85]. The higher reactivity of transition metal oxides and alkoxides are due to their higher degree of unsaturation[85].

Again, as the siloxane network is weakened and that Si-O-Zr bonds are clearly increasing, the formation of core-shell nanoparticles is fully justified. However, one has tried to understand the difference in reactivity between the four functional silanes at 100℃. The main difference between these four functional silanes resides in the nature of the functional groups. APTES having a primary amine, whereas the three others containing an organic chain (epoxy, vinyl and ethoxy). For steric consideration, the formation of siloxane bonds is more favourable than the formation of Si-O-Zr bonds, as the zirconium atom is approximately three times bigger than the silicon atom. However, the opposite behaviour is observed with APTES, which strongly suggests that the amine group plays a critical role in the preferential formation of the Si-O-Zr bonds, probably via the formation of a strongly reactive intermediate, as proposed in the following scheme.
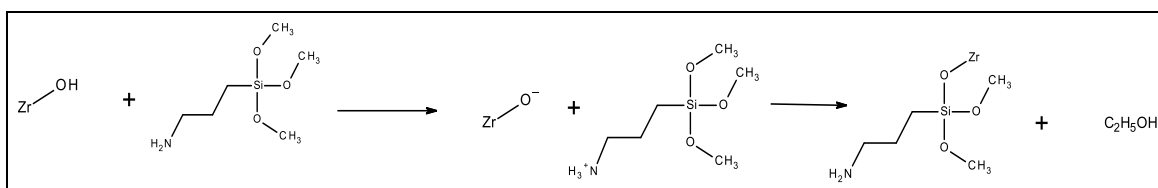
Scheme 7. 1: Reaction scheme of APTES with surface zirconium hydroxide groups

This proposed chemical reaction suggests that the amine maintains its initial functionality characterised by a strong hydrophilic character and only acts as a catalyst of the sol-gel condensation process. Aminosilanes have been shown to act as catalysts via the amine group which facilitate the formation of siloxane bonds[150]. This hypothesis is supported by the contact angle results shown in the previous section, where it was found that APTES maintains a hydrophilic character similar to GPTMS and VTES. ^{29}Si-NMR may give more insight into the reactivity of the materials and give a better indication of the FTIR results for the coatings cured at 100℃.

As the curing temperature increases, it can be observed that the high energy siloxane vibrations are increasing for all materials. This is due to the thermal activation of the condensation reactions of the residual un-hydrolysed alkoxide groups together. Interestingly, the reference material modified with GPTMS, VTES and TEOS show a complete disappearance of the Si-O-C bonds at a curing temperature of 150℃, suggesting their full condensation. However, APTES shows clearly the persistence of the Si-O-C bond even when cured at 150℃. This proves that APTES minimises the aggregation of the different particles together while maintaining a core-shell structure.
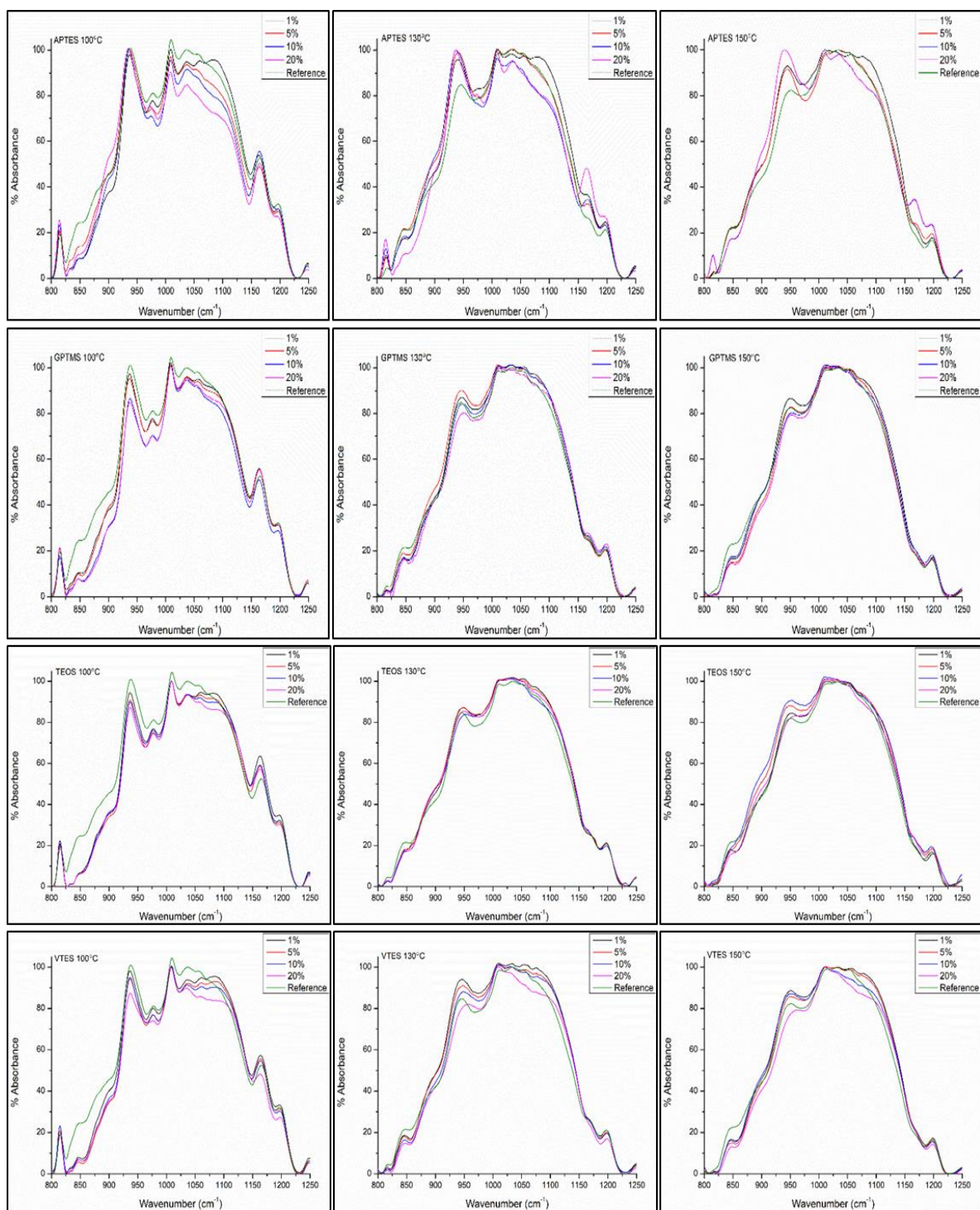
Figure 7. 9: FT-IR spectra of all silane functionalised materials

7.3.4 ^{29}Si-NMR

^{29}Si-NMR spectra were recorded for all the CSN materials from 1 to 20% silane concentration, 24 hours after synthesis and are shown below in Fig. 7.11. In order to characterise the reactivity of the functional silanes with the sol-gel nanoparticles, their ^{29}Si-NMR spectra were also recorded and are shown in Fig. 7.10.

A single sharp peak can be seen for each silane, translating to the high purity of the employed precursors. The peaks are located at -42.6, -82.3, -59.5, and 45.4, -42.4 ppm for MAPTMS, TEOS, VTES, APTES and GPTMS, respectively. These experimental results are in line with values found in the literature for MAPTMS[151], TEOS[115,152], GPTMS[153], APTES[154] and with the predicted results (MestReNova software) for VTES (-59.29 ppm), These chemical shift values represent the T_0 configuration for each precursor material (with the exception of TEOS, Q_0), and indicates that each material is un-hydrolysed and does not contain any bridging Si-O-Si groups within the organosilane. As TEOS contains 4 alkoxy groups, the notation used changes from T which represents a Si atom bound to 3 oxygen atom sand an organic group, to Q, which represents a Si atom that is bonded to 4 oxygen atoms to form a tetrahedron[155]. Similar to T notation, the subscript n represents the number of connected Si-O-Si units. The chemical shift ranges for TEOS can be seen in Table 7. 3.

The large upfield shift for VTES (-59.50 ppm), in comparison to APTES and GPTMS which both contain 3 alkoxy groups, may be attributed to the increase in electronegativity of the vinyl group. In comparison to the rest of the silane precursors TEOS shows the greatest upfield shift at -82.2 ppm. This has been attributed to the fact that TEOS contains 4 hydrolysable alkoxy groups. The relative concentration of T species within each material has been plotted against the concentration of the silane modifiers and are presented in Fig. 7.12.

As shown in Fig. 4.8, the reference sol-gel material itself does not contain any residual T_0 species and only 2.4% of T_1 species after 24 hours of ageing, thus any T_0 signals present in the ^{29}Si-NMR spectra (Fig. 7.11) can only be attributed to the individual silane precursors added to the sol-gel matrix and not to the original MAPTMS precursor.

APTES modification – For the materials modified with APTES, the signal of the pure precursor (-45.4 ppm) is absent for all concentrations, suggesting the interaction or reaction of the APTES with the sol-gel material. At concentrations of 1 and 5%, two singlet peaks located -45.9 and -47.0 ppm can observed. These signals, which are located at higher chemical shifts than that of the precursor, indicate that the electronic environment of the silicon is increased. According to references in the field[156–158], the chemical shift located at -47.0 ppm is attributed to T_1 species. The peak located at -45.85 can be attributed to T_0 species where the silicon is an obstructed environment, explaining its increased chemical shift in comparison with the pure precursor. A possible explanation for this could be due to the saturation of the surface of the reference sol-gel nanoparticles by APTES molecules, leading to unbound but closely entrapped molecules, as sketched in Fig. 7.13. At a concentration of 10 %, an additional signal is observed at – 44.6 ppm, which is located at a lower chemical shift than the pure APTES precursor (-45.4 ppm). This suggests that the electronic environment of the silicon atom has decreased and that this signal can only be attributed to T_0 species in a less obstructed environment probably associated to the substitution of an ethoxy group by a hydroxyl group (Si-OH).

At a concentration of 20%, an additional signal is observed at -43.4 ppm and the duplication of the chemical shift at -44.6 ppm into two doublets, further confirms the deshielding effect observed for the 5% sample. Therefore, the additional signal at -44.6 ppm is attributed to the T_0 species with two silanol groups $Si(OH)_2$, while the signal at -43.4 ppm would translate the formation of T_0 species with three silanol groups $Si(OH)_3$.

In conclusion, APTES is effectively covalently bound to the surface of the reference sol-gel nanoparticle and a 1% APTES concentration fully saturates the surface of the nanoparticles of the reference sol-gel material. Further addition of APTES provokes the formation of free hydrolysed APTES molecules.

GPTMS modification – The signal of the pure GPTMS precursor is absent in all spectra, suggesting its interaction or reaction with the sol-gel matrix. The main difference with the NMR spectrum of the sol-gel matrix is the appearance of T_1 species (between -50 and -52 ppm) and their growth (2, 4, 9 and 19%) as the GPTMS content increases (1, 5, 10 and 20%). This demonstrates that the GPTMS is fully bound to the surface of the sol-gel matrix. However, it is worthy to note that for the highest concentration of GPTMS, T_0 species appear at -41.9, -43.2 and - 44.9 ppm, suggesting the presence of free GPTMS molecules in a less obstructed environment. Again, similarly to the APTES, the explanation to this phenomenon is the hydrolysis at different degrees $Si(OH)_1$, $Si(OH)_2$, $Si(OH)_3$. These results prove that the GPTMS can be fully bound for concentration of up to 10% and the additional GPTMS molecules are present as free hydrolysed molecules within the overall system. Furthermore, it is important to note that in comparison with APTES, GPTMS has the ability to link with the sol-gel matrix from a concentration of 10%, whereas with the APTES it was seen that at a concentration of 1%, free APTES was detected. This clearly indicates that the APTES would form an electron rich shell around the sol-gel matrix, thanks to the free pair of electrons on the nitrogen group, thus provoking electronic repulsion of additional APTES molecules leaving them as free and unreacted hydrolysed molecules.

VTES modification – The introduction of VTES into the sol-gel matrix regardless of its concentration showed the appearance of a peak located at -60 ppm, related to the T_0 species of the VTES precursor. Because the condensed species of the VTES overlap with

the T_3 band of the sol-gel, they cannot be distinguished at low concentrations. However, for the 10 and 20%, the T_1, T_2 and T_3 of the VTES can be easily observed at – 64.2, -65.6 and -67 ppm, respectively, suggesting that the condensation with the sol-gel matrix has taken place. Therefore, the functionalisation of the surface of the reference matrix is effective.

TEOS modification – Similarly to GPTMS, Q_o signals are present at a concentration of 3.5 % for the highest concentration of TEOS. 4 signals are present at -78.61, -79.50, -80.41 and -81.33 ppm. These signals correspond to various hydrolysed species of TEOS that do not contain any bridging Si-O-Si groups and have been well reported in the literature[152,159]. Importantly, Q_1, Q_2 and Q_3 species are also present at concentrations of 3.4, 2.3 and 0.4%, the corresponding chemical shift ranges can be seen in Table 7.3. These species correspond to mono, di and tri substituted bridging Si-O groups[160], suggesting the binding of TEOS with the reference sol-gel nanoparticles.

These results indicate that the silanes are indeed bound both within the material, with such binding enabling the formation of core-shell nanoparticles, thus confirming our initial hypothesis on the formation of surface functionalised nanoparticles.

Structure	Chemical Shift Range (ppm)	Notation
$RSi(OR)_3$	-40 to -48	T_0
$RSi(OH)_2OSi$	-49 to -55	T_1
$RSi(OH)(OSi)_2$	-56 to -63	T_2
$RSi(OSi)_3$	-64 to -73	T_3

Table 7. 3: Chemical shift range, notation and structure of different chemical species in ^{29}Si-NMR

Structure	Chemical Shift Range (ppm)	Notation
$Si(OR)_4$	-72 to -82	Q_0
$Si(OH)_3OSi$	-82 to -89	Q_1
$Si(OH)_2(OSiR)_2$	-91 to -97	Q_2
$SiOH(OSiR)_3$	-100-104	Q_3
$Si(OSiR)_4$	-109 to -111	Q_4

Table 7. 4: Chemical shift range, notation and structure of different chemical species for TEOS
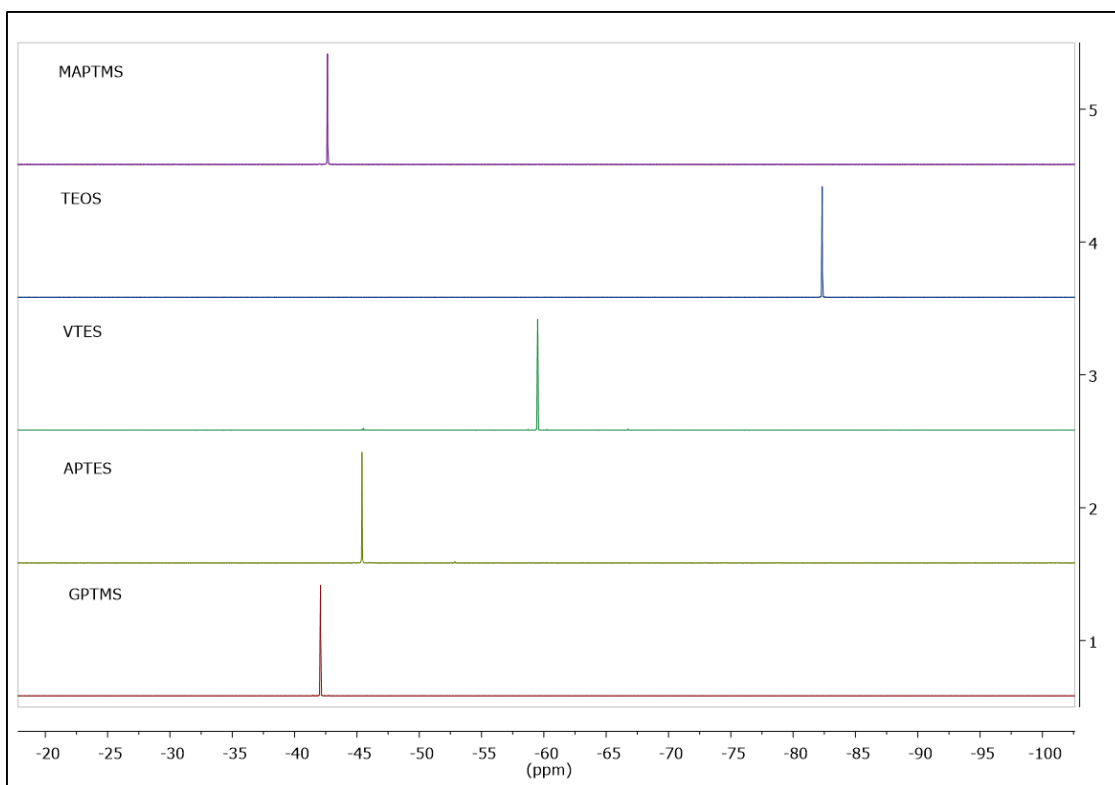
Figure 7. 10: ^{29} Si-NMR spectra of pure silane precursors
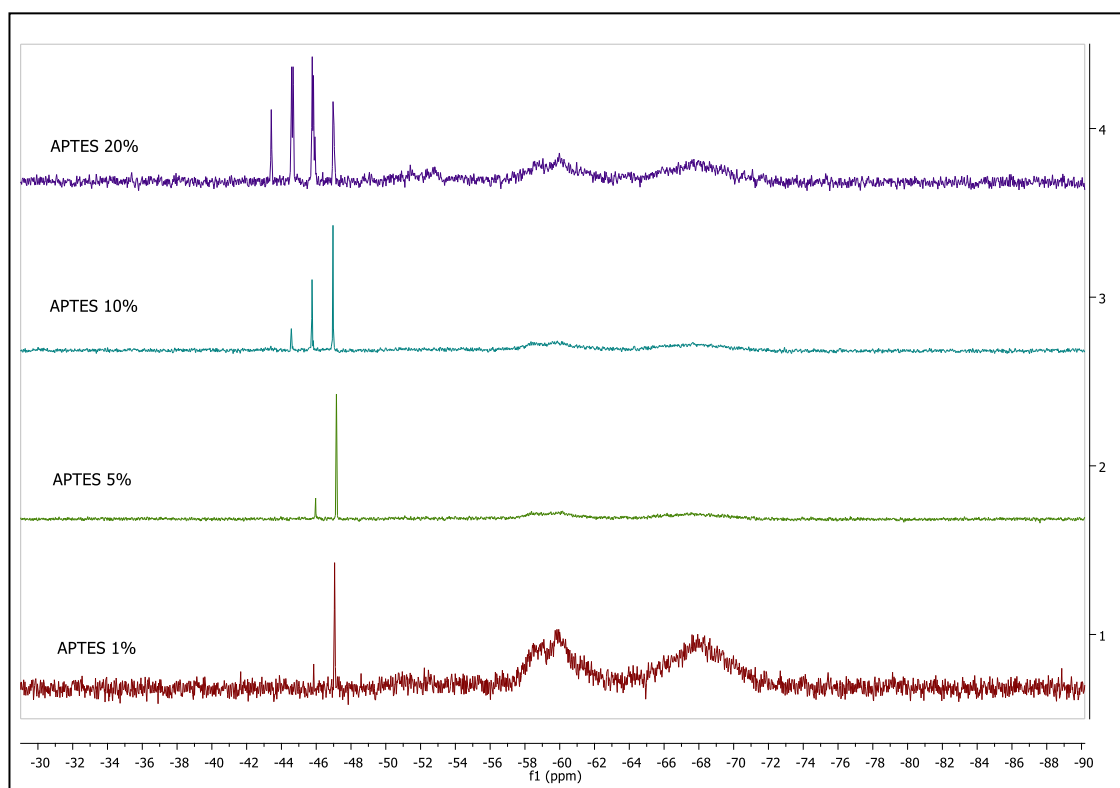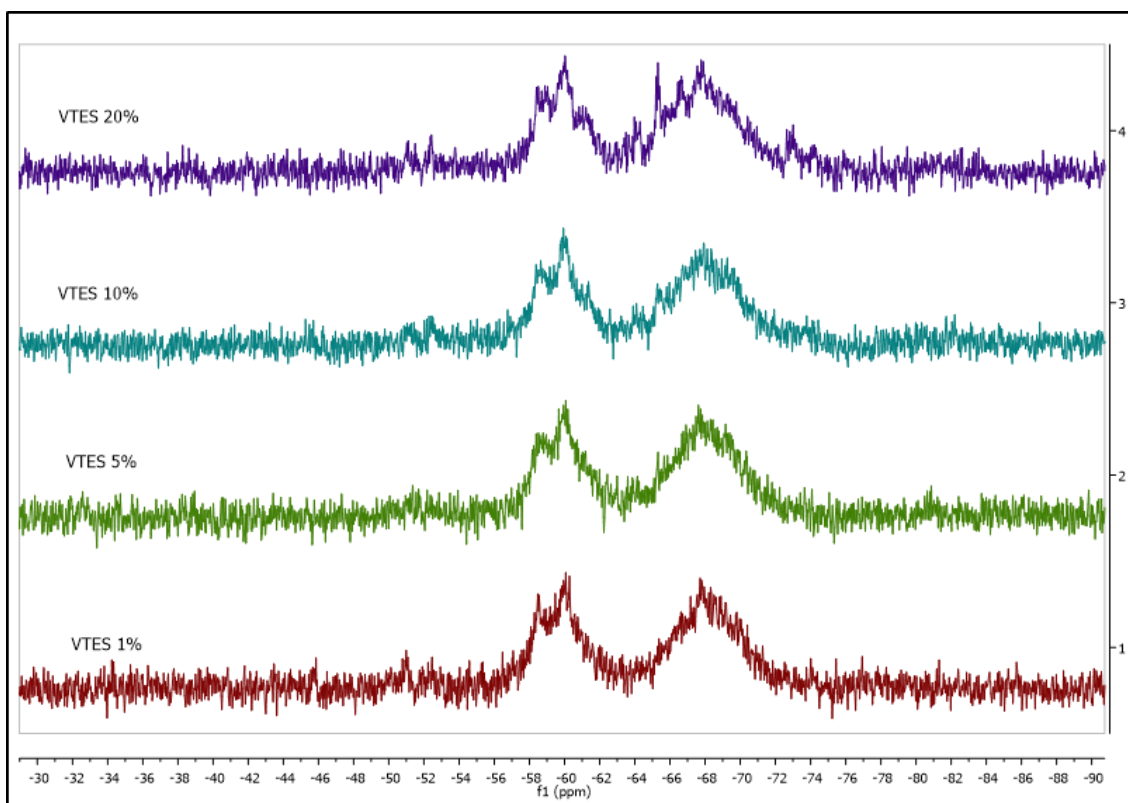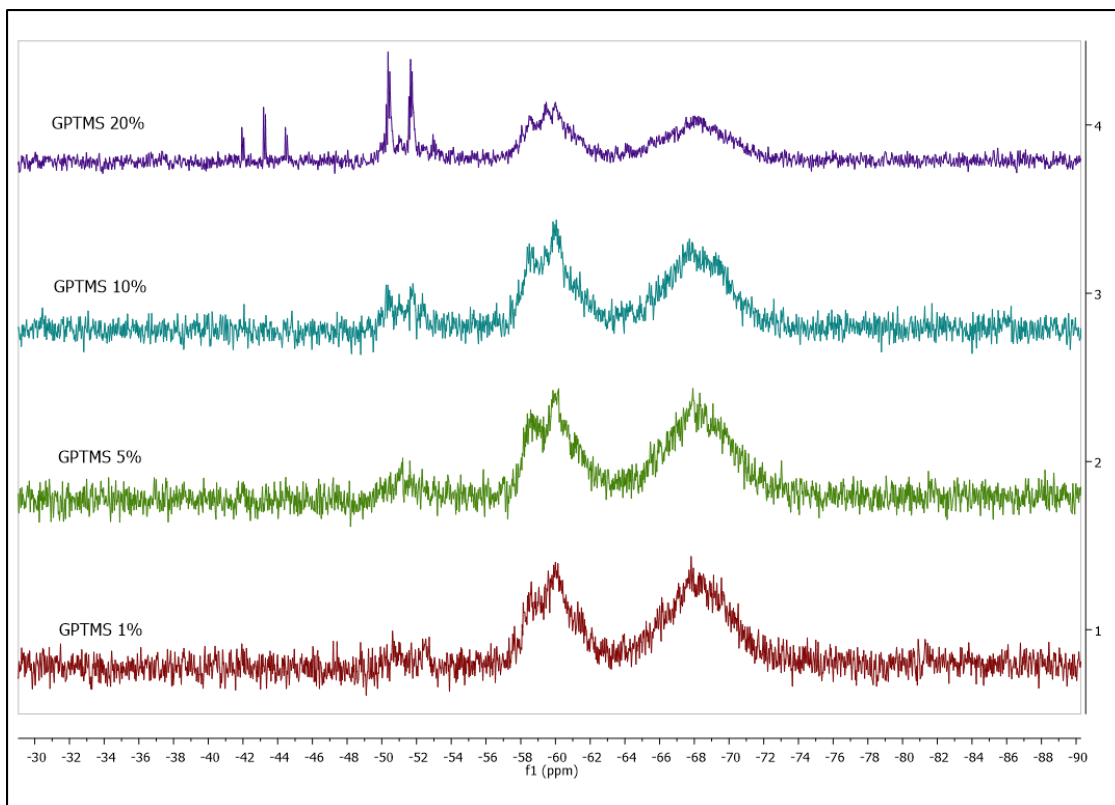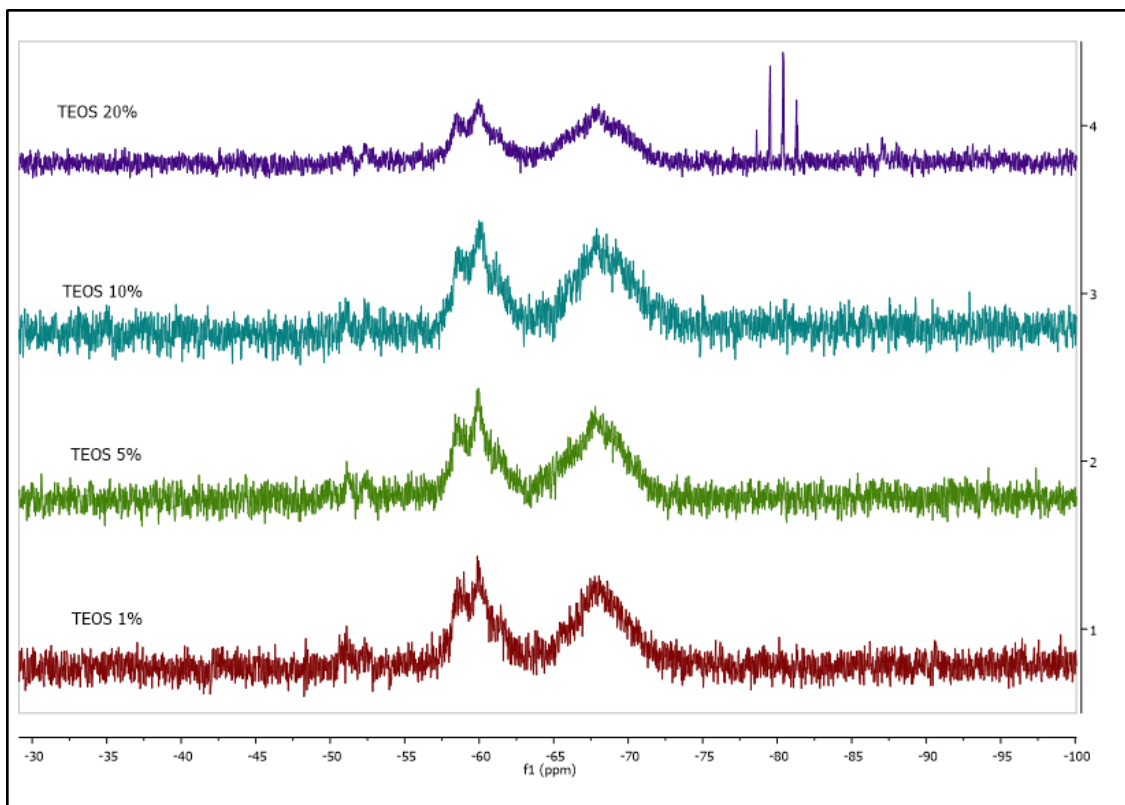
Figure 7. 11: [29] Si-NMR spectra for all CSN materials
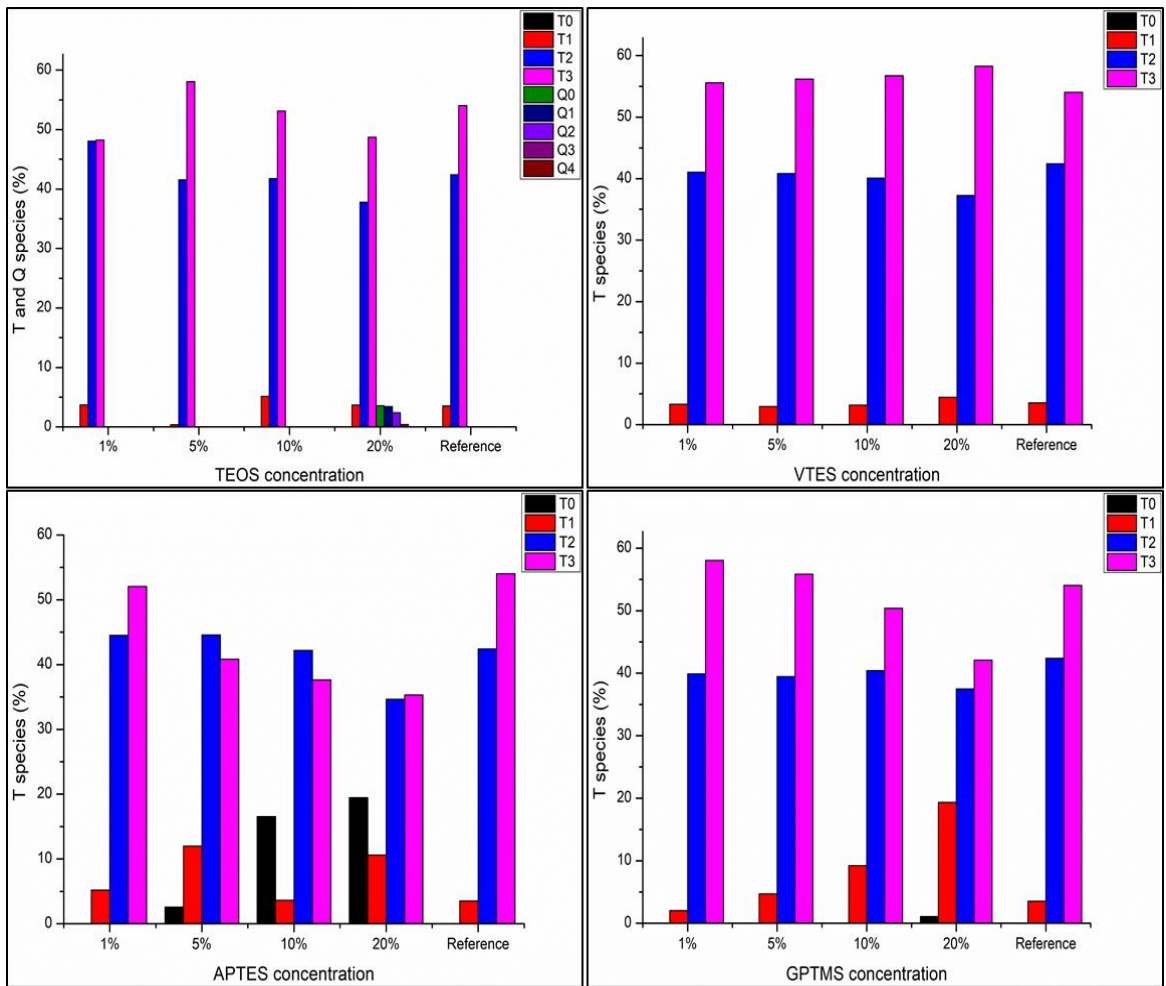
Figure 7. 12: T species concentration for all materials
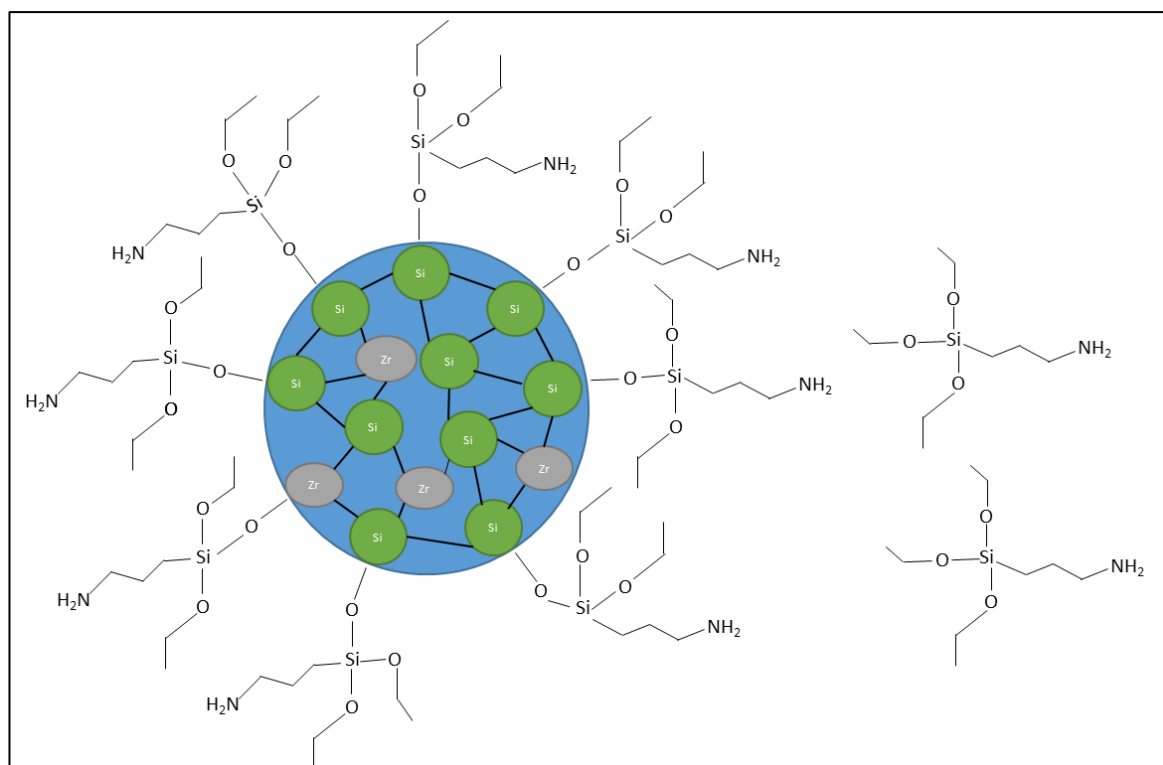
Figure 7. 13: Schematic representation of saturated reference sol-gel nanoparticle surrounded by unbound APTES

7.3.4 Thermal Analysis

The thermal behaviour of the core shell nanoparticle materials for 1, 5, 10 and 20% concentration of functional alkoxysilane are represented below in Fig. 7.14. The analysis was performed from $25 - 300°C$ on the sols, although the working temperature would likely be below 150°C. For each spectrum, three distinct thermal zones can be identified, between $25 - 70°C$, between $100 - 160°C$ and above 170°C. For all materials the large endothermic peak between $25 - 70°C$ can be attributed to the evaporation of the volatile solvents that are entrapped within the sol-gel network or are present in the precursor materials. It can be observed that for the material functionalised with APTES, there is a progressive shift towards higher temperatures for this band from $41 - 55°C$, as the concentration increases from $1 - 20\%$. For the materials functionalised with GPTMS and

190

TEOS a similar behaviour can be observed up to 5% and 10 % silane concentration for the materials functionalised with TEOS and GPTMS, respectively. For the material functionalised with GPTMS there is a decrease of 4℃ from 10 – 20% silane concentration. For VTES, there is a progressive decrease in temperature from 1 – 10% silane concentration and then an increase of 5° from 10-20% concentration. This behaviour may be explained by the increase of volatile solvents with the increase in concentration of functional silane. The exothermic peak above 170℃, which is the glass transition temperature (Tg) or the full solidification point of the network, can be seen to shift towards lower temperatures up to 5% and 10% silane concentration for the materials functionalised with APTES and VTES, respectively. A shift towards higher temperatures can also be observed up to concentrations of 20% for both these materials giving a final Tg of 196 and 197℃ at 20% silane concentration respectively. The opposite behaviour can be observed for GPTMS from 1 – 5% and from 5-20% silane concentration. For the material functionalised with TEOS there is no change in the Tg temperature from 1-5% silane concentration, with an increase from 10 – 20%.
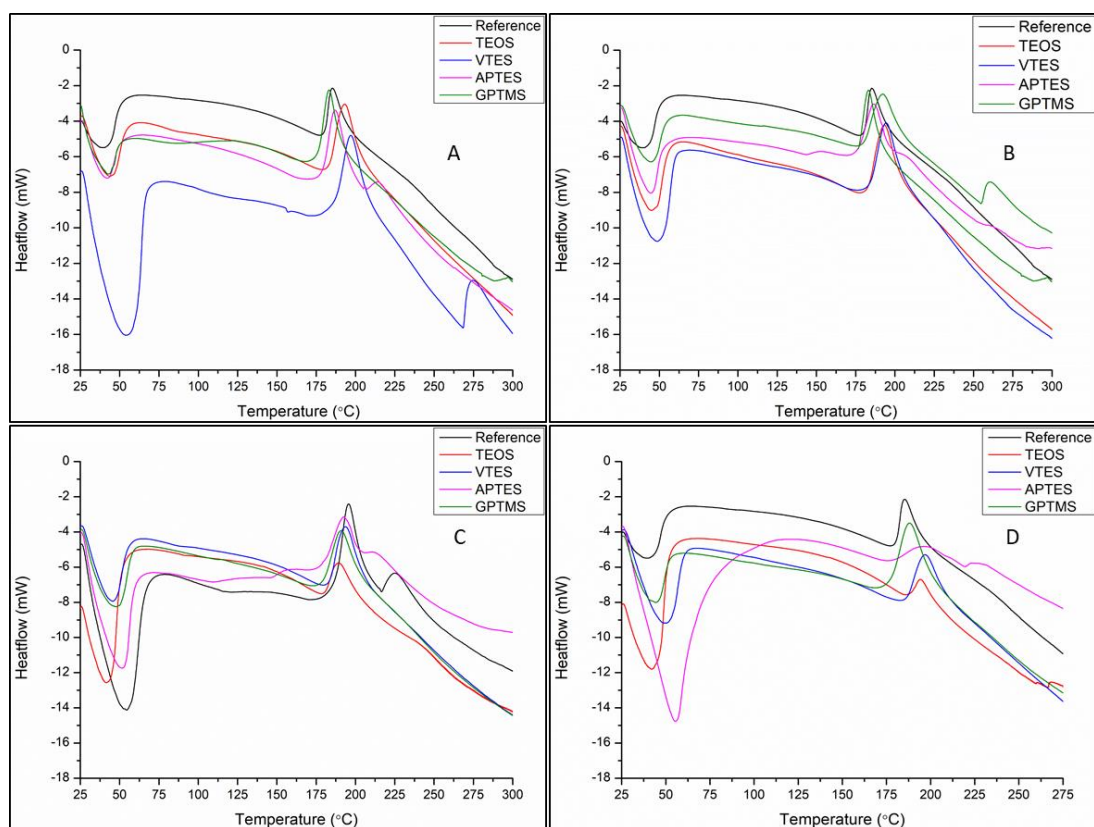
Figure 7. 14 : DSC spectra of materials at A) 1%, B) 5%, C), 10% and D) 20% silane concentration

7.4 Conclusion

The focus of this chapter was the incorporation of functional alkoxysilanes onto the surface of sol-gel nanoparticles as a route to the fabrication of core-shell nanoparticles. Four functional alkoxysilanes namely APTES, GPTMS, TEOS, and VTES were employed based on their different functional groups. The materials were then characterised using DLS, DSC, FTIR, ^{29}Si-NMR and CA measurements. The particle size analysis for all materials shows that the fabrication of core-shell nanoparticles does not provoke agglomeration 24 hours after fabrication of the materials. The ^{29}Si-NMR found that core-shell nanoparticles were indeed formed by the presence of T_0 species for the materials modified with APTES, GPTMS and VTES. Depending on the employed functional silane and its concentration, the CA values are seen to vary differently with the

curing temperature. The proposed mechanism of the variation of the CA values is associated to the reactivity of the functional silanes, primarily with the reference sol-gel matrix. Indeed, ^{29}Si-NMR results showed that APTES can form an effective electron-rich shell around the sol-gel matrix at a concentration of 1%, while the increase of the APTES concentration produces free hydrolysed APTES molecules that can decrease the hydrophilic properties of the coatings, with the greatest decrease in the CA (~20°). GPTMS, VTES and TEOS form shells around the reference matrix but with decreased hydrophilic properties, thus explaining the higher contact angle values recorded. TEOS seems to form richer siloxane shell nanoparticles that contribute to the increase of the CA values.

This chapter highlighted that it is indeed possible to fabricate core-shell nanoparticles via the incorporation of functional alkoxysilanes at the surface of the sol-gel nanoparticles, which can enable to significantly alter the structure and surface properties of the coatings. The next chapter will focus on investigating both physical and chemical strategies to improve the wettability of the sol-gel coatings, and to investigate the surface stability of the methods used.

8 Surface Treatment of the Reference Material

8.1 Introduction

The previous 4 chapters have investigated purely chemical routes to modify the surface properties of the sol-gel coatings. This chapter will focus on a combination of a physical (low pressure plasma treatment) and chemical (surface treatment) routes, to modify the surface properties of the sol-gel material with the aim of increasing the overall wettability of the coatings and improve their stability over time. Plasma is a gaseous state of matter that exists as electrons or ions. It can be described as a fully or partially ionised gas[161].

Plasma treatments can be classified as physical surface modification techniques. Reactive gas plasmas, such as air, O_2, Ar, N_2, NH_2 can be used to modify the surface of a material, which can lead to chemical changes of the surface of a material. One of the major advantages of using plasma treatments as a surface modification is that the surface of the materials are uniformly modified by the plasma and this modification does not affect the bulk material as it is limited to the first few nm of the coating[162].

The surface of the coatings will also be modified via a chemical modification. This will involve dipping the plasma treated samples into dilute silane washes of varying concentrations from 0.5% to 5% of APTES and GPTMS and a mixture of both silanes. The stability of the coatings over time will then be investigated using CA measurements to assess any hydrophobic recovery of the surface of the coatings. Hydrophobic recovery is the phenomenon by which a plasma activated surface will revert back to its original surface condition over time, which can be observed by the increase in CA over time[163,164]. The mechanism for the observed hydrophobic recovery of plasma treated surfaces may be due to the reorientation of the molecules on the surface of the coating[165]. The stability of the coatings will also be followed by FTIR. XPS analysis will be carried out to

investigate whether the silane washes have effectively modified the surface of the sol-gel coatings.

8.2 Materials Preparation

The reference sol-gel material was synthesised as in chapter 4.2 and coated onto aluminium substrates via dip-coating at a speed of 50 mm/min. These coatings were then cured in an oven at 130°C for 1 hour. Here, the surface treatments methodology consisted of the following processes which were applied individually or in combination:

1. N_2 Plasma treatment for 2 minutes
2. Air-plasma treatment for 2 minutes
3. Silane wash of varying concentrations and formulations (Table 8.1)

APTES and GPTMS have been selected as the silanes of choice for surface modification thanks to their amino and epoxy functionalities, respectively. Indeed, amino and epoxy functionalities are well-known as adhesion promoters in a number of industries including the paint industry where they are commonly employed as additives for surface adhesion. As our objective is to alter the surface of the coatings, ideally in the first few nm only, the silanes have to show a high reactivity to the surface while maintaining their surface functionality available for the wettability. In other words, the silane has to be fully hydrolysed and the organic functionality made available only at the surface of the coating, as sketched in Fig. 8.1. An important condition to optimise the effect of the surface modification is to minimise the gaps between the silanes at the surface of the coatings. Therefore, to try to meet these requirements, the following preparation conditions have been established:

<u>Over hydrolysis of the silane</u> – Here the silanes are largely over-hydrolysed with rates comprised between 1000% (for the 5% silane concentration) and 10000% (for the 0.5% silane concentration)

<u>Variation of the silane concentration</u> – The variation of the silane concentration will enable the alteration of the coating thickness and investigate this parameter for both the surface connectivity of the silanes and the surface treatment thickness.

<u>Dilution</u> – A dilution of 90% employing a non-reactive solvent (IPA) is employed to avoid the condensation step and maintain the reactive hydrolysed species, which can further polycondense with the sol-gel surface.

Employing these conditions, homogenous and clear solutions were obtained for all silane concentrations, which could be used to fabricate almost invisible surface treatments.
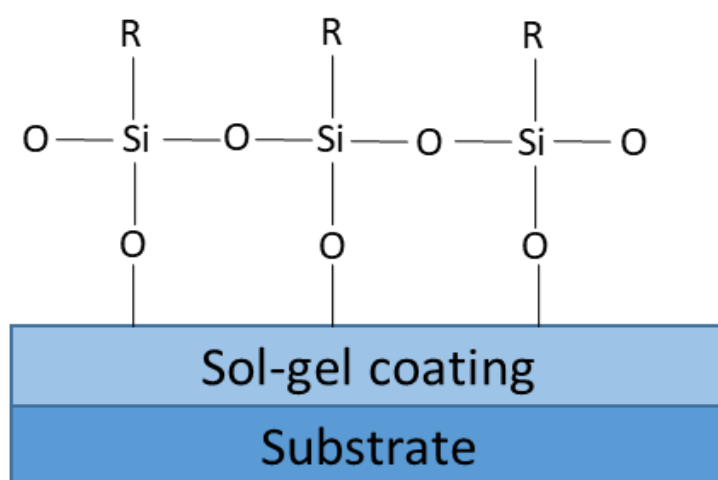
Figure 8. 1: Representation of a sol-gel surface modified with a functional silane

The samples were left to stand in the washes for 1 minute before being removed at a dip speed of 100 mm/min. The samples were then cured in an oven at 100°C for 1 hour to remove the liquid phase of the wash (water and IPA) and achieve touch-dry surfaces. For each batch of samples, a control sample (reference sol-gel) was also prepared. The control

samples were not subjected to the silane wash surface treatment, but all other parameters were kept the same. This was to investigate the effect of the plasma treatment on the stability of the bare reference sol-gel. The volumes used for each wash are represented in table 8.2. All washes were prepared in 100 ml plastic beakers.

The wettability of the coatings was investigated via CA measurements and their stability was investigated over a 4-week period. The structure of the coatings was investigated using FTIR and XPS analyses. The plasma parameters can be seen in table 8.2. A Henniker plasma chamber was used for this study (Fig. 8.2).

Silane concentration	IPA	Water
0.5% APTES	90% v/v	10% v/v
1% APTES	90% v/v	10% v/v
2.5% APTES	90% v/v	10% v/v
5% APTES	90% v/v	10% v/v
0.5 % GPTMS	90% v/v	10% v/v
1% GPTMS	90% v/v	10% v/v
2.5% GPTMS	90% v/v	10% v/v
5% GPTMS	90% v/v	10% v/v
0.5% GPTMS/APTES	90% v/v	10% v/v
1% GPTMS/APTES	90% v/v	10% v/v
2.5% GPTMS/APTES	90% v/v	10% v/v
5% GPTMS/APTES	90% v/v	10% v/v

Table 8. 1: Silane Wash composition

Silane Concentration	Silane Volume (ml)	IPA Volume (ml)	Water Volume (ml)
0.5% APTES	0.42	91.14	7.96
1% APTES	0.84	90.68	7.92
2.5% APTES	2.11	89.32	7.80
5% APTES	4.22	87.02	7.60
0.5% GPTMS	0.37	91.14	7.96
1% GPTMS	0.74	90.68	7.92
2.5% GPTMS	1.86	89.32	7.80
5% GPTMS	3.75	87.02	7.60
0.5% GPTMS/APTES	0.18/0.21	91.14	7.96
1% GPTMS/APTES	0.37/0.42	90.68	7.92
2.5% GPTMS/APTES	0.93/1.057	89.32	7.80
5% GPTMS/APTES	1.86/2.11	87.02	7.60

Table 8. 2: Volumes used to synthesis dilute silane washes

Gas Used	N_2, Air
Flow rate	9 standard cubic centimetres (sccm)
Pressure	0.55-0.60 mbar
Power	100%
Time	2 minutes

Table 8. 3: Henniker Plasma Parameters

Figure 8. 2: Henniker Plasma Chamber

8.3 Results and Discussion

8.3.1 CA Measurements

For clarity, this section will be broken down into two main sections. Firstly, the individual effects of the plasma surface treatments will be presented for the reference sol-gel only. Secondly, the dual effects of the plasma and silane washes will follow.

8.3.1.1 Effect of the plasma surface treatments

The effect of the plasma treatment and subsequent surface treatment on the wettability of the sol-gel coatings and their stability over time was investigated using CA measurements, and the recorded values presented in Fig. 8.3.

The CA values for the untreated sol-gel samples are situated around 59° prior to any treatment. Directly after plasma treatment on day 0, the CA values have decreased to 43 and 36° for the samples plasma treated with N_2 and Air-plasma, respectively.

There is a progressive hydrophobic recovery for both plasma treated samples with the CA values stabilising after day 21 for both samples and a CA increase of about 10º for the

199

untreated coating. The samples treated with Air-plasma remain the most hydrophilic samples and the most stable with an average CA of 54° after 21 days. The N_2 treated samples have a CA value of 60° after 21 days stable within the measurement error after 28 days. The untreated samples are the most hydrophobic of all 3 samples with an average CA value of 69° after day which stabilises within the measurement error after 28 days. In summary, over the 4-weeks CA monitoring, the air-plasma provides a 6° CA decrease, the N_2 has a negligible effect and the untreated coating shows an increase of the hydrophobic properties by about 10°. This could be explained by the fact that air-plasma would enable the formation of a hydrophilic oxygen rich surface, probably partly leading to the formation of stable hydrophilic OH groups on the reactive sol-gel centres (Si and Zr). Both N_2 plasma and air plasma will alter the surface of the coatings and will introduce polar functional groups to the surface the coatings[166]. For the samples treated with N_2 plasma it is likely that -O-C-N bonds have been introduced to the surface of the coatings which would increase its hydrophilicity[167]. For the samples treated with Air plasma it is likely that surface hydroxyl groups have been introduced at the surface of the coatings. XPS may be able to corroborate the increase in the hydrophilic nature of the surface coatings. The N_2 plasma treatment does not seem to enable the formation of stable hydrophilic functional nitrogen groups (such as amino groups) but more to the formation of rich N_2 layer, which tends to disappear over time. Surprisingly, the increase of the CA value with the untreated coating suggests that initial hydrophilic species located at the coating surface tend to transform into hydrophobic species, the most likely reason would be the polycondensation of the residual hydroxyl Si-OH and Zr-OH into hydrophobic Si-O-Si and Si-O-Zr groups.

8.3.1.2 Effect of the dual plasma surface treatments and silane functionalisation

The stability of the CA values over time has been plotted for each dual plasma treatment along with each individual silane wash at a given concentration and have been plotted in Fig. 8. 4-7.

The CA values for the lowest concentration of each silane wash (0.5%) can be seen in Fig. 8.4 as a function of the 3 different surface treatments. The average CA value for the bare coatings are situated between 57-61°, with same values as recorded in the previous section. For each silane wash- APTES, GPTMS and APTES/GPTMS the coatings treated with air-plasma give the most hydrophilic values directly after both treatments on Day 0 to give CA values of 42.5, 42.3 and 49.1°, respectively. Similarly, to the individual treatment, each coating undergoes a hydrophobic recovery regardless of surface treatment or silane wash.

For the samples treated with 0.5% GPTMS it can be noted that directly after plasma treatment the CA values decrease steadily from the silane only to the air treated samples. This trend can be seen throughout the entire 4-week period with the exception of day 7, the hydrophobic recovery of the N_2 plasma treated samples overtakes the silane sample. This trend can be seen for each concentration of the GPTMS wash.

Looking at the samples treated with 0.5% APTES and APTES/GPTMS, the opposite trend can be seen from day 1 onwards. The hydrophobic recovery increases from the silane only treated samples to the air treated samples up to day 21 for the 0.5% APTES samples and up to day 7 for the 0.5% APTES/GPTMS samples, the samples treated with N_2 plasma overtake both the silane and air treated samples from day 14 onwards. The N_2 samples stabilise after day 14 and the Air samples have stabilised after day 21.

The CA values for the 1 and 2.5% concentrations of the silane washes can be seen in Fig. 8.5 and 8.6, respectively. Again, a hydrophobic recovery for all the samples can be seen

over time regardless of the silane concentration or the pre-treatment used. For both concentrations the samples pre-treated with air-plasma have the most hydrophilic coatings directly after both surface treatments. The CA values are situated at 38.9, 44.4, and 50.3° for the 1% APTES, GPTMS/APTES and GPTMS samples and at 35.6, 47.1 and 50.5° for the 2.5% APTES, GPTMS/APTES and GPTMS samples respectively at day 0 for the air pre-treated samples. The 1 and 2.5% APTES samples show the highest hydrophobic recovery at day 28 regardless of the pre-treatment, with CA values of 76.6, 76.5 and 75.1° at 1% concentration for the reference sol-gel only air plasma and the N2 plasma treated samples respectively. For the 2.5% APTES concentration the CA values are 79.2, 73.3 and 75.0° for the reference sol-gel only, air plasma and N_2 plasma treated samples respectively.

The average CA values for the 5% concentration of washes can be seen in Fig 8.7. Similar to the previous results the samples pre-treated with air-plasma for both the APTES and GPTMS washes show the greatest decrease in their CA values directly after both surface treatments on day 0 with subsequent hydrophobic recovery over the course of the 28-day period. For the 5% GPTMS/APTES wash, the sample pre-treated with N_2 gave the most hydrophilic value of 52.7° at day 0. The CA values for the air pre-treated samples for APTES and GPTMS were 35.4 and 47.5°, respectively. It can be seen from these results that there is very little variation between the CA values for the 2.5 and 5% silane wash concentrations across the pre-treatments. It can also be seen that the samples treated with the APTES washes show the most hydrophobic CA values regardless of the pre-treatment at day 0. This indicates that the APTES silane wash is the most reactive wash and subsequently undergoes the largest hydrophobic recovery of all the samples after day 28.

In summary, the dual plasma and silane functionalisation enables the following conclusions:

The dual air-plasma / epoxy functionalisation enabled a significant decrease of 15° in comparison with the untreated sol-gel coating. This treatment provides the same effect as the air-plasma treatment only, suggesting that main effect is provided by the air-plasma. The epoxy functionality is more efficient in providing lower CA values than the amino functionality. This may be due to the possible higher reactivity of the amino groups with the sol-gel surface, with a possible reduction of its hydrophilic character. Nevertheless, The air-plasma treatment is more efficient than N_2 plasma to provide lower CA values and more stable hydrophilic properties. This is likely due to the formation of reactive hydroxyl groups that can covalently bind to the silanes and orientate the organic groups at the upper surface of the coating (as sketched in Fig. 8.1 above).
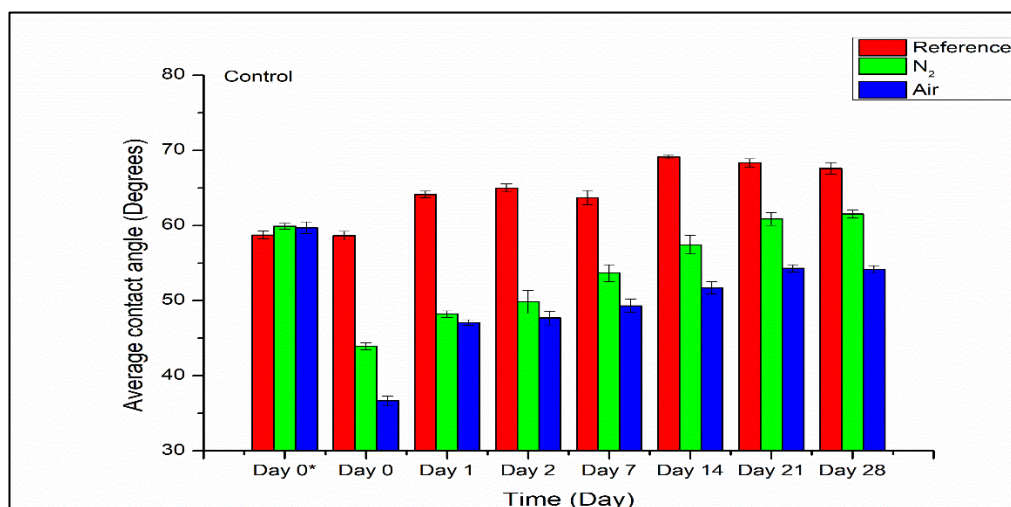
Figure 8. 3: CA measurements for the control samples for the N_2 and air-plasma and silane only treated samples (n=2)
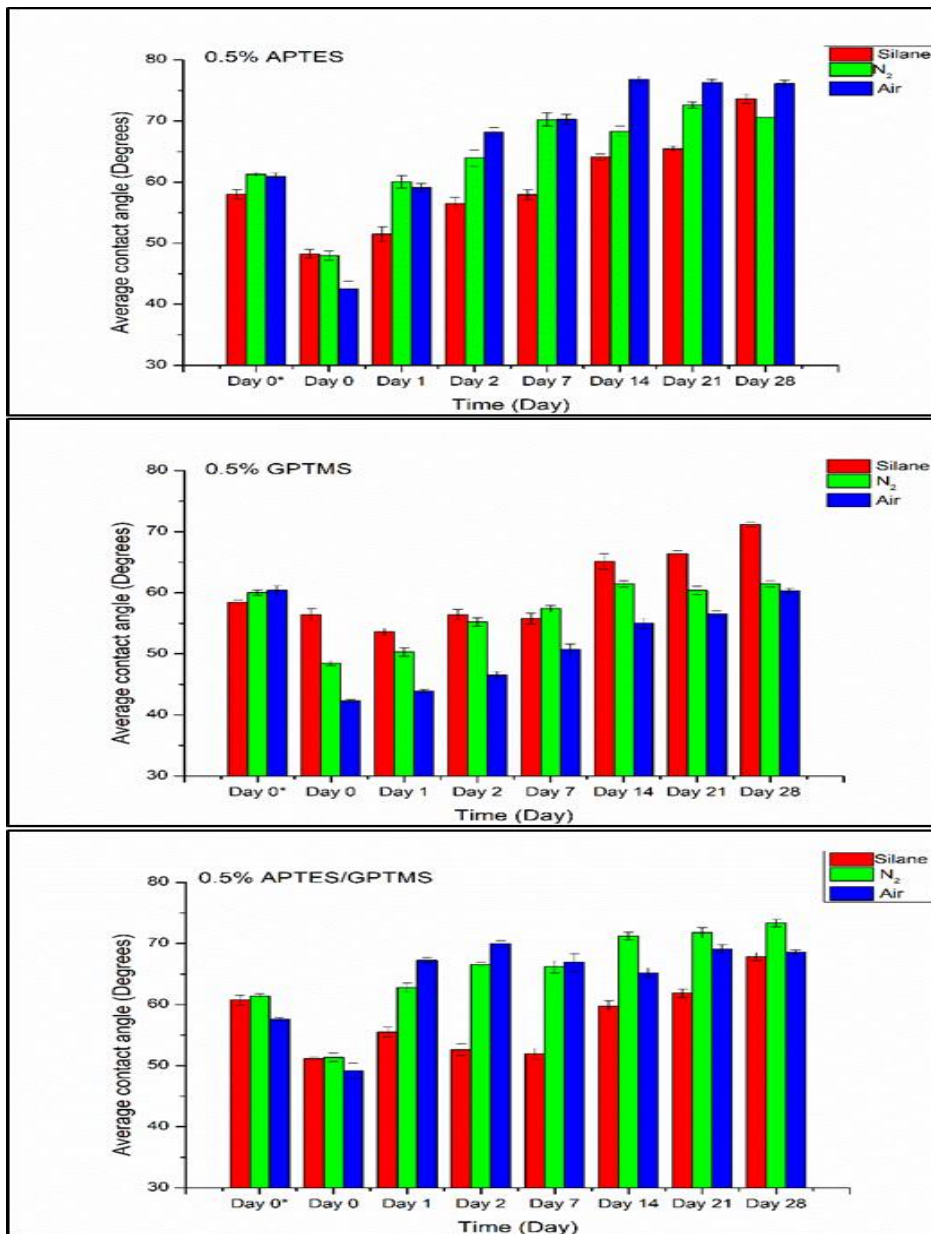
Figure 8. 4: CA measurements for treated samples with 0.5% APTES, GPTMS and APTES/GPTMS silane washes
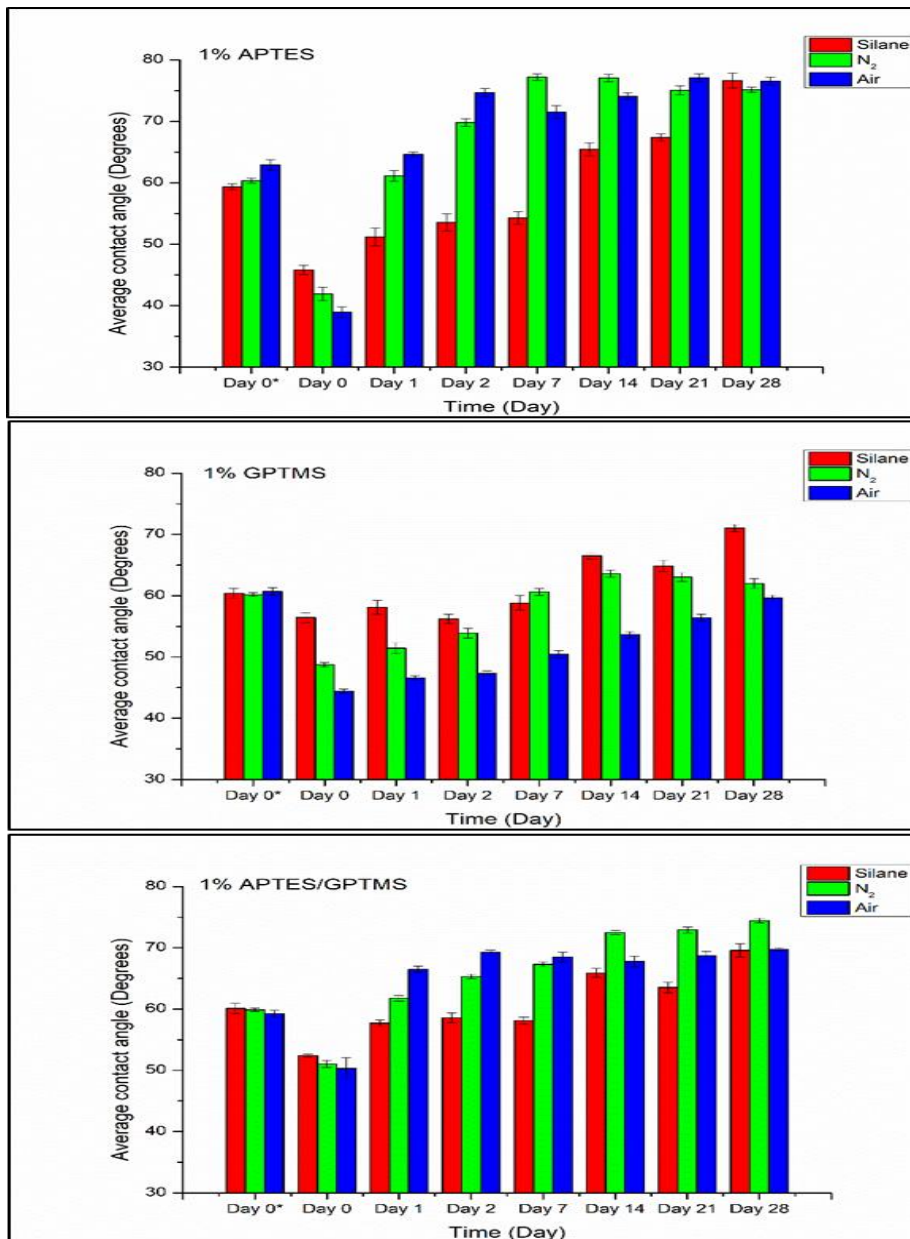
Figure 8. 5 CA measurements for treated samples with 1% APTES, GPTMS and
APTES/GPTMS silane washes
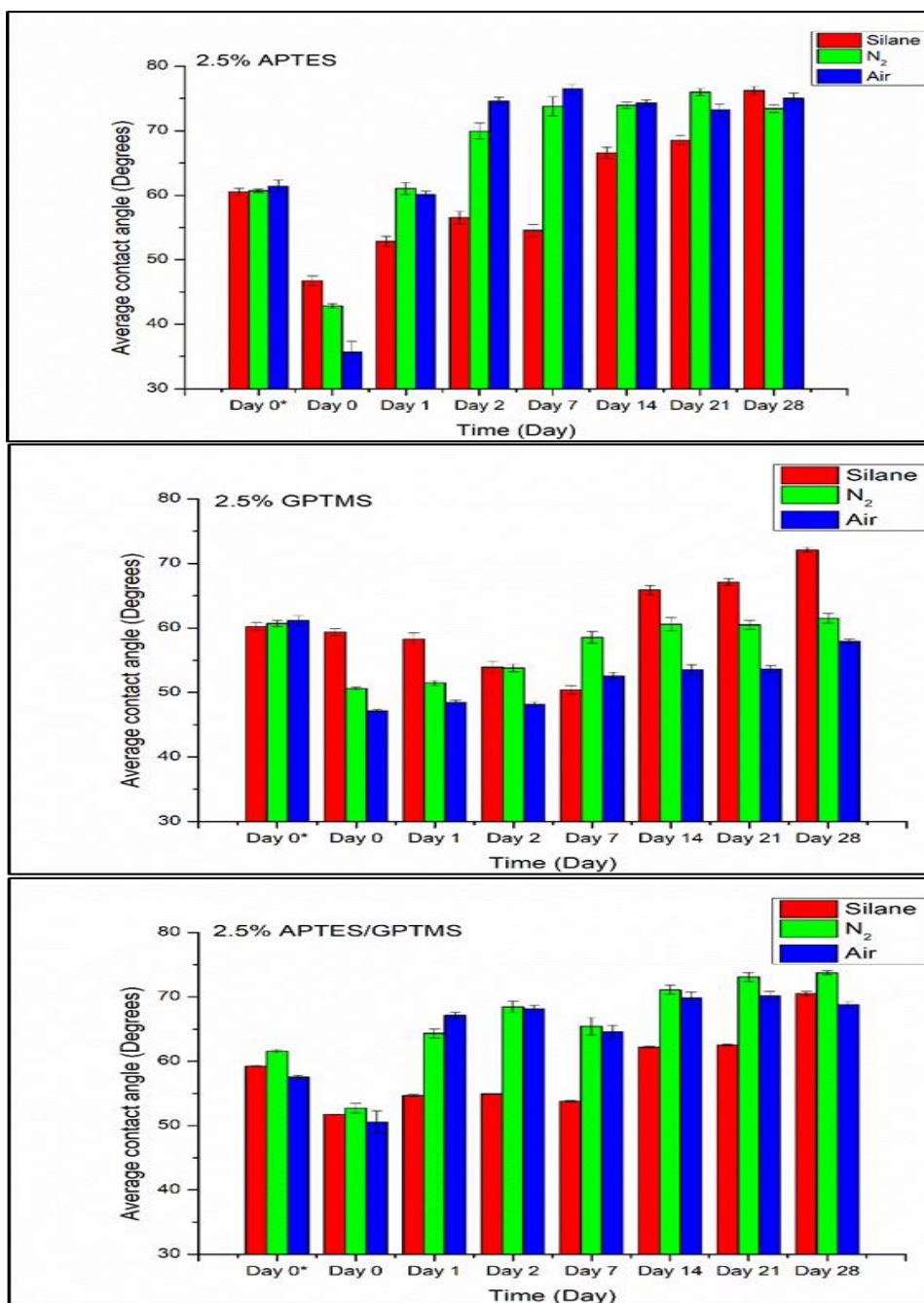
Figure 8. 6: CA measurements for treated samples with 2.5% APTES, GPTMS and APTES/GPTMS silane washes
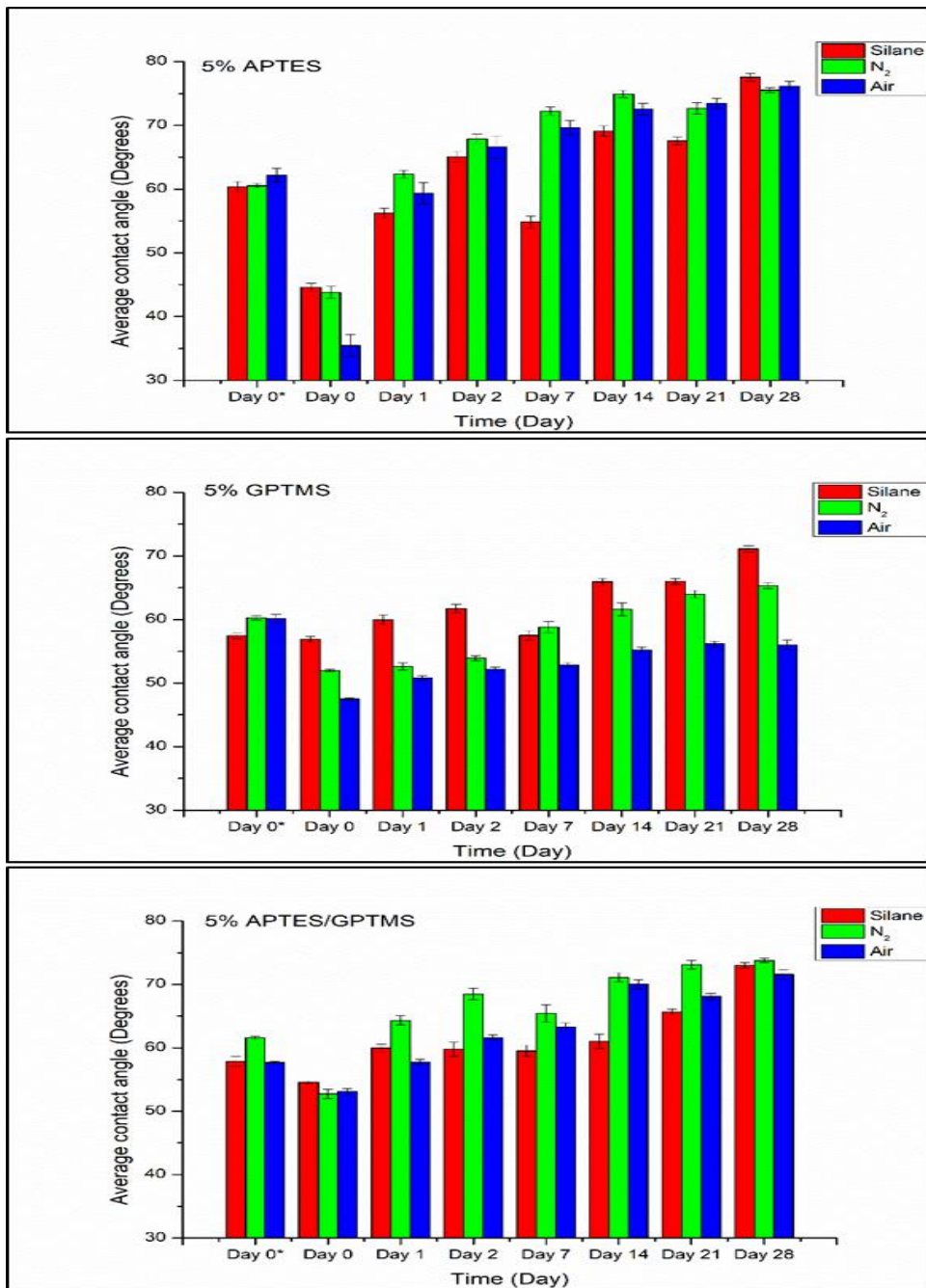
Figure 8.7: CA measurements for treated samples with 5% APTES, GPTMS and APTES/GPTMS silane washes

8.3.2 FTIR Analysis

As the most efficient process was found to be the air-plasma treatment only applied on the reference sol-gel coating, we have tried to understand the impact of this treatment on the structure of the material over time. In order to do this, FTIR spectra were recorded, and analysed in the region $800 - 1250 cm^{-1}$, where the typical vibrations of the silica backbone are present. The FTIR spectra were recorded over the same time period as the CA measurements with the objective to correlate both analyses together.

Concentrating on the control samples in Fig. 8.8, there is very little variation over the 28-day period for the bare silane samples. There is a slight increase in intensity for the Si-O-Si bonds located at 890 cm^{-1} over the 28-day period from day $1 - 28$. However, there is no change in intensity for the higher energy siloxane bonds located from $1010 - 1080$ cm^{-1}. In parallel, for the Si-O-Zr band located at 940 cm^{-1} there is very little change in the intensity of the band, the highest intensity can be seen for day 2 with a slight decrease in intensty for day 7 and day 28, respectively. These results suggest that the ageing slightly increases the condensation of the inorganic network especially in the formation of linear siloxane bonds, probably responsible for the increase of CA values as observed in section 8.3.1.1 (Fig. 8.3)

For the N_2 control samples a similar trend can be seen. The Si-O-Zr band decreases in overall intensity, while the intensity of the high energy siloxane bands at 1060 and 1080 cm^{-1} slightly increase for days $14 - 28$ compared with days $0 - 7$. Apart from these bands there is no significant viariation in the other bands of interest within the region. The evolution of the structure towards the formation of siloxane bonds, especially after 7 days of ageing explains why the CA values are found to dramatically increase for the same ageing time. This ageing process can only be ascribed to the converion of less stable Si-O-Zr bonds for the benefit of more stable siloxane bonds.

The air control samples show the most variation over the 28-day period. For the Si-O-Zr bond there is an overall decrease over the investigated period. The opposite trend can be seen for the high energy siloxane bonds located at 1060 and 1080 cm^{-1}. There is a slight decrease in the intensity of the Si-O-C band located at 1170 and 1200 cm^{-1}. Similarly to the N$_2$ plasma treatment, the air-plasma process shows an overall increase of the siloxane bonds over the 28 day period, meaning that a common ageing process takes place for both treatments, also similar to the one observed for the untreated sol-gel coating. Therefore, this can only be due to the inherent ageing process of the sol-gel material leading to a hydrophobic recovery. However, as the CA values were recorded at lower values for the air-plasma treatment, it is likely that this can only be ascribed to the alteration of the fine surface of the coating, probably in the first few nanometer, which cannot be detected by the FTIR technique. For this purpose, it has been decided to perform X-ray Photoelectron Spectroscopy (XPS) analyses to characterise the elemental composition of the fine surface and possibly achieve conclusions on the effectiveness of the various surface treatments.
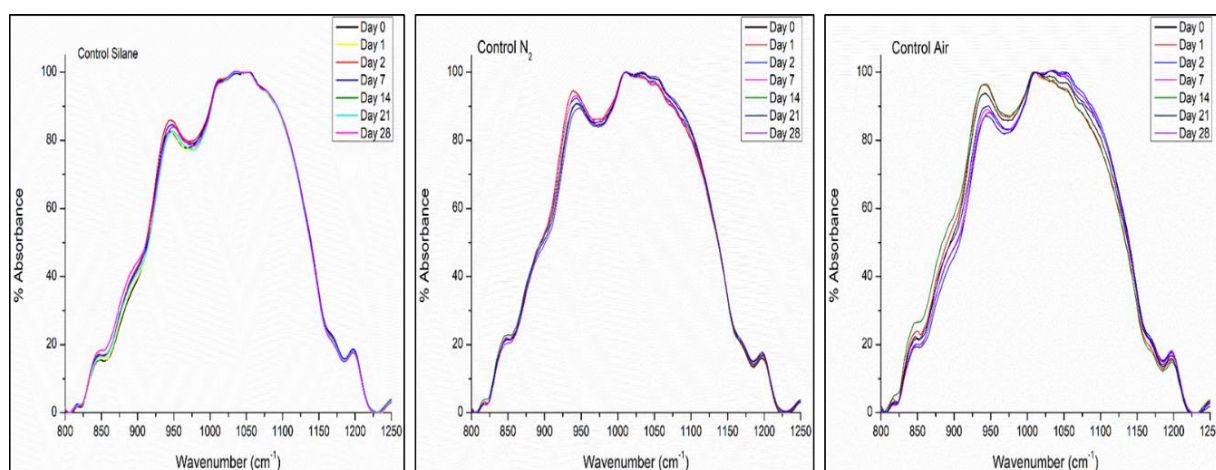
Figure 8. 8: FTIR spectra for control samples plasma treated with N$_2$, Air and on the silane only coatings

8.3.3 X-ray Photoelectron Spectroscopy (XPS)

As mentioned above, XPS analysis is performed to characterise the elemental composition of the fine surface of the various surface treatments. In addition to the plasma surface treatment of the reference sol-gel material, the dual plasma and silane modification employing the three silane washes are also investigated.

XPS spectra for the three series of samples are presented in Fig. 8.9 and the binding energies for the various detected elements are plotted in Fig. 8.10-12.

Silane surface treatment

The XPS characterisation of nitrogen on the untreated sol-gel coating shows a large band located in the range 396 – 409 eV, with a maximum centred at 403 eV. It can be clearly seen that this band is the superimposition of three bands centred around 397.5, 403.5 and 407.5 eV, suggesting the presence of atomic nitrogen in three different configurations[168]. As this coating does not contain any surface treatment, the detected nitrogen can only be originating from the nitric acid employed in the catalysis of the sol-gel reactions and that was immobilised in the sol-gel matrix.

The application of the silane washes provokes a shift of the maximum of the band towards lower energies, suggesting the removal of the nitrogen is facilitated. This can be explained by the fact that the APTES contains a nitrogen atom in the amino group in a free configuration at the top surface of the surface treatment. However, one can notice that, surprisingly the intensity of nitrogen emission is higher for the 0.5% APTES than for the 5% APTES. A plausible explanation for this may be in relation to the accessibility of the nitrogen group, probably due to the increased thickness of the surface treatment.

The emission of the silicon atom is detected within the energy range 100 – 109 eV with a maximum centred at 104 eV for the blank coating and the two different washes.

Similarly, to the nitrogen, the intensity measured for the 0.5% is higher than the 5%, probably for the same accessibility reason.

The detection of the zirconium atom is observed in the energy range 182 – 190 eV with a maximum intensity located at 185.5 eV for all samples. Here, the maximum intensity is observed for the untreated sample with a progressive decrease as the concentration of the silane wash increases. This clearly suggests that the thickness of the silane wash increases with its concentration, thus confirming that the surface treatment is taking place.

Dual Air-plasma / Silane surface treatment

The air-plasma treatment only shows the presence of three bands centred at 397, 403 and 408 eV, suggesting the presence of atomic nitrogen in three different configurations. This is a similar behaviour than the one observed for the non-plasma treated sample and can be explained by the presence of atomic nitrogen originating from the nitric acid sol-gel catalyst.

Again, similarly to the non-plasma treated sample, the emission of the atomic nitrogen is seen to shift towards the lower energies with now a maximum intensity recorded at 401.5 and 400.5 eV for the 0.5 and 5% washes, respectively. However, unlike the non-plasma treated sample, the intensity of the nitrogen for the 5% washes is slightly higher than the one recorded for the 0.5%, suggesting the accessibility of the excitation of the nitrogen would be facilitated in the 5% wash, which is further confirmed by the lower excitation energy. This can only be explained by the configuration of the nitrogen within the surface, which is probably located at the top surface of the surface treatment. In this configuration, the lone pair of electrons located on the nitrogen atom can be better accessed to provide hydrophilic properties. This fully confirms the CA results (section 8.3.1) which were found to be minimum for the air-plasma treatment.

The energy required for the silicon emission appears to be progressively decreasing as the concentration of the silane wash increases (maximum intensity recorded at 104.5, 104 and 103.5 eV for the blank, 0.5 and 5%, respectively), suggesting that overall the silicon is more accessible in thicker surface treatments. Importantly, in comparison with the non-plasma treated samples, the emission of the silicon atom appears at higher energies for the non-washed sample, suggesting the development of a thin barrier, probably an oxygen rich layer.

Similarly, to the non-plasma treated sample, the emission of the zirconium atom shows the highest intensity for the sample with no wash, and that this intensity is decreased as the concentration of the wash increases. Furthermore, when comparing the relative intensities of the 0.5 and 5% washes against the blank sample for the non-plasma and air-plasma treated plasma samples a decrease from 37 to 21% and from 10 to 2% for the 0.5 and 5%, respectively. This clearly suggests that the surface treatments are thicker for the air-plasma treatments, certainly favoured by a better adhesion of the functional silane onto the rich oxygen layer promoted by the air-plasma treatment.

Dual N_2 plasma / Silane surface treatment

The atomic emission of the nitrogen is seen to be higher than those recorded in the blank sample (untreated) for all silane washes. Interestingly, the concentration of the silane washes does not change the emission energy (400 – 405 eV), suggesting a similar configuration for the nitrogen regardless of the silane concentration, thus on the thickness of the surface treatment. However, the fact that the emission intensity is about 17% higher for the 0.5% suggests a higher content of nitrogen atoms at the very top surface of the treatment. This is probably related to the thickness effect, which could provoke a slightly higher entrapment of the nitrogen within the bulk of the surface treatment.

Similarly, to the nitrogen, the atomic emission of the silicon atom is favoured when the silane is applied, with no difference on the emission energy for both silane concentrations. Again, the emission shows a highest intensity for the 0.5%, translating a greater silicon population at the top surface of the surface treatment. This behaviour is however the opposite of the one observed for the air-plasma treatment, which clearly demonstrates that the accessibility to the silicon atom is facilitated that can only be explained by a higher content of silicon species at the top surface of the treatment, then with a less silicon bound to the sol-gel coating. Therefore, with the N_2 plasma treatment, it is likely that the silane washes are randomly distributed at the surface of the sol-gel coating, whereas a better structured treatment would be formed with the air-plasma treatment and where the silicon species would be oriented towards the surface of the sol-gel coating.

Finally, the emission of the zirconium atom is seen to decrease as the concentration of the silane wash increases, confirming that the thickness of the surface treatment increases.

In summary, the XPS results have enabled to achieve the following conclusions:

1. The surface treatment is successfully applied, and its thickness increases with the silane concentration

2. The hydrophilic properties of the surface treatment relies on the orientation of the hydrophilic species within the surface treatment and is favoured by the air-plasma treatment.

3. The adhesion of the surface treatment is favoured by the air-plasma treatment.

These results enable us to explain the more hydrophilic properties achieved with the air-plasma treatment, as identified in section 8.3.1.
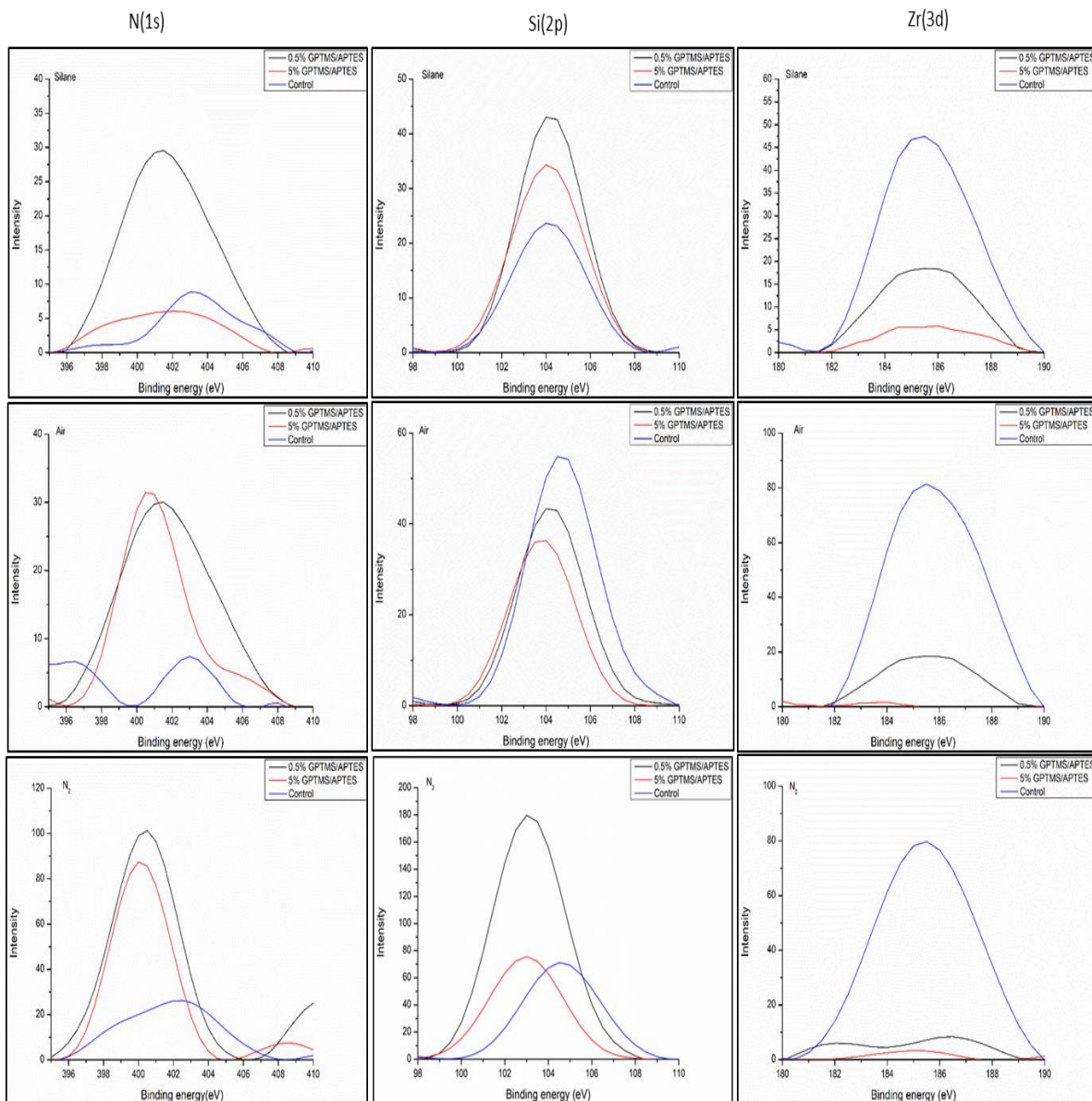
Figure 8. 9: XPS spectra for various surface treatments applied to the sol-gel coating

Species	Binding energy (eV)
O1s	534.0
C 1s	286.0
N 1s	402
Si 2p	104
Si 2s	155
Zr 3d	185

Table 8. 3: Binding energies for each species present in the spectra
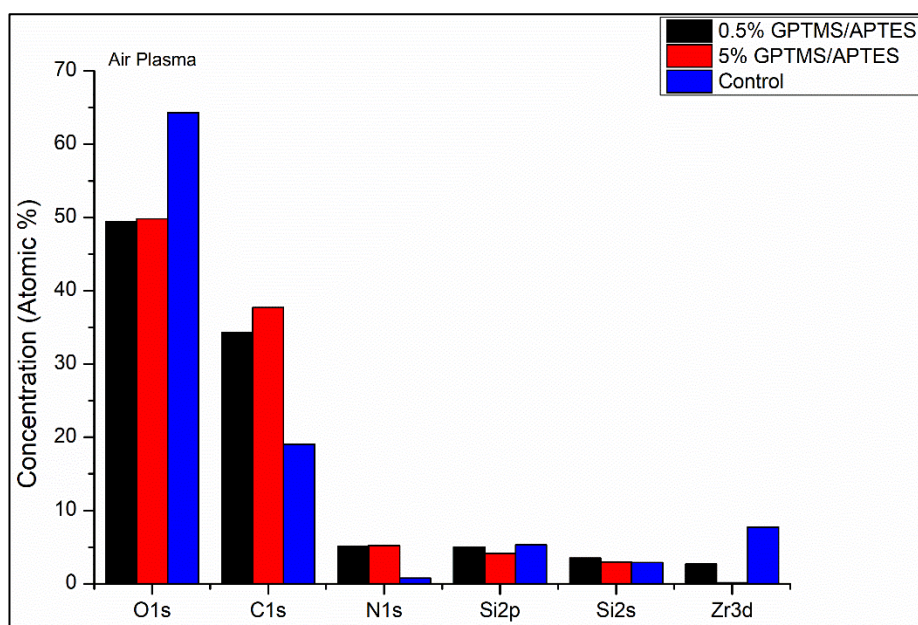
Figure 8. 10: % concentration of each element present in the samples pre-treated with

Air-plasma
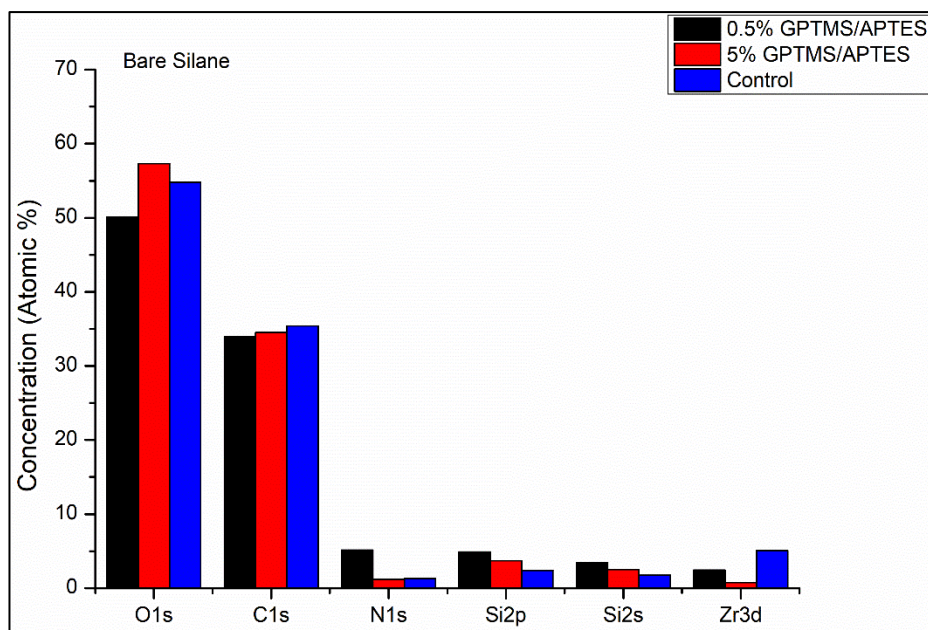
Figure 8. 11: % concentration of each element present in the bare silane pre-treated

samples
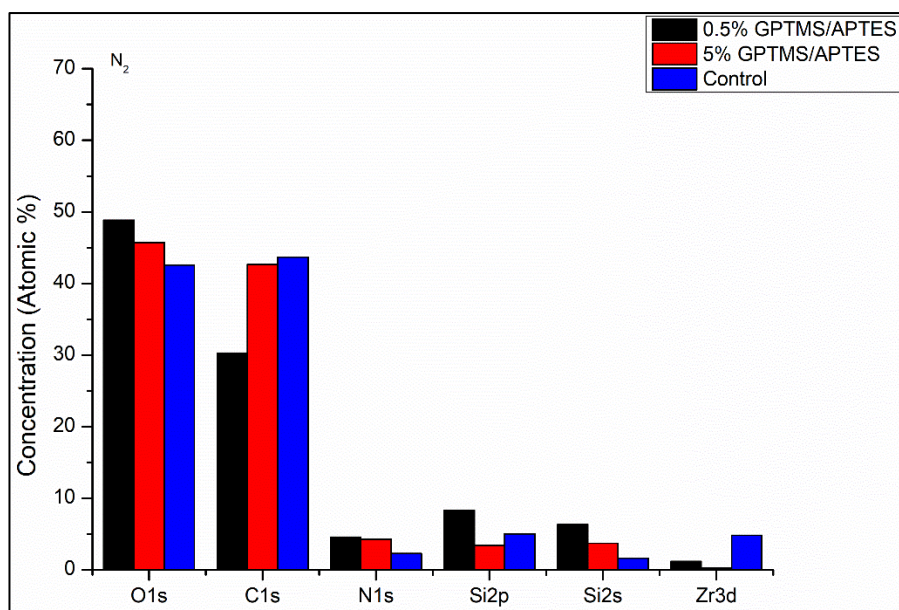
Figure 8. 12: % concentration of each element present in the samples pre-treated with

N_2 plasma

8.4 Conclusion

This chapter was concerned with the investigation of dual physical and chemical surface modification of the surface of the sol-gel coatings to improve the wettability and overall stability of the coatings towards microfluidic applications. The surface of the coatings were pre-treated via N_2 and air-plasma before being subjected to various concentrations of dilute amino and epoxy silane washes. The wettability of the coatings and stability were followed via CA measurements over a 4-week period. Hydrophobic recovery was seen for all the samples regardless of pre-treatment of the silane wash composition and concentration. The most hydrophilic and stable coatings were found to be the control samples that were pre-treated with air-plasma with an average CA value of 36° directly after both surface treatments and 54° after 28 days. The stability of the coatings was also followed via FTIR over the 4-week period. It was found that the stability of the coatings was able to be monitored via FTIR, in particular the Si O-Zr band and the high energy Si-O-Si bands.

XPS analysis of the coatings provided valuable information in regard to the effectiveness of the applied surface treatments and correlation with the CA measurements. Indeed, it was found that the all surface treatments are successfully applied, and their thicknesses rely on the silane concentrations. The hydrophilic properties of the surface treatment rely on the orientation of the hydrophilic species within the surface treatment and is promoted by the air-plasma treatment. The adhesion of the surface treatment is favoured by the air-plasma treatment. These results explain why the more hydrophilic properties were obtained with the air-plasma treatment.

Importantly this chapter demonstrated the importance of combined physical and chemical surface modifications on the sol-gel coatings in order to improve their wettability and stability towards microfluidic applications. Fundamentally, it is

shown for the first time that the orientation of the silane is critical in achieving greater hydrophilic properties and that this orientation relies on the applied plasma treatment.

The subsequent two chapters will focus on two different applications of hybrid materials, incorporating some of the results that have been achieved thus far within the project. The first application will focus on the fabrication of microfluidics and microstructures. The second chapter will focus on the fabrication of an optofluidic device fabricated using the reference hybrid material used throughout this work.

9 Microfabrication and characterisation of the reference hybrid sol-gel material

9.1 Introduction

This chapter is concerned with the microfabrication of the previously synthesised reference hybrid material towards the fabrication of linear micro-channels and a microfluidic sensor platform via a standard photolithography process.

The topic of microfluidics and the use of hybrid sol gel materials for the fabrication of microfluidic structures has already been established and discussed with regards to the current literature (chapter 2), and with regards to the microstructuration of the reference sol-gel material (chapter 4) of this thesis.

In addition to the surface properties that govern the flow of liquids within the platforms, it is essential to optimise the fabrication conditions to achieve fully stable microfluidic platforms with defined dimensions. As the aimed microfabrication technique is the photolithography process, the materials stability and dimensions of the microfluidic platforms will be defined by photo-reactivity of the material and the thickness of the coatings. Therefore, correlation between the fabrication conditions, the structure of the material and the effectively obtained microstructures is needed. In order to do this, a set of characterisation techniques has been established including optical, structural and imaging techniques. The Prism-Coupling technique will be used to identify the variation of the refractive index and thickness of the coatings as function of the UV-irradiation time and enable to define the optimum UV-irradiation duration to achieve materials that are fully cured- in terms of the complete photopolymerisation of the methacrylate groups of the materials. Stylus profilometry and SEM will be used to identify the profile of the

fabricated microchannels with the optimum UV-irradiation conditions including the step height and width of the fabricated microstructures.

The fluid flow within the channels will also be characterised via optical microscopy. The structure of the hybrid sol-gel material as a function of UV-irradiation will be monitored by FTIR. The stability of the photo-initiator within the sol-gel matrix will be followed via UV-visible spectroscopy.

9.2 Materials Preparation

The reference material that has been fully described previously in Chapter 4 was used to fabricate both the buffer layer (BL) and the guiding layer (GL) of the microfluidic channels and biosensor platform. In order to make the sol-gel material photo-reactive, a photo-initiator (PI) was added prior to use. Irgacure 184 (1-Hydroxycylohexyl-1-phenyl methanone, BASF, Germany) was selected as the PI for its long-term stability within strongly oxidising materials such as transition metal-based sol-gels[133] . The concentration was fixed to 5 mol % with respect to the methacrylate groups of the MAPTMS. The PI was added to the final sol and left to stir for 1 hour prior to use to ensure full dissolution. The structure of the PI is shown in Table 9.1. The synthesis of the sol-gel material is shown in Fig 9.1
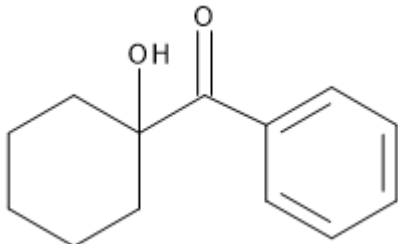
Chemical Name	Abbreviation	Formula	Structure
1-Hydroxycylohexyl-1-phenyl methanone (Irgacure 184)	I-184	$C_{13}H_{16}O_2$	

Table 9. 1: Chemical name, common abbreviation, molecular formula and structure of the photo-initator used in the synthesis of the photo-curable sol-gel material
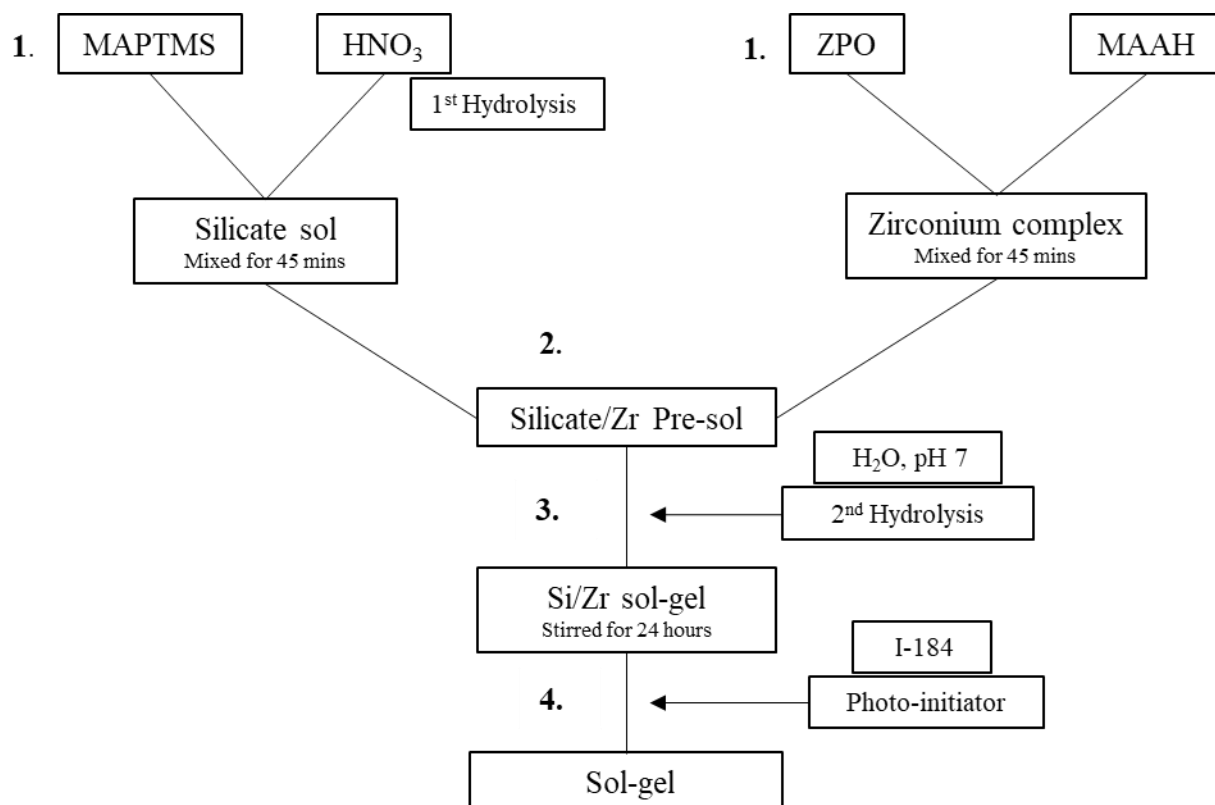
Figure 9. 1: Flow chart for the synthesis of the photo-curable sol-gel material

9.3 Results and Discussion

9.3.1 Refractive Index Measurement

In order to find the optimum curing time for the sol-gel material, the RI (refractive index) of the material was measured at different UV curing times using a UV power of 40 mW/cm^2. The RI values for the sol-gel material were then plotted against the UV irradiation time and is represented in Fig. 9.2 below. A two-regime behaviour can be observed. First, as the UV irradiation time increases from 0 – 100 seconds there is a sharp increase in the RI from 1.5058-1.5115, corresponding to an increase of 5.7x10^{-3} and suggesting a change in the structure of the material. The RI value after 250 s of UV irradiation is 1.5115. After 650 s, the RI values has increases to 1.5129 which corresponds to a variation of 1.5x10^{-3} in the RI of the material. However, knowing that the prism-coupling system provides measurements with an error of 5.10^{-4}, it can be considered that

the variation of the RI values from 250 s is negligible. Therefore, the coating is considered stable for UV-irradiation times of 250 s, which will be defined as the exposure time for the fabrication of microfluidic devices.

The thickness of the coating vs the irradiation time was also plotted and can be seen in Fig 9.3 below. Interestingly there is an increase in the thickness of the coatings from 5.7 microns at 0 s to 6.4 microns after 250 s. There is a sharp decrease in the coating thickness for the sample irradiated at 500 s to give a thickness of ~ 5.85 microns with a slight increase for 650 s to give a thickness of ~ 5.9 microns. FTIR may give further insight into the behaviour of the coatings as a function of UV irradiation time. The coating thickness measured here should be reflected in the step height measurements of the micro-channels fabricated under the same conditions.
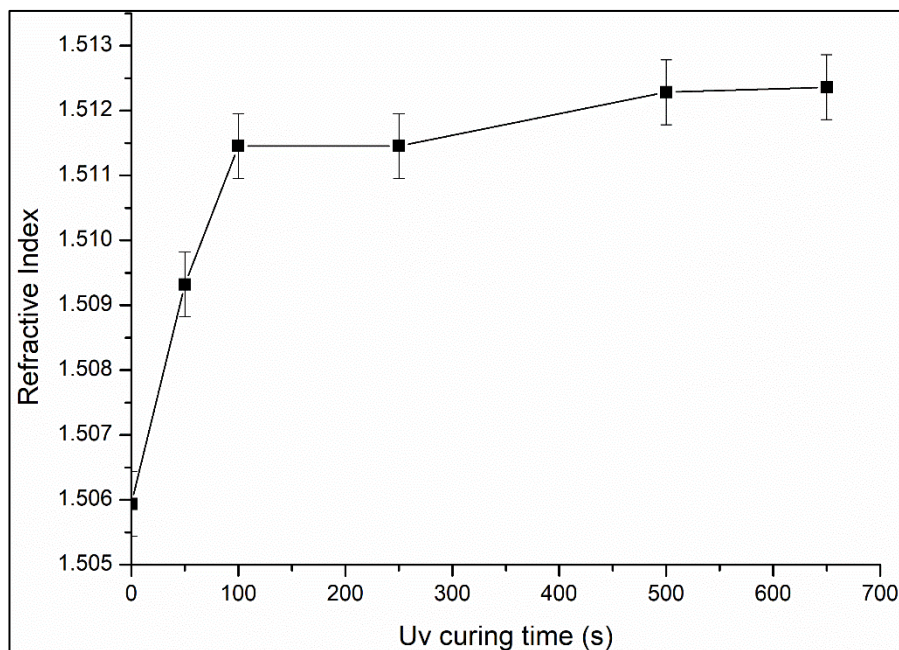
Figure 9. 2: Refractive index vs curing time for the reference sol-gel material
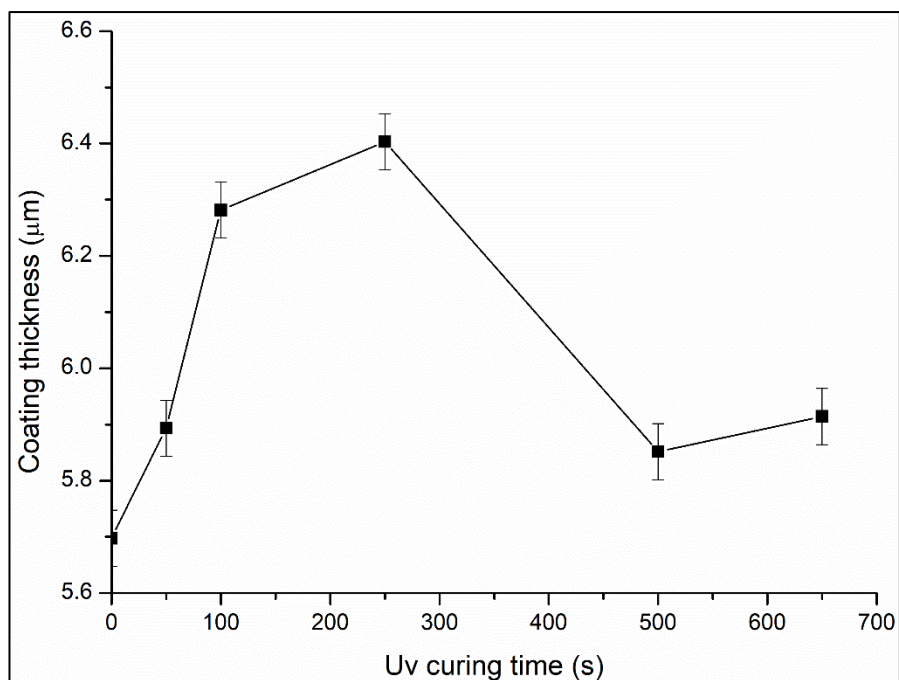
Figure 9. 3: Coating thickness vs curing time for the reference sol–gel material

The prism-coupling technique enabled us to define the optimum UV-irradiation conditions to achieve stable microstructures. The variation of the RI reflects the densification process progression of the organic network, due to the radical polymerisation taking place thanks to the presence of the PI and possibly involving inorganic condensation processes. However, it would be necessary to identify the evolution of the structure of the materials as function of UV-irradiation time to possibly conclude on the physico-chemical phenomena taking place in the microstructuration process of our hybrid sol-gel material. This is the purpose of the following section.

9.3.2 FTIR Analysis

The effect of thermal curing and UV curing was investigated for the reference sol-gel material via FTIR analysis and the full spectra can be seen in Fig. 9.4. Two regions of interest were investigated, namely the inorganic siloxane backbone from $800 - 1250$ cm^{-1} (Fig 9.6) and the organic carbonyl region from $1600 - 1800$ cm^{-1} (Fig 9.5a & b). The effect of thermal curing on the siloxane structure of the sol gel network within the $800 -$

223

1250 cm^{-1} has been previously investigated and discussed in chapter 4 and so will not be further discussed in detail here.

The effect of the UV-curing on the siloxane backbone of the material can be seen in Fig. 9.5 below. Concentrating on the Si-O-C bonds located at 815, 1170 and 1200 cm^{-1}, they can be seen to decrease as the curing time increases, but with a minimum intensity for the 500 s sample. The increase of the intensity of the Si-OH bond located at 840 cm^{-1} as the UV-curing increases further confirms that the UV-irradiation enables the conversion of the residual methoxysilane groups (Si-O-CH$_3$) into reactive silanol species. The high energy siloxane bonds 1050 – 1080 cm^{-1} can be seen to increase from 0 to 250s and decrease from 500 s. Except for the 650 s sample, the Si-O-Zr band decreases as the curing time increases.

These results converge towards the conclusion that the inorganic condensation is favoured for up to 250 s, with probably the organic polymerisation becoming prevalent for higher exposure times. This result may explain the increase in the coating thickness up to 250 s exposure time and the subsequent decrease in thickness for the sample exposed at 500 s.

Two bands can be seen within the region of 1600 – 1800cm^{-1} in Fig. 9.5a and are related to the methacrylic group of the MAPTMS. The two bands are found at ~1625, 1725 and a shoulder at ~1740 cm^{-1}. The band at 1625 cm^{-1} can be seen to decrease from 50 s curing to 100 s and stagnates up to 650 s. This band is attributed to the unsaturated C=C bond of the methacrylate groups within the MAPTMS precursor[169]. There is no change in the intensity of the band at 1725 cm^{-1} with the increase in UV curing time. This band is attributed to the carbonyl stretch C=O within the methacrylate groups of the MAPTMS[169]. There is a slight shoulder that appears at 1745 cm^{-1} and subsequent broadening of the peak, as the curing time increases from 100 seconds onwards, suggesting that the carbonyl

group gets into a denser network, due to the further crosslinking of the C=C bond within MAPTMS[170].

For comparison purposes, the effect of thermal curing was also investigated within the same region (1600 – 1800 cm^{-1}), as represented in Fig. 9.5b. Again, the band at 1625 cm^{-1} can be seen to decrease as the curing temperature increases from 100 – 130°C. There is no change in the intensity of the band from 130 – 150°C. The band attributed to C=O carbonyl vibration of the methacrylate is also present and can be seen in Fig. 9.5b. Interestingly in contrast with the same peak seen in Fig. 9.5a, there is a very distinct shift to longer wavenumbers as the curing temperature increases from 100 – 150°C. The band is centred at 1716 and 1717 cm^{-1} for 100 and 120°C - (C=O conjugated to C=C)[171], and centred at 1726 cm^{-1} for 130 – 150°C, although there is no change in the intensity of the band. Again this is attributed to the C=O bond within the methacrylate of the MAPTMS. This shift towards higher wavenumbers and the subsequent decrease in the C=C indicates the loss of conjugation to the C=C as the sol-gel network is polymerised[169]. It is evident from these spectra that the thermal curing has a greater effect on the polymerisation of the sol gel network in comparison with the photo-polymerisation of the network alone. This can be seen in the decrease of the band centred at 1625 cm^{-1} which corresponds to the consumption of the C=C bonds within the methacrylate of the MAPTMS as the network is polymerised[172].

In summary, FTIR results highlights that the radical photo-polymerisation is effective but is stopped from 250 s. This is an interesting result that explains why the RI does not significantly evolve from an irradiation time of 250 s, as seen in the previous section. The most likely explanation to this phenomenon is that the radical polymerisation can progress up to the formation of a rigidified and fully interconnected network, unable to further polymerise. Of the other valuable information obtained from the FTIR analyses is that the

organic polymerisation induced by UV-irradiation also has an impact on the inorganic polycondensation process, evidenced by the decrease of the residual methoxysilane groups and the increase of the high energy siloxane groups, which were also found to increase for up to 250 s, confirming that the maximum densified structure is achieved for that irradiation time.
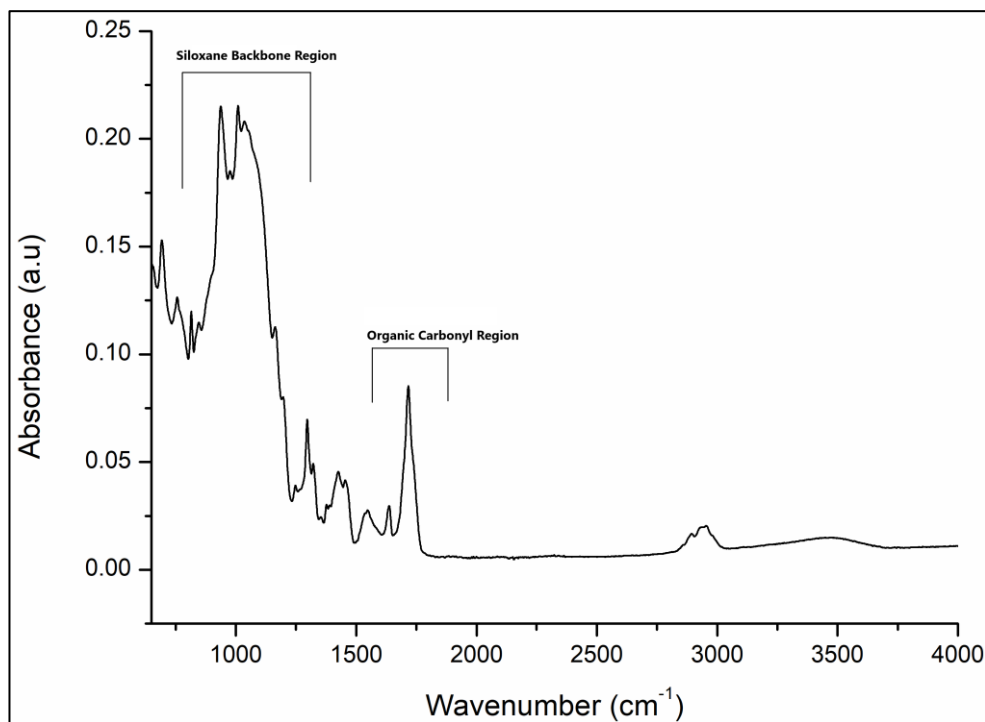
Figure 9. 4: FTIR spectra of reference material in the region of 4000 – 650 cm^{-1}
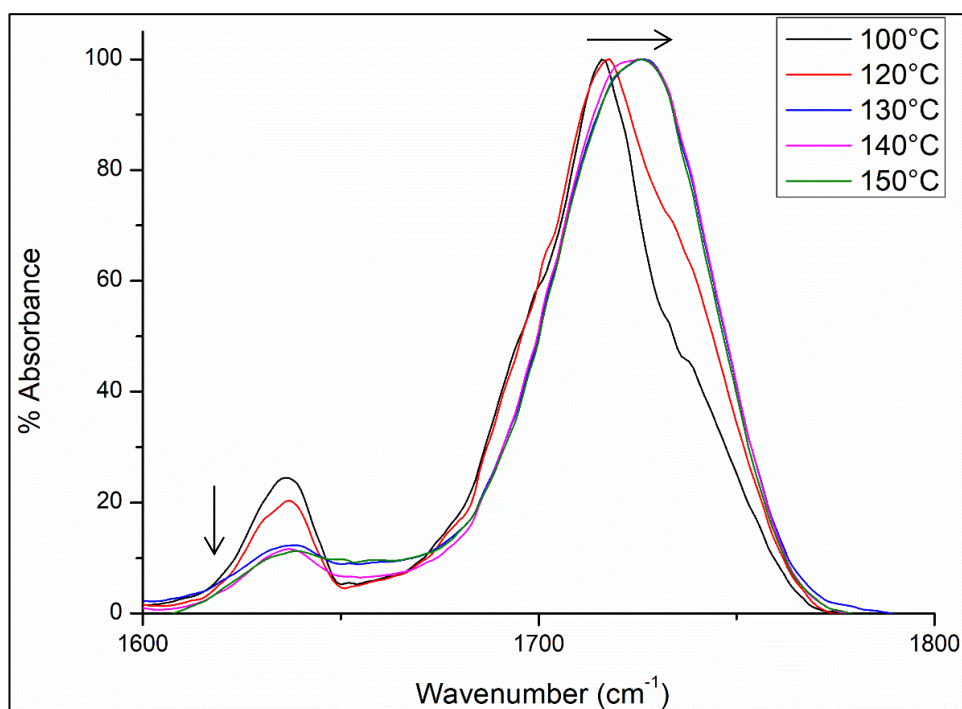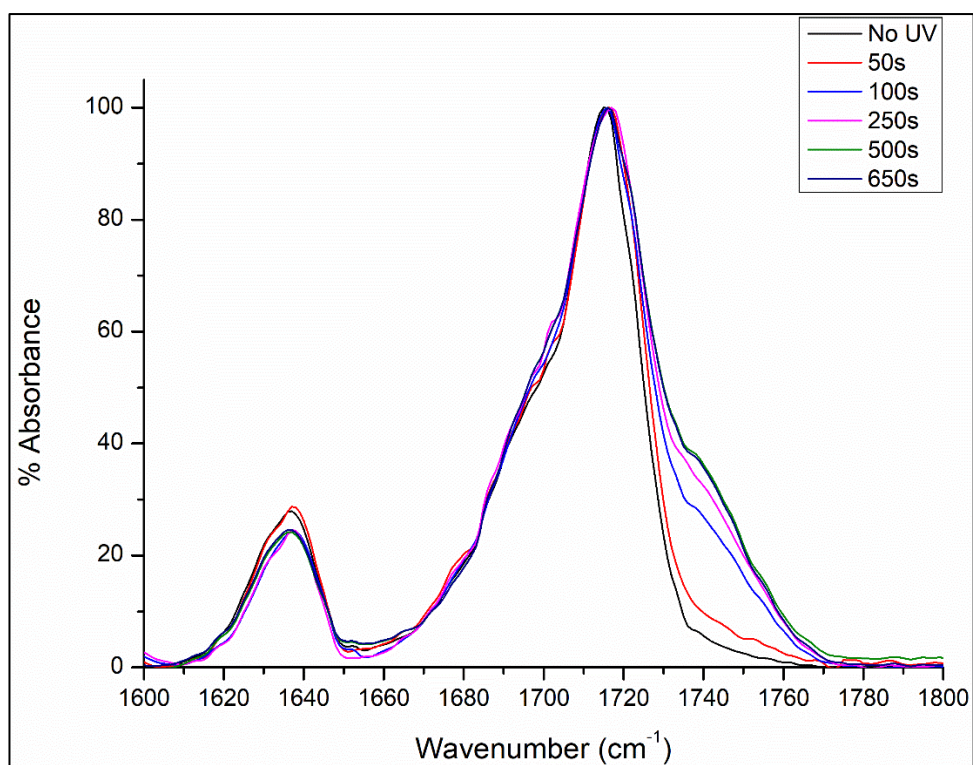
Figure 9. 5: a) UV curing of the reference material from 0 – 650 seconds in the region 1600 – 1800 cm^{-1} b) Thermal curing of reference materials in the region 1600-1800cm^{-1}
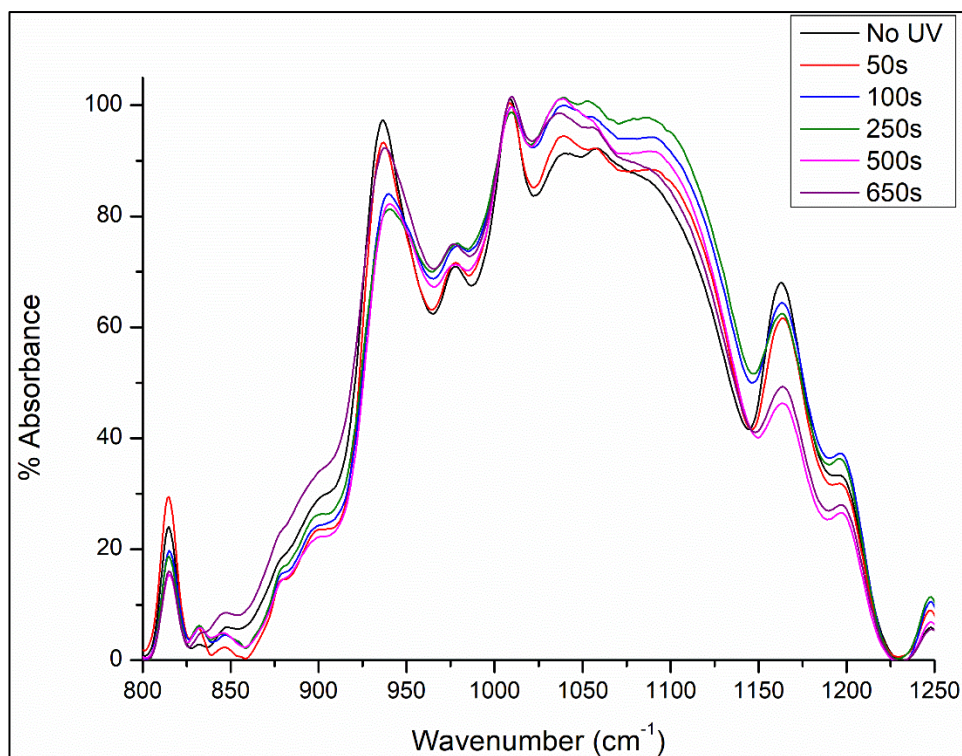
Figure 9. 6: UV curing of the reference material from 0-650 seconds in the region of 800-1250cm^{-1}

9.3.3 UV-Vis Measurements

In order to identify the optimum concentration of photo-initiator needed to photo-structure the sol-gel materials, UV-Vis measurements were performed on the liquid sol-gel material with varying concentrations of I-184 added from 0-5%. The spectra were run within the 250-400 nm spectral range and can be seen Fig. 9.7. It can be seen that as the concentration increases from 0 to 5% PI there is a progressive increase in the intensity of the band centred at ~335 nm. The occurrence of this band has been attributed to the PI used, I-184 and has previously been observed for similar materials [133].

The stability of the PI over 72 hours was also studied and is represented in Table 9.1 below; the absorbance was taken 330 nm. From this stability study, the optimum concentration of PI was chosen as 5% against the total methoxy groups of the MAPTMS. It can be seen that for all concentrations of PI there is a decrease in the absorbance at 330

nm from 24 – 48 hours after preparation, with an increase in absorption from 48 – 72 hours. Of the 4 different concentrations, the 5% is the most stable after 24 hours preparation.
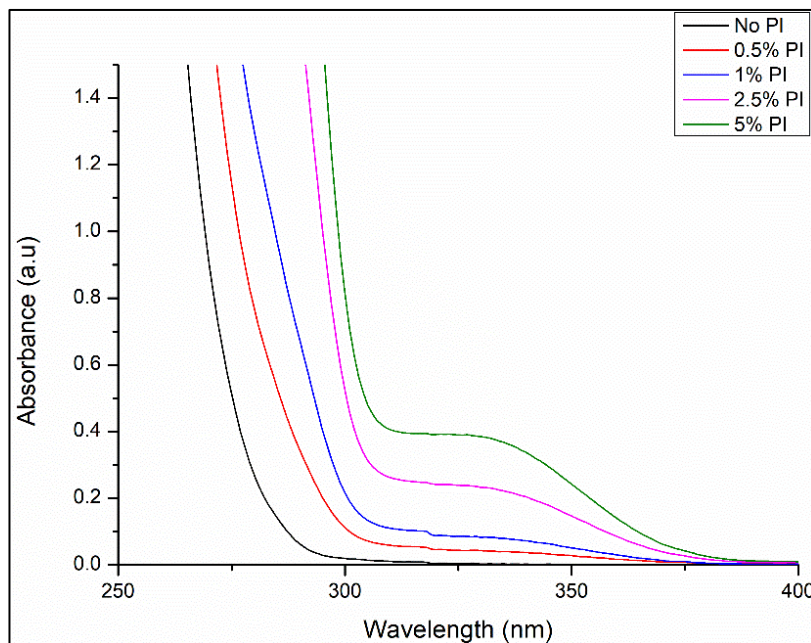
Figure 9. 7: UV-vis spectra of varying concentration of I-184 within the sol-gel matrix

Sample	Day 1	Day 2	Day 3
No PI	0.012	0.0064	0.012
0.5%	0.043	0.012	0.042
1%	0.082	0.067	0.072
2.5%	0.232	0.160	0.180
5%	0.385	0.331	0.333

Table 9. 2: Absorbance over 3 days after fabrication of PI at 330nm

9.3.4 Microfluidic channel and biosensor platform fabrication

Fabrication of the microfluidic channels and the microfluidic biosensor platform were performed via a mask-photolithography process as outlined in Fig. 9.8 below. Photomasks were designed to enable the fabrication of microfluidic channels with various

sizes and shapes and are presented in Fig. 9.9. The photomasks were designed using Autocad 2018 software. The biosensor photomask contains two platforms of different channel widths, 250 and 500µm. The linear photomask contains linear microchannels of 5 different channel widths, 75, 100, 250, 350 and 500 µm. The fabrication of the photomasks has been described in more details in section 3.4.1. The UV-exposure was performed using a Kloé UV-irradiation setup (KUB 2) (Fig. 9.10), the final parameters of which are outlined in Table 9.3. Silica wafers were used as a substrate to fabricate the biosensor platform and their properties are outlined in Table 9.4. The fabricated biosensor platform is presented in Fig. 9.11 below.

Prior to the optimisation of the process, varying parameters were altered including UV-curing time, UV-power and pattern development, as outlined in Table 9.5 below. The outcome of these studies will be discussed in the following section. These initial studies were carried out using Al AA2024-T3 as a substrate and dip-coating as the deposition process with a dip speed of 40 mm/min to achieve coating thicknesses close to 6 µm.

The initial photolithographic process has been described in Chapter 4.4. The process was further optimised by altering the following parameters:

Substrate – 4"x4" test grade Si wafers were used as a substrate instead of Al panels. The Si wafers were better suited for the spin-coating deposition process and were easier to handle in terms of SEM analysis.

Deposition Process – For the fabrication of microfluidic channels and the biosensor platform, the deposition process was altered from dip-coating to spin-coating as this method made it easier to coat the Si wafers in a more uniform manner.

Microstructure etching – The micro-patterns were simultaneously etched and sonicated in IPA for 1 minute. This was to ensure any sol gel material that was etched away was removed from the channels. They were then rinsed with IPA to remove any residual

debris and placed in an oven at 100℃ for 10 minutes to ensure the IPA had fully evaporated from the surface of the micro-channels.

As mentioned above the deposition process was altered from dip-coating to spin-coating. 4" Si wafers were used as a substrate. The Si wafer was placed in a saturated environment of IPA for 3 minutes to control the evaporation of the solvents during the deposition process. 5 ml of sol was filtered using a 0.45 µm Whatman syringe directly onto the Si wafer. The ramp up speed was set to 200 rpm, the spin speed to 900 rpm and the ramp down speed to 250 rpm to enable homogenous spread of the sol, thickness adjustment and slow evaporations of the solvents, respectively. These parameters were used for the deposition of the buffer layer and the guiding layer.

Emission Spectrum	365nm +/- 5 nm
Illumination	40 mW/cm^2 +/- 10%
Power	100%
Mode	Continuous
Time	500s
Plate Exposure	Full surface

Table 9. 3: Final Mask Aligner Parameters

Type	Si wafers, test grade
Diameter	4"
Orientation	<100>
Dopant	N (phos)
Resistivity	1-10 ohm/cm
Centre Thickness	525 ± 50µm
Surface	Single Side polished

Table 9. 4: Si wafer properties

Parameter	Alteration	Chosen parameter
UV curing time	200-500 seconds	500 seconds
Mask aligner power	75% and 100% (30 and 40 mW/cm^2)	100%
Pattern Development	Without/with sonication	With sonication

Table 9.5: Alteration of parameters for fabrication of micro-channels
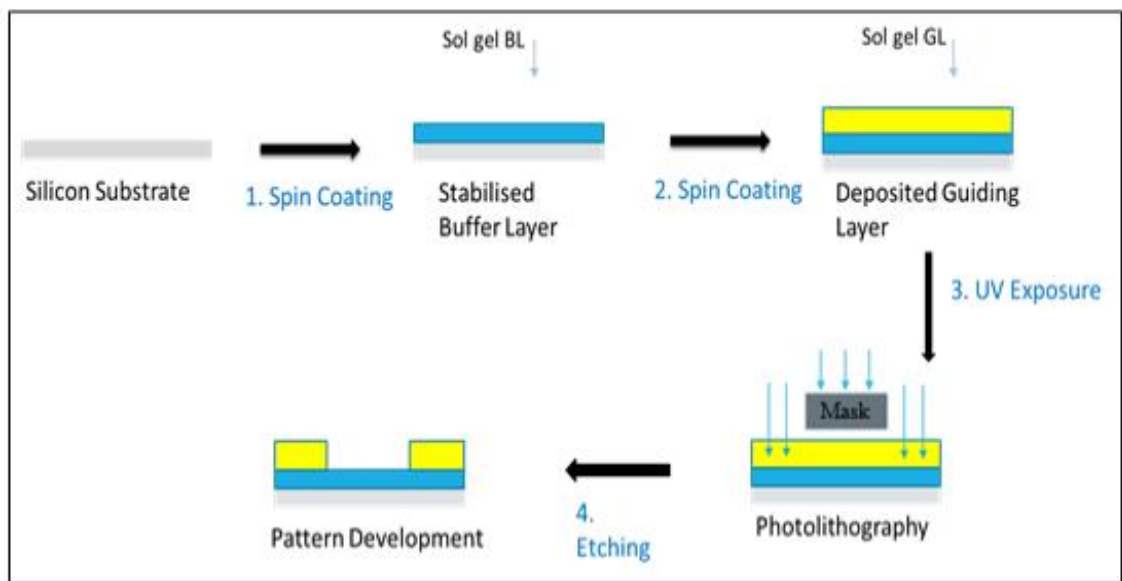
Figure 9. 8: Microfluidic channel fabrication process
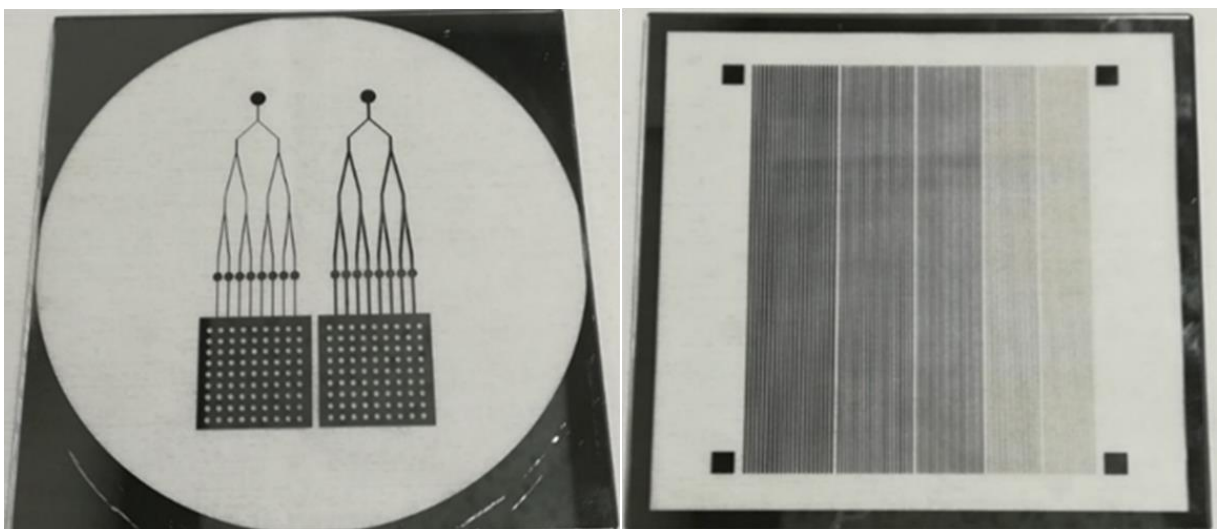
Figure 9. 9: Biosensor platform photomask- (left), linear microchannel photomask –

(right)

Figure 9. 10: Kloe Kub Mask Aligner
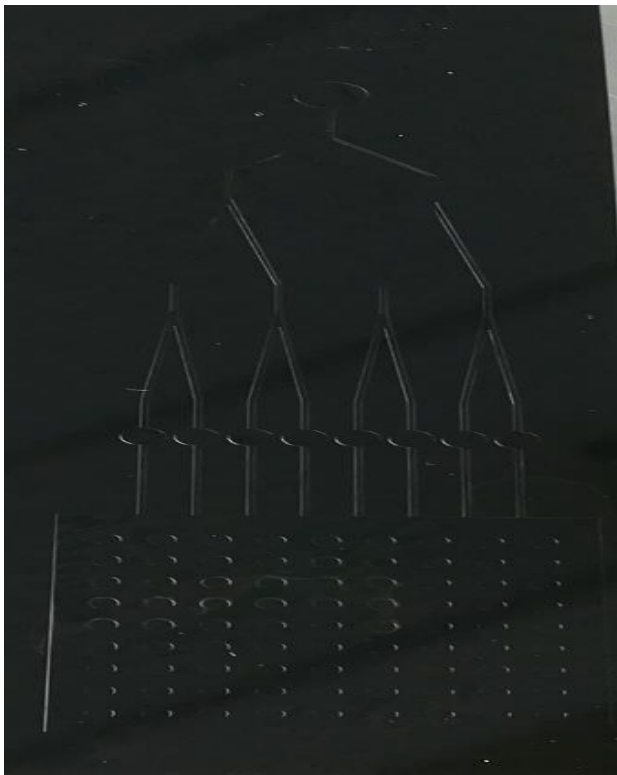
Figure 9. 11: Photograph of the fabricated biosensor platform on a Si wafer substrate

9.3.4.1 Profilometry Measurements

A DektakXT stylus profilometer (see section 3.1.2) was used to measure the step height and the width of the micro-channels and specific features of the microfluidic platform. Initial studies were carried out using Al as a substrate and concentrated on the 500 µm wide channels. The UV-irradiation time was varied from 200 to 500 seconds. Initially there were issues with sol-gel debris inside the microchannels after etching in IPA. This made the determination of the widths and step height of the channels quite difficult; a representative profile can be seen in Fig. 9.12 (top). This issue was resolved by simultaneously etching and sonicating the microstructures in IPA. This enabled the removal of the sol-gel debris to leave visibly cleaner channels. The average channel width values against the UV-irradiation time and etching time are tabulated in table 9.6 below. It can be seen that of the etch times investigated, the optimum etch time for the samples is 1 minute. For the 30 sec etch samples the width of the channels at the bottom are much narrower than the top of the channels. The average widths of the channels have been taken at the narrowest point in the channels (roughly at the bottom of the channels). For all the channels regardless of UV-curing time the top of the channels is slightly larger than at the bottom of the channels. This is much more pronounced for the samples sonicated for 30 seconds. It can also be noted that the opposite trend is seen for the channels as the sonication time increases. For the samples etched and sonicated for 30 seconds, the channel width decreases as the UV irradiation time increases which is an unexpected result. This result indicates that etch / sonication time may be inadequate to completely remove the un-polymerised sol-gel material to leave the desired microstructures. For the samples sonicated for 1 minute the channel widths increase as the UV irradiation time increases as expected. Therefore from this data it can be seen optimum etch / sonication time is 1 minute and the optimum UV-irradiation time for the channel width would be

500 s. This curing time was used for subsequent fabrication processes. The power of the mask aligner was also investigated. The UV-irradiation times that were chosen for this study were 250 and 500 s. The power of the KUB 2 was then varied between 75 and 100%. All other parameters were kept the same. It can be seen from this study (Table 9.7), that the optimum power for the fabrication of the micro-structures is 100%. The average channel widths at 75% power were found to be 423.9 microns and 243.6 microns for the samples irradiated for 250 and 500 s, respectively. The average widths for the samples irradiated at 100% power were found to be 473.15 and 480.70 irradiated at 250 and 500 s, respectively; translating to a process accuracy of 94 and 96%, respectively.

Once these conditions were optimised, the micro-channels were fabricated onto Si wafers. 5 different channels widths were fabricated ranging from 500 – 75 microns. It can be seen from Table 9.8 below the average channel widths and the difference between the fabricated widths and the intended widths. Over the 5 different channels widths there is an average difference of 23.6 microns between the fabricated and actual widths, corresponding to ~ 4.7 % difference. This means that our process enables the reproduction of about 96% of the desired dimensions of the micro-channels.

Specific features of the microfluidic platform were also profiled. The average diameter of the micro-pillars, sensor spots and inlets of the platform were measured and are shown in table 9.9. It can be seen that the diameter of the sensor spots and the inlet are smaller than the predicted diameters 1700 and 3000 µm, respectively; and the micro-pillars are larger than the expected diameter 1000 µm. The step height of the channels and the features were also calculated from the profilometry measurements and compared against the coating thickness at 500 s UV curing measured using the prism coupling refractometer. The coating thickness should determine the step height of any micro-structured features. It can be seen from Table 9.10 that the average step height of the

channels varied from 5.6 µm for the 75 µm channels to 5.7 µm for the 500 µm channels with an average difference between the calculated thickness of 5.851 microns to be 0.118 microns across the 5 channel widths. The step height of the micro-pillars, sensor spots and inlet were also calculated and found to be higher than the calculated thickness, by an average of 0.637 microns and are presented in Table 9.11.

These results show that the established fabrication process enables the reproduction of the designs of the microstructures with a precision of 98%.
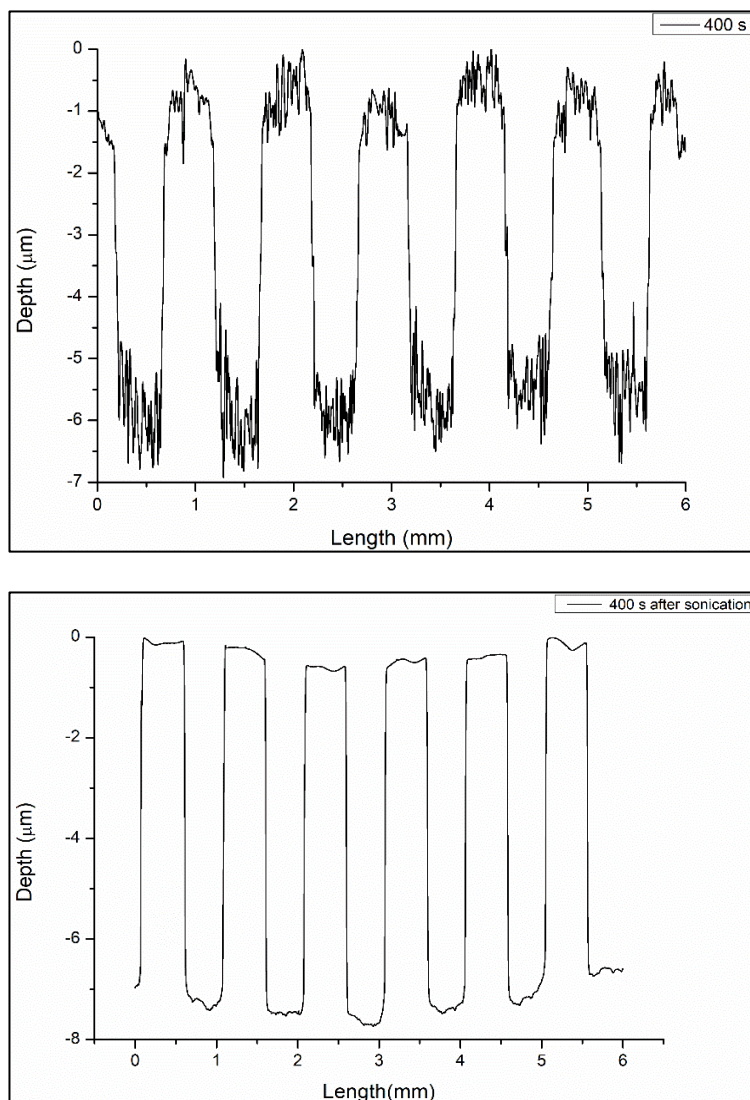
Figure 9. 12: Stylus profilometery spectra of micro-channels widths after 400 s UV irradiation, before sonication (top) and after sonication (bottom)

Irradiation time (s)	Average channel width after sonication 30 seconds (µm)	Average channel width after sonication 1 minute (µm)
200	466.26	473.16
250	430.87	473.16
300	430.87	474.15
400	405.42	477.94
500	385.87	480.70

Table 9. 6: Average channel widths for various curing times at 30 seconds and 1 minute sonication times etched in IPA

Irradiation time (s)	Average channel width at 75% Power (µm)	Average channel width at 100% Power (µm)
250	423.90	473.15
500	243.60	480.70

Table 9. 7: Average channel widths at 250 and 500 s UV irradiation and at 75 and 100% mask aligner power and 1minute sonication time etched in IPA

Expected channel Width (µm)	Average Channel Width – bottom of channels (µm)	Difference between expected and actual (µm)
75	54.4	20.6
100	73.5	26.5
250	226.7	23.3
350	325.0	25.0
500	479.0	21.0

Table 9. 8: Average widths for fabrication of micro-channels ranging from 75-500 µm on Si wafer

Features	Expected Diameter (μm)	Average Diameter (μm)	Difference (μm)
Micro-pillars	1000	1008.4	-8.4
Sensor spots	1700	1644.3	55.7
Inlet	3000	2960.5	39.5

Table 9. 9: Average diameter for micro-pillars, sensor spots and inlet for biosensor platform

Channel width	Average Step height (μm)	Difference between step height and thickness from RI (μm)
75	5.687	0.163
100	5.750	0.100
250	5.745	0.106
350	5.739	0.111
500	5.738	0.112

Table 9. 10 : Step height of the micro-channels fabricated on Si wafers

Feature	Average Step height (μm)	Difference between step height and thickness from RI (μm)
Micro-pillars	6.117	-0.326
Sensor spots	6.793	-0.942
Inlet	6.495	-0.644

Table 9. 11: Step height of the micro-pillars, sensor spots and inlet of the biosensor platform

9.3.4.2 Scanning electron and optical microscopy

In order to get a better idea of the channels widths and step heights of the linear micro-channels, SEM and optical microscopy measurements of each array of linear micro-channels were performed. Top-view and cross-section views were taken via SEM and top-views were taken using the Keyence optical microscope. Optical microscope images of the linear micro-channels at x 250 magnification can be seen for each channel width form 75 – 500 μm in Fig. 9.13. It can be noted that for each of the different channels widths, the width of mouth of the channels are between 93 and 99%, of the predicted widths fabricated on the photomask as seen in Fig. 9.9. The actual channel widths differ by roughly 20 microns for each channel width. These images further confirm the profilometry results from the previous section. This can be seen by darker areas within the channel itself that can be seen via optical microscopy in Fig. 9.13 and in the brighter areas at the edge of the channels in the SEM images in Fig. 9.14. Cross sections of the channel widths were also taken for the 75 and 500 µm channels and can be seen in Fig. 9.15. As the fabricated structures have already been sonicated, it is unlikely that these darker areas are due to residual sol-gel debris from the etching process. The sensor spots, micro-pillars and inlet of the biosensor platform were also investigated via optical microscopy and the sensor spots and micro-pillars by SEM and the corresponding images can be seen in Fig. 9.16 and 9.17, respectively. It can be seen that the walls of the channels are somewhat sloped towards the bottom of the channels, which would account for the difference between the widths of the channel at the mouth and at the bottom and further confirms the profilomtery measurements.

In summary, the SEM and optical images confirm that the established photolithography process has successfully permitted the fabrication of clean and well-defined micro-channels with dimensions of 95 – 98% close to the designed

patterns. This further confirms that the UV-irradiation conditions selected from the structural and optical characterisations analyses of sections 9.3.1 to 9.3.3 are correct for the fabrication of the desired microstructures.
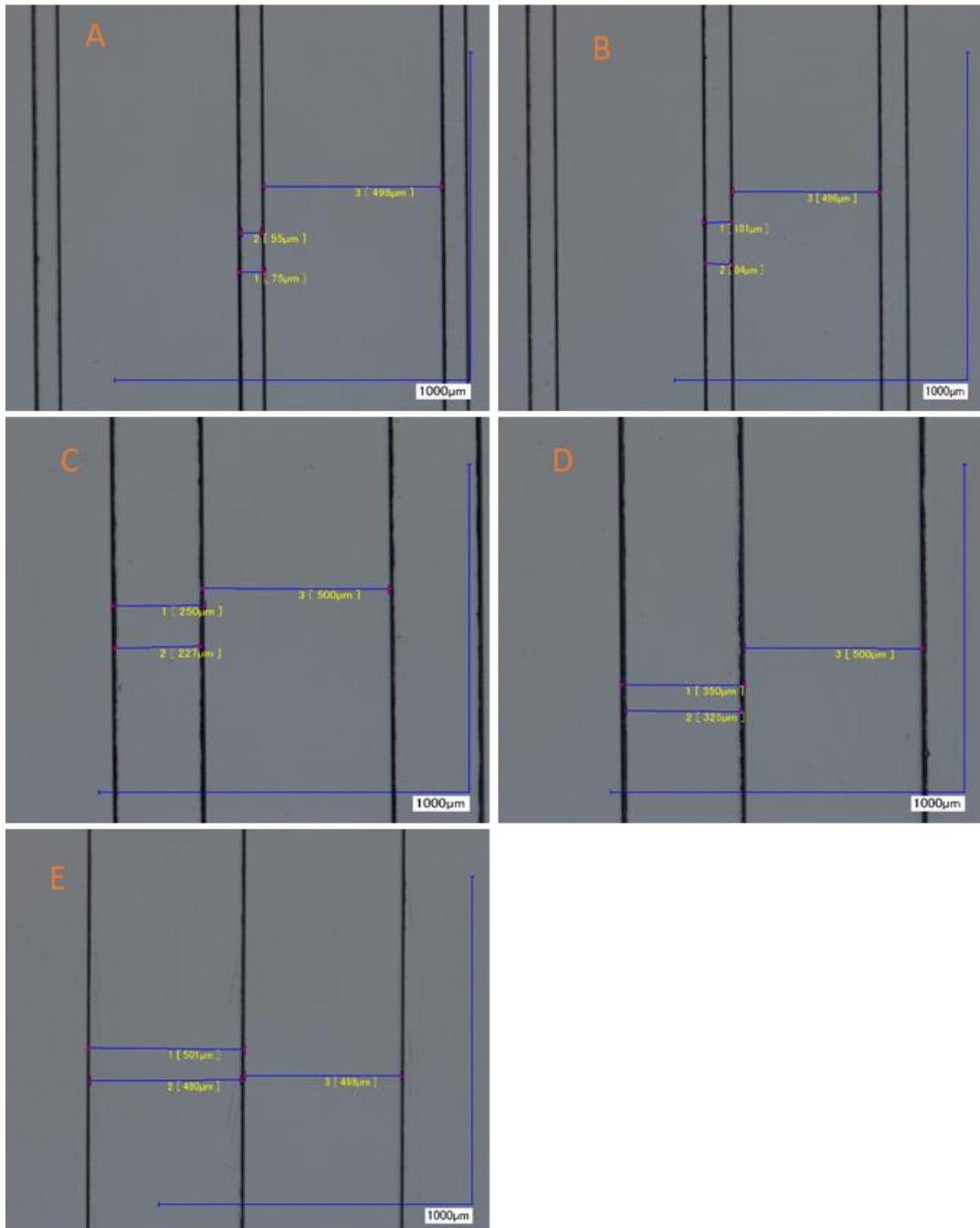
Figure 9. 13: Optical micrographs of the linear micro-channels from 75-500 microns (A-E) on Si wafers

Figure 9. 14: SEM images of the linear channel widths from 75-500 µm (A-E) on Si

wafers
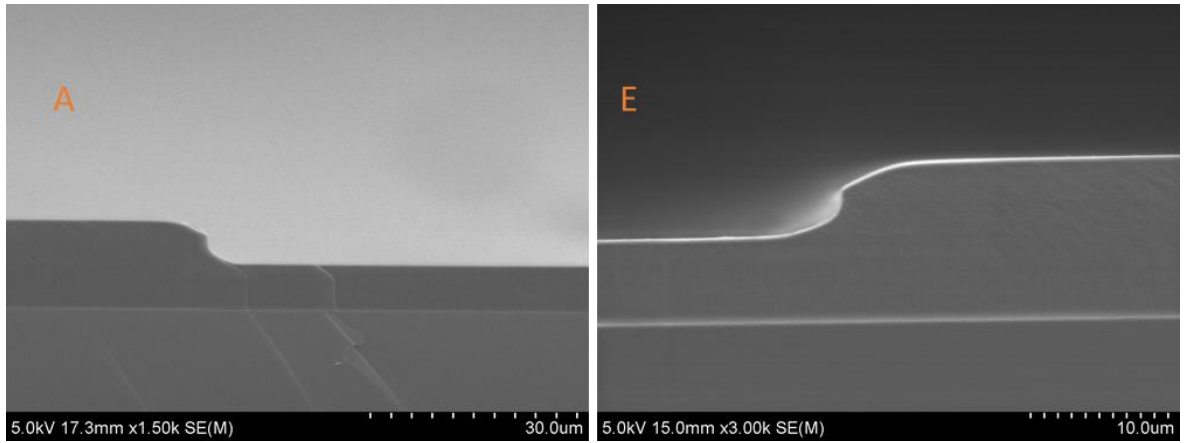
Figure 9. 15: SEM images of the cross sections of the 75 and 500 µm channels on Si wafers
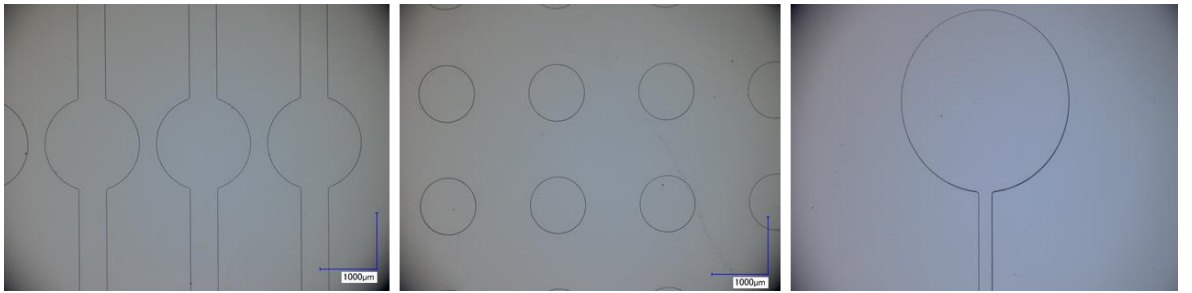
Figure 9. 16: Optical micrographs of the sensor spots, micropillars and inlet of the microfluidic platform
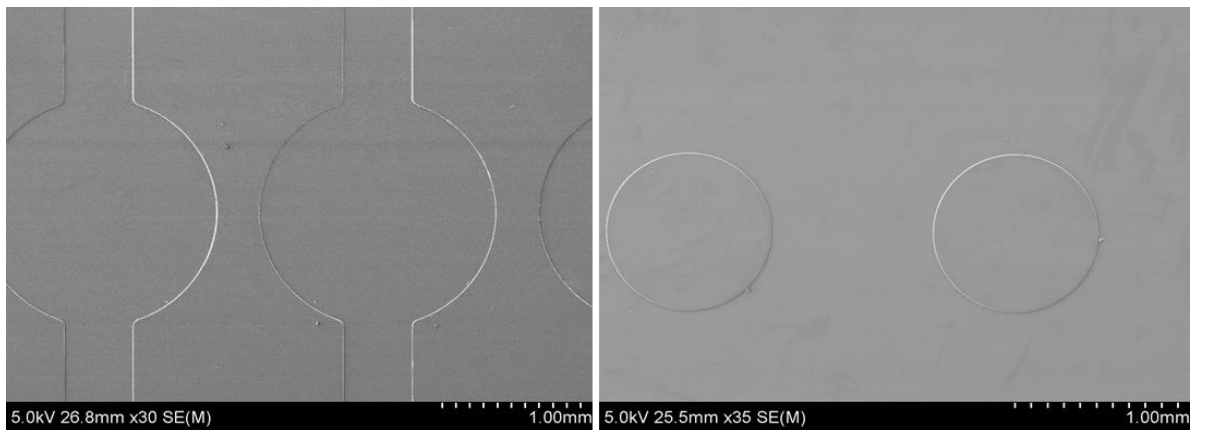
Figure 9. 17: SEM images of sensor spots, micropillars of the biosensor platform

9.3.5 Fluid Flow Characterisation

Once the microfluidic channels were fabricated, the fluid flow within the channels was characterised using a Keyence Optical Microscope. In order to produce a liquid that was easily identifiable within the microfluidic channels, deionised water was mixed with 10% v/v of green, blue and red food colouring (Goodalls Ireland).

Initial work was carried out on the samples fabricated on Al substrates using these liquids and tested on the microfluidic samples as they were fabricated. No fluid flow was observed within the channels. The channels were open to the air and were not sealed by a PDMS cap layer. To rectify this issue, the microfluidic channels were plasma treated using Air plasma for 2 min at a flow rate of 9 sccm. Air plasma was chosen due to the stability studies that were carried out in the previous chapter. The liquid was dropped onto the microfluidic samples and fluid flow was immediately seen. The 10 %v/v liquids were quite difficult to see as the small volumes (0.5µl) diluted the colour within the channels (Fig. 9.18). For this reason, the % v/v of the food colouring was increased to 50% v/v relative to the volume of deionised water to increase the depth of colours.

Although fluid flow within the channels and the platform was observed and can be seen in Fig. 9.18 and 9.19, no mathematical calculations of the fluid flow were carried out. This was in part due to the volume of liquid not being solely contained within the channels as volume of liquid was quite large for the width of the channels and there was also no cap present on the micro-channels or the platform, therefore any calculations performed would be unreliable.
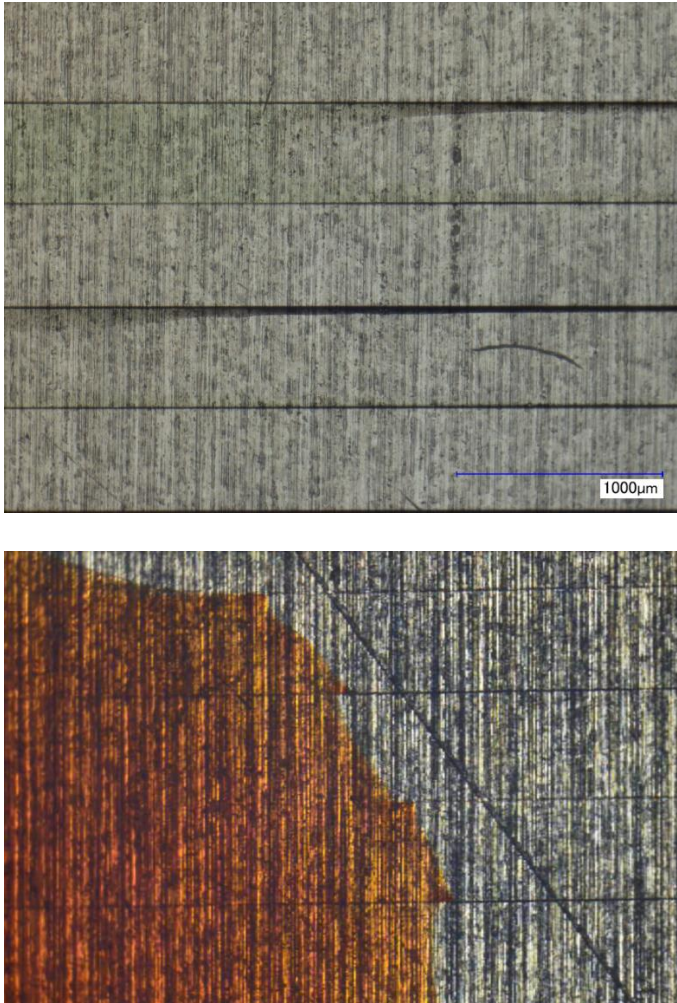
Figure 9. 18: Fluid flow in 500 µm channel on Al substrate with 10% v/v green food colouring (top) and 50% v/v red colouring (bottom)
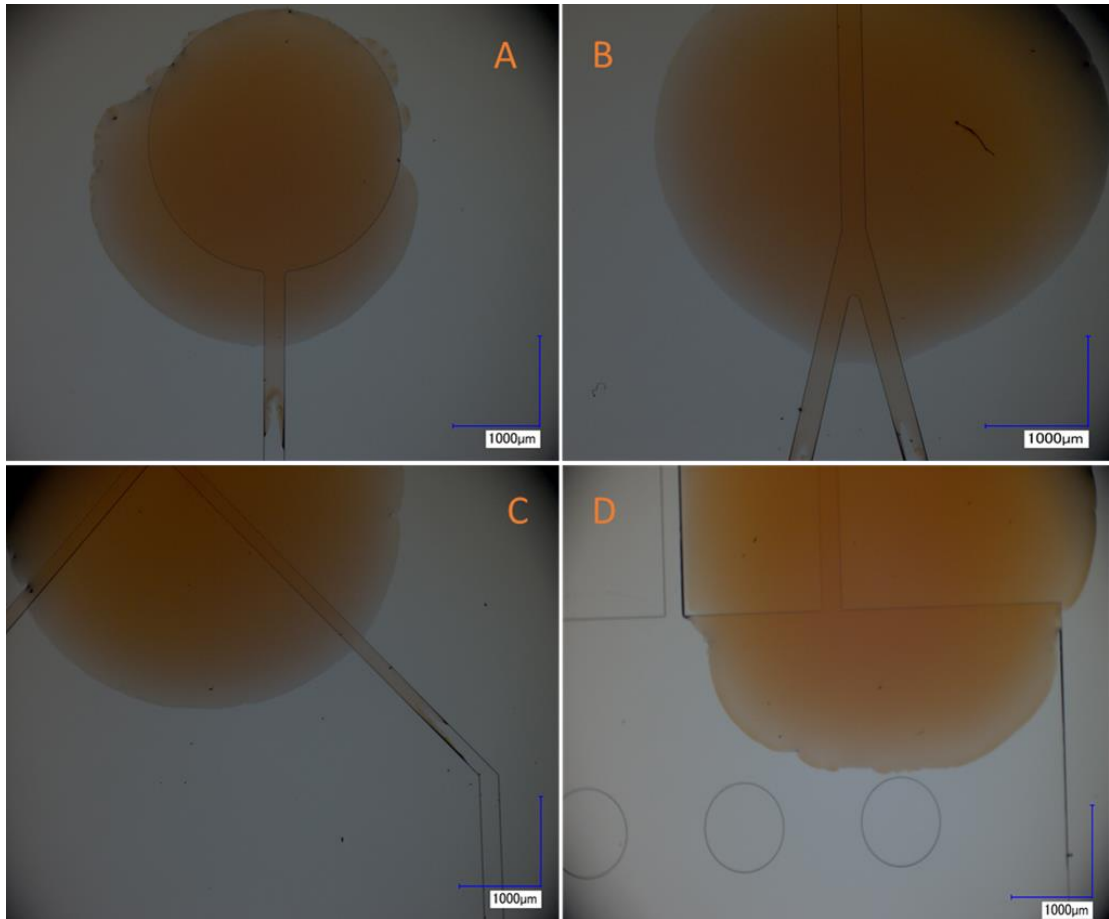
Figure 9. 19: Fluid flow within the biosensor platform on a Si wafer- A) inlet, B) and C) micro-channels, D) wicking zone

9.4 Conclusion

This chapter aimed at investigating two main objectives. First, to correlate the structure of the material to the UV-irradiation conditions and identify the fundamental aspects governing the photolithographic microfabrication of hybrid sol-gel materials. Second, to fabricate and characterise micro-channels, once the initial objective had been performed. Fundamentally, FTIR and prism-coupling results showed that radical organic photo-polymerisation reactions imply inorganic polymerisation of the silicate backbone and that this process stops due to rigidity of the hybrid network. This point is attained for a maximum UV-irradiation time of 500 s and for a UV-power of 40 mW/cm^2.

Employing these parameters, the fabrication of both linear micro-channels and a microfluidic platform using a standard photolithography process has been possible. Optimisation of the fabrication conditions by simultaneously sonicating and etching the microstructures has enabled to achieve clean microstructures as identified by SEM and optical microscopy. The fact that the fabricated microstructures showed sizes as close as 96% to the designed ones proved the success of the established fabrication process and that the correlation study of the materials structures and fabrication conditions was correct in predicting the photo-reactivity of the material. However, it is clear from this that the process could be further optimised to fabricate micro-channels with dimensions closer to the expected values. The effect of the photo-initiator on the sol-gel matrix was also investigated. It was found that the most stable concentration of PI was 5% concentration and the optimum curing time for the fabrication process was 500s UV irradiation. The fluid flow was also investigated within the microchannels, although it was not mathematically calculated.

Importantly this chapter demonstrated that it is indeed possible to fabricate micro-channels and microstructures with high resolutions using our hybrid sol-gel material and using a standard photolithography process. The next chapter will focus on the incorporation of the platform fabricated here with optical waveguides to form an optofluidic platform and to characterise this platform and test its suitability towards sensing applications.

10 Optofluidic Platform Proof of Concept and Sensing Applications

10.1 Introduction

This chapter aims at proofing the concept of the fabrication of a hybrid sol-gel optofluidic platform. It will target the integration of the microfluidic sensor platform that has been previously fabricated in chapter 9 and optical waveguides, which will be discussed further in this chapter. The results and discussion section of this chapter will be divided into the following three sections:

1. Design of the optofluidic and sensor devices.

2. Fabrication, characterisation and testing of the optical waveguides.

3. Fabrication, characterisation and testing of the optofluidic platform towards optical sensing and biosensing applications.

The optical waveguides and optofluidic platform will be fabricated via a standard photolithography process. The optical sensing capabilities of the platform will be tested using two fluorescent dyes, Atto 633 and Fluorescein sodium, both of which will be characterised using UV-Vis and fluorescence spectroscopies. The capabilities of the platform towards bio-sensing will also be carried out using a polyclonal primary IgG mouse antibody and a fluorescently labelled secondary IgG mouse antibody.

10.2 Design of the Optofluidic platform

As described in the literature review an optofluidic device consists of the integration of optical and microfluidic platforms to combine the advantages of both systems to target applications that can`t be attained by the individual technologies, such as displays, biosensors, lab-on-chip devices, lenses, and molecular imaging tools and energy.

Having successfully developed a hybrid sol-gel microfluidic device in chapter 9, the idea here would be to develop an innovative optofluidic device that will also take advantage of the versatile aspect of the sol-gel technology in tuning the functionality and optical properties of the materials.

Therefore, in researching a **monolithic** hybrid sol-gel optofluidic device, our investigations have led us to the design of an innovative waveguide-based optofluidic device that will integrate optical waveguides onto a microfluidic platform, as sketched in Fig. 10.1.
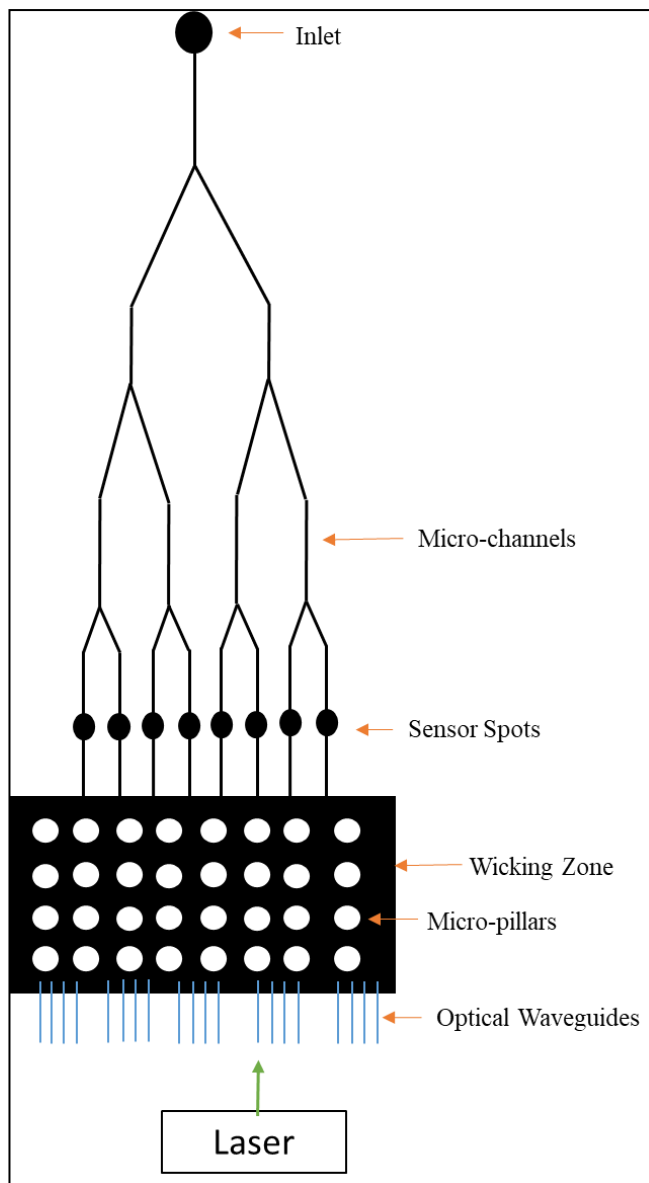
Figure 10. 1: Representation of the optofluidic platform

In this platform, the optical waveguides are coupled to a laser which acts as an optical source to illuminate the sensing zones namely the wicking zone of the microfluidic platform. Therefore, it may be possible to optically excite fluorophores immobilised in the wicking zone, which would then re-emit light.

Unlike microfluidic devices where the only required property for the material is a high surface energy, light propagation within optical waveguides can only occur when total internal reflection (TIR) is taking place at the interface between the core and the cladding of the waveguide, as sketched in Fig. 10.2. This phenomenon depends on the optical properties of the materials, the main property being the refractive index contrast (Δn) between the core of the waveguide and its cladding. Wavelength can impact TIR due to index dispersion[2,173–175]. TIR and self-consistency of the wave in the guide are the two conditions for light transverse confinement in the core region. The confined light can propagate along the waveguide axis and is then called a propagation mode. The higher the index difference, the core transverse size and the optical frequency, the higher the confinement and thus the number of propagation modes. The 2D intensity profile and the associated effective index of each mode can be computed for a 3D waveguide by solving Maxwell's or Helmoltz's equations using numerical schemes as finite differences or finite elements methods.

According to results reported in these studies, single mode waveguiding in the visible range with enough confinement occurs for a 4 to 7 μm^2 section squared waveguide when Δn comprises between 3.10^{-3} to 10.10^{-3}. As the objective in this chapter is to demonstrate the feasibility of the concept, a detailed study of the exact optical conditions for a specific wavelength will not be undertaken.
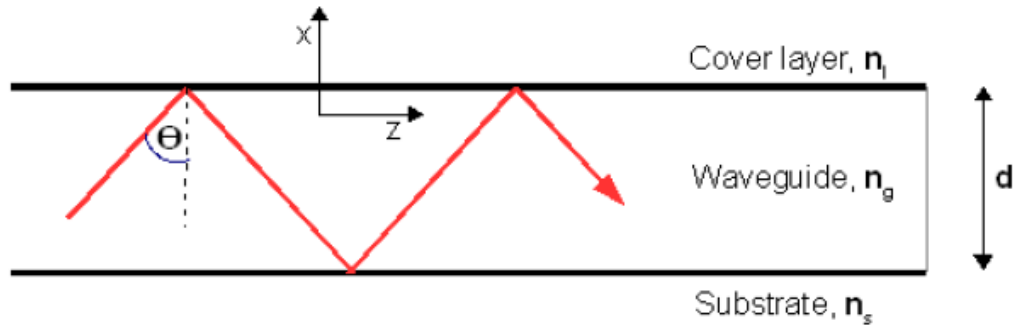
Figure 10. 2: Representation of the TIR phenomenon in single mode waveguide

10.3 Materials Synthesis

In order to ensure that there was a Δn of a minimum of 0.003 between the buffer/protective layer and the guiding layer used to fabricate the optofluidic platform, four different materials were synthesised, and their refractive index values were measured. The formulations for all 4 materials are shown in table 10.1 below. The hydrolysis degree for all formulations was fixed at 50%. It should also be noted that material D is the reference sol-gel material that has been used throughout this work.

Material Name	MAPTMS (mol. %)	ZPO /MAAH (mol. %)	Theoretical Hydrolysis Degree against total alkoxide groups (%)
A	84.39	15.61	50
B	82.65	17.35	50
C	81.64	18.36	50
D	80	20	50

Table 10. 1: Sol-gel formulations for the materials used in the fabrication of optical waveguides

10.4 Results and Discussion

10.4.1. Refractive Index Measurements

Four different formulations were synthesised and their R.I values were measured. The sol-gel materials were deposited onto a Si wafer via spin coating at 900 rpm. The coatings were then placed in an oven at 100℃ for 10 minutes to ensure both the stabilisation of the coatings and that they were also "touch dry". The wafers were then cleaved into 4 and subjected to varying UV irradiation times- 0, 50, 100, 250, 500 and 650 s respectively. The RI values for each formulation were then plotted against the UV irradiation time and can be seen in Fig. 10.3 below. As previously observed in chapter 9, for each material, the RI increases rapidly from 0 up to 250 s of UV-irradiation and stabilises within the measurement errors for higher exposure times. Interestingly, all materials show an increase of RI comprised between $6.5.10^{-3}$ to 7.10^{-3} from the lowest to the highest exposure times, achieving RI values of 1.507, 1.509, 1.511 and 1.512 for materials A-D, respectively. This suggests a similar behaviour takes place during the polymerisation process and that the only parameter governing the RI value is the content of zirconium. The likely explanations for this phenomenon would be in relation with the increase of the density of the materials or the polarisablity as the content of zirconium increases.

The thickness of the coatings was also measured as a function of UV curing time and can be seen in Fig. 10.4. It can be observed that all coatings swell with an average value of 5% against their initial thickness. Nevertheless, the fully cured coatings exhibit thicknesses comprised between 5.5 and 7 μm, thus verifying the thickness values used in the optical simulations described in the above reference.
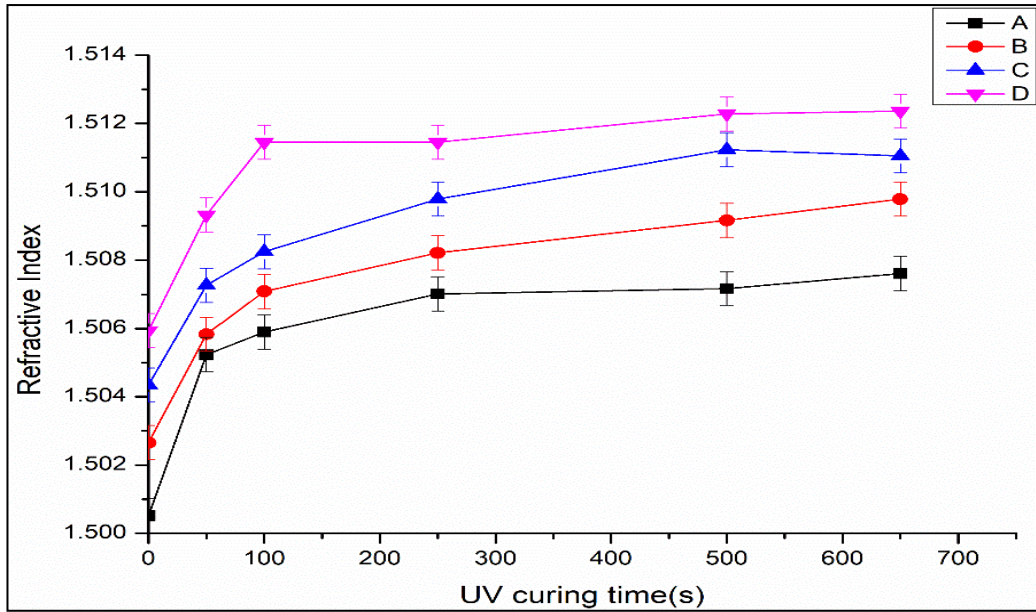
Figure 10. 3: UV curing time vs RI for materials A-D
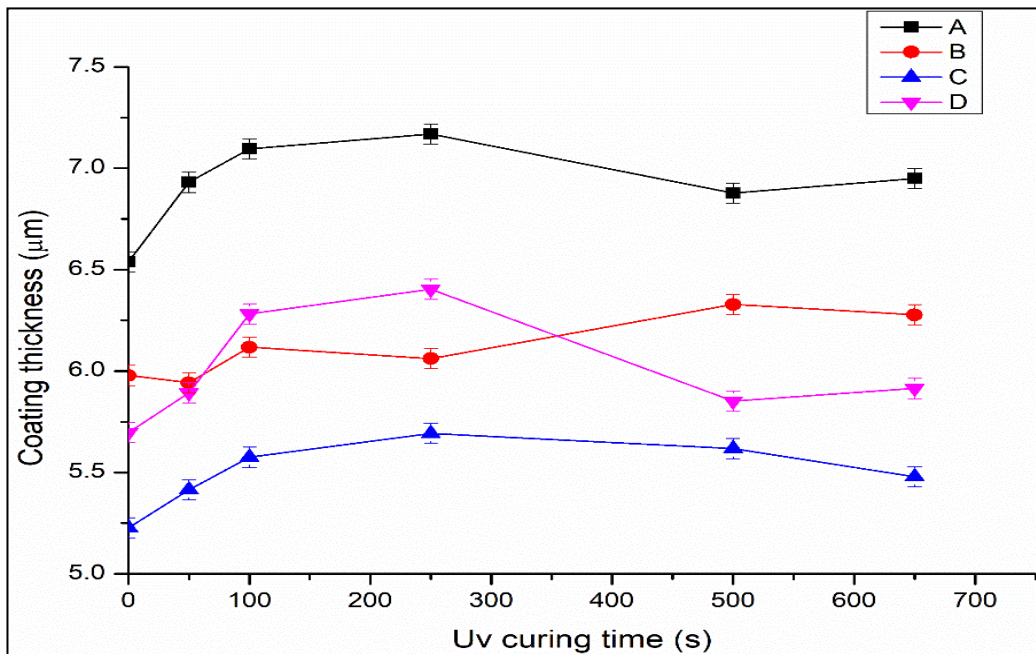
Figure 10. 4: Coating thickness vs UV curing time for all materials A-D

10.4.2 Waveguide Fabrication

The two materials that were selected for the fabrication of the optical waveguides were

materials B and D. Material B was used for the buffer and the protective layers and

material D was used for the guiding layer. These two materials were selected due to the RI difference of 0.0035 between the two materials.

The layers were deposited by spin-coating onto a silicon wafer substrate. Prior to deposition, the environment of the spin-coater was saturated with IPA for 3 minutes before the sol-gel was deposited onto the silicon wafer. About 5 ml of sol-gel was directly filtered onto the silica wafer. The spin-coater was then ramped up to speed for 10 seconds at 200 rpm. The sol-gel was then spun at 1000 rpm for 35 seconds to ensure a coating thickness of 5 – 6 microns. The spin-coater was then ramped down to 250 rpm to let the solvent evaporate off the surface of the coating. This layer was called the buffer layer and was stabilised in a Kloé UV KUB for 500 seconds to achieve the desired RI.

After the BL was stabilised a second sol-gel layer called the guiding layer (GL) was deposited in the same manner as the BL. Once this layer was deposited it was placed in an oven for 10 minutes at 100℃ to ensure the coating was touch dry without provoking condensation of the inorganic network and maintain UV-photo-reactivity. The wafers were then placed into the UV chamber and exposed for 500 seconds at a power of 40 mW/cm^2 to achieve the required RI contrast with the BL. The etching process involved placing the wafers in a petri dish containing ethanol for 2 min with a simultaneous sonication to minimise the residual debris in the non UV-exposed areas of the wafer. Finally, the wafer was placed into an oven at 100℃ for 2 mins to ensure the complete evaporation of the solvent.

10.4.3 SEM analysis

Top and cross section views were taken of the waveguide channels. The sol-gel coated silicon wafers were cleaved, and sputter coated with platinum/palladium to achieve a thickness of 6.1 nm and minimise charging.

The buffer layer showed a thickness of about 4 microns at a spin speed of 1000 rpm (Fig. 10.5). To increase optical isolation from the Si, the spin speed was decreased to 800 rpm for both the buffer layer and the guiding layer.

The edges of the waveguides were found to be wavy and not completely straight as can be seen in Fig. 10.5. Initially this was thought to be caused from the insufficient etching but was found not to be the case. Upon further examination of the waveguide photomask under an optical microscope, degradation of the waveguides was evident, thus explaining the edge pattern of the fabricated waveguides.
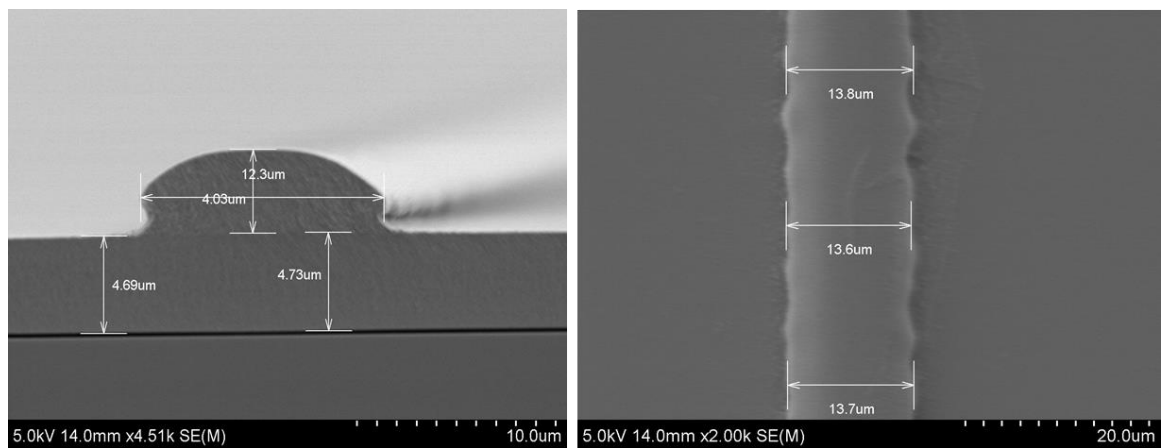
Figure 10. 5: Scanning electron micrographs of optical waveguides – cross section and top view

10.4.4 Optical Waveguide Testing

The waveguides were tested to ensure the light was properly propagating within the cores of the waveguides. The waveguides were coupled to an optical fibre and tested using a red laser diode in the visible region with a wavelength at 632 nm using the set up presented in Fig. 10.6. This work was carried out with the help and guidance of Dr Arun Mallick of the Photonic Research Group in TU Dublin. The optical fibre was coupled to the waveguide and the output was narrowed using a x10 objective lens and shone onto a white background. The propagation of light scattered from the fabricated optical

waveguide can be seen in Fig. 10.7 and the output from the waveguide can be seen via the appearance of a circular red dot in Fig. 10.8. It can be observed in Fig. 10.7 that the light is confined within the waveguide, demonstrating that the Δn we defined based on the previous studies (as explained above) is sufficient to avoid important light dissipation within the cladding. However, from this result, it is impossible to identify if the waveguide operates in a singlemode or multimode manner but importantly, we highlighted that the light is guided in a linear waveguide and could be used to shine onto a sensing spot where a fluorophore is immobilised.
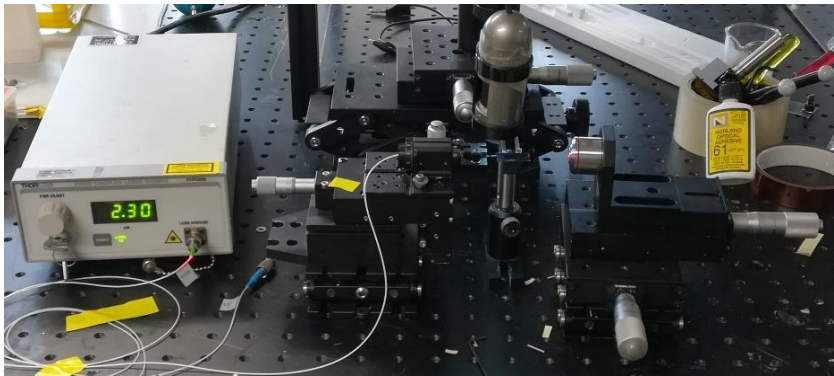
Figure 10. 6: Optical set up to for the waveguide testing
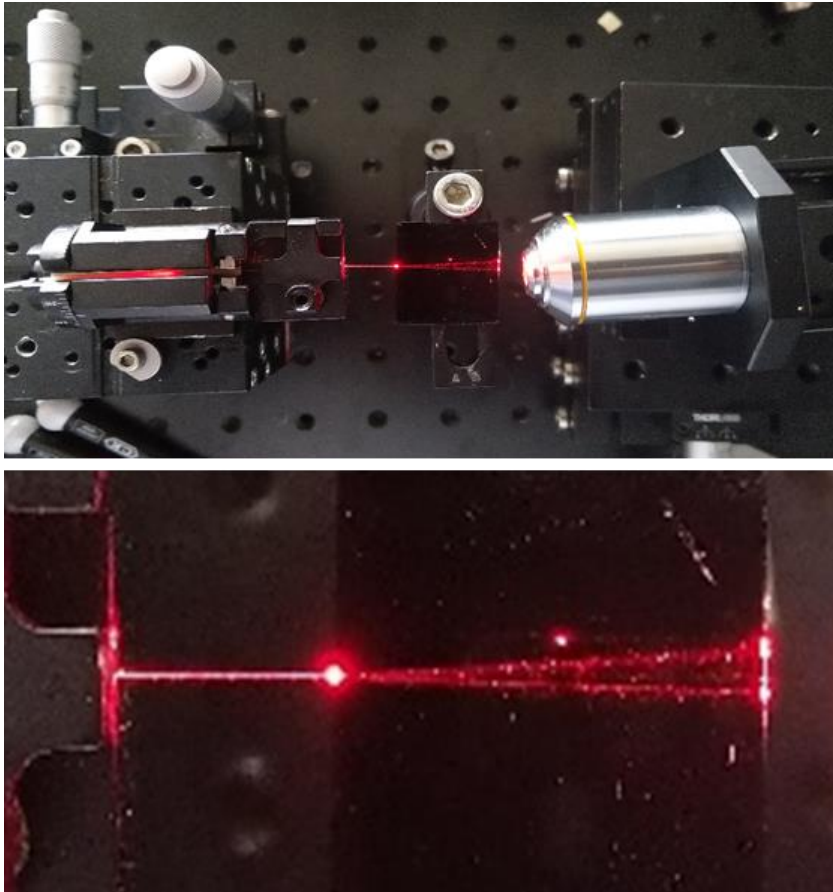
Figure 10. 7: Top view of the propagation of light within the waveguide
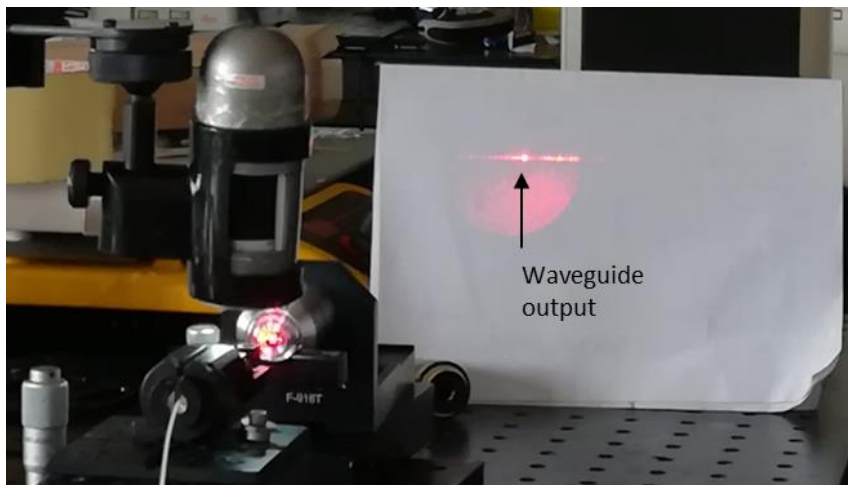
Figure 10. 8: Output from the propagation of light through the fabricated waveguides

10.4.5 Optofluidic Platform Fabrication

Once the optical waveguides had been fabricated and tested, the optofluidic platform was fabricated employing the process sketched in Fig. 10.9. The process consisted of the following steps:

1. Buffer layer deposition and stabilisation – Material B was deposited onto a Si wafer at a spin speed of 900 rpm and subsequently stabilised by UV-irradiation for 500s.

2. Optical Guiding layer – A second layer was deposited using the same spin speed as above but, material D was used. The layer was stabilised for 10 minutes at 100°C in an oven before being photo patterned. To ensure only a specific section of the wafer was photo-patterned with the waveguides, a portion was "blocked off" using a sample of Al. Once the sample had been photo-patterned, it was then etched in IPA and sonicated for 1 minute to ensure removal of the non-polymerised material.

3. Microfluidic/protective layer deposition and stabilisation – A second layer of material B was deposited under the same conditions as the previous layers. The role of this layer is for the microstructuration of the micro-channels, and to act as a protective cladding for the optical waveguides. This layer was stabilised at 100°C for 10 minutes to ensure touch dry coatings, the microfluidic sensor platform photomask was then placed onto the Si wafer, taking care to ensure correct placement of the waveguides within the wicking zone of the sensor platform. The sample was then photo-patterned using the mask aligner for 500s. The sensor pattern was simultaneously etched and sonicated in IPA for 1 minute and rinsed with IPA to remove any residual sol-gel debris. The platform was then placed in an oven at 100 degrees for 2 minutes to evaporate any remaining solvent. An optical micrograph of the optical waveguides within the wicking zone of the sensor platform can be seen in Fig. 10.10.
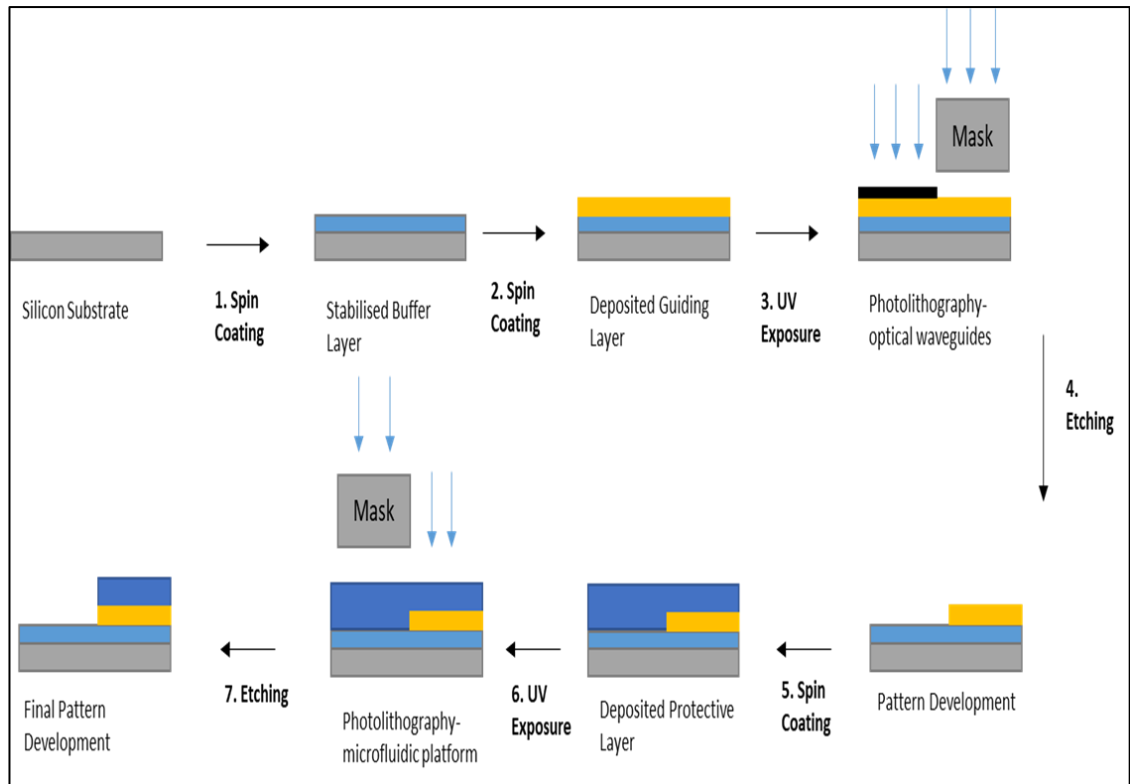
Figure 10. 9: Schematic of the fabrication of the optofluidic platform
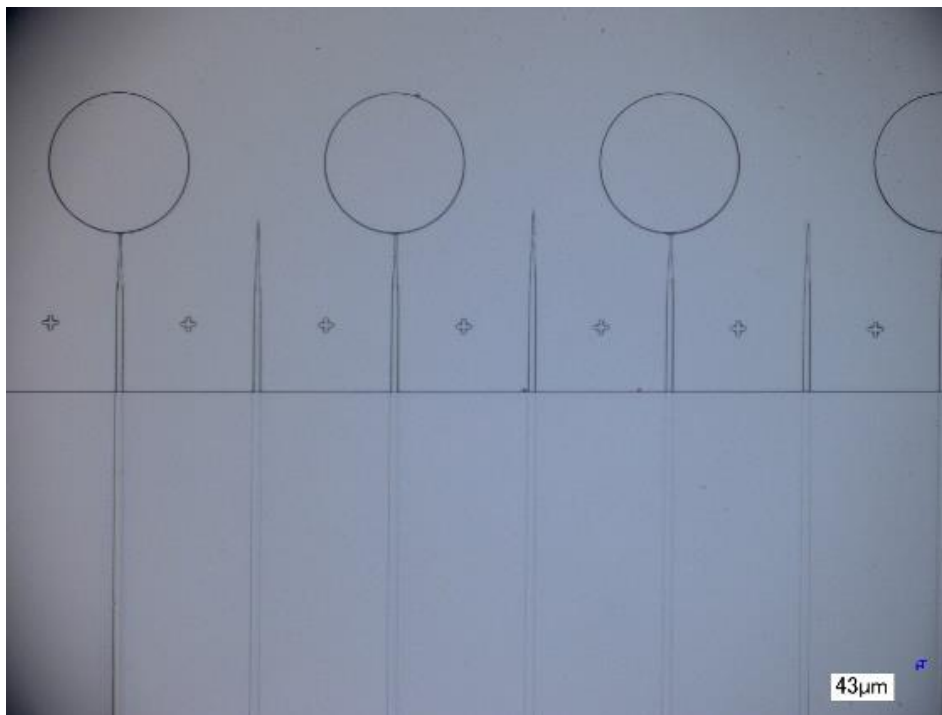
Figure 10. 10: Optical micrograph of the optical waveguides within the wicking zone of

the sensor platform

10.4.6 UV-vis and fluorescence Spectroscopy

UV-Vis and fluorescence spectroscopy were run on both the sodium fluorescein and Atto 633 dyes in order to get a better idea of absorption and emission spectra and their respective optimum excitation wavelength (λ_{max}). The UV-Vis absorption spectra of both fluorescein sodium and Atto 633 were measured using a Perkin Elmer Spectrometer in the 200 – 700 nm spectral range, with a concentration $1.65x10^{-5}$ g/ml and $1.2x10^{-5}$ g/ml, respectively.

It can be seen that fluorescein sodium exhibits 4 absorption bands located at 325, 375, 450 and 486 nm (λ_{max}). Having defined the λ_{max}, emission of fluorescein sodium was recorded employing a close excitation source tuned at 480 nm and the related spectrum is presented in Fig. 10.11. It can be observed that upon excitation at 480 nm, the sodium fluorescein exhibits a single emission band located in the spectral range 480 – 680 nm with a λ_{max} located at 522 nm. The overlap between the emission and absorption is confined within the spectral range between 480 and 525 nm. Therefore, any emission recorded outside this spectral range can only be attributed to fluorescence phenomena with no effect from the absorption.

The Atto 633 dye exhibits absorption in the range 290 – 685 nm with two absorption bands located at 580 and 633 nm (λ_{max}) and is presented in Fig. 10.12. The absorption below 500 nm and above 750 nm account for less than 5 % of the overall absorption. Employing an excitation wavelength of 633 nm Atto 633 is found to emit in the red region from 600 to 820 nm and shows a λ_{max} at 663 nm. The overlap between the emission and absorption can be seen within the spectral range between 600 and 680 nm. Therefore, any emission recorded outside this spectral range can only be attributed to fluorescence phenomena with no effect from the absorption.
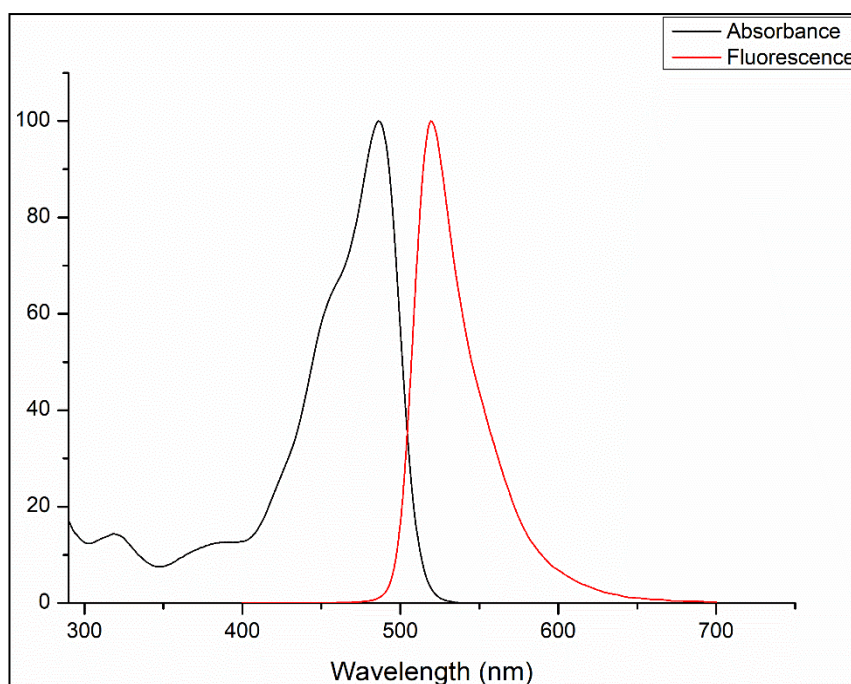
Figure 10. 11: Absorbance and emission spectra of Fluorescein Sodium dissolved in water and a concentration of 6.6×10^{-3} g/ml. Emission recorded with an excitation at 480 nm
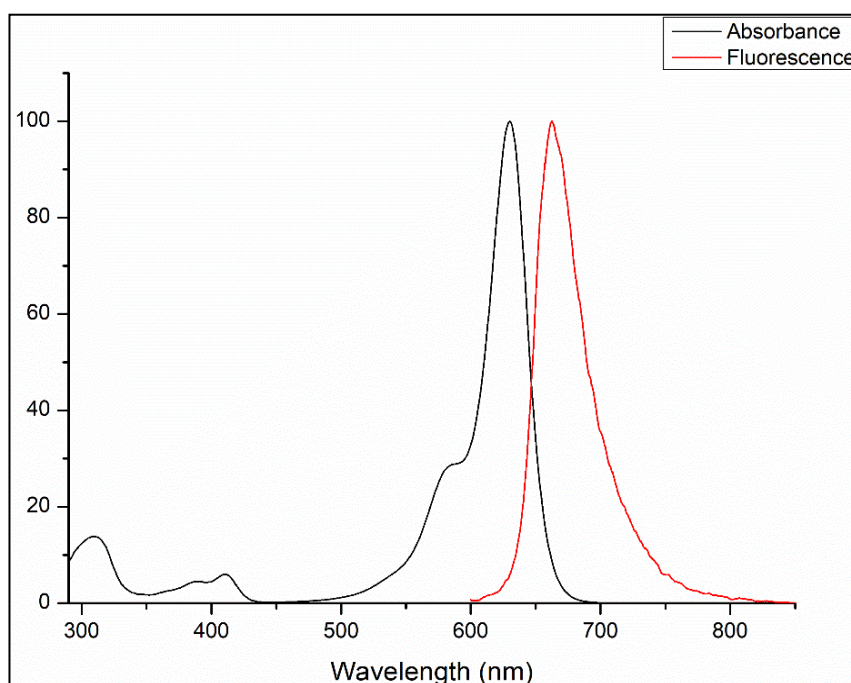
Figure 10. 12: Absorbance and emission spectra of Atto 633 dissolved in water and a concentration of 1.2×10^{-5} g/ml. Emission recorded with an excitation at 633 nm

10.4.7 Optofluidic platform testing – Optical sensing applications

The fabricated optofluidic platform was tested using an available green laser line tuned at 532 nm excitation and the emission of fluorescein sodium dye was investigated. In order to do this an optical bench comprising of lasers, optical mirrors, confocal lenses and 3D adjustment platforms all mounted on an optical table were used, as represented in Fig. 10.12. A schematic of the laser source, platform and spectra analyser are presented in Fig 10.13. To investigate the effect of content of matter and the possible impact this may have on the radiative and non-radiative emissions, three different concentrations of fluorescein sodium dissolved in water were used, A) 6.6×10^{-3}g/ml, B) 1.65×10^{-4}g/ml and C) 1.65×10^{-5}g/ml. The green laser beam tuned at 532 nm was narrowed using a series of confocal lenses and the optofluidic platform was placed as close to the beam as possible. The beam was then aligned with a waveguide and the output was measured using a spectrometer. The intensity of the laser was set to 0.2 and 0.1 mW. 0.5 µl of each concentration of the dye was pipetted directly onto the output of the waveguide and the emission spectrum was measured for a total of 5 minutes for each concentration and for both intensities and can be seen in Fig 10.15 and 16, respectively.

The emission of sodium fluorescein appears to rely strongly on the concentration, excitation power and exposure time. Prior to depositing the dye on the platform at 0 s, a single sharp band can be seen with a λ_{max} at 532 nm which is the output from the laser itself and can be seen in Fig 10.14. After deposition of the dye, it can be seen that this band undergoes a deformation towards higher wavelengths along with the appearance of a large band centred at 550 nm. As this band was absent in the absorption spectrum it can only be due to the emission of the sodium fluorescein. Therefore, the developed waveguide-based optofluidic platform effectively operates as an exciting platform for the recognition of fluorescent dyes. The intensity of the band can be seen to decrease over

time from 15 s – 5 min, which may be due to photobleaching or fading of the fluorescein sodium molecule[176]. As the excitation wavelength used was 532 nm and not 480 nm as seen in Fig. 10 12, the shift to a higher wavelength can be expected as the excitation wavelength and concentration of the dye molecule both have an effect on the emission spectra[177]. For concentration B of the fluorescein sodium dye a similar spectrum can be seen -although with the appearance of a 3rd band centred at 520 nm. Again, the intensity of all bands can be seen to decrease over time. For concentration C- the lowest concentration of the dye, there is very little to no decrease in intensity over time for the band centred at 520 nm while the band centred at higher wavelength of 550 nm has almost disappeared. It is worth noting that the intensity of the bands are much lower compared to the first two concentrations. This decrease in intensity of the emission bands as the concentration decreases may be due to a phenomena known as re-absorption or re-emission. Which is due to the possible excitation of the dye molecules by the absorption of a photon previously emitted by another dye molecule[178]. It is clearly evident that two behaviours are observed as the concentration of the dye decreases. Firstly, the appearance of an emission band at 520 nm takes place, the maximum intensity of which is seen for sample B. As this band is absent for the sample A, the highest concentration of the dye, it is probably due to the occurrence of non-radiative emission between neighbouring molecules and due to energy transfer between the molecules[177].

Secondly, the intensity of the band located around 532 nm is at a maximum for sample B followed by sample C and finally by sample A. These results suggest that it is very likely that as the concentration of the dye increases, competition between radiative and non-radiative emission takes place. Indeed, this phenomenon is known as non-radiative transfer due the proximity of the dyes caused by higher concentrations.

The emission spectra for the same concentrations of the dye but at a lower intensity of 0.1 W can be seen in Fig. 10.16. A similar trend can be seen with the intensity decreasing over time, the intensity of the fluorescein peak is also much lower than at higher intensities. This shows that the intensity of the emission from the fluorophore is dependent both on the concentration used and on the intensity of the laser used to excite the fluorophore in the dye. The fluorescence emission of fluorescein sodium at a concentration of $6.6x10^{-3}$g/ml on the optofluidic platform can be seen in Fig. 10.19.

The Atto 633 dye was also used with the platform with two concentrations: A) $1.2x10^{-5}$ g.ml and B) $1.2x10^{-6}$ g/ml, and excited with a red laser tuned at 632 nm at an available power of 0.1W. The emission spectra of the output of the red laser itself is presented in Fig 10.17. The emission spectra for both concentrations can be seen in Fig. 10.18 below. At the highest concentration A, there is a broad band centred at 663 nm can be seen that decreases in intensity over time. Again, this may be due to photo-bleaching of the molecule. For the lower concentration B, the band centred at 633 nm is still visible although at much lower intensities and the decay over time is not as evident. A second peak centred at 632 nm, which is the emission from the output of the waveguide, is also visible and also increases over time as the band at 663 nm decreases.

In summary, the results reported here show that the developed optofluidic device has the potential to act as waveguide-based fluorescent biosensor platform. Based on these results, the next step would consist of investigating the potential of our platform towards bio-sensing applications. For this purpose, the detection of fluorescently labelled antibodies usually employed in medical diagnostic applications will be performed in the next section.
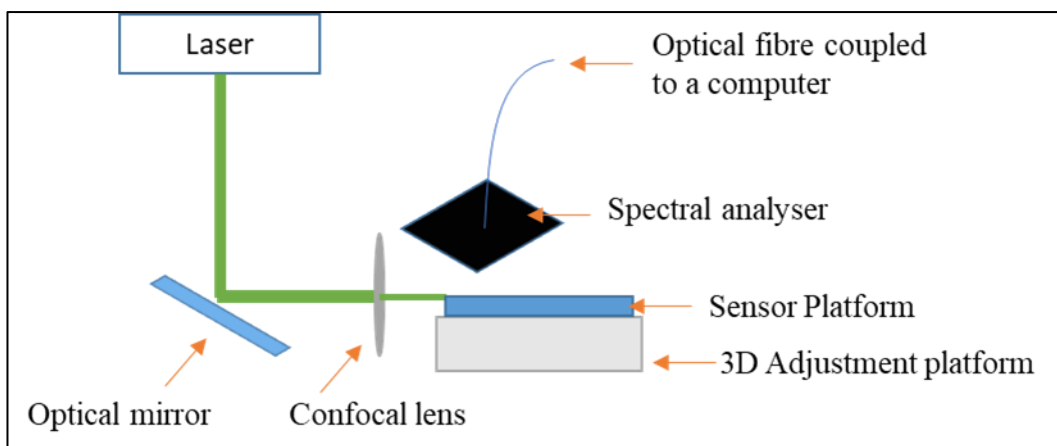
Figure 10. 13: Schematic representation of the optical set up for fluorescence studies
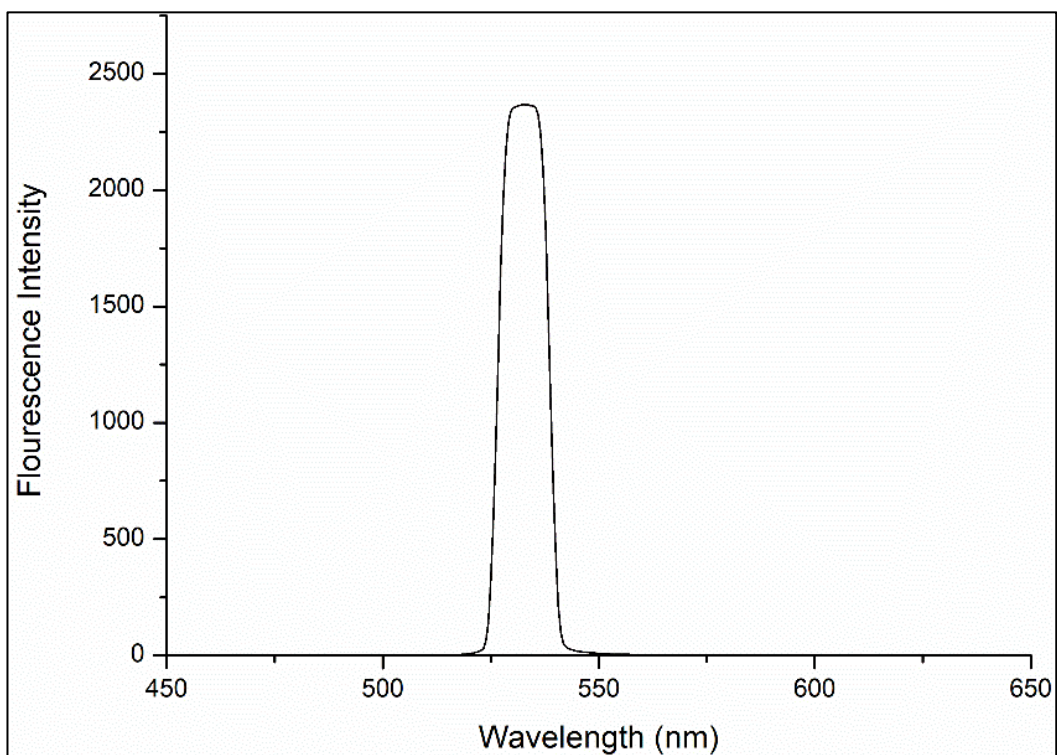
Figure 10. 14: Emission spectrum from the green laser output at 532nm at 0s dye

emission
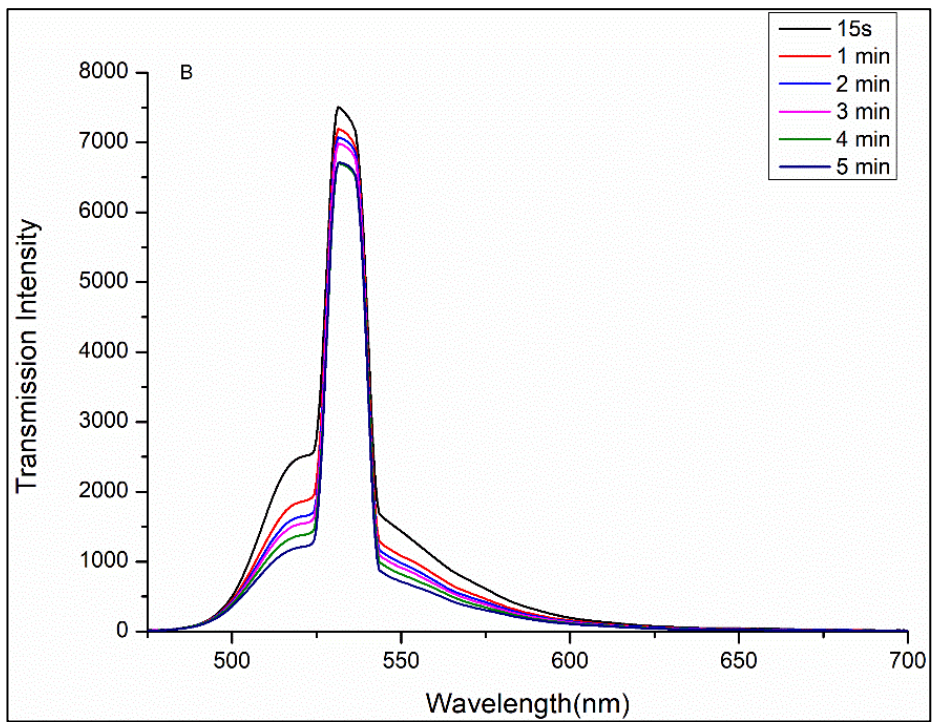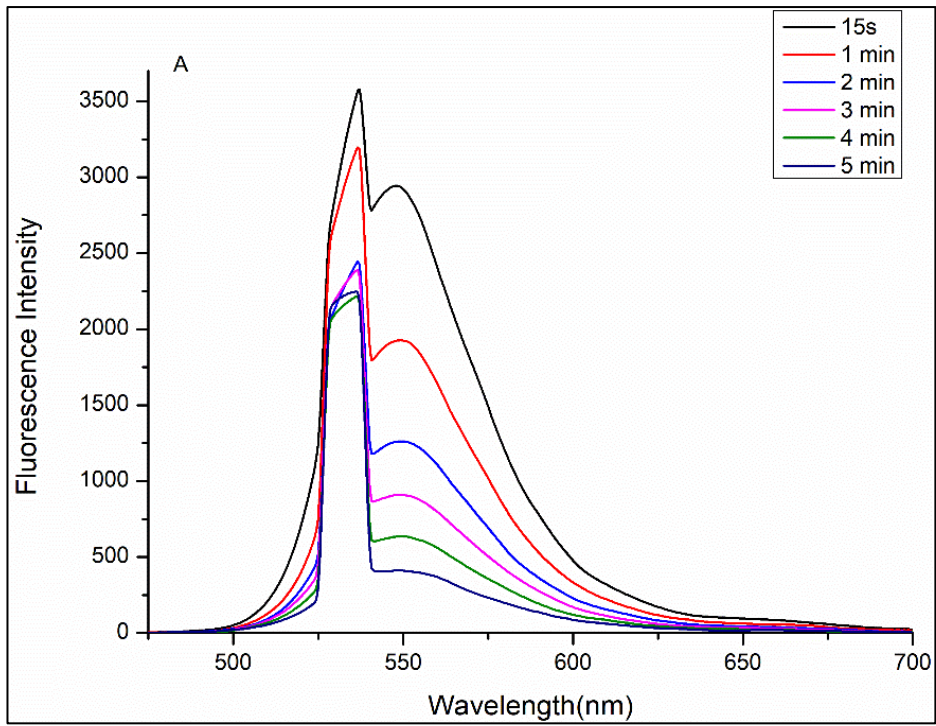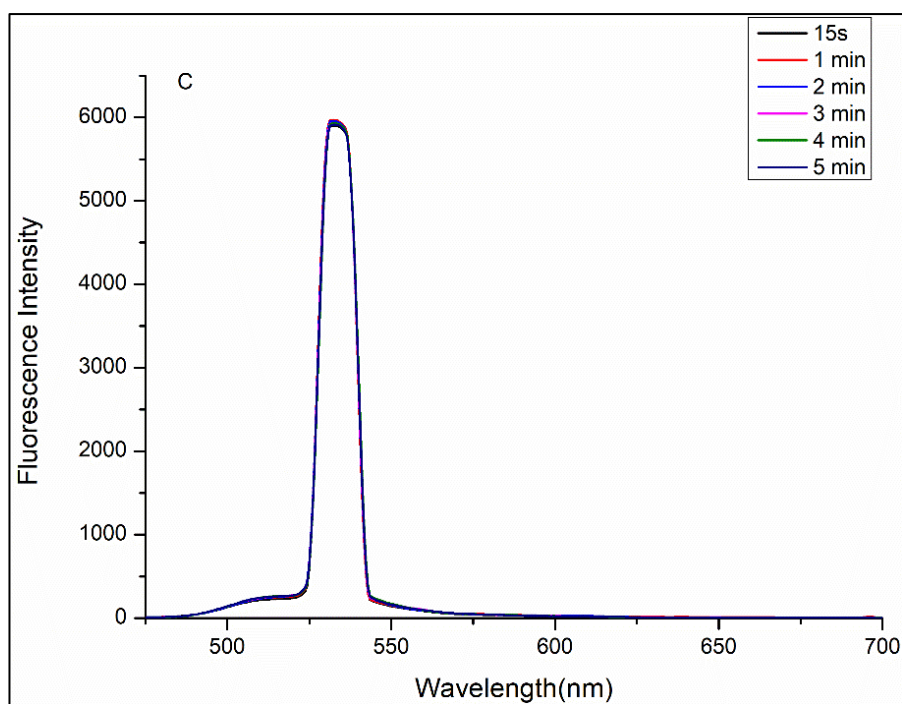
Figure 10. 15: Emission spectra of fluorescein sodium dye at concentrations A) 6.6×10^{-3} g/ml, B) 1.65×10^{-4} g/ml and C) 1.65×10^{-5} g/ml at 0.2 W
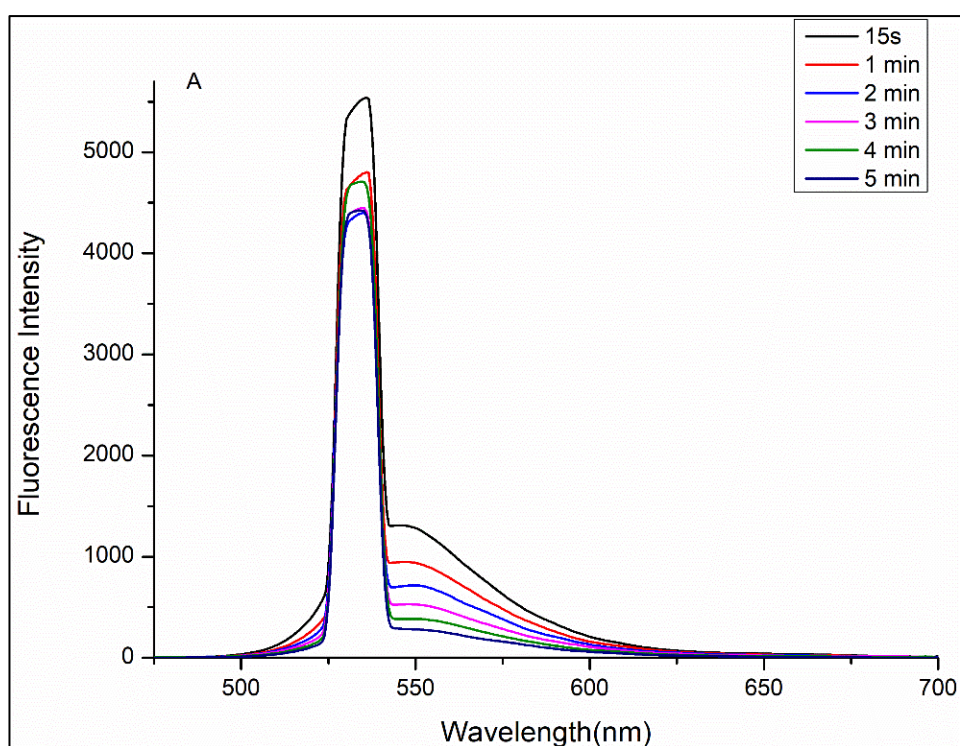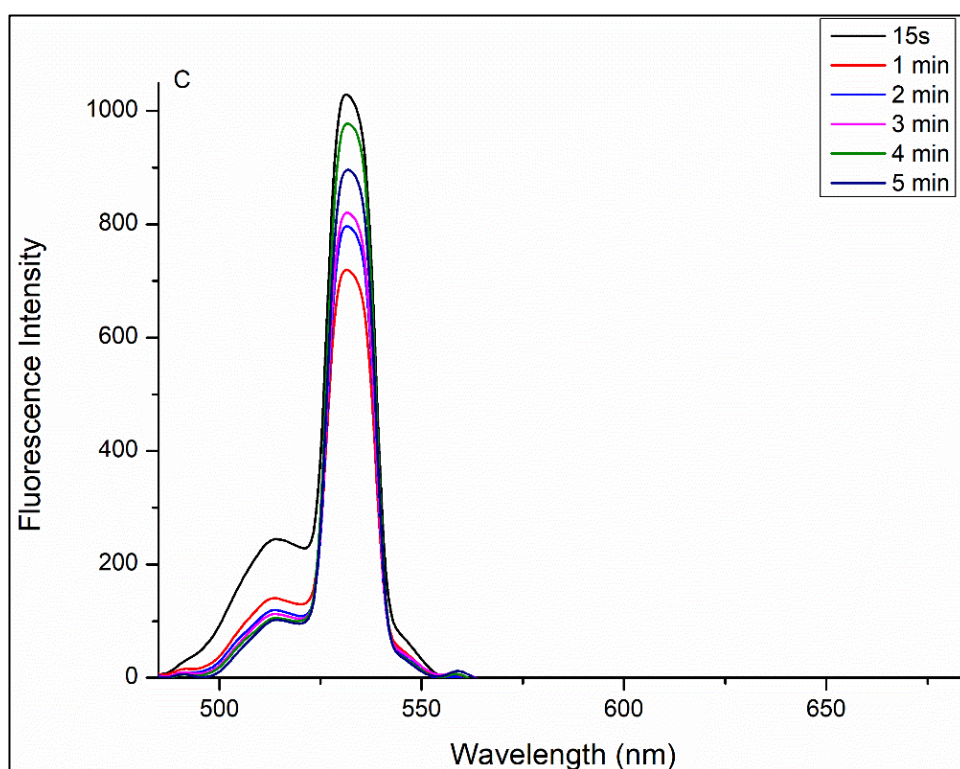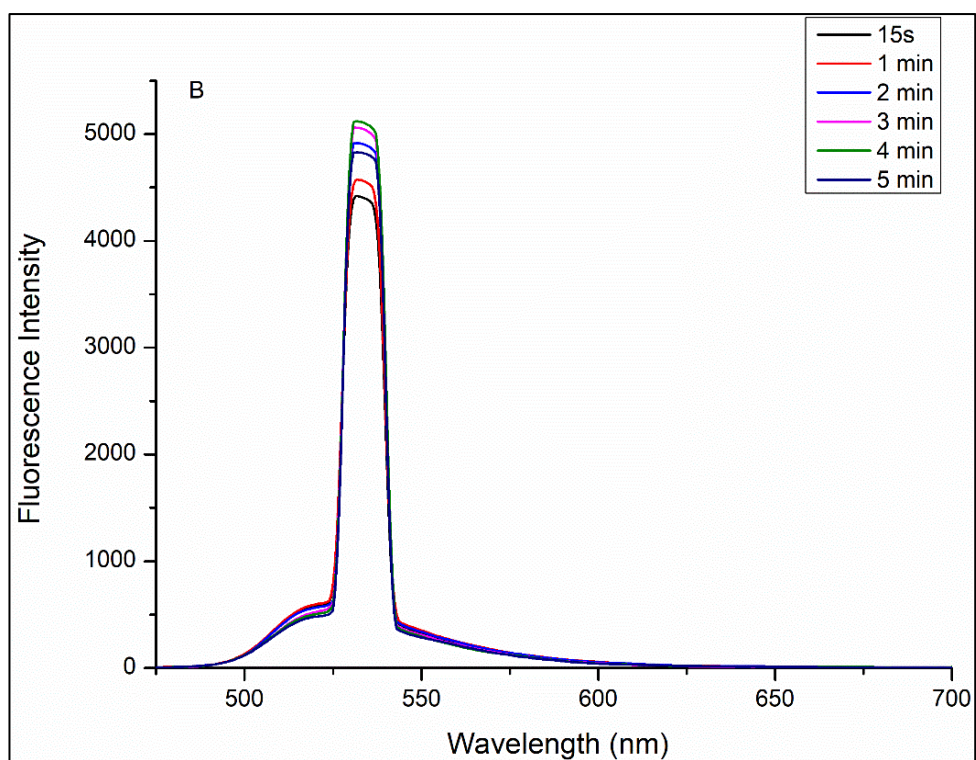
Figure 10. 16: Emission spectra for fluorescein sodium dye at concentrations A) 6.6x10^{-3} g/ml, B) 1.65x10^{-4} g/ml and C) 1.65x10^{-5} g/ml at 0.1 W
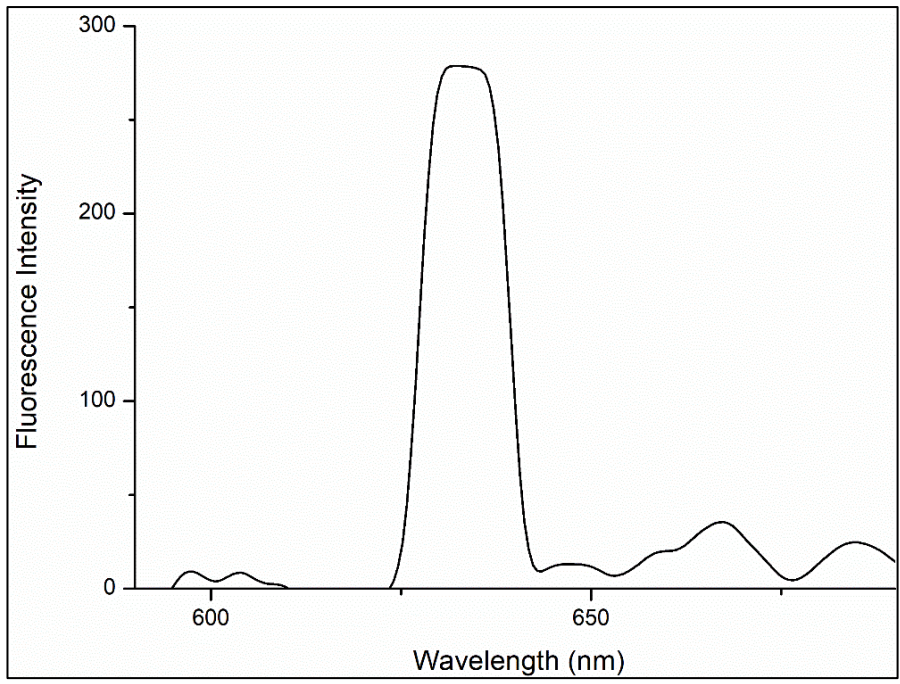
Figure 10. 17: Emission spectra of red laser output at 632nm at 0s dye emission
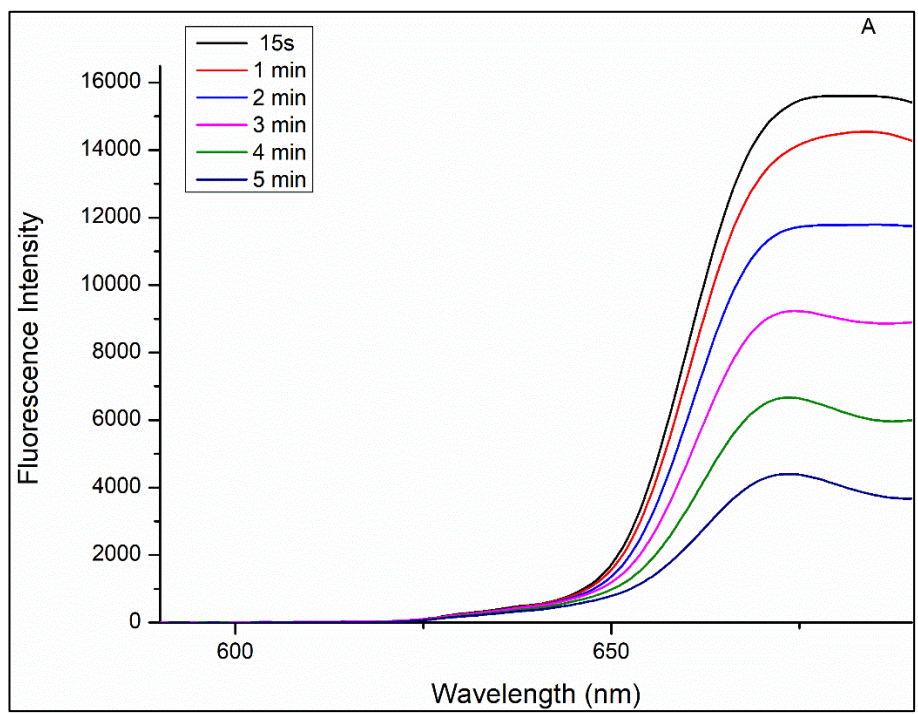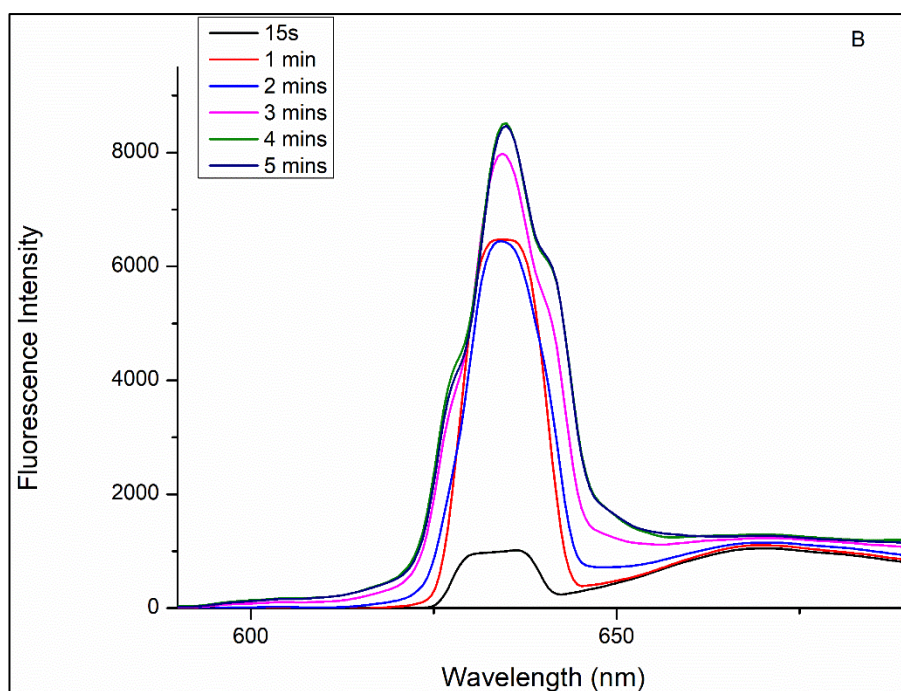
Figure 10. 18: Emission spectra of Atto 633 dye at 0.1 W at A) 1.2×10^{-5} g/mol and B) 1.5×10^{-6} g/ml
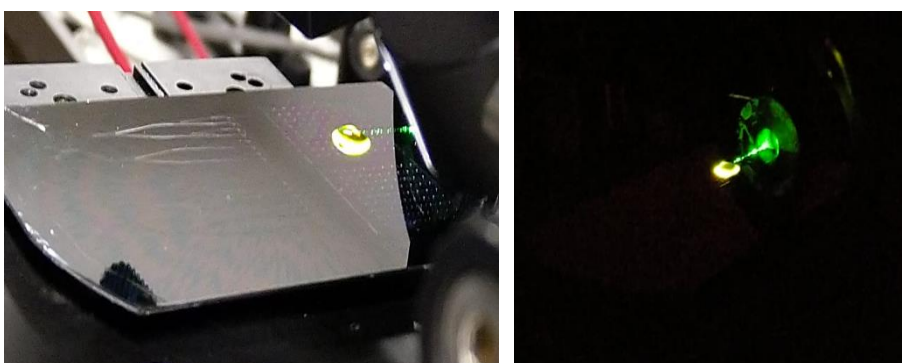
Figure 10. 19: Optofluidic platform with optically activated fluorescein sodium dye

10.4.8 Optofluidic platform testing – Bio-sensing applications

Another possible application for the optofluidic platform would be towards bio-sensing. To this end, an IgG mouse primary antibody was immobilised onto the surface of the platform in specific areas, a schematic of which can be seen in Fig. 10.20. Firstly, the surface of the platform was functionalised using a dilute 5% APTES wash, as this wash gave the most hydrophilic CA result of 44°, when coated on the bare silane coated sol-gel

samples as discussed in section 8.3.1. The primary antibody (antigen) was bound to the surface of the functionalised platform in specific areas using EDC/NHS coupling chemistry as described in section 3.5. Full experimental details are provided in section 3.5. The fluorescently labelled secondary antibody was then pipetted onto the previously bound primary antibody and left to bind via diffusion for 2 hours. The platform was then washed with PBS to ensure any residual unbound antibodies were removed, which can contribute to non-specific binding on the platform surface and compete with the radiative emission. Five antibody concentrations were prepared, 500, 200, 100, 50 and 10 µg/ml and each concentration of antibody was bound to a specific area on the platform. A blank was also prepared and the primary antibody was placed onto the platform but was not bound via EDS/NHS coupling chemistry and so should not have been bound to the surface of the platform. The highest concentration (500 µg/ml) of the secondary antibody labelled with the CF 555 dye was then pipetted onto the platform and left to bind for 2 hours. This blank would act as a background for any non-specific binding of the secondary antibody. Each individual spot was exposed to the green laser at 532nm with a pulse rate of 3 seconds per spot. This was to avoid the possibility of photobleaching of the fluorescently labelled CF555 antibody. No change in the emission signal was captured. In order to asses if the fluorescently labelled antibodies did indeed emit at the wavelength of the laser, 5 µl of each concentration of antibody was pipetted onto the specific spot at the output of the waveguides and excited for 3 second intervals. Five secondary antibody concentrations fluorescently labelled with CF 555 were prepared – 500, 200, 100, 50 and 10 µg/ml. The expected absorbance and emission spectra of the antibodies labelled with CF 555 dye can be seen in Fig 10.21. The change in fluorescence was captured via a spectral analyser and the subsequent concentration curve is plotted in Fig 10.22. It can be seen that as the antibody concentration increases there is a progressive increase in the

fluorescence intensity. A limit of detection of 50 µg/ml was achieved. This result indicates that the optics of the platforms do indeed work and the CF 555 fluorescent fluorophore will fluoresce when excited with the green 532 nm laser. As the fluorescently labelled antibodies were pipetted directly onto the platform and not bound to the primary antibody (antigen), one cannot definitively say whether the fluorescence is due to the antigen-antibody interaction or to non-specific binding of the fluorescently labelled antibody with residual OH groups on the surface of the platform. The experimental optical set up can be seen in Fig. 10.23.

Further optimisation would be needed to assess the binding interactions between the antigen and antibody on the platform as this was a proof of concept only.
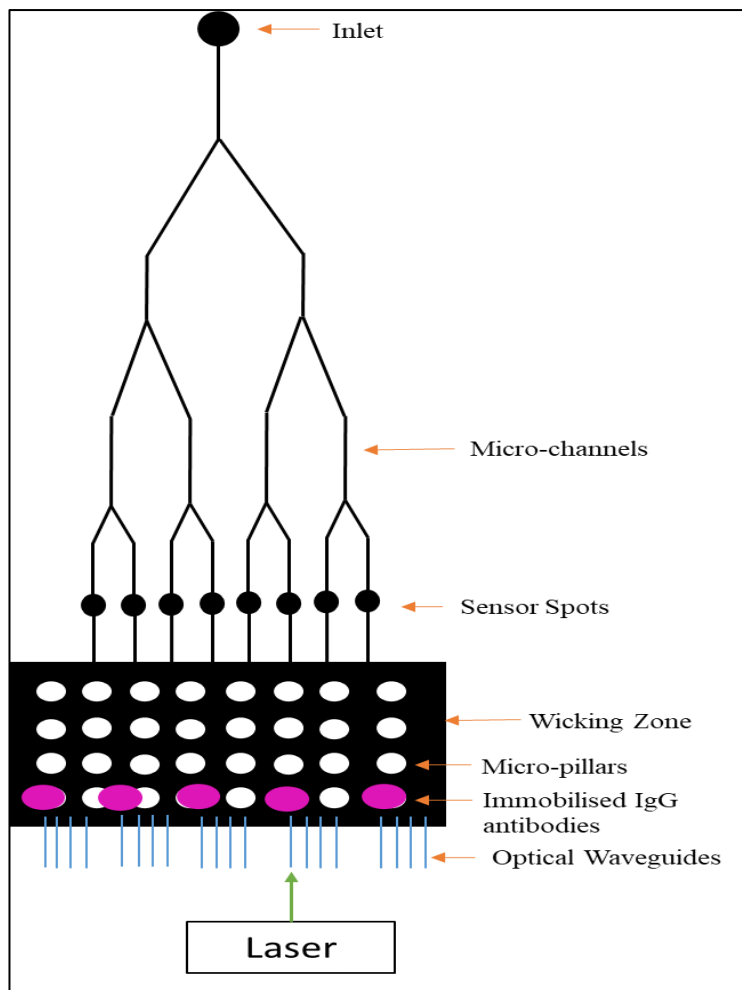
Figure 10. 20: Schematic of the biosensor platform with the location of the IgG immobilised antibodies spots
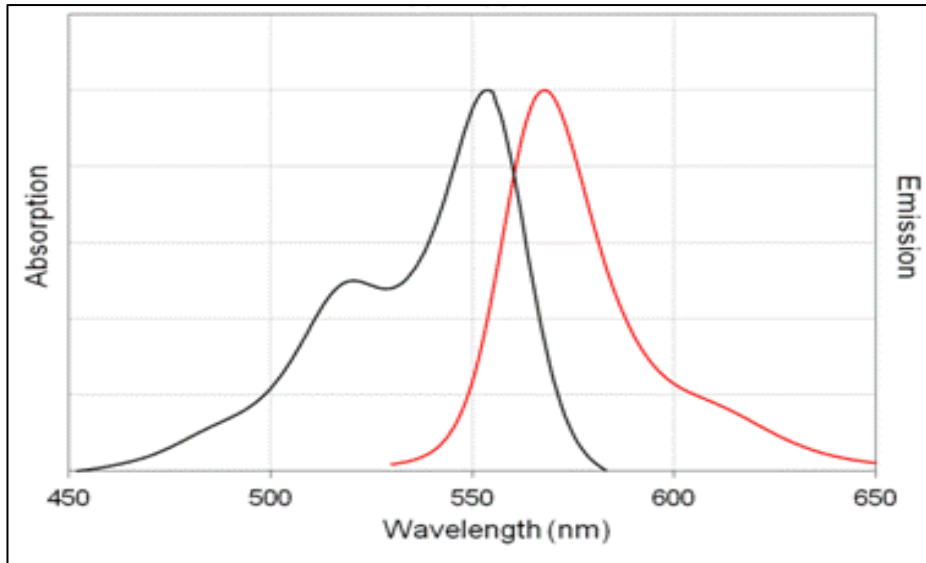
Figure 10. 21: Expected emission and absorbance spectra for the CF 555 labelled antibodies
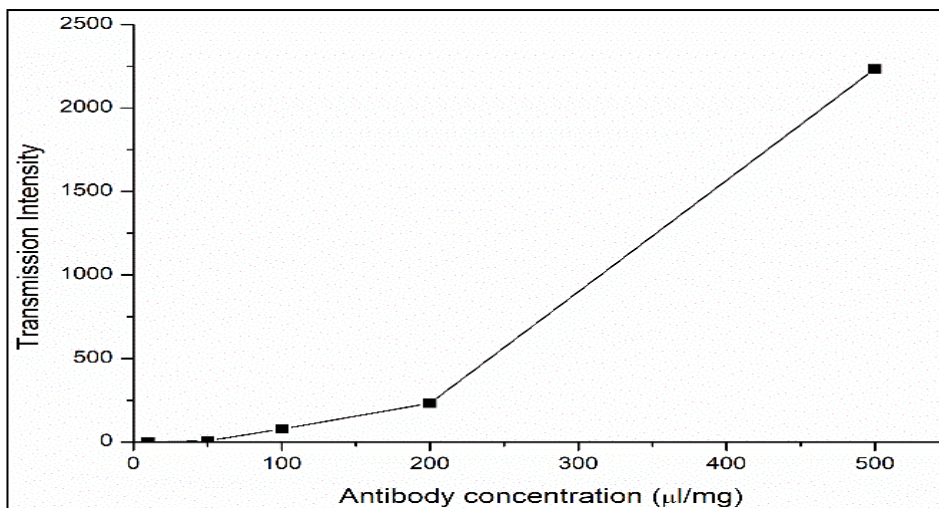
Figure 10. 22: Antibody concentration curve @ 574 nm
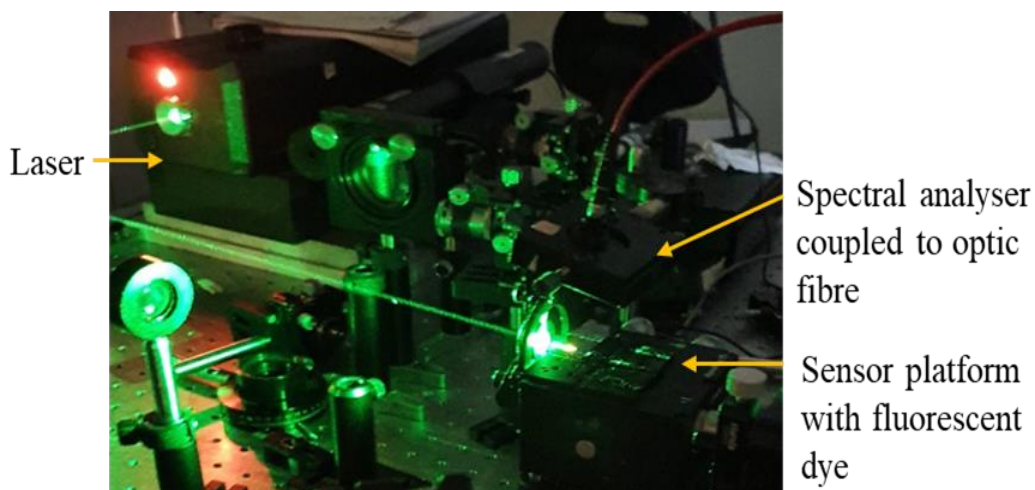
Figure 10. 23: Experimental optical set-up for the monitoring of the emission of the fluorescent dyes and the immunofluorescence

10.5 Conclusion

This chapter was concerned with the fabrication and proof of concept of a novel optofluidic device fabricated via a standard photolithography process. The optofluidic platform was fabricated using 2 different sol-gel formulations that had a refractive index contrast of 0.0035 to ensure the correct insulation for the optical waveguides. The capability of the platform as an optical sensor was tested using a green and red laser line to excite various concentrations to two fluorescent dyes. The capability of the platform towards optical bio-sensing was also carried out, although definite conclusive results would need further optimisation to be achieved.

This chapter therefore has demonstrated the fabrication of a novel optofluidic device and investigated two proof-of-concept applications towards optical sensing and bio-sensing. Importantly to our knowledge, the fabrication of optical waveguides and their integration onto a microfluidic biosensor platform is a novel concept particularly where the sol-gel fabrication material is concerned.

11 General Conclusion and Future Work

The work reported in this thesis aimed at developing a high surface energy hybrid sol-gel material and its application towards the fabrication of microfluidic and optofluidic platforms via standard photolithography processing.

In order to achieve this, a reference photo-reactive hybrid sol-gel material was first developed from a suitable combination of MAPTMS and a zirconium complex and fully characterised in terms of surface properties, structure and thermal behaviour as well as photoreactivity for structuration of micro-channels. It was highlighted for the first time to our knowledge that the curing process can dramatically affect the structure and wettability of hybrid sol-gel coatings, a work that we have reported[179]. The microstructuration of the reference material was also clearly demonstrated and micro-channels with widths measuring 100 µm were successfully fabricated. Following these initial results, 3 purely chemical routes were investigated and a mixture of a physical and chemical route was also investigated to improve the overall wettability and stability of the hybrid materials towards microfluidic and optofluidic applications.

Firstly, the effect of the transition metal concentration and curing process on both the structure and surface properties of the materials was investigated. It was found that the concentration of transition metal governs the condensation process of the silicate network and as its concentration increases, the structure densifies, and further thermal densification is minimised. However, the surface properties maintained a similar behaviour to the reference material. This result was corroborated by both ^{29}Si-NMR and FTIR studies, and it was found that the increase in curing temperature provokes the formation of surface hydroxyl groups, thus explaining the decrease of the CA.

The 2nd strategy involved varying the hydrolysis degree from 25 to 100% with ZPO concentrations of 1 to 30%. By varying the hydrolysis degree and the ZPO concentration,

it was observed that it was possible to control the condensation of the sol-gel network. Although, it is found that the curing process provokes a similar decrease of the CA, the evolution of the CA is more pronounced with the increase of the ZPO and HD, suggesting that the ZPO has a critical role in the surface properties. This is further confirmed by the FTIR and NMR results.

The 3rd strategy consisted of the incorporation of functional alkoxysilanes onto the surface of the sol-gel nanoparticles using 4 different alkoxysilanes- APTES, VTES, GPTMS and TEOS. FTIR and DLS and ^{29}Si-NMR results demonstrated the effective formation of core-shell nanoparticles. In this series of materials, it was found that TEOS showed an increase of the CA in comparison with the reference material, due to the formation of a hydrophobic siloxane shell at the surface of the NPs. GPTMS and VTES showed a similar behaviour to the reference material and a progressive decrease of the CA as the curing temperature increases. Originally APTES, exhibited a decrease of the CA by 22°, the lowest results of all the series investigated here.

The final strategy focused on the combination of a physical (plasma treatment) and chemical route (surface treatment) to modify the surface of the sol-gel coatings in order to improve the surfaces properties and increase the overall wettability and stability over time. Two different plasma pre-treatments were used namely N_2 and Air plasma. The surface treatment consisted of dipping the coatings into dilute silane washes that were composed of varying concentrations of APTES, GPTMS and a mixture of both. CA measurements were employed to monitor the wettability and stability of the coatings over time. The stability was also measured using FTIR focusing on the Si-O-Zr bonds within the silicate backbone of the material. XPS analysis of the coatings provided valuable information regarding the effectiveness of the applied surface treatments. The control samples that were pre-treated with air plasma were found to be the most hydrophilic and

stable, with an average CA value of 36° directly after both surface treatments and 54° after 28 days. Importantly, this strategy demonstrated the importance of combined physical and chemical surface modifications on the sol-gel coatings in order to improve their wettability and stability towards microfluidic applications. Fundamentally, it is shown for the first time that the orientation of the silane is critical in achieving greater hydrophilic properties and that this orientation relies on the applied plasma treatment.

The fabrication and characterisation of the reference material towards microfabrication of both linear micro-channels and a microfluidic sensor platform was also investigated. A standard mask-photolithography process was employed to fabricate micro-channels of varying widths. The optimum curing time was found to be 500s via RI measurements, for the fabrication of the micro-channels. The step height and width of the linear micro-channels and the various micro-structures within the sensor platform were measured with an accuracy between 94-96%, suggesting the development of an adequate fabrication process. More importantly, this demonstrated that it is indeed possible to fabricate micro-channels and microstructures using our hybrid sol-gel material using a standard mask-photolithography process.

Finally, the fabrication of an optofluidic device was established. This device was fabricated via the integration of the previously fabricated microfluidic sensor platform with optical waveguides also fabricated onto the platform by the same mask-photolithography process. Two proof-of concept applications towards optical and bio-sensing applications were demonstrated. Importantly to our knowledge, the fabrication of optical waveguides and their integration onto a microfluidic biosensor platform is a novel concept particularly where the sol-gel fabrication material is concerned.

Although the work reported here has contributed to advance the fundamental aspects of hybrid sol-gel materials and proposed some innovative applications in the fields of

microfluidics and optofluidics for sensing applications, there are a number of questions and challenges that would deserve to be further investigated.

Further characterisation techniques that could be employed to investigate the structure of the materials, in particular with regards to the fabrication of core-shell nanoparticle materials would be both solution and solid state ^{16}O NMR, ^{1}H NMR, ^{13}C NMR and ^{15}N NMR. XPS characterisation could also be employed to look at the first few nm of the surface of the coatings obtained.

The plasma processing could also be further investigated, in particular with emphasis on investing the effect of O_2 plasma towards the wettability and stability of the coatings.

Optimisation of the microfluidic process to ensure less variation between the fabricated and predicated structure widths. Further development towards the sensing applications for the optofluidic device, including the fabrication of an integrated micro and optofluidic photomask for the fabrication of integrated platforms to ensure exact reproducibility. Optimisation of the immunofluorescence technique to ensure the chosen antibodies are bound to the surface of the platform.

Finally, the fields of microfluidics and optofluidics, which were tackled here by the original approach of microstructuration of hybrid sol-gel materials, are multidisciplinary in nature with high societal and economic impacts and will be the subject of future long-term and exciting transdisciplinary collaborative studies in the development of multianalyte biosensor platforms strongly required by both medical industries and people.

References

1. Prakash, S., Pinti, M. & Bhushan, B. Theory, fabrication and applications of microfluidic and nanofluidic biosensors. *Philos. Trans. R. Soc. A Math. Phys. Eng. Sci.* **370**, 2269–2303 (2012).

2. Oubaha, M., Gorin, A., McDonagh, C., Duffy, B. & Copperwhite, R. Development of a multianalyte optical sol-gel biosensor for medical diagnostic. *Sensors Actuators, B Chem.* **221**, 96–103 (2015).

3. McDonagh, C., Sheridan, F., Butler, T. & MacCraith, B. Characterisation of sol-gel-derived silica films. *J. Non. Cryst. Solids* **194**, 72–77 (1996).

4. Brusatin, G. & Della Giustina, G. Hybrid organic-inorganic sol-gel materials for micro and nanofabrication. *J. Sol-Gel Sci. Technol.* **60**, 299–314 (2011).

5. Copperwhite, R. *et al.* Development and characterisation of integrated microfluidics on waveguide-based photonic platforms fabricated from hybrid materials. *Microfluid. Nanofluidics* **11**, 283–296 (2011).

6. Tabeling, P. *Introduction to Microfluidics*. **24**, (OUP Oxford, 2005).

7. Qin, D., Xia, Y., Rogers, J. A., Jackman, R. J. & Whitesides, G. M. Microfabrication,Microstructures and Microsystems. in *Topics in Current Cheimstry* **194**, (1998).

8. Whitesides, G. M. The origins and the future of microfluidics. *Nature* **442**, 368–73 (2006).

9. Guilhem Velvé Casquillas and Timothée Houssin. Microfluidics and microfluidic devices: a review – Elveflow. Available at: http://www.elveflow.com/microfluidic-tutorials/microfluidic-reviews-and-tutorials/microfluidics-and-microfluidic-device-a-review/. (Accessed: 8th October 2015)

10. Wu, W. I., Sask, K. N., Brash, J. L. & Selvaganapathy, P. R. Polyurethane-based microfluidic devices for blood contacting applications. *Lab Chip* **12**, 960–970 (2012).

11. Chanmanwar, R., Balasubramaniam, R. & Wankhade, L. Application and Manufacturing of Microfluidic Devices: Review. *Int. J. Mod. Eng. Res.* **3**, 849–856 (2013).

12. Beebe, D. J., Mensing, G. a & Walker, G. M. Physics and applications of microfluidics in biology. *Annu. Rev. Biomed. Eng.* **4**, 261–286 (2002).

13. Squires, T. M. & Quake, S. R. Microfluidics: Fluid physics at the nanoliter scale. *Rev. Mod. Phys.* **77**, 977–1026 (2005).

14. Sackmann, E. K., Fulton, A. L. & Beebe, D. J. The present and future role of microfluidics in biomedical research. *Nature* **507**, 181–9 (2014).

15. Davies, M. J., Marques, M. P. C. & Radhakrishnan, A. N. P. Microfluidics Theory in Practice. in *Microfluidics in Detection Science* 29–60 (RSC, 2015).

16. Davies, M. J., Marques, M. P. C. & Radhakrishnan, A. N. P. *Microfluidics in Detection Science*. (Royal Society of Chemistry, 2014). doi:10.1039/9781849737609

17. Vollrath, C. & Dittrich, P. S. Microfluidics: Basic Concepts and Microchip Fabrication. in *Unravelling Single Cell Geonmics: Micro and Nanotools* (eds. Bontoux, N., Dauphinot, L. & Potier, M.-C.) (Royal Society of Chemistry, 2010). doi:10.1039/9781849732284

18. Lei, K. I. N. F. Materials and Fabrication Techniques for Nano- and Microfluidic Devices. in *Microfluidics in Detection Science:Lab-on-a-chip Technologies* (ed. Fatima H Labeed, H. O. F.) 1–28 (Royal Society of Chemistry).

19. Oh, K. W. & Ahn, C. H. A review of microvalves. *J. Micromechanics*

Microengineering **16**, (2006).

20.   Laser, D. J. & Santiago, J. G. A review of micropumps. *J. Micromechanics Microengineering* **14**, (2004).

21.   Sainiemi, L., Nissilä, T., Kostiainen, R., Ketola, R. A. & Franssila, S. A microfabricated silicon platform with 60 microfluidic chips for rapid mass spectrometric analysis. *Lab Chip* **11**, 3011–3014 (2011).

22.   Franssila, S. *et al.* A microfabricated nebulizer for liquid vaporization in chemical analysis. *J. Microelectromechanical Syst.* **15**, 1251–1259 (2006).

23.   Tiggelaar, R. M. *et al.* Fabrication of a high-temperature microreactor with integrated heater and sensor patterns on an ultrathin silicon membrane. *Sensors Actuators, A Phys.* **119**, 196–205 (2005).

24.   Harrison, D. J. *et al.* Micromachining a miniaturized capillary electrophoresis-based chemical analysis system on a chip. *Science (80-.).* **261**, 895–897 (1993).

25.   Easley, C. J., Humphrey, J. A. C. & Landers, J. P. Thermal isolation of microchip reaction chambers for rapid non-contact DNA amplification. *J. Micromechanics Microengineering* **17**, 1758–1766 (2007).

26.   Xia, Y. & Whitesides, G. M. Soft lithography. *Annu. Rev. Mater. Sci.* **28**, 153–184 (1998).

27.   Toepke, M. W. & Beebe, D. J. PDMS absorption of small molecules and consequences in microfluidic applications. *Lab Chip* **6**, 1484 (2006).

28.   Prakash, S. & Yeom, J. Chapter 4 - Advanced Fabrication Methods and Techniques. in *Nanofluidics and Microfluidics: Systems and Applications* 87–170 (2014). doi:http://dx.doi.org/10.1016/B978-1-4377-4469-9.00004-4

29.   Ayoib, A., Hashim, U., Thivina, V. & Nordin, N. K. S. *Microfluidics Photomask Design using AutoCAD software for the Application of DNA Extraction in Lab-*

On-A-Chip Biosensing Devices.

30. Photomask | Applied Materials. Available at:

    http://www.appliedmaterials.com/semiconductor/products/photomask/info.

    (Accessed: 20th April 2020)

31. R., H., M., H. & I., A. Design, Fabrication, and Testing of Flexible Antennas. in

    Advancement in Microstrip Antennas with Recent Applications (InTech, 2013).

    doi:10.5772/50841

32. Lei, K. F. *Microfluidics in Detection Science*. (Royal Society of Chemistry,

    2014). doi:10.1039/9781849737609

33. Akbulut, O., Yu, A. A. & Stellacci, F. Fabrication of biomolecular devices via

    supramolecular contact-based approaches. *Chem. Soc. Rev.* **39**, 30–37 (2010).

34. Weibel, D. B. & Whitesides, G. M. Applications of microfluidics in chemical

    biology. *Curr. Opin. Chem. Biol.* **10**, 584–91 (2006).

35. Meijer, H. E. H., Singh, M. K., Kang, T. G., Den Toonder, J. M. J. & Anderson,

    P. D. Passive and active mixing in microfluidic devices. *Macromol. Symp.* **279**,

    201–209 (2009).

36. Velvé Casquillas, G. & Houssin, T. Microfluidic mixers : a short review -

    Elveflow. Available at: https://www.elveflow.com/microfluidic-

    reviews/microfluidic-flow-control/microfluidic-mixers-a-short-review/.

    (Accessed: 20th April 2020)

37. Yeo, L. Y., Chang, H. C., Chan, P. P. Y. & Friend, J. R. Microfluidic devices for

    bioapplications. *Small* **7**, 12–48 (2011).

38. Carrilho, E., Martinez, A. W. & Whitesides, G. M. Understanding wax printing:

    A simple micropatterning process for paper-based microfluidics. *Anal. Chem.* **81**,

    7091–7095 (2009).

39. Hu, J. *et al.* Portable microfluidic and smartphone-based devices for monitoring of cardiovascular diseases at the point of care. *Biotechnology Advances* **34**, 305–320 (2016).

40. Wong, R. & Tse, H. *Lateral flow immunoassay*. (Springer Science & Business Media, 2008, 2008).

41. Horowitz, V. R., Awschalom, D. D. & Pennathur, S. Optofluidics: Field or technique? *Lab Chip* **8**, 1856–1863 (2008).

42. C. Monat, P. Domachuk, B. J. E. Integrated Optics: A new river of light. *Nat. Photonics* **1**, (2007).

43. Pang, L., Chen, H. M., Freeman, L. M. & Fainman, Y. Optofluidic devices and applications in photonics, sensing and imaging. *Lab on a Chip* **12**, 3543–3551 (2012).

44. Psaltis, D., Quake, S. R. & Yang, C. Developing optofluidic technology through the fusion of microfluidics and optics. *Nature* **442**, 381–386 (2006).

45. Heng, X. *et al.* Optofluidic microscopy - A method for implementing a high resolution optical microscope on a chip. *Lab Chip* **6**, 1274–1276 (2006).

46. Levene, M. J. *et al. Zero-Mode Waveguides for Single-Molecule Analysis at High Concentrations. Phys. Rev. Lett* **416**, (2002).

47. Wolfe, D. B. *et al. Dyanmic control of liquid-core/liquid-cladding optical wavequides.* **101**, (2004).

48. Lee, S. K. *et al.* Optofluidics technology based on colloids and their assemblies. *Microfluid. Nanofluidics* **4**, 129–144 (2008).

49. Sinton, D., Gordon, R. & Brolo, A. G. Nanohole arrays in metal films as optofluidic elements: Progress and potential. *Microfluidics and Nanofluidics* (2008). doi:10.1007/s10404-007-0221-0

50. Fan, X. & White, I. M. Optofluidic microsystems for chemical and biological analysis. *Nature Photonics* (2011). doi:10.1038/nphoton.2011.206

51. Masmanidis, S. C. *et al.* Multifunctional nanomechanical systems via tunably coupled piezoelectric actuation. *Science (80-.).* **317**, 780–783 (2007).

52. Lo, S. M. *et al.* Photonic crystal microring resonator for label-free biosensing. *Opt. Express* **25**, 7046 (2017).

53. Cubillas, A. M. *et al.* Photonic crystal fibres for chemical sensing and photochemistry. *Chem. Soc. Rev.* **42**, 8629–8648 (2013).

54. Chen, Y. F. *et al.* Optofluidic opportunities in global health, food, water and energy. *Nanoscale* **4**, 4839–4857 (2012).

55. Mehrotra, P. Biosensors and their applications - A review. *J. Oral Biol. Craniofacial Res.* **6**, 153–159 (2016).

56. Ansari, M. I. H., Hassan, S., Qurashi, A. & Ahmad, F. Biosensors and Bioelectronics Micro fl uidic-integrated DNA nanobiosensors. **85**, 247–260 (2016).

57. Eggins, B. R. Introduction. in *Biosensors: an Introduction* 1–12 (Vieweg+Teubner Verlag, 1996). doi:10.1007/978-3-663-05664-5_1

58. Sidwell, J. S. & Rechnitz, G. A. 'Bananatrode' - An electrochemical biosensor for dompamine. *Biotechnol. Lett.* **7**, 419–422 (1985).

59. Wang, J. & Lin, M. S. Mixed plant tissue carbon paste bioelectrode. *Anal. Chem.* **60**, 1545–1548 (1988).

60. Rackus, D. G., Shamsi, M. H. & Wheeler, A. R. Electrochemistry, biosensors and microfluidics: a convergence of fields. *Chem. Soc. Rev.* **44**, 5320–40 (2015).

61. Damborský, P., Švitel, J. & Katrlík, J. Optical biosensors. *Essays Biochem.* **60**, 91–100 (2016).

62. Fan, X. *et al.* Sensitive optical biosensors for unlabeled targets: A review. *Anal. Chim. Acta* **620**, 8–26 (2008).

63. Homola, J. Surface plasmon resonance sensors for detection of chemical and biological species. *Chem. Rev.* **108**, 462–493 (2008).

64. Bo Liedberg, Claes Nylander, I. L. Surface plasmon resonance for gas detection and biosensing. *Sensors and Actuators* **4**, 299–304 (1983).

65. Farré, M. *et al.* Part per trillion determination of atrazine in natural water samples by a surface plasmon resonance immunosensor. *Anal. Bioanal. Chem.* **388**, 207–214 (2007).

66. Zhang, G. J., Chua, J. H., Chee, R. E., Agarwal, A. & Wong, S. M. Label-free direct detection of MiRNAs with silicon nanowire biosensors. *Biosens. Bioelectron.* **24**, 2504–2508 (2009).

67. Yeom, J. & Shannon, M. A. Detachment lithography of photosensitive polymers: A route to fabricating three-Dimensional structures. *Adv. Funct. Mater.* **20**, 289–295 (2010).

68. Hasan, A. *et al.* Recent advances in application of biosensors in tissue engineering. *Biomed Res. Int.* **2014**, (2014).

69. Marazuela, M. D. & Moreno-Bondi, M. C. Fiber-optic biosensors - An overview. *Analytical and Bioanalytical Chemistry* **372**, 664–682 (2002).

70. Geng, T., Morgan, M. T. & Bhunia, A. K. Detection of low levels of Listeria monocytogenes cells by using a fiber-optic immunosensor. *Appl. Environ. Microbiol.* **70**, 6138–46 (2004).

71. Tang, H. *et al.* A new amperometric method for rapid detection of Escherichia coli density using a self-assembled monolayer-based bienzyme biosensor. *Anal. Chim. Acta* **562**, 190–196 (2006).

72. Magrisso, S., Erel, Y. & Belkin, S. Microbial reporters of metal bioavailability. *Microb. Biotechnol.* **1**, 320–30 (2008).

73. Rathnayake, I. V. N., Megharaj, M., Bolan, N. & Naidu, R. Tolerance of Heavy Metals by Gram Positive Soil Bacteria. *Int. J. Environ. Eng.* **2**, 191–195 (2010).

74. Ali, J., Najeeb, J., Asim Ali, M., Farhan Aslam, M. & Raza, A. Biosensors: Their Fundamentals, Designs, Types and Most Recent Impactful Applications: A Review. *J. Biosens. Bioelectron.* **08**, 1–9 (2017).

75. Antonacci, A., Arduini, F., Moscone, D., Palleschi, G. & Scognamiglio, V. Commercially Available (Bio)sensors in the Agrifood Sector. *Compr. Anal. Chem.* **74**, 315–340 (2016).

76. Wu, J., Dong, M., Rigatto, C., Liu, Y. & Lin, F. Lab-on-chip technology for chronic disease diagnosis. *npj Digit. Med.* **1**, (2018).

77. Hou, H. H., Wang, Y. N., Chang, C. L., Yang, R. J. & Fu, L. M. Rapid glucose concentration detection utilizing disposable integrated microfluidic chip. *Microfluid. Nanofluidics* **11**, 479–487 (2011).

78. Srivastava, S. *et al.* Mediator-free microfluidics biosensor based on titania-zirconia nanocomposite for urea detection. *RSC Adv.* **3**, 228–235 (2013).

79. Niederberger, M. & Pinna, N. *Metal Oxide Nanoparticles in Organic Solvents*. (2009). doi:10.1007/978-1-84882-671-7

80. Pierre, A. C. *Introduction to Sol-Gel Processing*. **1**, (Springer US, 1998).

81. S&TR | May 2005: Novel Materials from Solgel Chemistry. Available at: https://str.llnl.gov/str/May05/Satcher.html. (Accessed: 23rd January 2018)

82. Ebelman, J. J. Mémoire sur de nouvelles combinaisons de l'acide borique avec les éthers, et sur l'éther sulfureux. *Ann. Chim. Phys.* **57**, 331 (1846).

83. Hurd, C. B. Theories for the Mechanism of the Setting of Silicic Acid Gels.

Chem. Rev. **22**, 403–422 (1938).

84. Sakka, S. History of the Sol–Gel Chemistry and Technology. in *Handbook of Sol-Gel Science and Technology* 1–27 (Springer International Publishing, 2016). doi:10.1007/978-3-319-19454-7_87-1

85. Sanchez, C. & Ribot, F. Design of Hybrid Organic-Inorganic Materials Synthesized Via Sol-Gel Chemistry. *New J. Chem.* **18**, 1007–1047 (1994).

86. Schubert, U. Part One Sol – Gel Chemistry and Methods. *Sol-Gel Handb. Synth. Process.* 1–28 (2015).

87. Schottner, G. Hybrid Sol - Gel-Derived Polymers : Applications of Multifunctional Materials. *Chem.Mater* **13**, 3422–3435 (2001).

88. Malucelli, G. Hybrid Organic/Inorganic Coatings Through Dual-Cure Processes: State of the Art and Perspectives. *Coatings* **6**, 10 (2016).

89. Tjong, S. C. & Chen, H. Nanocrystalline materials and coatings. *Mater. Sci. Eng. R Reports* **45**, 1–88 (2004).

90. Politechnika Wrocławska., D., Higgins, C., Klukowska, A., Maccraith, B. D. & Mcdonagh, C. *Materials science. Materials Science Poland* **Vol. 25**, **No. 3**, (Technical University of Wrocław, 2007).

91. PARK, M., KOMARNENI, S. & CHOI, J. Effect of substituted alkyl groups on textural properties of ORMOSILs. *J. Mater. Sci.* **33**, 3817–3821 (1998).

92. Gabrielli, L. *et al.* Exploring GPTMS reactivity against simple nucleophiles: Chemistry beyond hybrid materials fabrication. *RSC Adv.* **4**, 1841–1848 (2014).

93. Li, Y. S., Wang, Y., Tran, T. & Perkins, A. Vibrational spectroscopic studies of (3-mercaptopropyl)trimethoxylsilane sol-gel and its coating. *Spectrochim. Acta - Part A Mol. Biomol. Spectrosc.* **61**, 3032–3037 (2005).

94. Catauro, M., Cristina, M. & Bollino, F. Acta Astronautica Sol – gel hybrid

materials for aerospace applications : Chemical characterization and comparative investigation of the magnetic properties. *Acta Astronaut.* **117**, 153–162 (2015).

95.   Wen, J., Vasudevan, V. J. & Wilkes, G. L. Abrasion resistant inorganic/organic coating materials prepared by the sol-gel method. *J. Sol-gel Sci. Technol.* **5**, 115–126 (1995).

96.   Zheng, S. & Li, J. Inorganic-organic sol gel hybrid coatings for corrosion protection of metals. *J. Sol-Gel Sci. Technol.* **54**, 174–187 (2010).

97.   Skrdla, P. J., Saavedra, S. S., Armstrong, N. R., Mendes, S. B. & Peyghambarian, N. Sol-gel-based, planar waveguide sensor for water vapor. *Anal. Chem.* **71**, 1332–1337 (1999).

98.   Elmaghrum, S. *et al.* Development of a sol-gel photonic sensor platform for the detection of biofilm formation. *Sensors Actuators, B Chem.* **177**, 357–363 (2013).

99.   Owens, G. J. *et al.* Sol-gel based materials for biomedical applications. *Prog. Mater. Sci.* **77**, 1–79 (2016).

100.   El-Batal, F. H., El-Kheshen, A. A., Abd El Aty, A. A. & El-Bassyouni, G. T. Studies of Bone-Bonding Ability and Antibacterial Properties of Ag+, Cu2+ or Zn2+ ions Doping within Hench's Bioglass and Glass-Ceramic Derivatives. *Silicon* **10**, 1231–1241 (2018).

101.   Jaiswal, S., McHale, P. & Duffy, B. Preparation and rapid analysis of antibacterial silver, copper and zinc doped sol-gel surfaces. *Colloids Surfaces B Biointerfaces* **94**, 170–176 (2012).

102.   Bracco, G. & Holst, B. *Surface science techniques*. *Springer Series in Surface Sciences* **51**, (2013).

103.   Ghadimi, M. R. & Dolati, A. Preparation and characterization of superhydrophobic and highly oleophobic FEVE-SiO2 nanocomposite coatings.

Prog. Org. Coatings **138**, 105388 (2020).

104. Nuraje, N., Khan, W. S., Lei, Y., Ceylan, M. & Asmatulu, R. Superhydrophobic electrospun nanofibers. *J. Mater. Chem. A* **1**, 1929–1946 (2013).

105. Conroy, M. & Armstrong, J. A comparison of surface metrology techniques. in *Optical Micro- and Nanometrology in Microsystems Technology* (eds. Gorecki, C., Asundi, A. K. & Osten, W.) 61880B (2006). doi:10.1117/12.663390

106. Di Gianfrancesco, A. Technologies for chemical analyses, microstructural and inspection investigations. in *Materials for Ultra-Supercritical and Advanced Ultra-Supercritical Power Plants* 197–245 (Elsevier Inc., 2016). doi:10.1016/B978-0-08-100552-1.00008-7

107. Holbrook, R. D., Galyean, A. A., Gorham, J. M., Herzing, A. & Pettibone, J. Overview of Nanomaterial Characterization and Metrology. in *Frontiers of Nanoscience, Volume 8 - Characterization of Nanomaterials in Complex Environmental and Biological Media* **8**, 47–87 (2015).

108. Lucius, A. L., Veronese, P. K. & Stafford, R. P. Dynamic light scattering to study allosteric regulation. *Methods Mol. Biol.* **796**, 175–86 (2012).

109. DLS Based Analysis Service - Creative Proteomics. Available at: https://www.creative-proteomics.com/support/dls-based-analysis-service.htm. (Accessed: 11th January 2018)

110. Rahaman, A.-U. *Nuclear Magnetic Spectroscopy - Basic Principles*. (Kluwer Academic Publishers, 1986).

111. Du, Y. *et al.* An overview on phase equilibria and thermodynamic modeling in multicomponent Al alloys: Focusing on the Al–Cu–Fe–Mg–Mn–Ni–Si–Zn system. *Calphad* **35**, 427–445 (2011).

112. differential-thermal-analysis-differential-scanning-calorimetry-6-638.jpg

(638×479). Available at:

https://image.slidesharecdn.com/differentialthermalanalysis-140806013352-

phpapp01/95/differential-thermal-analysis-differential-scanning-calorimetry-6-

638.jpg?cb=1407290261. (Accessed: 10th January 2018)

113.   Smith, B. C. *Fundamentals of Fourier Transform Infrared Spectroscopy*.

Fundamentals of Fourier Transform Infrared Spectroscopy (CRC Press, 2011).

doi:10.1201/b10777

114.   F. BLOCH, W. W. H. and M. P. The nuclear induction experiment. *Phys. Rev.*

70, 474–485 (1946).

115.   Uhlig, F. & Dortmund, D. Si NMR Some Practical Aspects. *Inorg. Chem.* **2**,

208–222 (2000).

116.   Zhou, W., Apkarian, R. P. & Wang, Z. L. Fundamentals of Scanning Electron

Microscopy. *Scanning Microsc. Nanotechnol.* 1–40 (2007). doi:10.1007/978-0-

387-39620-0_1

117.   Schematic diagram of the SEM working principle [32]. Available at:

https://www.researchgate.net/figure/261702149_Figure-1-Schematic-diagram-of-

the-SEM-working-principle-32. (Accessed: 31st January 2018)

118.   Newton, B. Ionic Contamination and Analytical Techniques for Ionic

Contaminants. *Dev. Surf. Contam. Clean. - Fundam. Appl. Asp.* 653–673 (2008).

doi:10.1016/B978-081551555-5.50013-7

119.   Huang, Y. Nanocharacterisation of Nanocomposite Materials. in *Nanocomposite*

Coatings and Nanocomposite (ed. Öchsner, A. Ahmed, W. Ali, N.) 51–91 (Trans

Tech Publications Ltd, 2009).

120.   Energy dispersive x ray (EDX) elemental analysis of ZnSe powder,... Available

at: https://www.researchgate.net/figure/FIG-2-Energy-dispersive-x-ray-EDX-

elemental-analysis-of-ZnSe-powder-chemical-composition-of_261708250_fig2. (Accessed: 31st January 2018)

121.   Mather, R. R. *Surface modification of textiles by plasma treatments*. *Surface Modification of Textiles* (Woodhead Publishing Limited, 2009). doi:10.1533/9781845696689.296

122.   Hertz, H. Ueber einen Einfluss des ultravioletten Lichtes auf die electrische Entladung. *Ann. Phys.* **267**, 983–1000 (1887).

123.   Toulhoat, Herve Raybaud, P. Catalysis by Transition Metal Sulfides: from molecular theory to industrial application. in *Focus on Catalysts* **2014**, 8 (2014).

124.   Öchsner, A., Ahmed, W. & Ali, N. *Nanocomposite Coatings and Nanocomposite Materials*. *Trans Tech Publications Ltd* (Trans Tech Publications Ltd, 2009).

125.   Attia, S., Wang, J., Wu, G., Shen, J. & Ma, J. Review on Sol—Gel Derived Coatings: Process, Techniques and Optical Applications. *J. Mater. Sci. Technol.* **18**, 211–218 (2002).

126.   Prakash, S. & Yeom, J. *Nanofluidics and Microfluidics - Systems and Applications*. *Elsevier* (Elsevier, 2014).

127.   Ulrich, R. & Torge, R. Measurement of Thin Film Parameters with a Prism Coupler. *Appl. Opt.* **12**, 2901 (1973).

128.   Zhang, J. Z. Spectroscopic Techniques for Studying Optical Properties of Nanomaterials. in *Optical Properties and Spectroscopy of Nanomaterials* 11–46 (2009). doi:10.1142/9789812836663_0002

129.   Shakar Kumar Selvaraja, P. S. Review on Optical Waveguides. in *Intech* **i**, 13 (2016).

130.   Idachaba, F., Ike, D. U. & Hope, O. Future Trends in Fiber Optics Communication. in *Proceedings of the World Congress on Engineering 2014* **I**,

2–6 (2014).

131. Keleştemur, S., Altunbek, M. & Culha, M. Influence of EDC/NHS coupling chemistry on stability and cytotoxicity of ZnO nanoparticles modified with proteins. *Appl. Surf. Sci.* **403**, 455–463 (2017).

132. Kim, J., Seidler, P., Wan, L. S. & Fill, C. Formation, structure, and reactivity of amino-terminated organic films on silicon substrates. *J. Colloid Interface Sci.* **329**, 114–119 (2009).

133. Oubaha, M. *et al.* Influence of hybrid organic–inorganic sol–gel matrices on the photophysics of amino-functionalized UV-sensitizers. *J. Mater. Sci.* **46**, 400–408 (2011).

134. Brinker, C. J. HYDROLYSIS AND CONDENSATION OF SILICATES: EFFECTS ON STRUCTURE. *J. Non. Cryst. Solids* **100**, 31–50 (1988).

135. C. Brinker & Scherer, G. *Sol-Gel Science: The Physics and Chemistry of Sol-Gel Processing. Advanced Materials* **3**, (1990).

136. Buckley, A. M. & Greenblatt, M. *The Sol-Gel Preparation of Silica Gels.*

137. Morrow, B. A. & McFarlan, A. J. Surface vibrational modes of silanol groups on silica. *J. Phys. Chem.* **96**, 1395–1400 (1992).

138. Pickup, D. M., Mountjoy, G., Wallidge, G. W., Newporta, R. J. & Smithb, M. E. Structure of (ZrO2)x(SiO2)1-x xerogels (x-0.1,0.2,0.3 and 0.4) FTIR, 29Si and 17O MAS NMR and EXAFS. *Phys. Chem. Chem. Phys.* 2527–2533 (1999). doi:10.1039/A901401B

139. Lerot, L. & Low, P. F. Effect of swelling on the infrared absorption spectrum of montmorillonite. *Clays Clay Miner.* **24**, 191–199 (1976).

140. Elvira, M. R. *et al.* Study and Characterization of Organically Modified Silica-Zirconia Anti-Graffiti Coatings Obtained by Sol-Gel. *J. Chem. Chem. Eng* **7**,

120–131 (2013).

141. Handke, M. & Kwany, M. Infrared spectroscopic study of octahydridooctasilsesquioxane hydrolytic polycondensation. *Vib. Spectrosc.* **74**, 127–131 (2014).

142. Hanuhov, T., Asulin, E. & Gvishi, R. Evaluation of opto-mechanical properties of UV-cured and thermally-cured sol-gel hybrids monoliths as a function of organic content and curing process. *J. Non. Cryst. Solids* **471**, 301–311 (2018).

143. Versace, D. L., Soppera, O., Lalevée, J. & Croutxé-Barghorn, C. Influence of zirconium propoxide on the radical induced photopolymerisation of hybrid sol-gel materials. *New J. Chem.* **32**, 2270–2278 (2008).

144. Gizdavic-Nikolaidis, M. R., Zujovic, Z. D., Edmonds, N. R., Bolt, C. J. & Easteal, A. J. Spectroscopic characterization of GPTMS/DETA and GPTMS/EDA hybrid polymers. *J. Non. Cryst. Solids* **353**, 1598–1605 (2007).

145. Cullen, M. *et al.* Correlation between the structure and the anticorrosion barrier properties of hybrid sol – gel coatings : application to the protection of AA2024-T3 alloys. (2017). doi:10.1007/s10971-017-4349-4

146. Mahi, A., Belbachir, M., Ammari, A., Meghaber, R. & Ferrahi, M. I. Synthesis and characterization of poly(N-phenyl succinimide-thiophene) conducting polymer catalyzed by Maghnite-H+. *J. Electroanal. Chem.* **823**, 92–97 (2018).

147. Belhocine, M., Haouzi, A., Ammari, A., Chaker, Y. & Bassou, G. On the effect of Benzethonium intercalation process: Structural and dielectric properties of exchanged montmorillonite. *Colloids Surfaces A Physicochem. Eng. Asp.* **577**, 224–230 (2019).

148. Aboulkacem, K. *et al.* Thermally activated charge transport in modified tetragonal zirconia thin films prepared by sol-gel method. *Jpn. J. Appl. Phys.* **57**,

(2018).

149. Rahman, I. A. & Padavettan, V. Synthesis of Silica nanoparticles by Sol-Gel: Size-dependent properties, surface modification, and applications in silica-polymer nanocompositesa review. *J. Nanomater.* **2012**, (2012).

150. Marques, M. E., Mansur, A. A. P. & Mansur, H. S. Chemical functionalization of surfaces for building three-dimensional engineered biosensors. *Appl. Surf. Sci.* **275**, 347–360 (2013).

151. Oubaha, M., Smaïhi, M., Etienne, P., Coudray, P. & Moreau, Y. Spectroscopic characterization of intrinsic losses in an organic–inorganic hybrid waveguide synthesized by the sol–gel process. *J. Non. Cryst. Solids* **318**, 305–313 (2003).

152. Echeverría, J. C. *et al.* Kinetics of the acid-catalyzed hydrolysis of tetraethoxysilane (TEOS) by 29Si NMR spectroscopy and mathematical modeling. *J. Sol-Gel Sci. Technol.* **86**, 316–328 (2018).

153. Gabrielli, L. *et al.* Epoxide opening versus silica condensation during sol-gel hybrid biomaterial synthesis. *Chem. - A Eur. J.* **19**, 7856–7864 (2013).

154. Caravajal, G. S., Leyden, D. E., Quinting, G. R. & Maciel, G. E. Structural Characterization of and Carbon- 13 Nuclear Magnetic Resonance. *Society* 1776–1786 (1988).

155. Mazúr, M., Mlynárik, V., Valko, M. & Pelikán, P. The time evolution of the sol-gel process:29Si NMR study of the hydrolysis and condensation reactions of tetraethoxysilane. *Appl. Magn. Reson.* **18**, 187–197 (2000).

156. Sardon, H., Irusta, L., Fernández-Berridi, M. J., Lansalot, M. & Bourgeat-Lami, E. Synthesis of room temperature self-curable waterborne hybrid polyurethanes functionalized with (3-aminopropyl)triethoxysilane (APTES). *Polymer (Guildf).* **51**, 5051–5057 (2010).

157. Kim, T. W., Kim, I. Y., Park, D. H., Choy, J. H. & Hwang, S. J. Highly stable nanocontainer of APTES-anchored layered titanate nanosheet for reliable protection/recovery of nucleic acid. *Sci. Rep.* **6**, 1–12 (2016).

158. Khanjanzadeh, H. *et al.* Surface chemical functionalization of cellulose nanocrystals by 3-aminopropyltriethoxysilane. *Int. J. Biol. Macromol.* **106**, 1288–1296 (2018).

159. Pouxviel, J. C., Boilot, J. P., Beloeil, J. C. & Lallemand, J. Y. NMR study of the sol/gel polymerization. *J. Non. Cryst. Solids* **89**, 345–360 (1987).

160. Mishra, A. K., Allauddin, S., Narayan, R., Aminabhavi, T. M. & Raju, K. V. S. N. Characterization of surface-modified montmorillonite nanocomposites. *Ceram. Int.* **38**, 929–934 (2012).

161. Vandencasteele, N. & Reniers, F. Plasma-modified polymer surfaces: Characterization using XPS. *J. Electron Spectros. Relat. Phenomena* (2010). doi:10.1016/j.elspec.2009.12.003

162. Prakash, S., Karacor, M. B. & Banerjee, S. Surface modification in microsystems and nanosystems. *Surf. Sci. Rep.* **64**, 233–254 (2009).

163. Abourayana, H. M. & Dowling, D. P. Plasma Processing for Tailoring the Surface Properties of Polymers. in *Surface Energy* (InTech, 2015). doi:10.5772/60927

164. Fabbri, P. & Messori, M. Surface Modification of Polymers: Chemical, Physical, and Biological Routes. in *Modification of Polymer Properties* 109–130 (Elsevier Inc., 2017). doi:10.1016/B978-0-323-44353-1.00005-1

165. Oláh, A., Hillborg, H. & Vancso, G. J. Hydrophobic recovery of UV/ozone treated poly(dimethylsiloxane): Adhesion studies by contact mechanics and mechanism of surface modification. *Appl. Surf. Sci.* **239**, 410–423 (2005).

166. Junkar, I., Vesel, A., Cvelbar, U., Mozetič, M. & Strnad, S. Influence of oxygen and nitrogen plasma treatment on polyethylene terephthalate (PET) polymers. *Vacuum* **84**, 83–85 (2009).

167. Vesel, A., Junkar, I., Cvelbar, U., Kovac, J. & Mozetic, M. Surface modification of polyester by oxygen- And nitrogen-plasma treatment. *Surf. Interface Anal.* **40**, 1444–1453 (2008).

168. Jasksa, G. AFM and XPS Study of Aminosilanes on Si. 3–6 (2014).

169. Kang, D. J., Han, D. H. & Kang, D. P. Fabrication and characterization of photocurable inorganic-organic hybrid materials using organically modified colloidal-silica nanoparticles and acryl resin. *J. Non. Cryst. Solids* **355**, 397–402 (2009).

170. Liu, J., O'Reilly, J. M., Smith, T. W. & Prasad, P. N. Photopatterning hybrid sol-gel glass materials prepared from ethylene tellurate and alkoxysilane. *J. Non. Cryst. Solids* **351**, 2440–2445 (2005).

171. Lavrencic Stangar, U. *et al.* IR and NMR time-resolved studies on the hydrolysis and condensation of methacryloxyalkylsilanes. *J. Sol-Gel Sci. Technol.* **49**, 329–335 (2009).

172. Graziola, F. *et al.* UV-photopolymerisation of poly(methyl methacrylate)-based inorganic-organic hybrid coatings and bulk samples reinforced with methacrylate-modified zirconium oxocluster. *Polymer (Guildf).* **49**, 4332–4343 (2008).

173. Mazingue, T., Kribich, R. K., Etienne, P. & Moreau, Y. Simulations of refractive index variation in a multimode interference coupler: Application to gas sensing. *Opt. Commun.* **278**, 312–316 (2007).

174. Chu, S. T., Huang, W. P. & Chaudhuri, S. K. Simulation and analysis of

waveguide based optical integrated circuits. *Comput. Phys. Commun.* **68**, 451–484 (1991).

175. Ab-Rahman, M. S., Aziz, A. N. A., Nordin, R. & Jumari, K. Optimum design of an optical waveguide: Determination of the branching angle of s-bend waveguides. *Optik (Stuttg).* **200**, 163249 (2020).

176. Song, L., Hennink, E. J., Young, I. T. & Tanke, H. J. Photobleaching kinetics of fluorescein in quantitative fluorescence microscopy. *Biophys. J.* **68**, 2588–2600 (1995).

177. Goldberg, M. F. & Romanchuk, K. G. *DIAGNOSTIC AND SURGICAL TECHNIQUES Fluorescein. Physicochemical Factors Affecting Its Fluorescence*. *SURVEY OF OPHTHALMOLOGY* **26**,

178. Fahmy, H. M., Negm, N. A., Elwahy, A. H. M. & Abou Kana, M. T. H. Laser induced fluorescence, photo-physical parameters and photo-stability of new fluorescein derivatives. *J. Mol. Liq.* **229**, 31–44 (2017).

179. MacHugh, E., Cullen, M., Kaworek, A., Duffy, B. & Oubaha, M. The effect of curing and zirconium content on the wettability and structure of a silicate hybrid sol-gel material. *J. Non. Cryst. Solids* **525**, 1–7 (2019).

Publications

Maikki Cullen, Muhammed Morhsed, Mary O'Sullivan, **Emma MacHugh**, Brendan Duffy, Mohamed Oubaha. "Correlation between the structure and anticorrosion properties of hybrid sol-gel coatings: applications for the protection of AA2024-T3 alloys." Journal of Sol-Gel Science and Technology, February 2017, Volume 82, Issue 3, 801–816

MacHugh, E., Cullen, M., Kaworek, A., Duffy, B. & Oubaha, M. The effect of curing and zirconium content on the wettability and structure of a silicate hybrid sol-gel material. *J. Non. Cryst. Solids* **525**, 1–7 (2019)